FAILURE OF SLOPES

Thesis by

Paul Brian Burridge

In Partial Fulfillment of the Requirements

for the Degree of

Doctor of Philosophy

California Institute of Technology

Pasadena, California

1987

(Submitted March 13, 1987)

TABLE OF CONTENTS

Page

Page

Page

Page

ACKNOWLEDGMENTS

This investigation of slope failure was conducted with the guidance and support of Professor R.F. Scott, whose interest and suggestions were always a source of inspiration and encouragement, and to whom I extend my sincere thanks.

Many other people contributed in various ways to this study, and to each and every one of them I am also grateful:

John Lee built most of the lucite mold of Section 2.5.2 and designed the pencil lead support circuitry of Section 2.7, while Elmer Szombathy assisted in the construction of the pencil lead transducers of Section 2.6.2.

Film digitization would not have been possible without access to the facilities of the Jet Propulsion Laboratory and the expertise of Joe Fulton and June Lee, and Garrett Jeong helped with subsequent processing of the digitized images at Caltech.

Stewart Silling developed the finite difference algorithm of Chapter 7 during a study of plane finite elastostatics, and was of invaluable assistance in applying the algorithm to the analysis of slope stability.

Richard Gomez developed and printed most of the photographs, Cecilia Lin finalized the line drawings, and Crista Potter typeset Table 5.1.

Jason Wakugawa, Jim Kamm, Scott Patton and Doug O'Handley contributed many helpful discussions, as did Agnès Allard who also lent a helping hand on the centrifuge when needed. The support of my roommates and other fellow students is also acknowledged with thanks.

Finally, I am especially grateful to Mum, Dad, Jennifer and David, and my close friends met through extracurricular sport, for their constant encouragement and support throughout my studies at Caltech.

ABSTRACT

The dynamic mechanism of slope failure is studied both experimentally and analytically to establish the spatial and temporal process of failure initiation and propagation during collapse of a natural or man-made slope.

Model slopes, constructed of a brittle cemented sand material, are tested to collapse in a geotechnical centrifuge and the dynamics of failure recorded by motion picture film and mechanical detectors within the slope specimen. Shear failure is observed to initiate at the toe and propagate rapidly to the crest in the presence of crest tension cracking.

A finite difference approach is taken to numerically solve the plane strain slope stability problem under gravity, based on unstable material behavior. Using a Lagrangian differencing scheme in space and explicit integration in time with dynamic relaxation, the numerical method finds the equilibrium state of the slope as the large-time limit of a dynamic problem with artificial parameters. The solution predicts localized shear failure zones which initiate at the slope toe and propagate to the slope crest in the manner and geometry observed in the centrifuge tests. In so doing, the finite difference algorithm also demonstrates an apparent ability to predict shear failure mechanisms in solid continua in general.

LIST OF FIGURES

Figure Page

Figure Page

Figure **Page**

Figure **Page**

Figure **Page**

Figure **Page**

LIST OF TABLES

LIST OF SYMBOLS

b_f	body force magnitude
c	local wave speed
$\overline{c}$	area-average wave speed
c_M	cohesion
e	Lagrangian strain
e_*	most negative principal strain
f_ν	$\dfrac{2(1+\nu)}{3(1-2\nu)}$
g	Earth's gravitational acceleration
h	time step
m	mass
p	confining pressure
r	radial distance from crack tip
t	time
t_r	ramp time
$[t_1, t_2]$	time interval ($t_1 \leq t \leq t_2$)

A	area
C	closed curve
D	quadrilateral region
E	modulus of elasticity
G	conventional shear modulus ($G = \tau_S / \gamma_S$)
K	bulk modulus
K_2	soil constant
L	characteristic length
S	shear modulus ($S = \tau_M / \epsilon_M$)
S_{eff}	effective shear modulus
S_1 , S_2	soil constants
$\mathcal{R}$	region of reference configuration
$\mathcal{R}^*$	region of deformed configuration
$\partial\mathcal{R}$	boundary of region $\mathcal{R}$
$\mathbf{a}$	acceleration
$\mathbf{b}$	Cauchy body force
$\mathbf{b}_0$	Piola body force

$\mathbf{f}_{\text{int}}$	nodal force from internal stresses
$\mathbf{f}_{\text{body}}$	nodal force from body forces
$\mathbf{f}_{\text{bdry}}$	nodal force from boundary tractions
$\mathbf{f}_{\text{tot}}$	total nodal force
$\mathbf{v}$	velocity
$\mathbf{x}$	location of material particle in reference configuration
$\mathbf{y}$	location of material particle in deformed configuration
$\hat{\mathbf{y}}$	deformation
$\mathbf{Y}$	specified deformation
α, β	component in plane $(\alpha, \beta = 1, 2)$
γ_s	principal engineering shear strain
$\delta_{\alpha\beta}$	Kronecker delta
ϵ	zone width
$\epsilon_1, \epsilon_2, \epsilon_3$	principal strains
ϵ_v	volumetric strain
ϵ_M	radius of Mohr's circle of strain
ϵ_{M1} , ϵ_{M2}	soil constants

η	$\frac{\xi h}{2}$
θ	dilatation
λ^*	modified Lamé constant
μ^*	modified Lamé constant
ν	Poisson's ratio
ξ	damping coefficient
ρ	mass density
σ	Piola stress
$\sigma_1, \sigma_2, \sigma_3$	principal stresses
σ'_m	mean principal effective stress in psf
σ_N	normal stress acting on failure plane
τ	Cauchy stress
τ_F	shear stress to cause failure
τ_M	radius of Mohr's circle of stress
τ_S	principal shear stress
τ_P	peak shear stress
τ_R	soil constant

ϕ	friction angle
ψ	any sufficiently smooth field
$\omega_{\max}$	highest natural angular frequency of undamped mesh

Superscripts

i	column index of node
j	row index of node
n	time step index

Subscripts

0	reference configuration
α, β, γ	indices ($\alpha, \beta, \gamma = 1, 2$)
k	index ($k = 1, 2, 3$)
$\mathbf{x}$	with respect to reference configuration
$\mathbf{y}$	with respect to deformed configuration

Chapter 1

INTRODUCTION

1.1 SLOPE FAILURE

The failure of earth structures such as natural slopes or man-made embankments, excavations and dams is an age-old phenomenon which has inflicted heavy loss of life and property on communities worldwide. The understanding of slope failure, however, has generally been inadequate to prevent destruction in every case, with the result that this soil mechanics problem remains incompletely resolved to the present day.

Slope failure, shown schematically in Figure 1.1 and photographically in Figure 1.2, typically involves formation of a curved failure surface through a slope of cohesive soil, followed by relative sliding between the two created blocks of soil along this surface. Bulging at the toe and tension cracking along the slope crest are also commonly observed. Although soil which is highly sensitive or has preferred planes of weakness gives rise to slightly different modes of failure, it is the "rotational" mode of Figure 1.1 which is the most common and thus the subject of study here.

Historically, slope failure appears to have been first addressed by Collin in

1846 [20] with studies of clay landslides in France, but it was not until the 1920's that Fellenius [28] developed a practical engineering solution to the problem during construction of the Swedish railroads, when rotational embankment collapses were prolific. The Fellenius method, however, and subsequent derivatives (see Section 1.2.1), required many oversimplifying assumptions to make a mathematical solution possible and hence could not model the phenomenon in sufficient detail to permit an accurate prediction of the slope failure mechanism. Since the sequence of events which constitute the mechanism of slope failure has never been clearly understood, it was the aim of this study to conduct a series of experiments to observe the initiation and propagation of a failure surface through a slope, and to use these observations as the basis for development of an improved method of slope stability analysis.

1.2 SLOPE STABILITY ANALYSIS

1.2.1 Available methods

All but a few of the methods which have traditionally been used to analyse the stability of a slope under static gravity loading (*e.g.*, [11,14,17,28,45,46,60,95,106, 107]) give upper bound solutions based on the global principle of *limit equilibrium*. Such methods start by *assuming* the profile of a two or three dimensional surface through the slope (typically an inclined plane, circular arc or logarithmic spiral) on which failure is postulated to occur. They proceed to compute the destabilizing

and available resisting forces acting on this surface in an integrated or *global* sense, and establish a *factor of safety* against failure as the ratio of available resisting force to destabilizing force. The process is repeated for another assumed surface until, by trial and error, the critical or correct failure surface is found with the lowest factor of safety. There is, however, no guarantee that the correct failure surface will be one of those assumed for trial, hence placing a heavy burden on the engineering judgment of the analyst. Aside from this dilemma, these methods usually fail to represent the distribution of stresses along the failure surface correctly, since equilibrium is satisfied in a global sense only. Given this kinetic deficiency, and the initial kinematic assumption of a fully developed failure surface, the limit equilibrium principle precludes capture of the local stress-strain details considered important to any method of analysis which hopes to follow the evolution (*i.e.*, initiation and propagation) of slope failure.

Dynamic analysis is accommodated by the limit equilibrium approach in a pseudo-static manner. The stability of a slope subjected to earthquake loading, for example, is usually determined by the addition of a static lateral destabilizing force, representing the peak horizontal acceleration of the earthquake, to an otherwise normal static analysis (*e.g.*, [82,84,85,94]). More complex earthquake analyses (*e.g.*, [6,18,66,82–85,93]) are based on the same principle but treat the earthquake as a series of simple pulses or shocks. With the slope failure mass considered as a rigid block on a plane frictional surface, these methods also permit an estimate of

the earthquake-generated displacements of the failing slope mass.

An alternative approach to global slope stability analysis uses the calculus of variations (*e.g.*, [9,75]) to find the critical failure surface, by minimizing a factor of safety functional. For a homogeneous, isotropic slope, this surface is found to be generated by a straight line or logarithmic spiral. Although there are several drawbacks, including inability to capture the evolution of failure (typical of upper bound limit equilibrium methods), difficulty of application to inhomogeneous (*e.g.*, layered) slopes, and evidence pointing to a defective functional [24], this "inverse" approach at least tackles slope failure in a fundamentally more realistic manner, by asking the physics of the problem to naturally dictate the geometry of the critical failure surface, rather than requiring the analyst to correctly assume it in advance.

The finite element method (*e.g.*, [10,118]) has also been applied to both static and dynamic slope stability analysis (*e.g.*, [19,54,97,105,111,115]) by obtaining a lower bound stress-strain solution for the entire slope which satisfies equilibrium at any *local* point. The local stress-strain details are hence free to dictate failure surface initiation and propagation in a natural way. Without modification, however, the method has not permitted localization of deformation into sufficiently narrow zones to predict the evolution or final profile of a distinct failure surface, and it is only recently that special joint elements have been used to improve the method's slope failure performance [111].

1.2.2 Possible alternative approaches

Although the slope failure problem presently remains resistant to analysis by local stress-strain methods, the same methods have been applied with some success to other solid mechanics problems and these are summarized below in the context of their possible modification and application to the prediction of slope failure. Some of the approaches discussed are investigated further in Chapters 6 and 7 in the quest for an improved method of slope stability analysis.

Localization of deformation into narrow zones has been a major issue in solid mechanics for some time, and work by Rice, Rudnicki, Needleman, Asaro, and Vardoulakis (*e.g.*, [7,53,62–64,72,77,79,81,112,114]), among others (*e.g.*, [40,80]), has contributed to a better understanding of the phenomenon. Prediction of the formation of shear bands, however, has remained cast in a predominantly theoretical framework of mathematics, with few efforts to solve the many practical problems to which localization of deformation applies. The problems which have been addressed (*e.g.*, [2,53,58,62,72,73,112]) include metal tension and soil compression tests, for which the finite element method has been coaxed into predicting shear band formation by element yielding. Prévost and Hughes [73], for example, achieved encouraging results by "seeding" their nonlinear material model of a displacement-controlled compression specimen with a weak element, while Needleman *et al.* (*e.g.*, [53,72,112]) introduced a boundary imperfection to promote shear band development in a tension specimen. The shear bands predicted by the latter

approach, however, and probably also by the former, required a special element geometry and orientation and hence were highly mesh dependent. Shear band formation has also been addressed within the theoretical framework of bifurcation phenomena (*e.g.*, [40,63,114]), but as yet, numerical solution of bifurcation problems seems to be confined to those of structural mechanics, fluid mechanics, and reaction-diffusion processes (*e.g.*, [42,44,47,51,64,74]).

By treating a shear band as a crack, fracture mechanics (*e.g.*, [38]) offers a completely different way of propagating a failure surface through a solid body. This framework allows both linear (*e.g.*, [33,34]) and nonlinear (*e.g.*, [25,43]) fracture to be handled, with a variety of displacement and energy criteria available for crack growth (*e.g.*, [27,37,43,99,116,117]), and analyses of such situations often make use of a special tool called the *J-integral* (*e.g.*, [76,78]). To date, however, fracture mechanics problems have been formulated almost exclusively in terms of a pre-existing crack assumed to grow in a straight line with few efforts directed toward predicting the *trajectory* of a growing crack (*e.g.*, [37,116,117]), and hence, with metal fracture traditionally being the motivation for the study of crack propagation under conditions of tension (Mode I) and anti-plane shear (Mode III), only a small amount of work has been done on crack growth in clay (*e.g.*, [69]) and rock (*e.g.*, [5]), where conditions of shear (Mode II) predominate, to form a basis for the study of slope failure as a fracture mechanics problem.

Although the finite element method remains the most common and successful

numerical solution technique for solid mechanics problems in general, boundary element methods (*e.g.*, [22]) may also be worthy of further investigation, especially for linearly elastic fracture mechanics solutions which might be applied to modeling the evolution of slope failure. In the same vein, a finite difference approximation and solution to the dynamic field equations of continuum mechanics for a soil slope might also successfully capture the initiation and propagation of the all-important failure surface.

1.3 SLOPE FAILURE EXPERIMENTS

The present lack of a realistic and accurate method of slope stability analysis is due not only to the difficulty experienced by stress-strain methods in accommodating and predicting localized deformation, but also to a general lack of understanding of the details of the slope failure mechanism itself. While toe bulging and crest tension cracking are features which have commonly been observed immediately prior to the collapse of real slopes, the point of initiation of the failure surface and its subsequent propagation in space and time through the slope are not clear and have not been investigated in detail due to the difficulty of their capture. Since the development of any scientific theory or engineering analysis should be based on a sound understanding of the physical principles governing the problem at hand, there has been a clear need for a series of experiments to observe the mechanism of slope failure directly.

Direct observation of the failure of a real, full-scale slope would be the ideal experiment, but is impractical for several reasons. For an existing full-scale slope, or one specially constructed either by excavation or by building a suitably inclined embankment, there would be inadequate control over failure (*if* and *when* it occurred) and only one chance of recording the desired information, since the high cost of such an experiment would prohibit its repetition. These problems can all be overcome by conducting the failure experiments on model slopes in a geotechnical centrifuge (*e.g.*, [87]).

Although use of a centrifuge to study the slope stability problem is not a new concept, previous experiments (*e.g.*, [4,8,21,26,29–32,41,48,52,55–57,59,68,86,109]) have not specifically looked for the local or microscopic details of the slope failure mechanism, as defined by the initiation and propagation in time and space of the failure surface through the slope. Various mechanisms are possible (*e.g.*, [8,12,15, 17,49,71,102,103,109]) including evolution from slope toe to slope crest (supported by the observation of toe bulging), crest to toe (supported by the observation of crest tension cracking), or initiation deep within the slope mass followed by simultaneous propagation to the toe *and* crest. Due to the natural stress concentration which occurs at the toe of a slope under gravity loading, the toe to crest hypothesis is favored as postulated below in terms of the centrifuge environment.

The slope failure mechanism depicted in Figure 1.3 assumes failure to be a progressive phenomenon originating at the slope toe as the centrifuge is started,

and propagating slowly toward the slope crest with increasing gravitational acceleration. At a sufficiently high gravity level, the mass of soil between the failure surface and slope face can no longer be supported by the intact material near the slope crest and in the final stages the failure surface propagates rapidly to the crest to allow subsequent slope collapse. Since the aim of the experimental part of this study was to examine the above hypothesis, a series of centrifuge model slopes was failed under increased gravitational acceleration, and the dynamics of failure recorded with movie film and mechanical failure detectors. A model slope material and geometry was specially chosen for these experiments to give a well-defined failure surface, and still photographs of the slope specimen in flight were taken at $5g$ increments during centrifuge spin-up to record the progressive nature of failure, however it developed.

1.4 THESIS OUTLINE

The slope stability problem requires a better understanding of the mechanism of failure by direct observation, *and* an improved method of analysis to predict it, and thus the present study involved an experimental investigation of slope failure, followed by an analytical effort to model the experimental results.

The mechanism of slope failure was directly observed in a series of geotechnical centrifuge tests, the equipment and instrumentation for which are presented in Chapter 2. Since a special soil was used for these experiments, a series of tri-

axial and unconfined compression tests was also conducted to identify this soil's engineering properties, and these results appear in Chapter 3. Chapters 4 and 5, respectively, describe the procedure and present the results of the centrifuge slope tests. Based on these experimental observations of slope failure, several attempts were then made to develop an improved method of slope stability analysis, as described in Chapter 6, before the successful approach of Chapter 7 was discovered. This method is employed in Chapter 8 to represent the observed mechanism of slope failure, and permitted the conclusions and recommendations of Chapter 9 to be made.

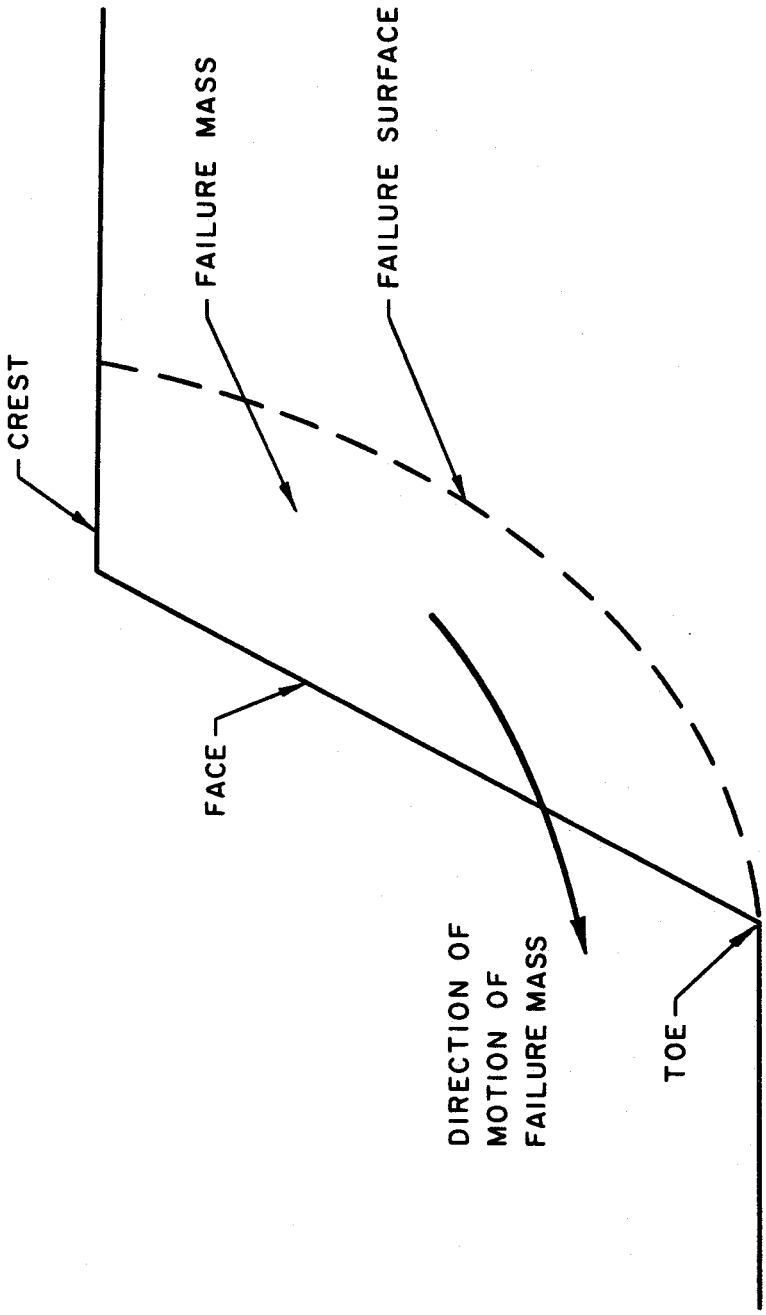

Figure 1.1 Slope failure

Figure 1.2 Slope failure at Alaskan Native Hospital, Anchorage during Great Alaskan Earthquake 1964

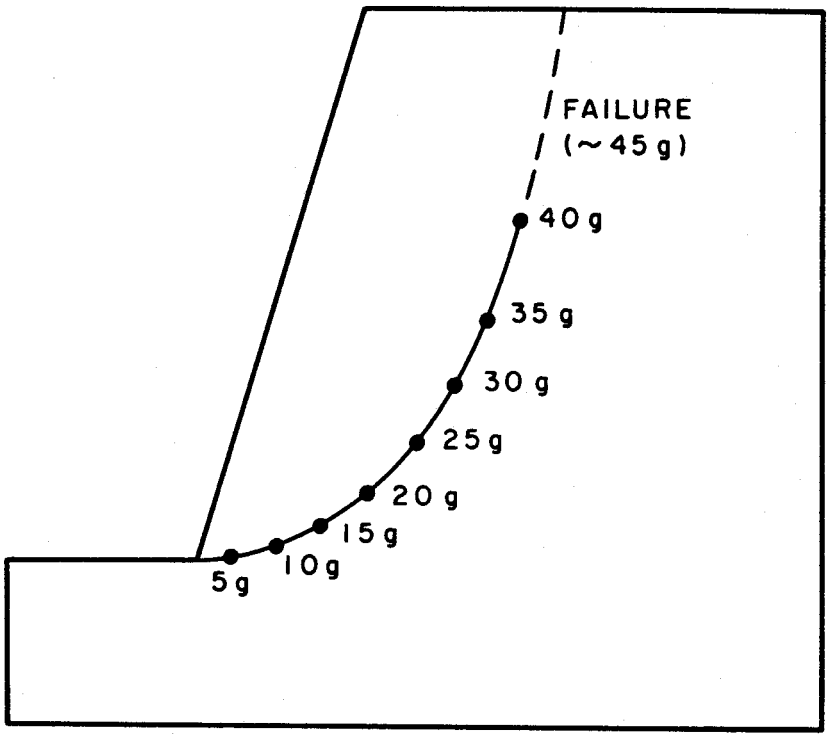

Figure 1.3 Postulated centrifuge slope failure mechanism showing propagation of failure surface from toe to crest with increasing gravitational acceleration

Chapter 2

CENTRIFUGE EQUIPMENT AND INSTRUMENTATION

2.1 INTRODUCTION

The need for a centrifuge in experimental slope stability studies arises from the nonlinear material behavior of soil and the gravity-induced nature of the soil stresses. If a scale model of a prototype slope is to deform like the prototype when the same soil is used, homologous points in the model and prototype must experience the same stresses, and these conditions are best created in a centrifuge by subjecting the $1/N$ scale model to a gravitational field of Ng, where N is the lineal scale factor and g is Earth's gravitational acceleration. These physical considerations alone establish the scaling relations between prototype and model parameters for the centrifuge environment and have been presented elsewhere (*e.g.*, [67]).

2.2 CENTRIFUGE

The centrifuge used to conduct the slope failure experiments is shown in Figure 2.1 and has been described elsewhere (*e.g.*, [89,91]). With the test container

of Section 2.3 mounted on the end of the centrifuge arm, the maximum gravitational acceleration which could be applied to a model slope was approximately $100g$. Each slope failure test was run from within a control shed separated from the centrifuge by a concrete wall and wire fence. Figure 2.2 shows the Zenith 120 computer and other electronic equipment for experiment control and data acquisition housed within the shed.

2.3 TEST CONTAINER

The test container in which the centrifuge slope specimens were placed, was designed and built in 1982 for studying the response of centrifuge models to simulated earthquake motions. For reasons discussed in Section 4.2.1, this dynamic loading capability was also essential to the slope failure experiments. The main features of the soil container and dynamic loading system are shown in Figures 2.3 and 2.4, while the manner in which this apparatus allows any form of dynamic horizontal motion, ranging from a single impulse to an entire simulated earthquake, to be applied to the centrifuge model is described elsewhere (*e.g.*, [3]).

2.4 PHOTOGRAPHIC EQUIPMENT

2.4.1 Introduction

The centrifuge slope failure tests were recorded on 16 mm movie and 35 mm still film with cameras and lighting mounted directly on the centrifuge arm near

the central vertical axis, as shown in Figures 2.5 and 2.6. The lines of sight for the 16 mm and 35 mm cameras were along the centrifuge arm to the 45° mirror attached to the test container (see Figure 2.3). When in flight, the mirror directed camera vision down onto the side of the slope specimen through the combination glass and lucite front wall of the test container.

2.4.2 16 mm photography

A Wollensak Fastax (Model WF3) high speed camera was used to expose 16 mm movie films through either a 25 mm standard or 50 mm telephoto lens. Power to the Fastax camera was provided by a Goose control unit (Model WF-301), set to 60 V for filming at 1600 frames per second, and 180 V for filming at 5000 frames per second.

Lighting was provided by four General Electric DXC floodlamps until the completion of slope test 11 (see Table 5.1), and by a General Electric No. 4556 aircraft landing lamp for subsequent tests. This change in lighting between tests 11 and 12 was in response to a need for more intense, directed light. The 500 W floodlamps were connected to the 110 V supply of the centrifuge arm, while power for the aircraft landing lamp came from three Globe 12 V, 4.5 amp.hr. "gel/cell" batteries linked in series and mounted inside the arm. When permitted by closure of a heavy duty, 24 V automotive starter motor relay, the fully charged 41 V of the "gel/cell" battery package dropped to the required 28 V of the 1000 W aircraft lamp while drawing 36 A of current. The relay used to complete the landing lamp

circuit was mounted on the centrifuge arm and closed through the sliprings from the control shed with two of the same "gel/cell" batteries connected in series.

Eastman (Kodak) Ektachrome 7250 Tungsten high speed video news film was used in the 16 mm camera throughout the slope failure tests. This 400 ASA color film was exposed through an aperture midway between $f2.8$ and $f4$ at 1600 frames per second with the four floodlamps, and through an aperture midway between $f4$ and $f5.6$ at 5000 frames per second with the aircraft landing lamp.

2.4.3 35 mm photography

An Asahi Pentax MX camera with motor drive unit and 40–80 mm zoom lens was used for in-flight 35 mm profile photographs of the slope specimen. Power to the motor drive unit came through the sliprings from a 6 V supply in the control shed, while relay closure of the motor drive contacts for frame exposure and advance was controlled by the Zenith computer.

Lighting was provided by a Sunpak Auto 511 electronic flash unit connected to the 110 V of the centrifuge arm for power, and to the Pentax camera for synchronization.

Kodak Panatomic-X black and white print film was used for the clarity and high resolution afforded by its fine-grained emulsion. Each frame of this 32 ASA film was exposed through an aperture of $f11$ for $1/60\,\mathrm{th}$ of a second.

2.5 SLOPE TEST SPECIMEN

2.5.1 Introduction

A typical, prepared slope specimen used for the centrifuge experiments is shown in Figure 2.7. The specimen has a 60° slope to ensure passage of any failure surface through the toe of the sample (*e.g.*, [88,108]) and is constructed of a sand-plaster of Paris mixture, the properties of which are described in Chapter 3. The slope geometry, and material, were chosen to give a test specimen with repeatable properties that was sufficiently unstable to fail with a distinct failure surface at a convenient and approximately constant level of gravitational acceleration.

2.5.2 Lucite mold

The slope test specimen introduced above was prepared in a specially designed lucite mold according to the procedure of Section 4.1, the lucite mold being shown as built in Figures 2.8 and 2.9. The thickness of the lucite was 12 mm (15/32 in) throughout, and the separate pieces were assembled with 8-32 brass flathead screws, except at the toe and crest joints which were permanently cemented.

2.6 PENCIL LEAD TRANSDUCERS

2.6.1 Introduction

It became apparent after slope test 11 (see Table 5.1 and Section 5.1.3) that a transducer to detect slope failure mechanically might overcome resolution problems of the movie film and independently establish the mechanism of slope failure. With this goal in mind, brittle pencil lead transducers were devised for insertion into the face of all subsequent slope test specimens.

The concept of the pencil lead transducers is that ordinary pencil leads break in a brittle manner at low shear and bending loads, and also conduct electricity. A pencil lead could therefore be used as a circuit breaker in an electrical circuit containing a timing device and power supply. The timing device could be externally activated and would stop as soon as its power supply was cut by breakage of the pencil lead. When applied to the detection of slope failure in a centrifuge experiment, a row of pencil leads could be inserted into the face of the slope specimen across the path to be taken by the failure surface, and, as failure propagated through the specimen, creating a displacement discontinuity across the failure surface, the pencil leads would break cleanly because of their brittle nature. Their breakage *sequence* would establish where the slope failure surface originated and how it propagated by comparison of the final times frozen on the simultaneously started timing devices. Individual leads wired to timing circuits were inserted into slope specimens in the configuration shown in Figure 2.10.

2.6.2 Transducer construction

The pencil lead transducers were constructed as shown in Figures 2.11 and 2.12, with 0.9 mm diameter Pentel HB leads and 34 AWG Belden 8083 wire. The first step was to drill a 10/1000 inch hole through one end of the lead, which later became the "pile tip" when the transducer was driven into its pre-made hole in the face of the slope specimen with a small hammer (see Section 4.1). Secondly, the insulation near the end of a length of 34 AWG wire was removed by passing it first through the flame of a cigarette lighter and then several times between a fold of fine carborundum paper. This allowed the wire-to-lead connection shown in Figure 2.12 to be made by passing the clean end of wire through the hole, wrapping the main body of wire around the leader to form a spiral, and lastly coating the connection with electrically conductive nickel print "glue." A similar spiral connection, but without hole and leader, was made at the other end of the lead with the clean end of another length of 34 AWG wire and nickel print "glue."

The pencil lead transducer design described above was the end result of trials with 0.5 mm and 0.7 mm diameter leads without tip holes, 40 AWG wire, and lead insertion by driving into pre-made holes or directly into intact material. These transducers were in general too fragile to cope with insertion by driving, and without a tip hole the nickel print bond between wire spiral and lead was easily broken, rendering the transducer inoperative by allowing the wire spiral to slide the length of the lead during driving.

2.7 PENCIL LEAD SUPPORT CIRCUITRY

In accordance with the original pencil lead concept of Section 2.6.1, each transducer was the "breaker" in a circuit containing its own timing device. More specifically, the pencil lead transducers inside the centrifuge slope specimen were connected to the "bounce eliminator" box mounted on the test container (see Figure 2.13) and described below, and from there via the sliprings to a circuit board housed inside the Zenith 120 computer in the control shed. The pencil lead timing devices were mounted on the TTL circuit board of Figure 2.14 in the form of Intel 8253 digital counting chips. A schematic of the integrated circuits supporting the pencil lead transducers and digital counters is presented in Figure 2.15, and a brief description of their operation is given below. Of the twelve possible pencil lead transducers able to be supported by this circuitry, a maximum of ten were used in any centrifuge slope failure test (see Figure 2.10).

The "bounce eliminator" box of Figure 2.13 contains two Motorola MC 14490 contact bounce eliminator chips which output a clean digital signal in the event that their mechanical (pencil lead transducer) inputs bounce during breakage as the failure surface propagates through the slope. In so doing, these CMOS chips introduce a short time delay between input and output, which is the same for all pencil leads and hence does not affect the relative time between breaking leads. Once through the bounce eliminator chips, the pencil lead signals are transmitted by the centrifuge sliprings to the integrated circuit board of Figure 2.14.

The pencil lead signals coming into the circuit board pass between 10 kΩ pull-up and 2 kΩ pull-down resistors which prevent a slightly fluctuating voltage, sometimes introduced by the sliprings, from being misinterpreted as a broken lead. A broken lead signal will pass between the resistors, only if a pencil lead transducer has completely broken and triggered the bounce eliminator box to send the appropriate signal. Once past these resistors, the pencil lead signals are inverted by LS 14 chips and simultaneously sent to LS 86 XOR gates, LS 08 AND gates and the 8253 digital counters. The LS 86 XOR gates are the first of several checkpoints before the pencil lead signals are permitted to trigger the 8253 digital counters.

As mentioned briefly in the test procedure of Section 4.2.1, the computer reads the status of the pencil leads during centrifuge spin-up and excludes from further consideration any leads which break before dynamic loading of the slope specimen by an impulse sent to the test container. The pencil lead status is read through LS 244 buffers and broken leads excluded from the pending digital counting cycle by sending a signal to the appropriate pins of the LS 86 XOR gates through LS 373 latches (see pins A to L on the LS 373 latches of Figure 2.15). Once this has been done, an S 133 NAND gate hands control over to pin X on one of the LS 373 latches, which is the master control switch thrown just before the impulse is sent to the test container. It allows the pencil lead signals to pass through the LS 08 AND gates and enables the digital timers to begin counting simultaneously

when the first subsequent pencil lead breaks. Thereafter, each digital counter stops when its own pencil lead breaks, and holds its final count for later retrieval by the computer program controlling the experiment.

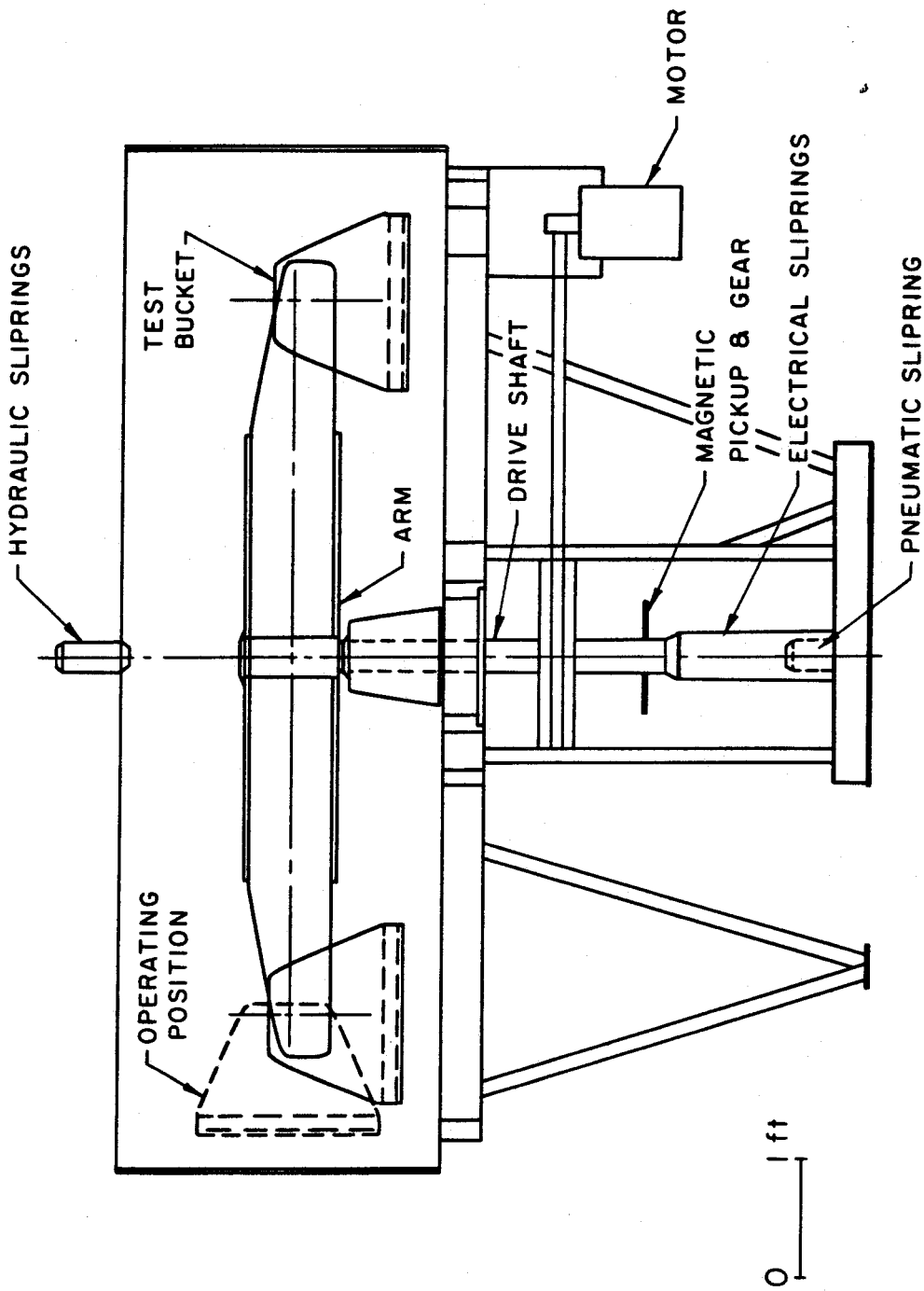

Figure 2.1 Caltech centrifuge

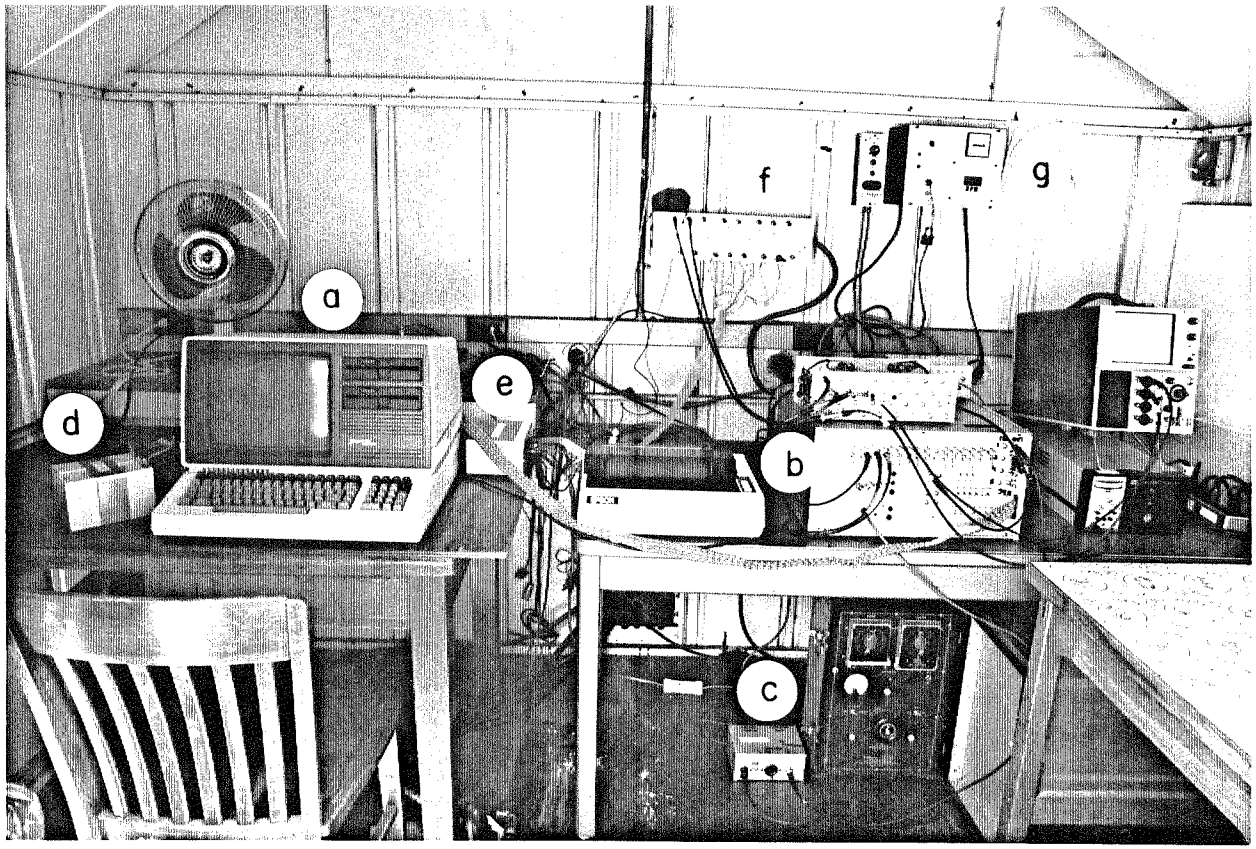

Figure 2.2 Electronic equipment for experiment control and data acquisition
a = Zenith 120 computer, b = analog-to-digital converter
c = Goose control unit for 16 mm Fastax camera
d = gel/cell batteries for closure of aircraft landing lamp relay
e = 6 V power supply for 35 mm Pentax camera
f = signals from pencil lead transducers and sliprings
g = centrifuge speed control and rpm counter

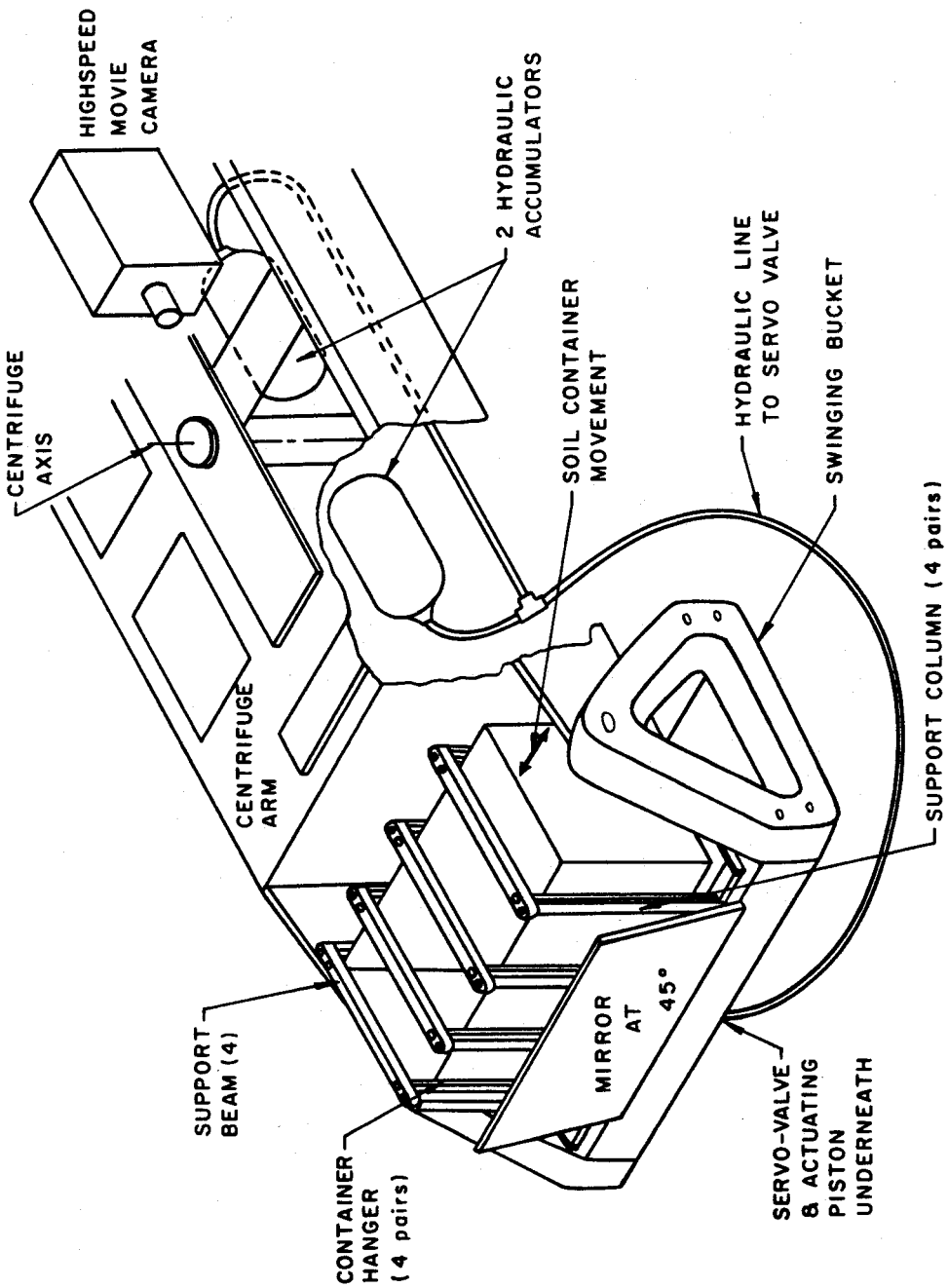

Figure 2.3 Centrifuge test container and components of dynamic loading system

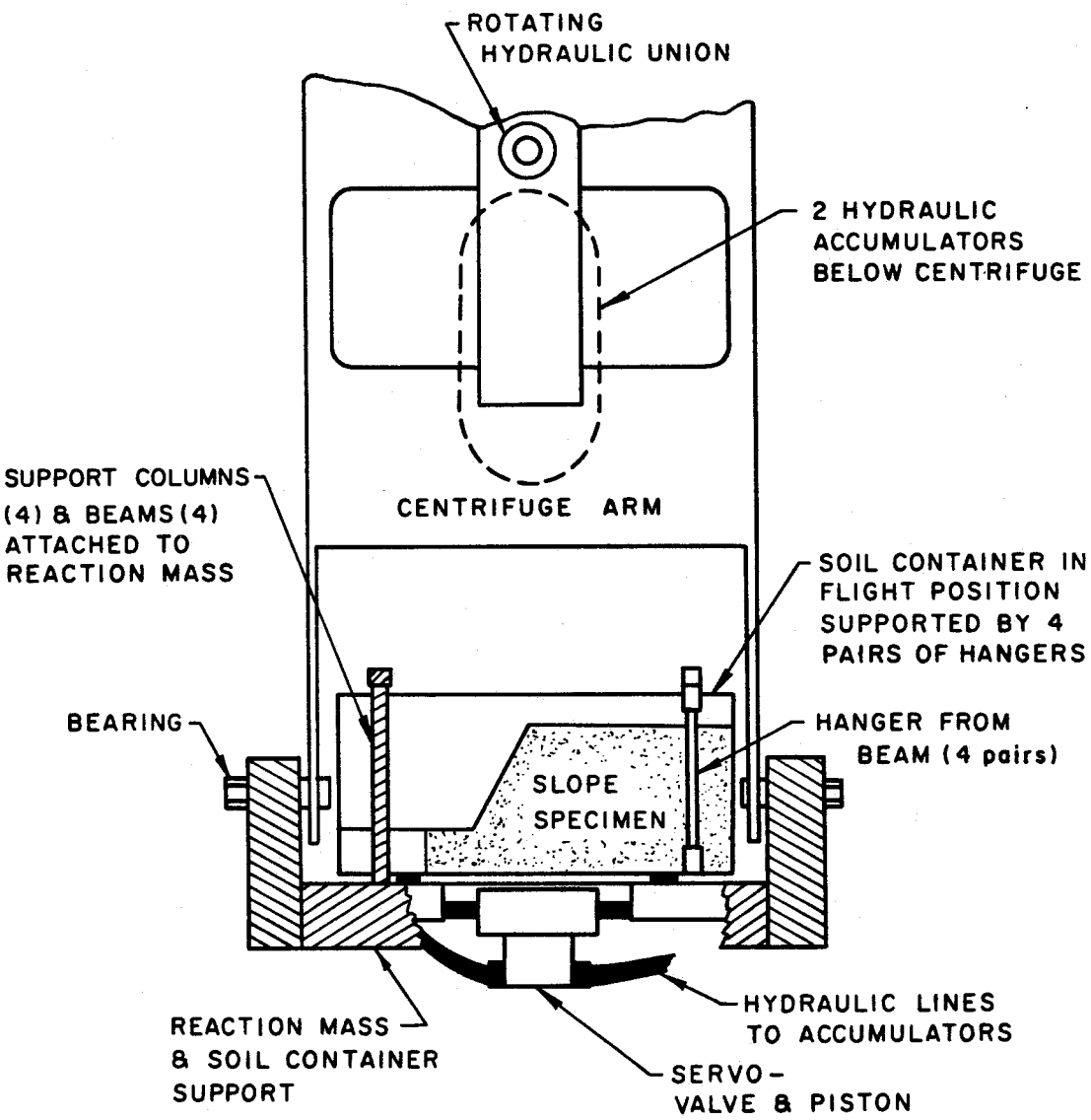

Figure 2.4 Plan view of centrifuge arm showing servo-valve and actuating piston for dynamic loading (test container in flight position)

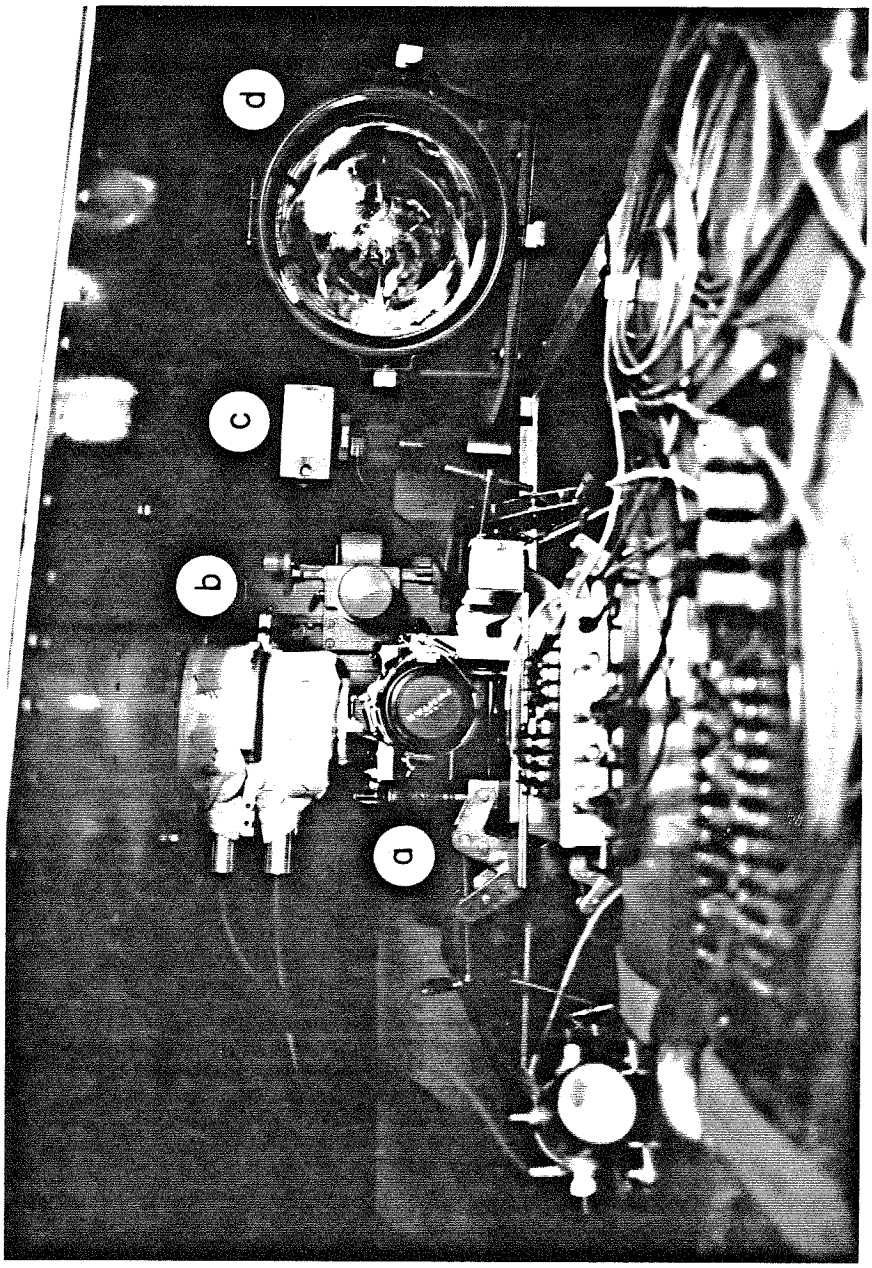

Figure 2.5 View from test container of photographic equipment mounted near rotation axis of centrifuge arm
a = 35 mm still camera, **b** = 16 mm movie camera
c = flash unit, **d** = aircraft landing lamp

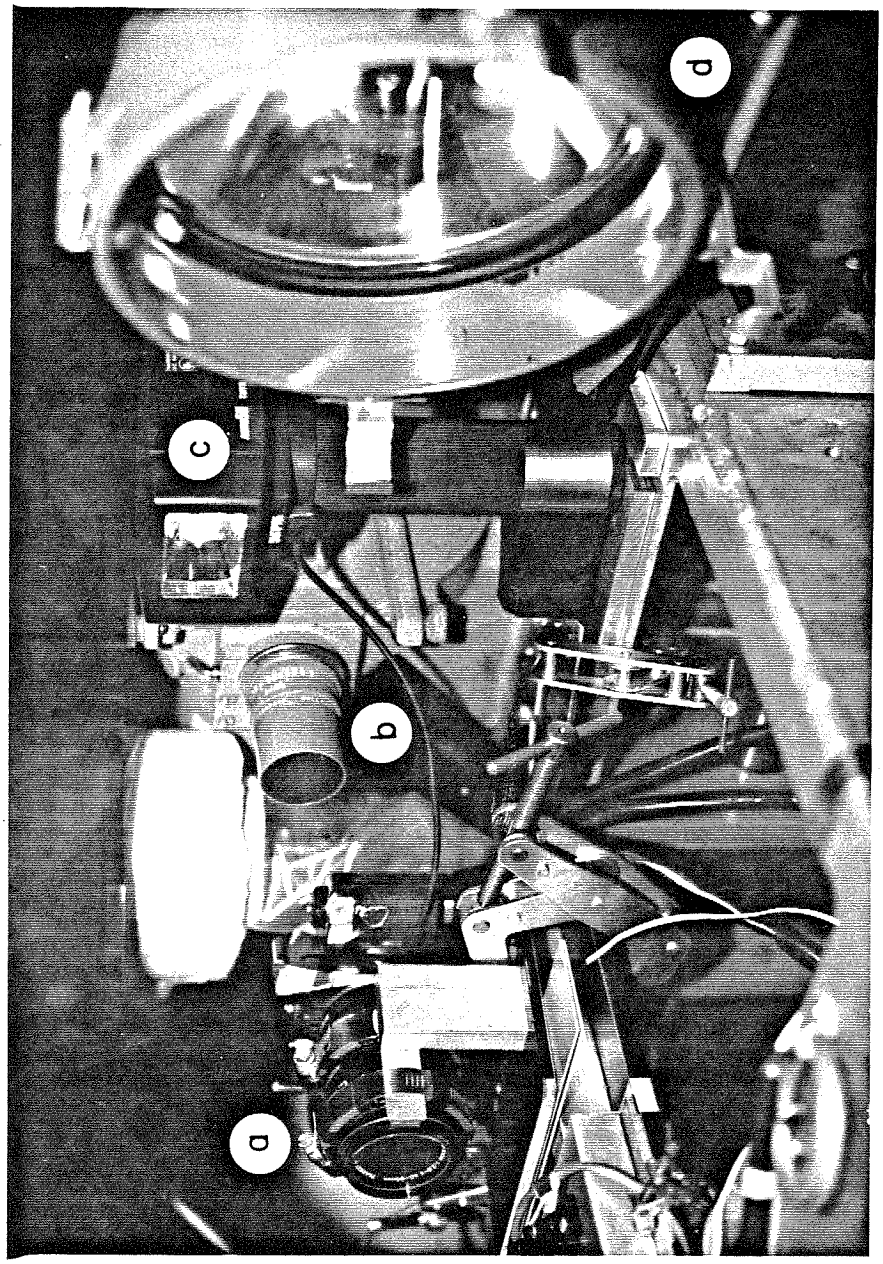

Figure 2.6 Photographic equipment mounted near rotation axis of centrifuge arm
a = 35 mm Pentax still camera, **b** = 16 mm Fastax movie camera
c = Sunpak flash unit, **d** = General Electric aircraft landing lamp

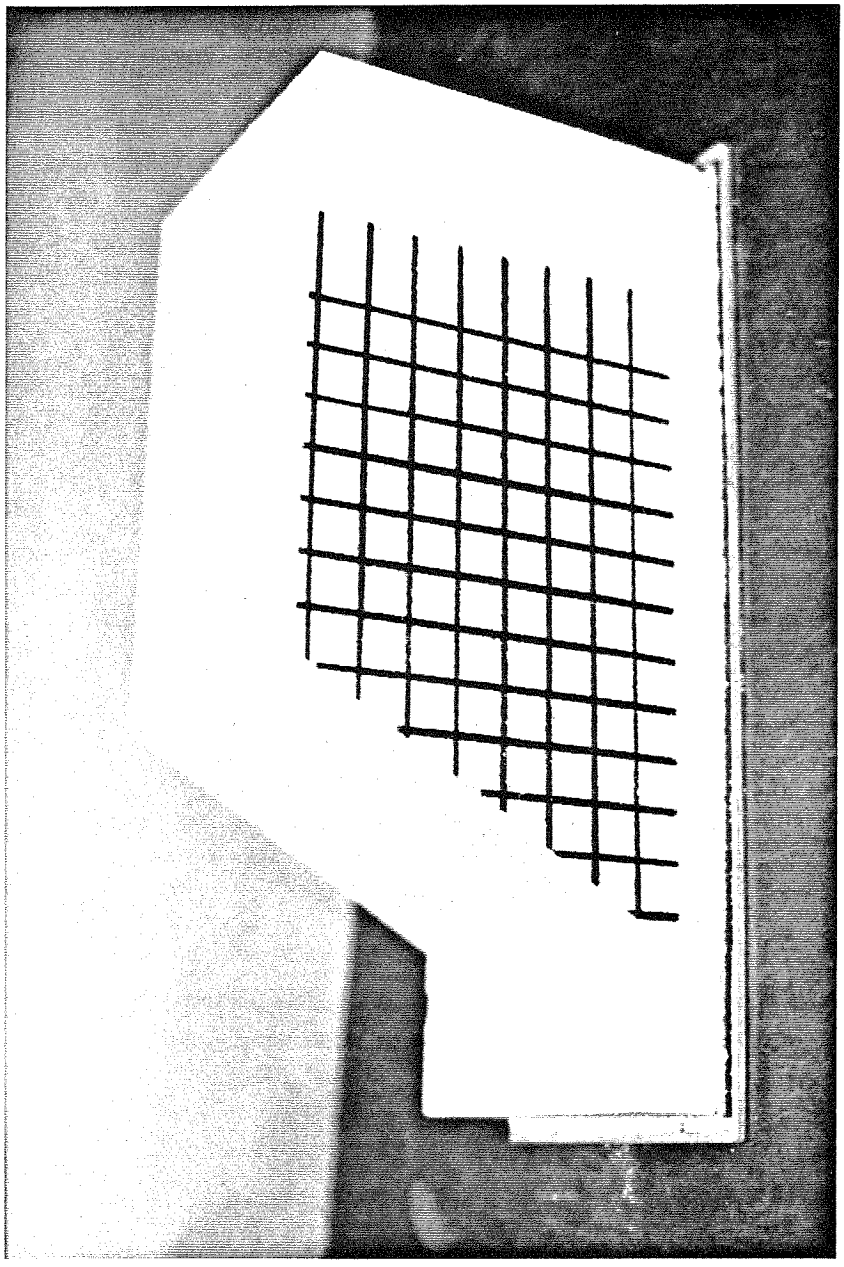

Figure 2.7 Slope test specimen

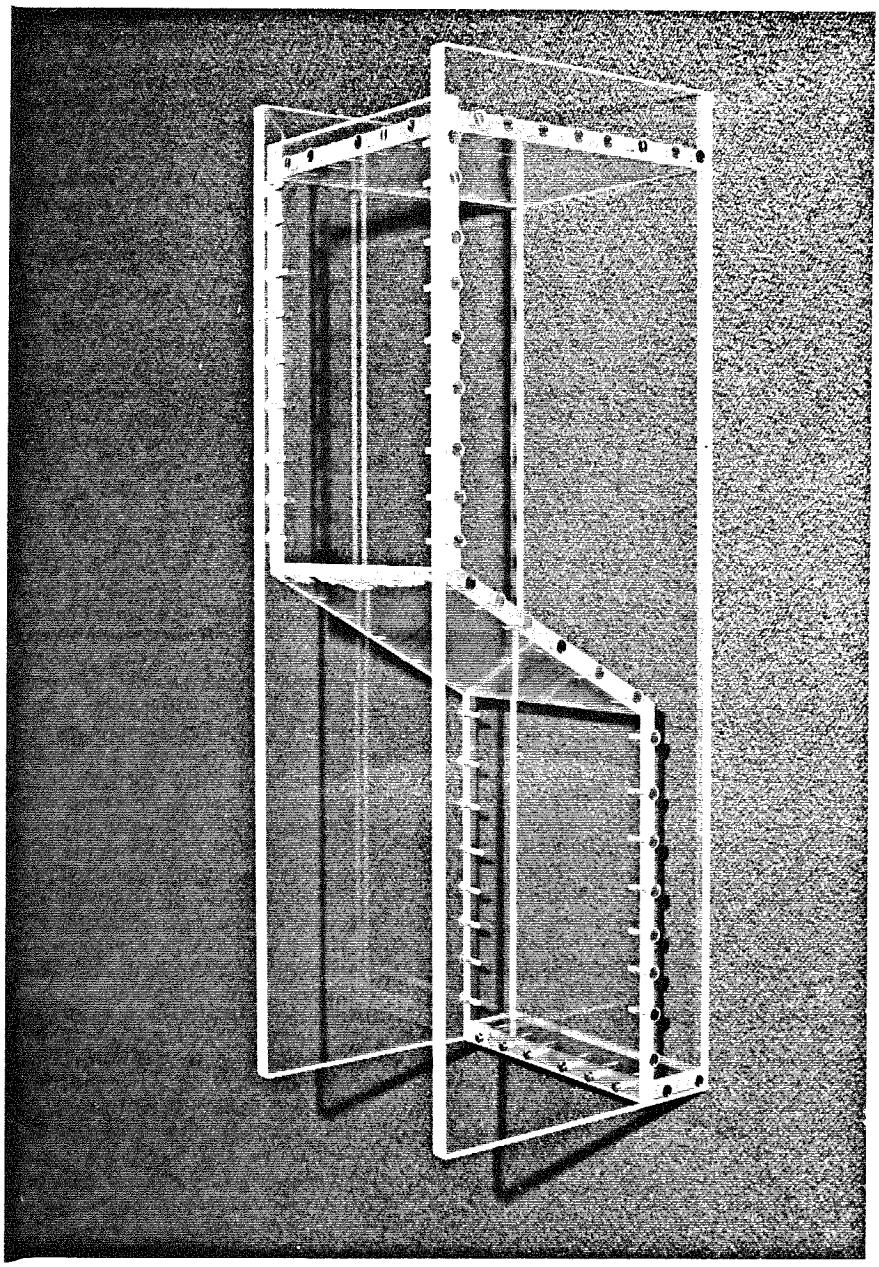

Figure 2.8 Lucite mold for slope test specimen

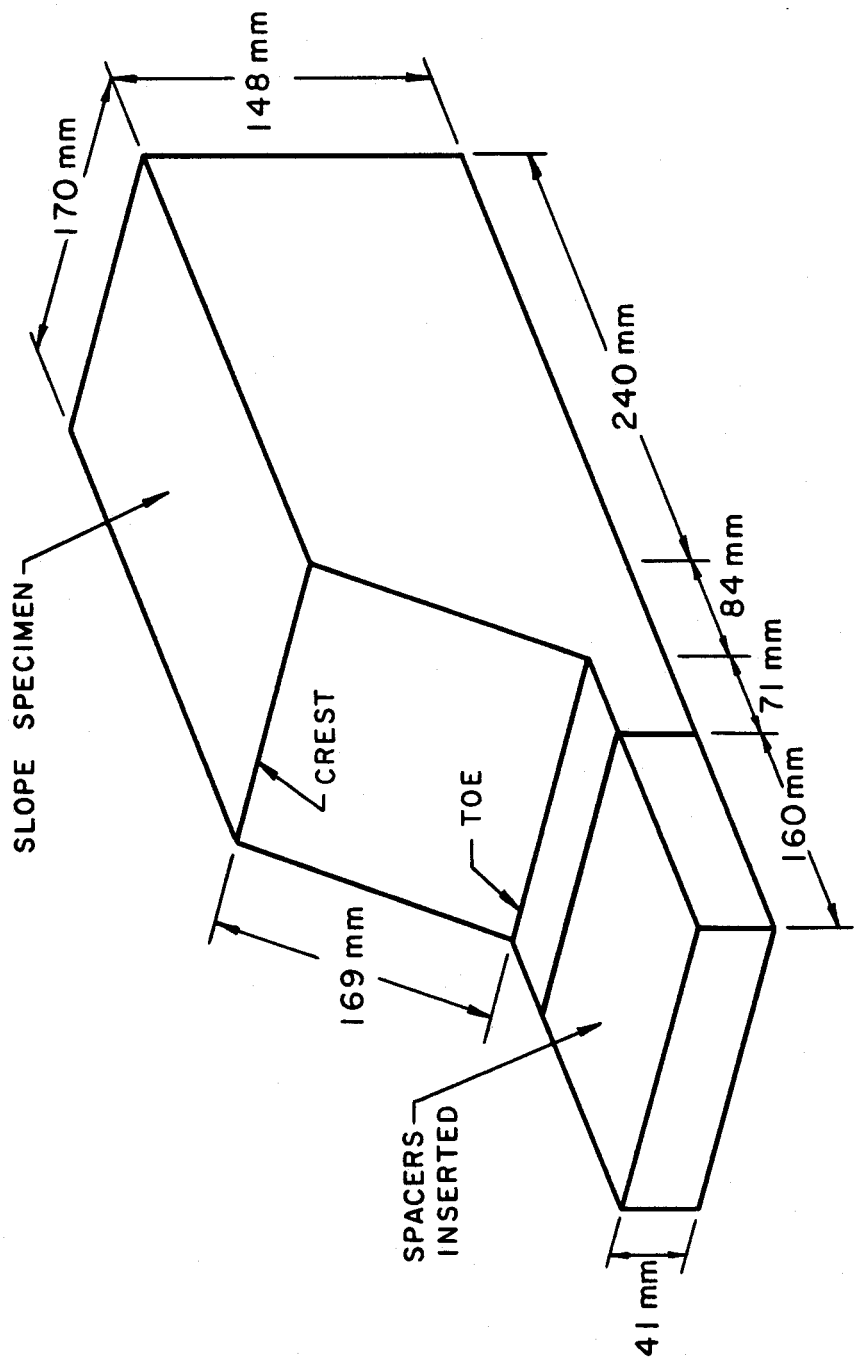

Figure 2.9 Inside dimensions of lucite mold and slope specimen

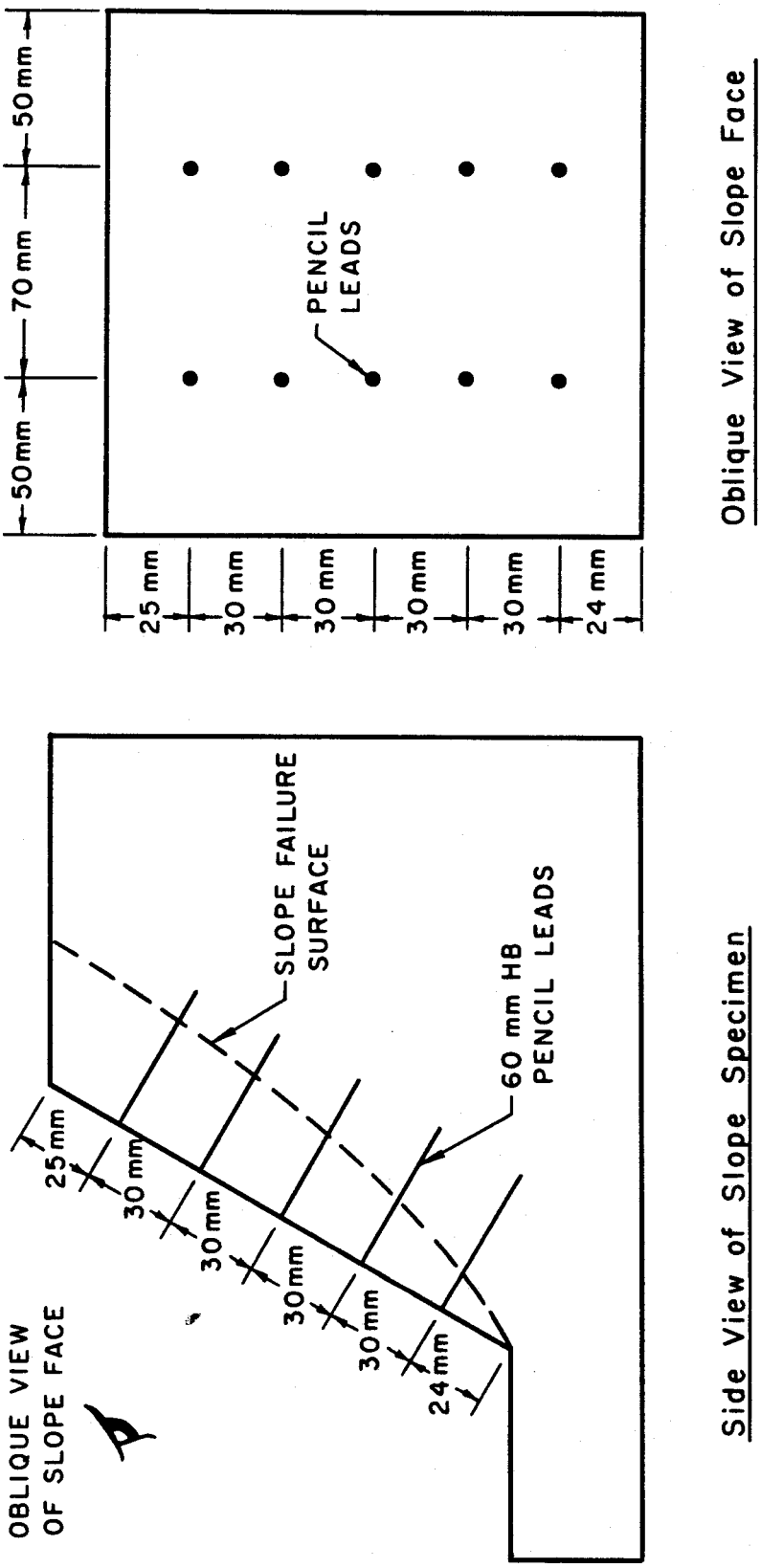

Figure 2.10 Configuration of pencil lead transducers inserted into face of slope specimen

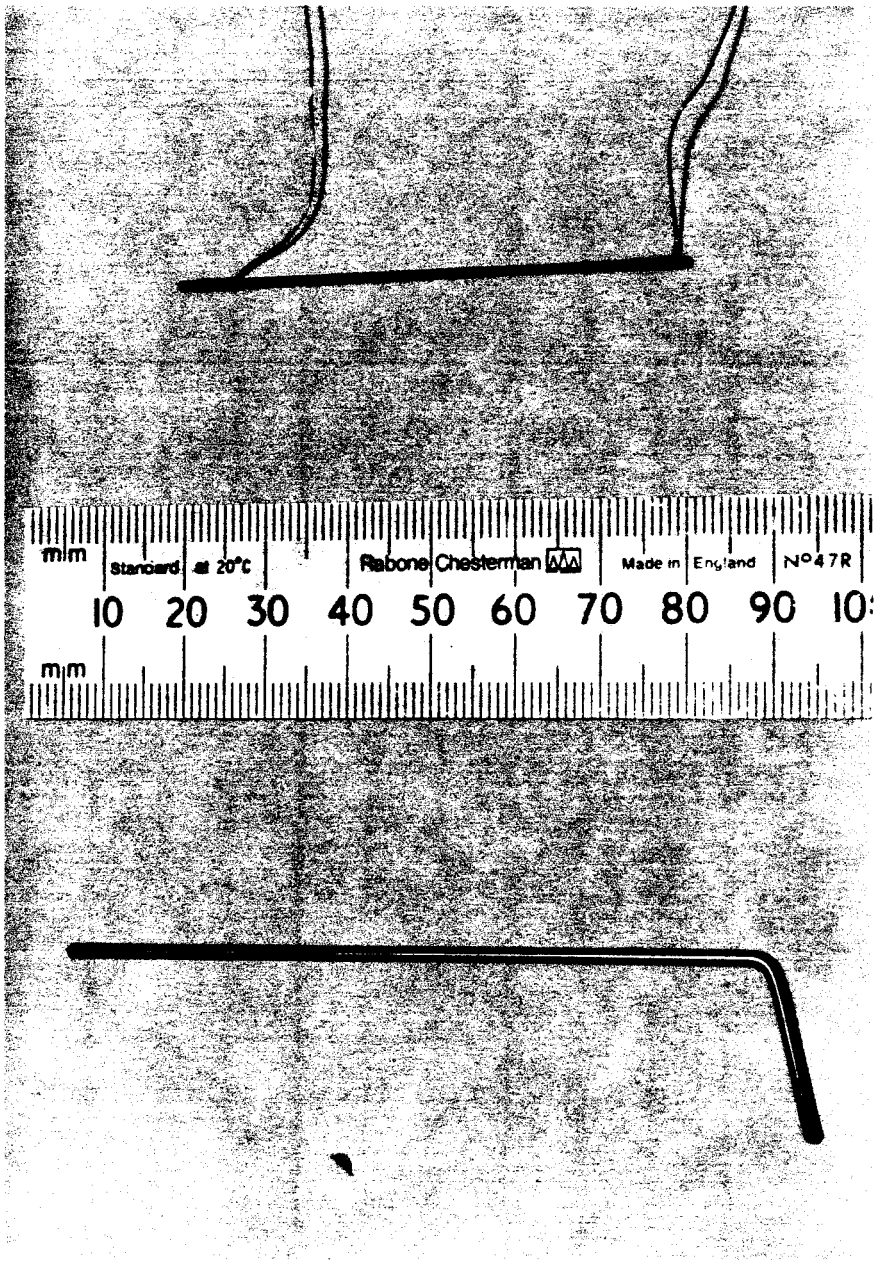

Figure 2.11 Stainless steel rod (left) and pencil lead transducer (right)

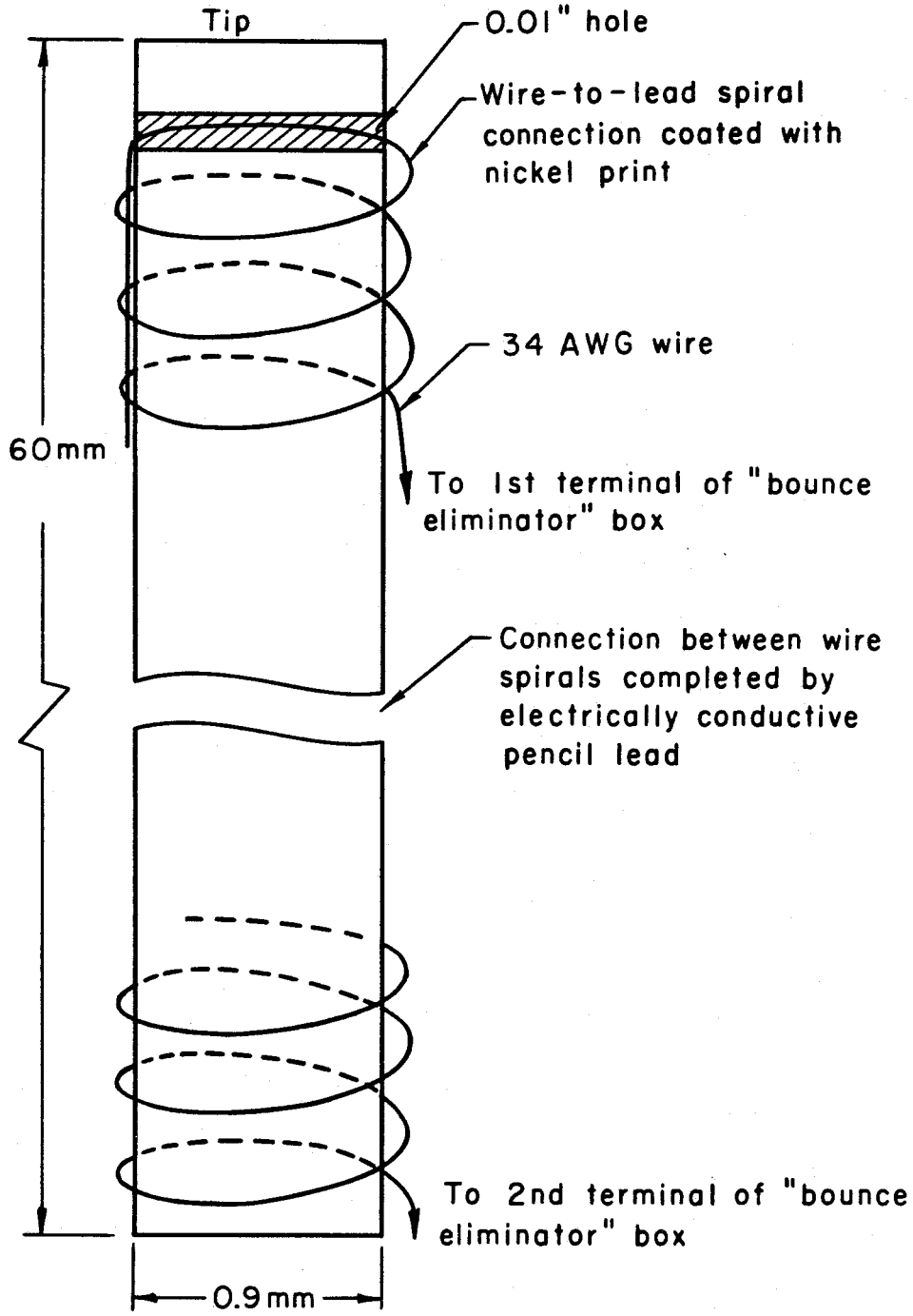

Figure 2.12 Construction of pencil lead transducers (exaggerated scale)

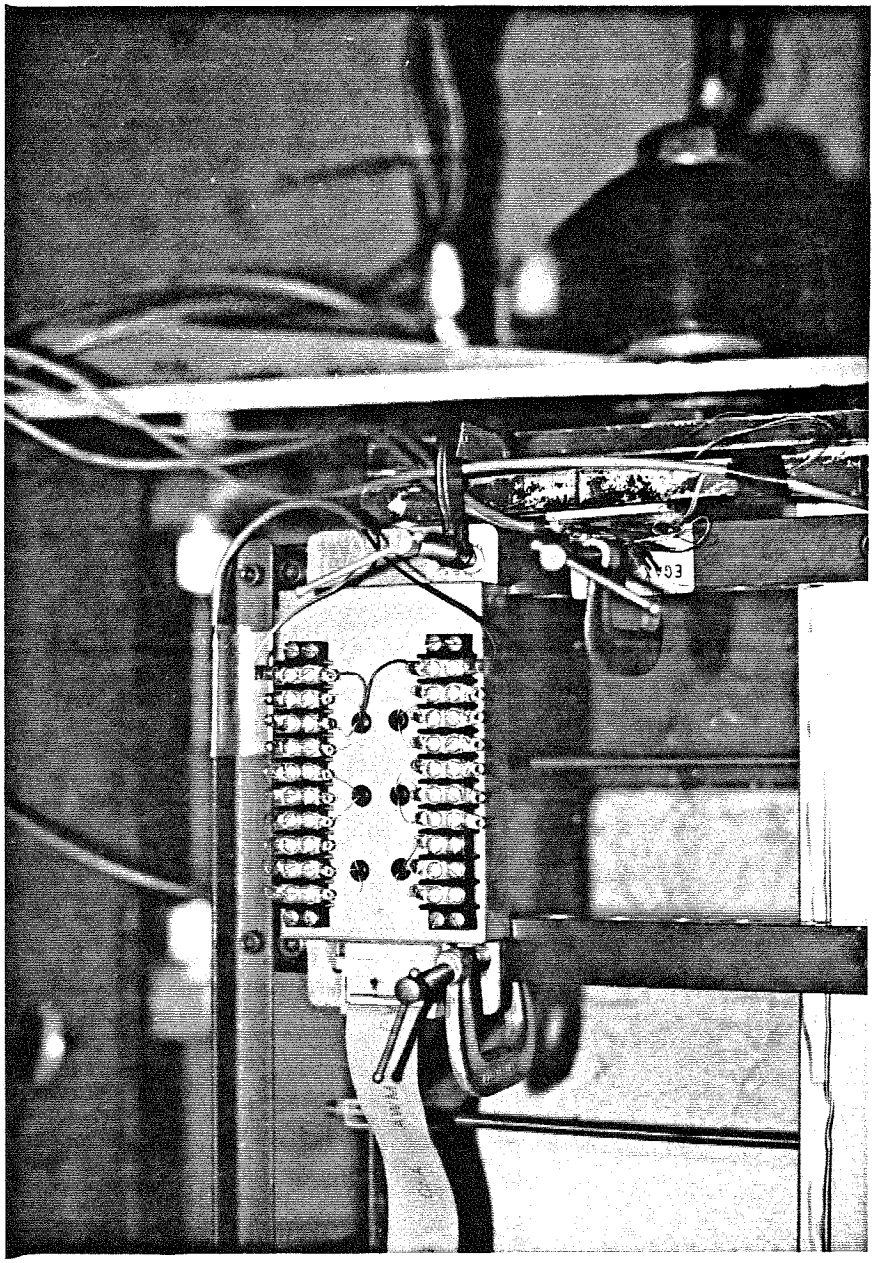

Figure 2.13 Bounce eliminator box mounted on centrifuge test container

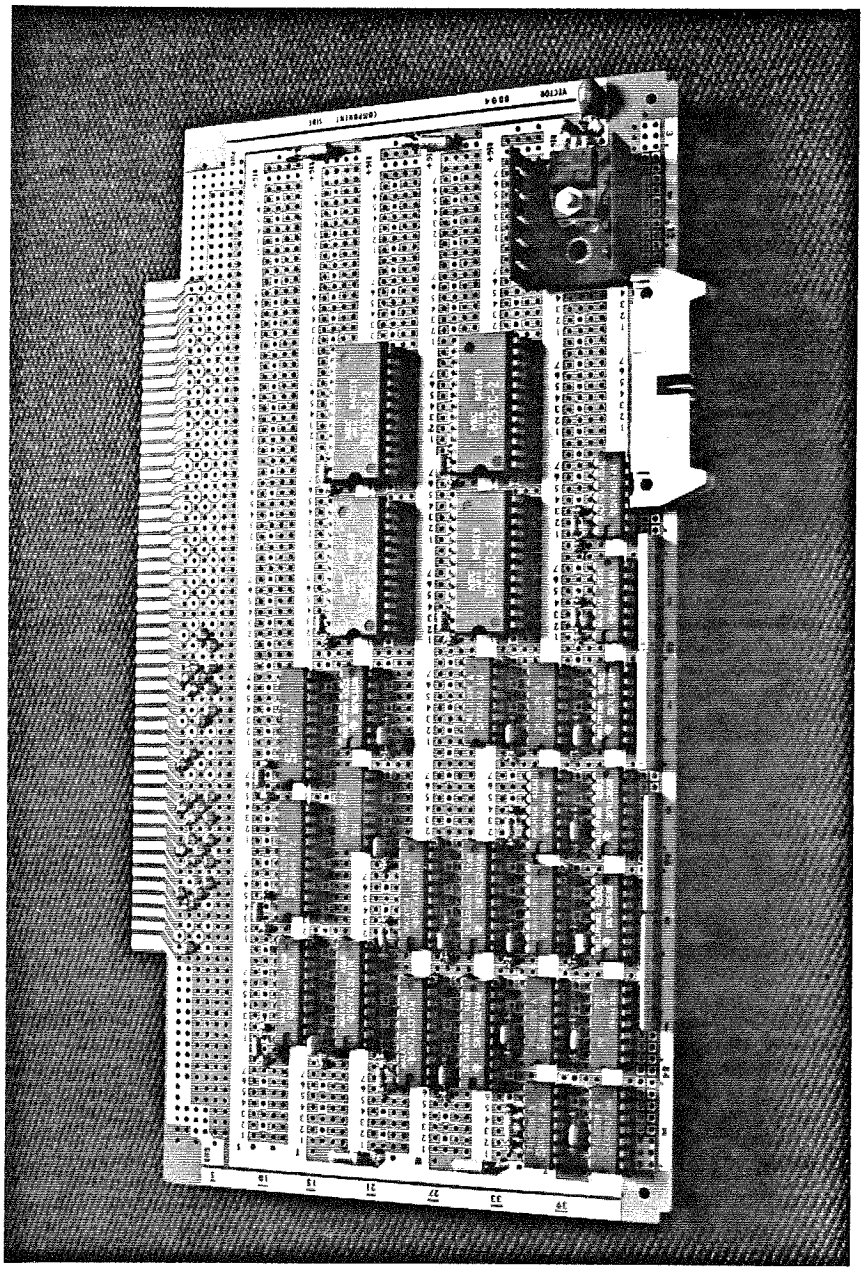

Figure 2.14 Integrated circuit board to support pencil lead transducers

Figure 2.15 Schematic of integrated circuits supporting pencil lead transducers and digital counters

Fold out ⟶

PENCIL LEAD #

+5V

MC 14490

PULL-UP & PULL-DOWN RESISTORS

LS 14

SLIPRINGS

BOUNCE ELIMINATOR BOX

8253

LS08

LS86

S133

LS 08

LS 244

PORT 54 H

PORT 50 H

LS 32

LS138 $\overline{Y5}$

LS138 $\overline{Y4}$

$\overline{IN} = \overline{RD}$

LS14

$\overline{OUT} = \overline{WR}$

LS 373

10 kΩ PULL-UP

2 kΩ PULL-DOWN

GROUND

Chapter 3

MODEL SOIL

3.1 INTRODUCTION

The centrifuge slope failure experiments required a model soil whose properties could be controlled to permit repeatable experiments. In particular, the soil needed to be weakly cohesive so that a slope specimen made stable at $1g$ would become unstable at a higher gravity level, and to be brittle in nature to ensure slope failure with a distinct failure surface as opposed to failure by general settlement or flow.

A natural soil satisfying these requirements would have been ideal, with immediate extension to the understanding of prototype slope failures. To this end, two types of natural soil were used for the early slope failure experiments, the first being a silty sand from Seal Beach, California, and the second a New Hampshire silt. Both soils derived their cohesion from appropriate contents of fines and added water. The pore water distribution within the constructed slope specimens, however, could not be adequately controlled to give repeatable and well-defined slope failures at an approximately constant gravity level, and no further attempts were made with these soils. Normally consolidated clay was also abandoned as a

possible model soil, without being tested, on similar grounds of nonrepeatability, and high deformability.

An artificial soil was then tried to see if the shortcomings of natural soil could be overcome. Based on a series of centrifuge tests conducted on square pyramids some years earlier [90], in which the pyramids were constructed of a sand-gypsum mixture, it was hoped that a similar material, with plaster of Paris replacing gypsum, would work well for the slope failure experiments. A material combining by weight, 1 part plaster of Paris, 2.5 parts water and 60 parts silica 20 sand (see Figure 3.1), was thus tested in the centrifuge and found to give repeatable and well-defined slope failures at an approximately constant gravity level, as required. The sand-plaster of Paris material, of approximate unit weight 93 pcf, was dry for testing and avoided the problem of sensitivity to moisture content experienced with the natural soils used initially. The mixing procedure and method of compaction of the sand-plaster of Paris material for the construction of the slope specimen are described in detail in Section 4.1.

3.2 LABORATORY TESTS

A series of triaxial (*e.g.*, [13]) and unconfined compression tests was conducted on the selected granular material to identify its engineering properties, and of particular importance were its stress-strain characteristics, Poisson's ratio, cohesion and friction angle.

The triaxial tests (*e.g.*, [16]) were conducted on cylindrical material specimens of approximately 38 mm diameter and 85 mm length. Confining pressures in the range of the gravity-induced stresses experienced by the material in the centrifuge experiments were applied to the samples by means of an adjustable vacuum, and changes in sample volume were measured by the displacement of water surrounding the specimen in the triaxial cell. Three tests were carried out at each of three confining pressures: one-third vacuum (4.4 psi, 0.03 MPa), two-thirds vacuum (8.8 psi, 0.06 MPa), and full vacuum (13.3 psi, 0.09 MPa). The unconfined compression tests were conducted as triaxial tests at *atmospheric* pressure. The unconfined compression specimens were therefore still surrounded by water allowing volume change to be measured, but giving a confining stress varying linearly with vertical distance from the water surface. This level of confining pressure was negligible, however, compared to the strength of the specimens. The displacement-controlled loading rate for both the triaxial and unconfined compression tests was 0.1 inches per minute (2.5 mm per min).

During a triaxial or unconfined compression test on a soil sample, axial load and deformation are measured, as well as total volume change. The numerical constitutive model defined in Section 7.4, however, is a relationship between the radii of the Mohr's circles of stress τ_M and strain ϵ_M at any material point and hence it is these quantities which must ultimately be determined from the laboratory tests.

Let σ_1 , σ_2 , and σ_3 be the *principal stresses*, ϵ_1 , ϵ_2 , and ϵ_3 the *principal strains*, and assume the principal stress and strain tensors to be coaxial. For an axisymmetric cylindrical soil specimen in a triaxial or unconfined compression test, the axial direction is principal and conventionally given the subscript "1", while the "2" and "3" directions are any two mutually orthogonal directions, also principal, lying in a circular cross-sectional plane of the sample. Due to axial symmetry, $\sigma_2 \equiv \sigma_3$, and due to assumed isotropy in a cross-sectional plane, $\epsilon_2 \equiv \epsilon_3$.

From the axial load and deformation measured during a test, the axial stress σ_1 and strain ϵ_1 are computed, and the volume change of the sample gives the *volumetric strain* or *dilatation* ϵ_v . If the stresses σ_1 , σ_2 , and σ_3 , and strains ϵ_1 , ϵ_2 , and ϵ_3 are positive for compression, negative for tension, and ϵ_v is positive for a volume increase, negative for a volume decrease, then the relationship for volumetric strain becomes

$$-\epsilon_v = \epsilon_1 + \epsilon_2 + \epsilon_3 = \epsilon_1 + 2\epsilon_3 \quad , \tag{3.1}$$

from which ϵ_3 may be expressed as

$$\epsilon_3 = -\frac{(\epsilon_v + \epsilon_1)}{2} \quad . \tag{3.2}$$

The *radius of the Mohr's circle of strain* is given by

$$\epsilon_M = \frac{\epsilon_1 - \epsilon_3}{2} \quad , \tag{3.3}$$

and substituting for ϵ_3 from (3.2) yields

$$\epsilon_M = \frac{1}{4}(3\epsilon_1 + \epsilon_v) \quad . \tag{3.4}$$

The *radius of the Mohr's circle of stress* is given by

$$\tau_M = \frac{\sigma_1 - \sigma_3}{2} \tag{3.5}$$

where σ_3 is the sample confining pressure.

An experimental determination of *Poisson's ratio* ν may also be made from a triaxial or unconfined compression test according to the definition

$$\nu = -\frac{\epsilon_3}{\epsilon_1} = \frac{1}{2}\left(1 + \frac{\epsilon_v}{\epsilon_1}\right) \quad , \tag{3.6}$$

where (3.2) has been used in the substitution for ϵ_3.

3.3 SAND-PLASTER OF PARIS MATERIAL PROPERTIES

3.3.1 Unconfined compression test results

The results of a typical unconfined compression test on the sand-plaster of Paris material are shown in Figures 3.2 to 3.4. Figure 3.2 is a continuous plot of the initial part of the test, showing axial and shear stress versus axial and shear strain, and providing higher resolution than the discrete, reduced data of Figures 3.3(a) and 3.4(a) for the same test. It should be noted that the first recorded data point of Figures 3.3(a) and 3.4(a) fails to capture the peak of Figure 3.2, and hence an estimate of the cohesion of the material is made as one-half the peak axial stress of Figure 3.2, or 2 psi (14 kPa). Because of the material's low cohesion and very brittle nature, the soil skeleton begins to break down and the stress-strain

curve becomes nonlinear almost immediately after initial application of the load and hence the values of Poisson's ratio given in Figure 3.4(b) (computed from data points already in the nonlinear range) are poor estimates of this material property. Better estimates of ν would require more detailed volume change readings on the initial rising limb of the stress-strain curve of Figure 3.2 (at deviatoric stresses below approximately 1 psi).

3.3.2 Triaxial test results

Typical results of the three triaxial tests conducted on the sand-plaster of Paris material at each confining pressure of one-third, two-thirds, and full vacuum are shown in Figures 3.5 through 3.10, where Figures 3.5 and 3.6 are the results for one-third vacuum, and the two-thirds and full vacuum results appear in Figures 3.7 and 3.8, and 3.9 and 3.10 respectively. Note that the two-thirds vacuum test (Figures 3.7 and 3.8) included three post-peak unloading-reloading cycles to determine the sand-plaster of Paris material's unloading characteristics for incorporation into the numerical soil model of Section 7.4.

In all three sets of vacuum tests, the presence of confining pressure increased the strain at which peak stress occurred and diminished the magnitude of the post-peak reduction in strength compared to the unconfined compression tests (see Section 3.3.1). Neither of these observations, however, validate the estimates of Poisson's ratio given in Figures 3.6(b), 3.8(b) and 3.10(b), and although ν is seen to lie in the range 0.2 to 0.45 at low strain, with a plausible average value of

approximately 0.35, this is still an inaccurate estimate for the same reasons given in Section 3.3.1, and highlights the inadequacy of the triaxial tests as conducted for the measurement of Poisson's ratio.

3.3.3 Idealized constitutive relation

The primary aim of the laboratory tests of Sections 3.3.1 and 3.3.2 was to provide experimental values for the numerical soil model parameters of Section 7.4. In particular, test values were required for soil constants S_1 and S_2 of (7.31) and Poisson's ratio ν of (7.34). Poisson's ratio was measured to lie in the range 0.2 to 0.45, as discussed in Section 3.3.2.

Estimates of S_1 and S_2 were obtained from Figure 3.2 and the τ_M versus ϵ_M curves of Figures 3.6(a), 3.8(a) and 3.10(a) where τ_M and ϵ_M were computed for each triaxial test data point from (3.5) and (3.4) respectively. S_1 represents the *shear modulus* of the material *at zero confining pressure* (*i.e.*, unconfined) and was obtained by finding the slope of the chord joining the origin to the peak of Figure 3.2, with the ordinate and abscissa of the peak expressed in terms of the radii of the Mohr's circles of stress τ_M and strain ϵ_M , respectively. Here τ_M equals 2.05 psi, with ϵ_M equal to 5.6×10^{-4} , giving an estimate for S_1 of 3660 psi or 25 MPa. Since the stress-strain curve of Figure 3.2 climbs almost linearly to its low strain peak, S_1 may be taken as the tangent shear modulus at the onset of loading, even though it was technically computed as a secant modulus.

S_2 represents the *variation of shear modulus with confining pressure* and its determination is described below. From Figures 3.6(a), 3.8(a), and 3.10(a), an estimate of the tangent shear modulus of the material at the onset of loading at each confining pressure was obtained by finding the slope of the chord joining the origin to the first data point. This tangent shear modulus was plotted against its confining pressure in Figure 3.11 for each of the three triaxial tests conducted at each confining pressure (*i.e.*, a total of 9 triaxial tests). Figure 3.11 shows that the shear modulus varies significantly at each confining pressure and also shows the estimate of S_1 plotted at zero confining pressure. A dashed line representative of the data was then drawn by eye within the shear modulus bounds of Figure 3.11 to quantify the variation of shear modulus S with confining pressure p given by (7.31). The slope of this line gives S_2 as 300 MPa/MPa while the ordinate intercept gives S_1 as 20 MPa. Hence (7.31) becomes

$$S = 20 + 300p \quad \text{MPa} \tag{3.7}$$

and it is this expression for S which is the basis of the results presented in Section 8.3.

In terms of the *conventional shear modulus* G, where $G = S/2$, (3.7) represents a variation of G with p given by

$$G = 10 + 150p \quad \text{MPa} \quad , \tag{3.8}$$

which may be compared with an alternative expression proposed by Seed and

Idriss [96] for medium-dense sand of the form

$$G = 1000\, K_2\, (\sigma'_m)^{\frac{1}{2}} \quad \text{psf} \quad , \tag{3.9}$$

where σ'_m is the *mean principal effective stress* (or confining pressure) *in psf* and K_2 is a constant which depends on the sand's relative density and strain level. Replacing σ'_m by p, the metric equivalent of (3.9) is

$$G = 6.9\, K_2\, \sqrt{p} \quad \text{MPa} \quad . \tag{3.10}$$

For sands of all relative densities in the strain range 10^{-4} to 10^{-3} (within which the peak of Figure 3.2 falls), K_2 has a value of 20. The variations of shear modulus with confining pressure given by (3.7), (3.8) and (3.10), with $K_2 = 20$, are plotted for more direct comparison in Figure 3.11.

Estimates of the other required soil constants ϵ_{M1} , ϵ_{M2} , and τ_R of the numerical soil model of Section 7.4 (see Figure 7.4), assumed for simplicity to be independent of confining pressure, are based on the stress-strain curve of Figure 3.2 for unconfined compression. ϵ_{M1} is the *radius of the Mohr's circle of strain corresponding to the peak* of Figure 3.2, equal to 5.6×10^{-4}, and rounded off to 1×10^{-3} for the numerical soil model of Section 7.4. ϵ_{M2} is the *radius of the Mohr's circle of strain at which the residual shear strength* τ_R *of the material is reached*, equal to 4×10^{-3} from Figure 3.2 and for the numerical soil model. τ_R is the *radius of the Mohr's circle of stress corresponding to the residual stress* of Figure 3.2, and is equal to 40 percent of the peak shear stress (*i.e.*, $0.4\, S_1\, \epsilon_{M1}$ or 8×10^{-3} MPa in the numerical soil model).

Assuming the shear modulus variation with confining pressure of (3.7), and ϵ_{M1} to be a fixed constant of 1×10^{-3}, independent of confining pressure (even though constant ϵ_{M1} is *not* a good assumption according to the triaxial test results), the equivalent friction angle ϕ of the numerical soil model can be determined, as described below. It is to be noted that this is not the usual friction angle of the real sand-plaster of Paris material, as discussed in Section 3.4.

If τ_P is the peak shear stress (*i.e.*, the shear stress at which shear failure of the material takes place) given by

$$\tau_P = S\,\epsilon_{M1} \quad , \tag{3.11}$$

and the Mohr-Coulomb condition on the failure plane of a granular material has the form

$$\tau_F = c_M + \sigma_N \tan\phi \tag{3.12}$$

where τ_F is the shear stress to cause failure, c_M is the cohesion of the material and σ_N is the normal stress acting on the failure plane, then (3.12) may be rewritten as

$$\tau_P = c_M + p \tan\phi \tag{3.13}$$

and, differentiating with respect to confining pressure p,

$$\frac{d\tau_P}{dp} = \tan\phi \quad . \tag{3.14}$$

From (3.11), however,

$$\frac{d\tau_P}{dp} = \epsilon_{M1}\ \frac{dS}{dp} \tag{3.15}$$

since ϵ_{M1} is a constant, and from (7.31) and (3.7),

$$\frac{dS}{dp} = S_2 = 300 \quad . \tag{3.16}$$

Combining (3.14), (3.15), and (3.16) gives

$$\tan\phi = S_2\,\epsilon_{M1} \tag{3.17}$$

and substituting for S_2 from (3.16), with $\epsilon_{M1} = 1 \times 10^{-3}$, yields

$$\phi = \arctan 0.3 = 16.7^\circ \quad . \tag{3.18}$$

3.4 DISCUSSION

The sand-plaster of Paris material ultimately used for the centrifuge slope failure experiments was only weakly cohesive and extremely brittle. As such, the cohesion and skeletal structure of the material in the failure zone of the sample broke down almost immediately upon application of the load during the laboratory tests. Once this breakdown had occurred, at very low strain (10^{-3}), the sand-plaster of Paris material effectively became a cohesionless, coarse sand. It was therefore considered more appropriate to determine the engineering properties of the intact material from its initial response to load application, rather than from its behavior at higher strain levels. This was the reason for determining the cohesion of the material from the almost immediate peak of Figure 3.2 during a typical unconfined compression test, and for determining the variation of

shear modulus with confining pressure, and hence friction angle, from the initial response of the material during the triaxial tests. This procedure deviates from the common practice of determining the friction angle from the envelope to the Mohr's circles corresponding to the peak stresses of triaxial tests conducted at different confining pressures. The latter practice is valid for a clay-type soil which retains its cohesion even at the large strain corresponding to peak stress, but not for the brittle soil considered here. In the triaxial tests conducted on the sand-plaster of Paris material at confining pressures of one-third, two-thirds, and full vacuum, the strain level corresponding to peak stress is approximately 10 percent, from which a conventional friction angle of approximately 35° is obtained. The friction angle of 16.7° determined at a strain level between 10^{-4} and 10^{-3} is almost half this value and indicates that the frictional resistance of the sand-plaster of Paris material is not fully mobilized at the strain level at which its cohesion breaks down.

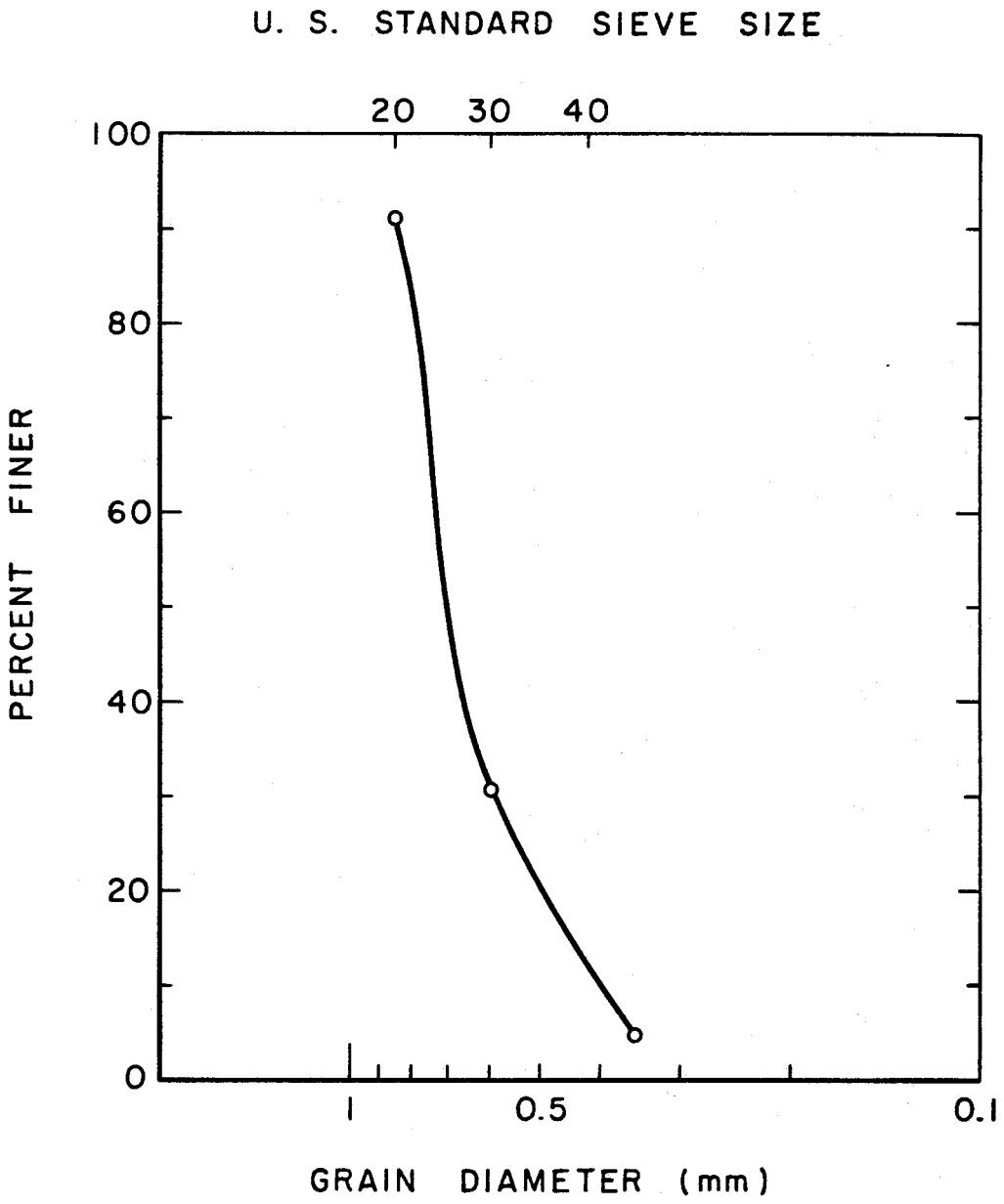

Figure 3.1 Grain size distribution of silica 20 sand

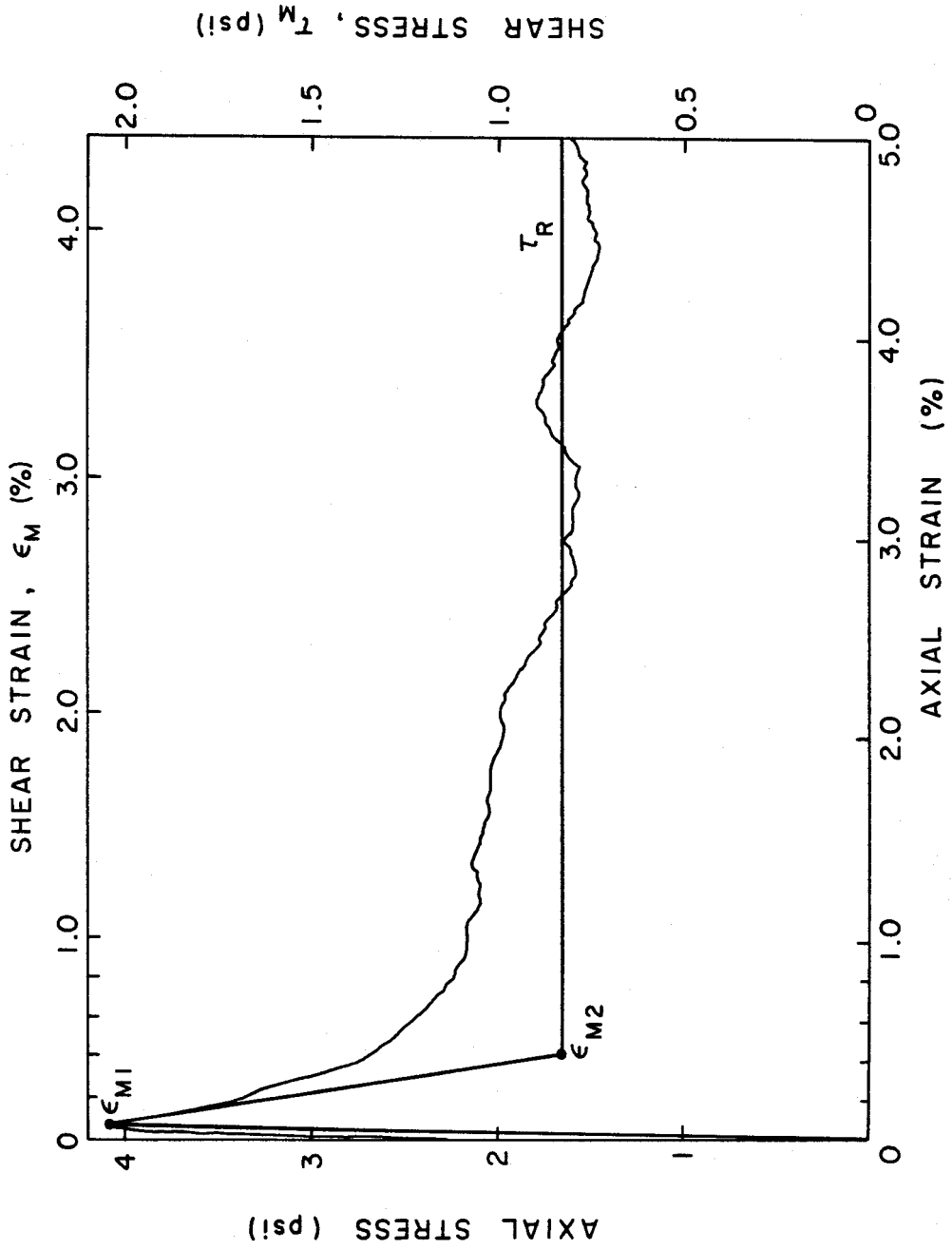

Figure 3.2 Unconfined compression test results for sand-plaster of Paris material

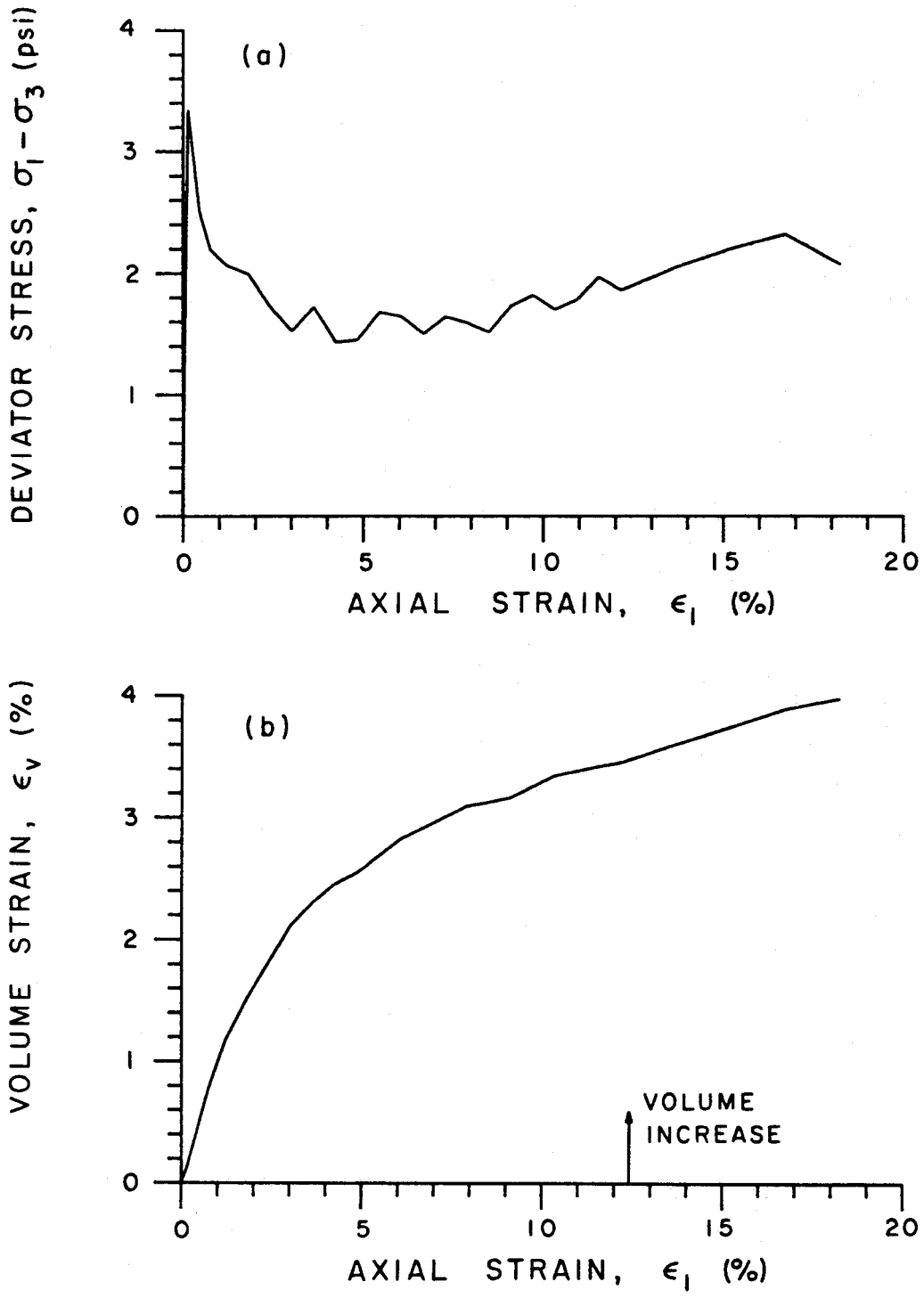

Figure 3.3 Unconfined compression test results for sand-plaster of Paris material
(a) Deviator stress versus axial strain
(b) Volume strain versus axial strain

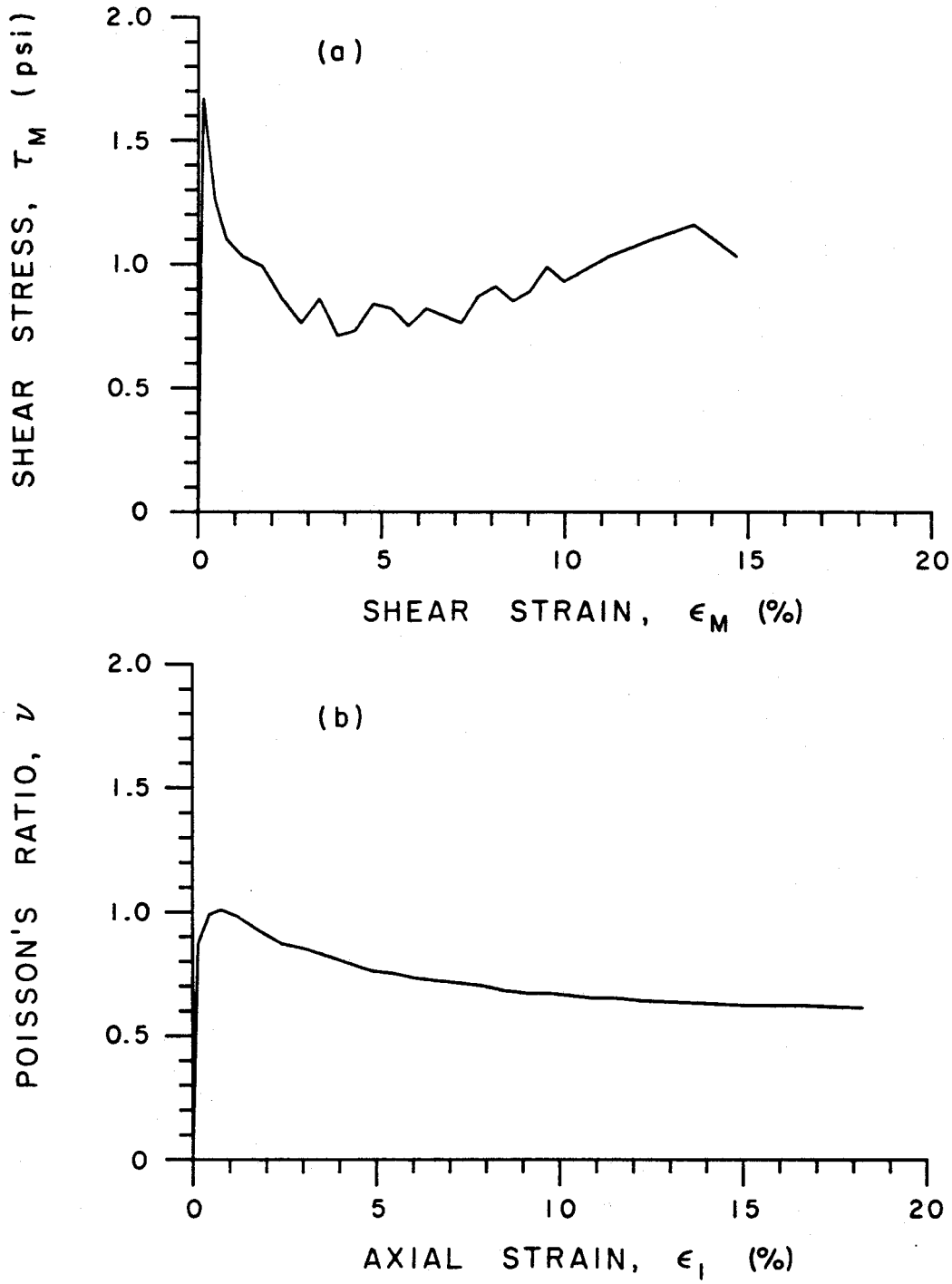

Figure 3.4 Unconfined compression test results for sand-plaster of Paris material
(a) Shear stress (radius of Mohr's stress circle) versus shear strain (radius of Mohr's strain circle)
(b) Poisson's ratio versus axial strain

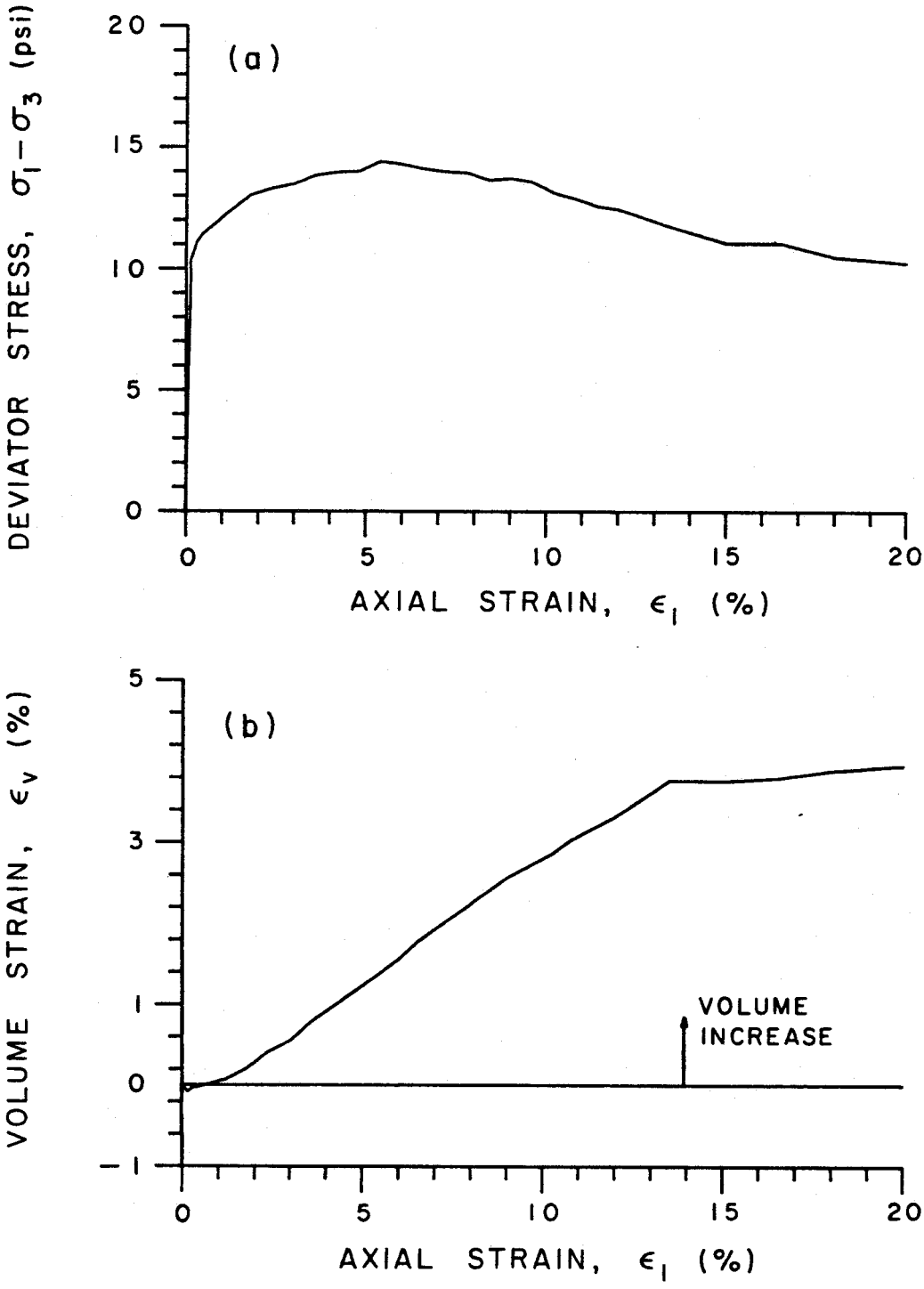

Figure 3.5 One-third vacuum triaxial test results for sand-plaster of Paris material
(a) Deviator stress versus axial strain
(b) Volume strain versus axial strain

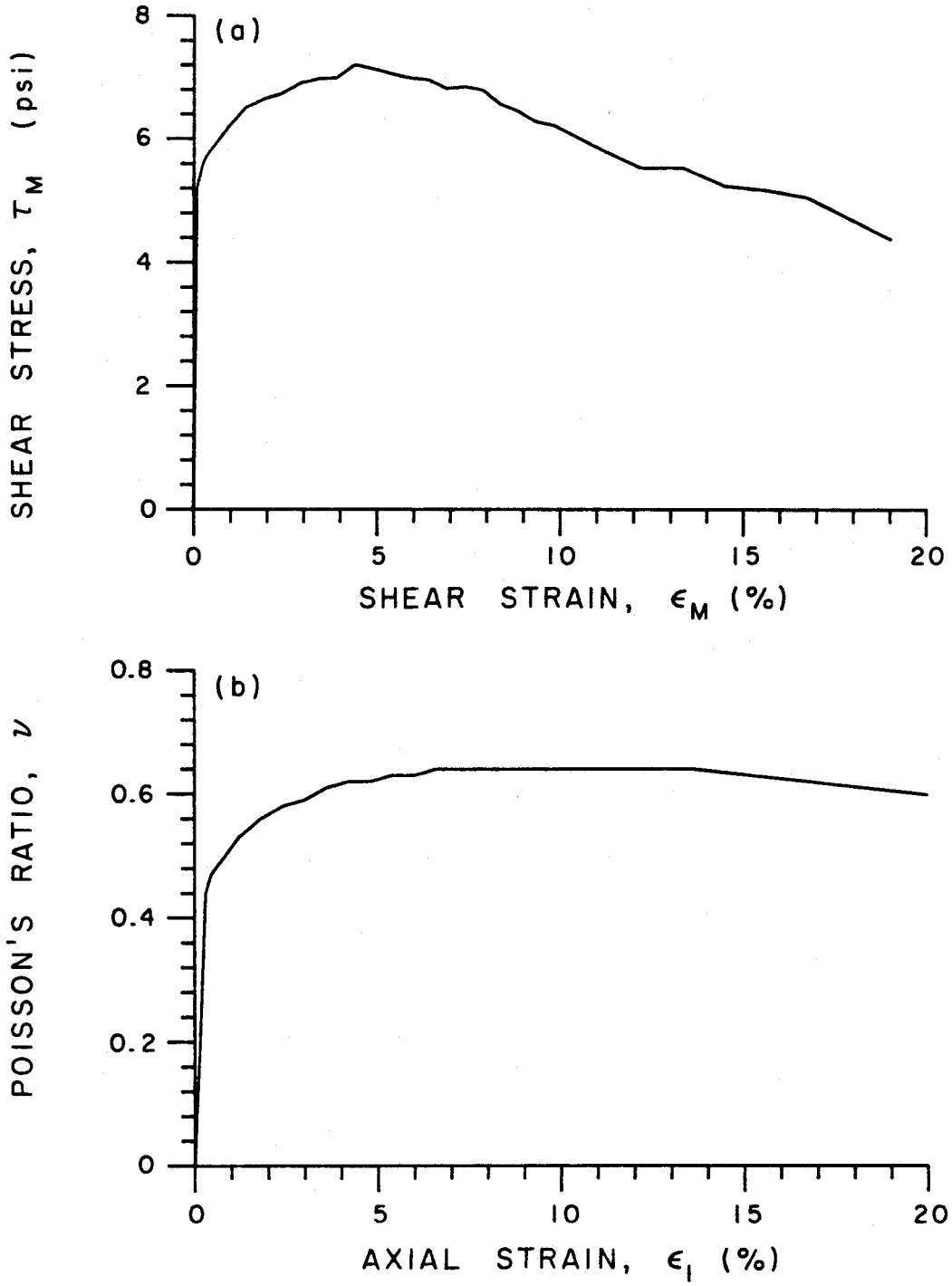

Figure 3.6 One-third vacuum triaxial test results for sand-plaster of Paris material
(a) Shear stress (radius of Mohr's stress circle) versus shear strain (radius of Mohr's strain circle)
(b) Poisson's ratio versus axial strain

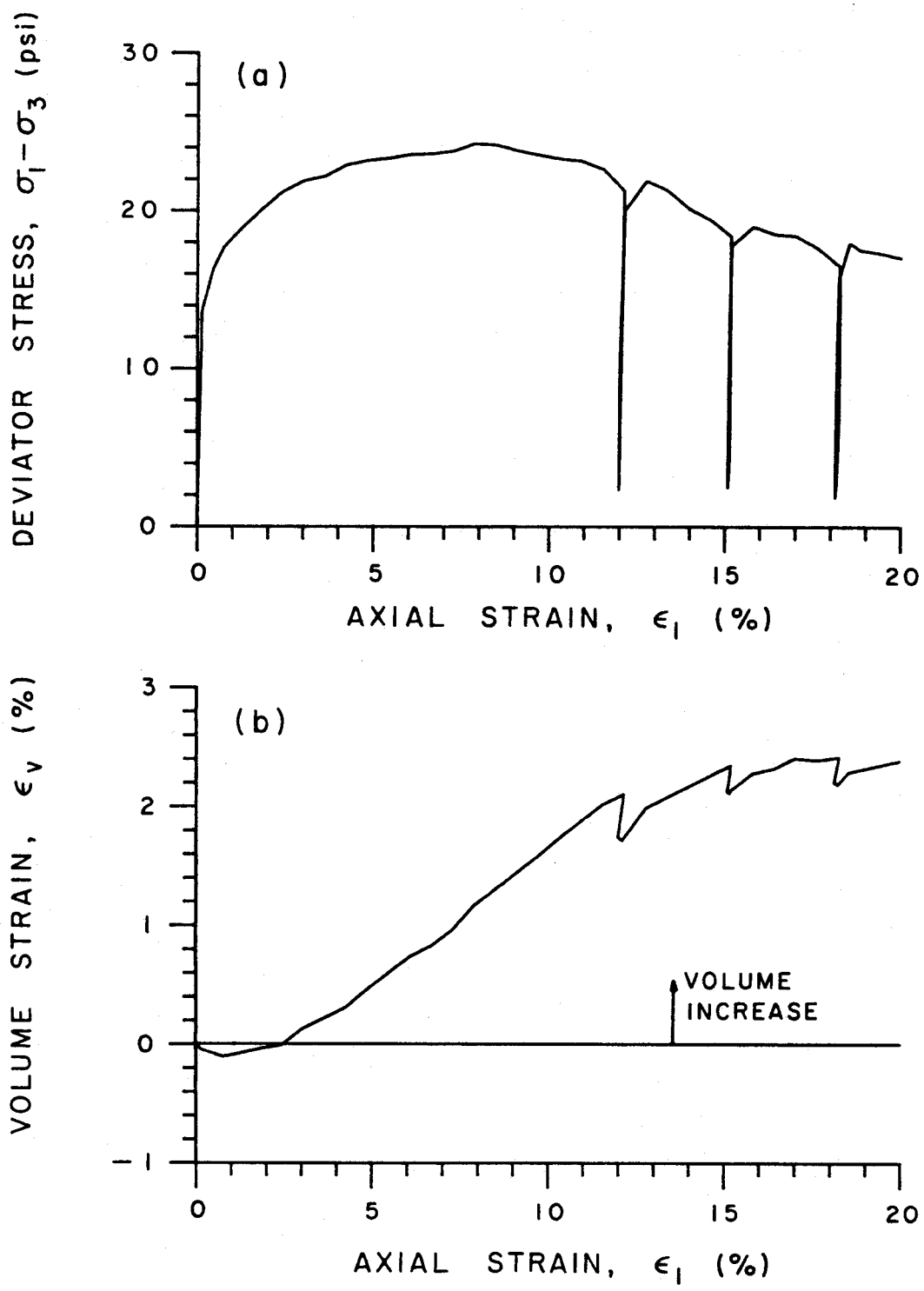

Figure 3.7 Two-thirds vacuum triaxial test results for sand-plaster of Paris material
(a) Deviator stress versus axial strain
(b) Volume strain versus axial strain

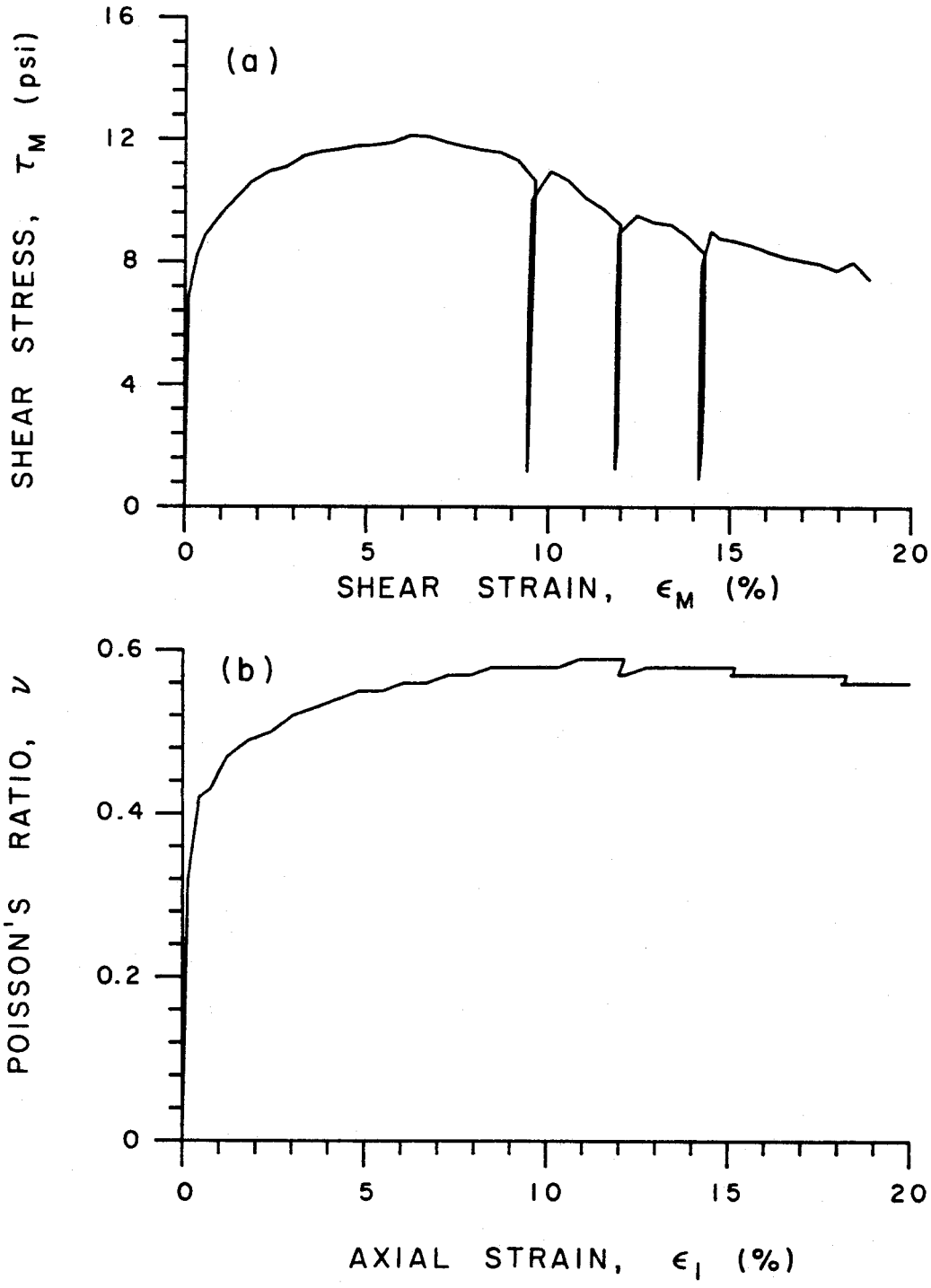

Figure 3.8 Two-thirds vacuum triaxial test results for sand-plaster of Paris material
(a) Shear stress (radius of Mohr's stress circle) versus shear strain (radius of Mohr's strain circle)
(b) Poisson's ratio versus axial strain

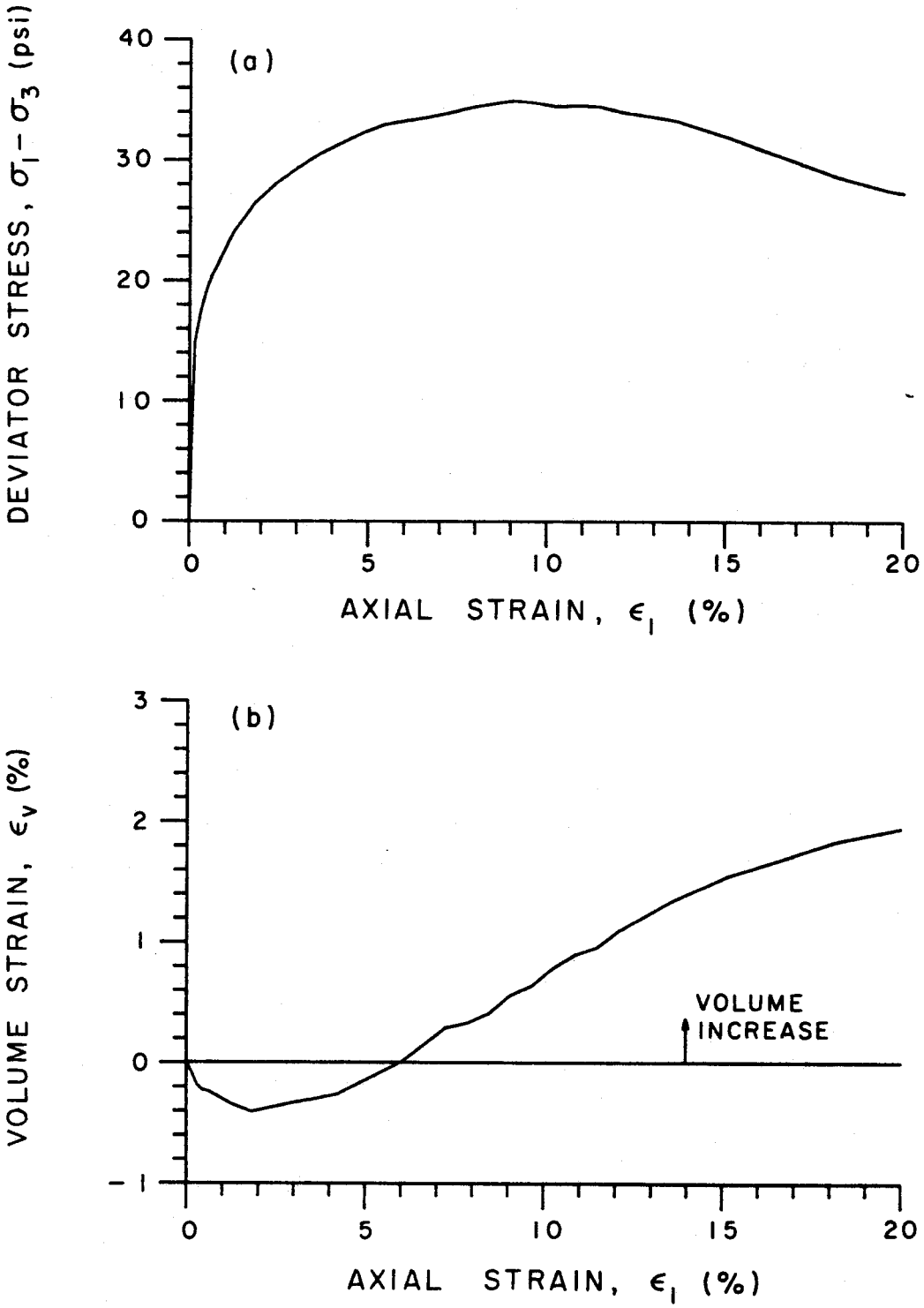

Figure 3.9 Full vacuum triaxial test results for sand-plaster of Paris material
(a) Deviator stress versus axial strain
(b) Volume strain versus axial strain

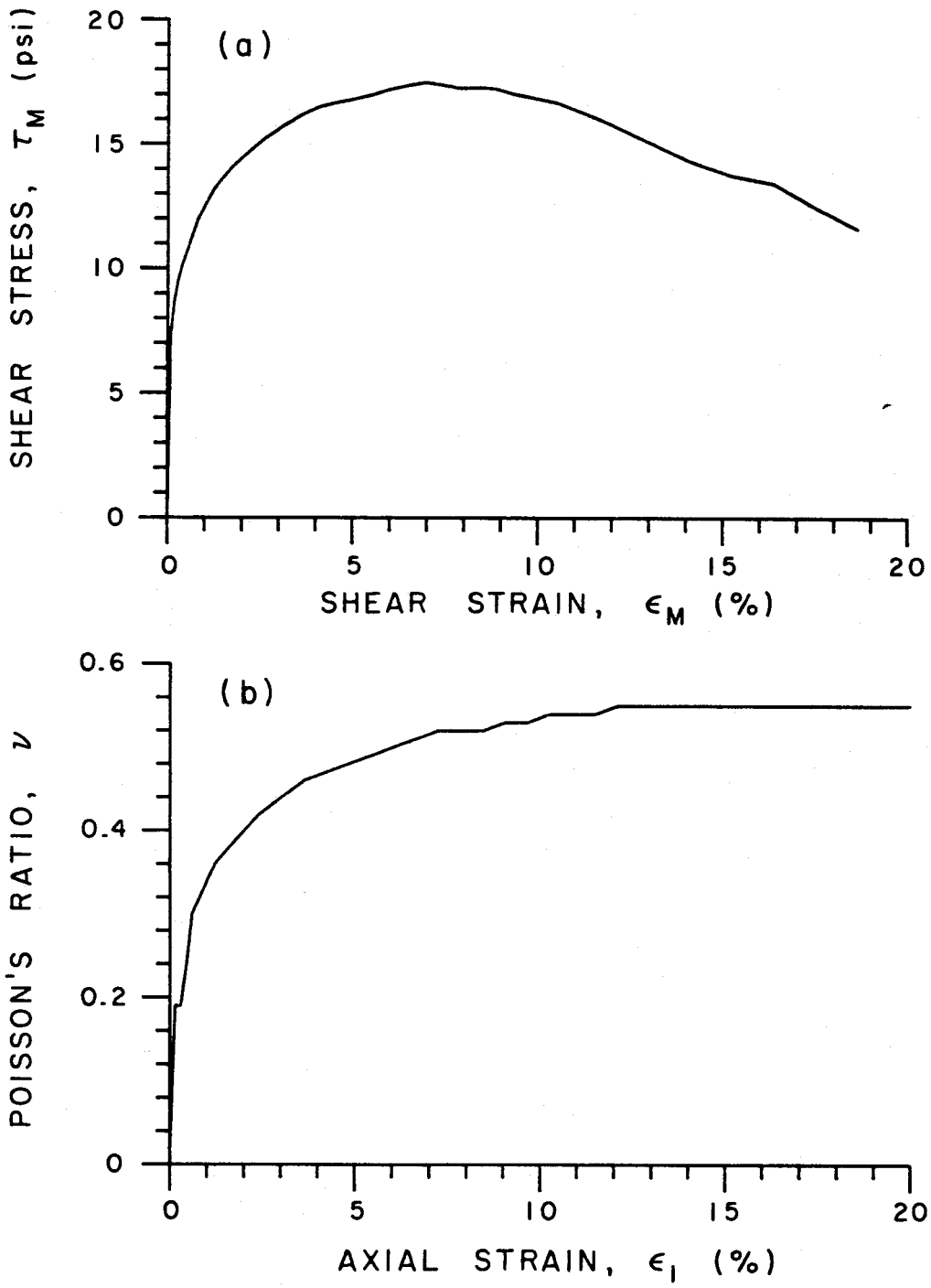

Figure 3.10 Full vacuum triaxial test results for sand-plaster of Paris material
(a) Shear stress (radius of Mohr's stress circle) versus shear strain (radius of Mohr's strain circle)
(b) Poisson's ratio versus axial strain

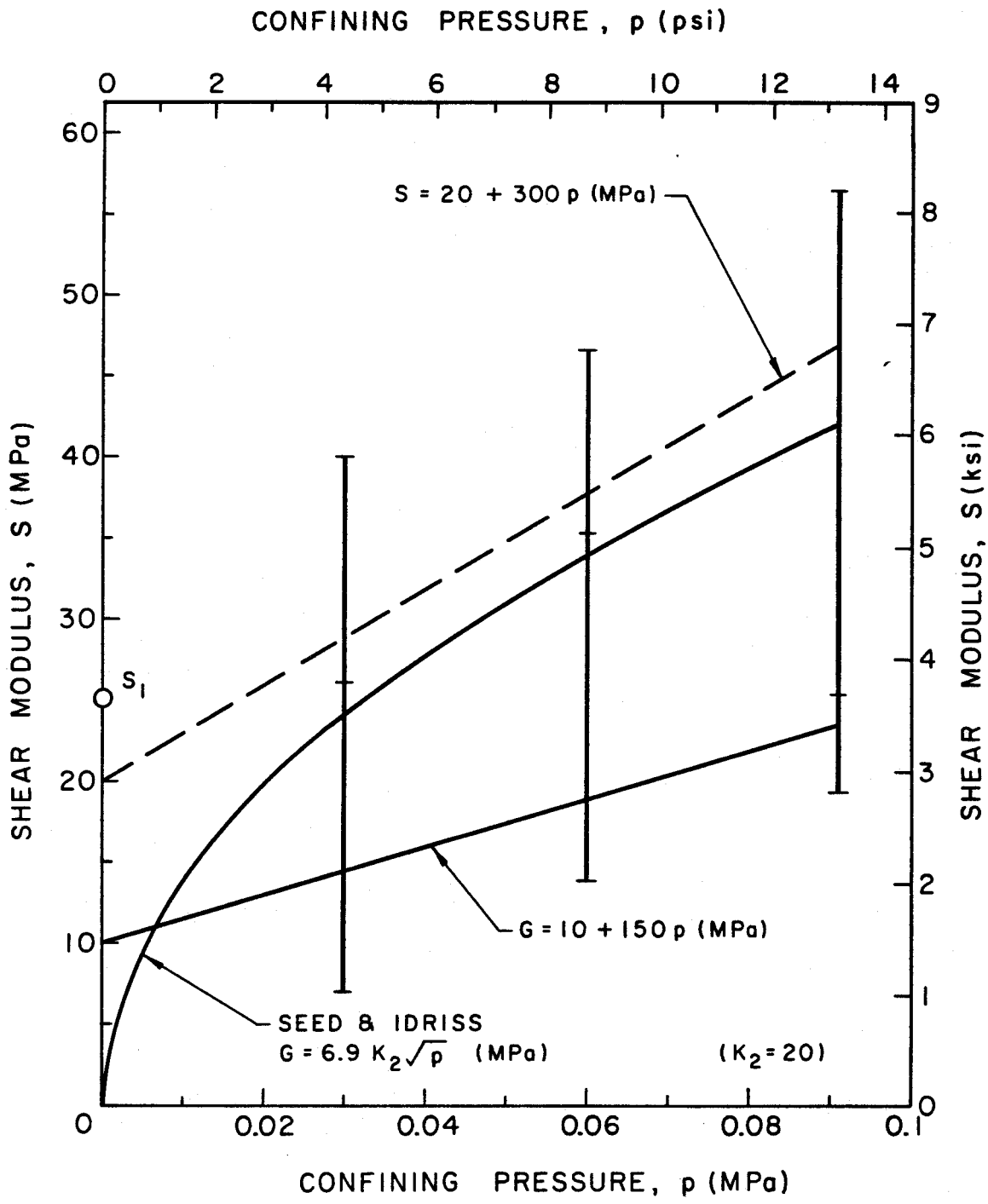

Figure 3.11 Variation of shear modulus with confining pressure from triaxial and unconfined compression test results

Chapter 4

EXPERIMENTAL PROCEDURE

4.1 SAMPLE PREPARATION

The slope specimen used in the centrifuge experiments of Sections 4.2 and 5.1 was constructed of approximately 34 pounds of the 60:1 sand-plaster of Paris material whose properties are given in Chapter 3. A sufficient quantity of this material was made from $4\frac{1}{2}$ batches each of 8 pounds silica 20 sand, 0.13 pounds plaster of Paris and 182 ml (0.4 pounds) water. Each batch of ingredients was combined and mixed in a kitchen mixer by pouring the dry sand into the empty mixing bowl, setting the mixer running at its slowest speed, and gradually adding the water to the dry sand. With the mixer still running, the plaster of Paris was then slowly added to the moist sand, signifying the start of the plaster's chemical reaction. At this point, the mixer was briefly stopped to scrape any unblended plaster of Paris from the beater and sides of the bowl, before being restarted. As soon as the material had been mixed to a uniform consistency, the mixer was stopped and the contents of the mixing bowl emptied into the lucite slope mold, turned upside down as shown in Figure 4.1. Eight pound batches of sand were used since this was the capacity of the kitchen mixer. It should also be noted that

while it is usually desirable for better mixing in cooking to blend all dry ingredients before adding liquids, this procedure was found unsatisfactory for the sand-plaster of Paris material. The coarse sand grains were unable to trap the very fine plaster of Paris in their void spaces and prevent the plaster from settling to the bottom of the mixing bowl before addition of the water, and thus the plaster of Paris had to be added to the moist sand instead.

Once in the lucite mold, each 8 pound batch of soil was compacted into a layer between $1\frac{1}{2}$ and 2 inches thick (of approximate unit weight 93 pcf) with a $\frac{3}{4}$ inch diameter aluminum rod. The fourth batch needed to be added in two halves, with half the compactive effort applied to each, to avoid excessive spillage over the sides of the mold during compaction. Approximately half of batch "$4\frac{1}{2}$" of the soil was added to overfill the mold and any excess discarded as the compacted slope specimen was levelled off with the open bottom of the mold (see Figure 4.2). Holes for the pencil lead transducers were then made in the sample according to the configuration shown in Figure 2.10 by inserting 1.6 mm diameter stainless steel rods (see Figure 2.11) through pre-drilled holes in the face of the lucite mold. The mold, complete with compacted slope specimen and stainless steel rods was then put in a 130°F oven for approximately 12 hours to hasten and ensure complete setting of the plaster of Paris within the moist sand (see Figure 4.3).

After removing the slope sample from the oven and allowing it to cool, the entire mold was turned onto its side and the upward-facing side wall removed to

expose the hardened sand-plaster of Paris material. A grid of orthogonal black lines was then spray-painted onto the exposed side (see Figure 4.4), and the side wall of the mold replaced. The slope specimen, with stainless steel rods still in place (see Figure 4.5), was then transported from the basement soil mechanics laboratory to the rooftop centrifuge room, fully supported in the lucite mold.

Once in the centrifuge room, a rubber pad and aluminum plate were placed on the upward-facing bottom of the slope before inverting the entire specimen and mold. This turned the slope sample right way up onto the rubber pad and aluminum baseplate, allowing the stainless steel rods to be removed and the lucite mold to be dismantled from around the sample, screw by screw from alternate sides, beginning at the bottom of the specimen. Wire hook lifting handles were then attached to each end of the aluminum baseplate (see Figure 4.6) and the free-standing slope specimen was lifted and lowered into the rectangular test container on the end of the centrifuge arm. After removing the lifting hooks, a check was made to ensure that the grid-painted side of the specimen was in contact with the combination glass and lucite front wall of the test container. A plate of tempered glass was then inserted between the slope specimen and rear aluminum wall of the test container to provide the same rear boundary condition to the slope sample as existed at the front wall. Any gaps between the slope specimen and the crest-end or rear walls of the test container were filled and compacted with cohesionless silica 20 sand, while the gap between the toe of the slope sample and the toe-end

wall was bridged by a wooden block firmly wedged into place (see Figures 4.2 and 4.7). These measures were taken to ensure that plane strain conditions would be met across the slope specimen, and that the slope sample would be subjected to the same horizontal motions as those given to the test container by the servo-valve and actuating piston. At this stage, the pencil lead transducers were lightly driven into their pre-made holes with a small hammer. Three tie-rods were also inserted and tightened between the tops of the front and rear walls of the test container, to prevent flexing and maintain plane strain conditions across the slope specimen during centrifuge flight (see Figure 4.7).

4.2 THE CENTRIFUGE SLOPE FAILURE EXPERIMENT

4.2.1 Test procedure

The configuration of the centrifuge arm for a typical slope failure test is shown in Figures 4.8 and 4.9. Each slope failure test was controlled by the Zenith computer through a program combining BASIC and assembly language routines, and a test was ready to be run once the wires from the pencil lead transducers had been connected to the bounce eliminator box. To begin a test, and for reasons given in Section 5.1.1, the centrifuge was spun up to $42g$ (given by 200 rpm and a centrifugal radius of 37 inches to the centroid of the slope sample) and photographs were taken of the grid-painted side of the slope specimen at $5g$ increments by the 35 mm still camera mounted on the arm. During spin-up, the computer continually

monitored the status of the pencil leads through an assembly language routine and noted the time and slope location of any lead breakage. At $42g$, the computer excluded any already broken leads from further consideration and readied the digital counters for simultaneous counting, to be triggered by the first subsequent lead to break. One more pre-failure photograph was taken by the 35 mm camera before the aircraft landing lamp was turned on, the movie camera started and a single impulse of approximately $15g$ peak acceleration directed horizontally from slope crest to slope toe given to the test container by the servo-valve and actuating piston. The ensuing slope failure was recorded on 16 mm movie film while the sequence and timing of pencil lead breakage were stored in computer memory. Horizontal acceleration and displacement of the test container were also recorded during slope failure with appropriate transducers and a high speed analog-to-digital converter. The aircraft landing lamp was then turned off, a post-failure photograph taken by the 35 mm camera, and the centrifuge brought to rest to complete the test.

Although the recording of a static slope failure on film would have been desirable, the passage of a 100 ft roll of film through the high-speed movie camera, even at its slowest framing rate, placed an impossible constraint on the time of occurrence of a static failure. Hence the time of initiation of failure needed to be controlled and this was best done by dynamically loading the slope specimen in a gravity field in which it was marginally stable. A single horizontal impulse was

considered the minimum dynamic perturbation to static gravitational loading.

4.2.2 Example results

The first slope failure experiment to include pencil lead transducers and 35 mm in-flight photographs was test 12 (see Table 5.1), and the results from this test are presented below to illustrate the test procedure of Section 4.1. Those tests yielding valuable information about the mechanism of slope failure, both prior and subsequent to test 12, are presented and discussed in Section 5.1.

Figures 4.10 and 4.11 are, respectively, the pre-failure and post-failure photographs of slope sample 12, taken at $30g$ by the 35 mm camera mounted on the centrifuge arm. Test 12 was conducted at $30g$ instead of $42g$ since minor damage to the face of the slope specimen prior to test commencement was expected to cause premature slope failure below $42g$. Figure 4.12 shows the horizontal impulse given to slope specimen 12, as well as the resulting horizontal acceleration and displacement of the test container, and points out that the impulse of $15g$ peak acceleration and 0.1 seconds duration (see Figure 4.12(b)) given to the model slope at $30g$ actually represents a short, intense prototype earthquake of $0.5g$ peak acceleration and 3 seconds duration. The vertical spike appearing in Figure 4.12(a) and marked by an arrow is caused by the analog-to-digital converter losing a binary digit during its rapid sampling and storing cycle. The high frequency accelerations commencing at approximately 0.10 seconds in Figure 4.12(b) and also marked by an arrow are believed to be caused by debris from the collaps-

ing slope striking the accelerometer mounted near the bottom of the toe-end wall of the test container, independently of the already noisy accelerometer signal.

Although Section 4.1 mentioned that the pencil lead transducers were lightly driven into their pre-made holes in the face of the slope specimen with a small hammer, this procedure was an improvement over the original method used for test 12, in which a weak plaster of Paris solution (2 parts water to 1 part plaster) was injected into each hole with a hypodermic syringe before lead insertion into the slope face by a push of the hand. The intention of this procedure was to cement each pencil lead to the surrounding slope material with a thin coating of plaster of Paris. As shown in Figures 4.13 and 4.14, however, the injected plaster of Paris solution effectively grouted the porous slope material around the pencil leads, forming "columns" of disproportionately high shear strength which prevented complete slope and pencil lead failure and forced partial collapse to take place in the ungrouted material farther from the pencil leads. Figure 4.15 shows the configuration of pencil leads for test 12 and the order of those which broke during the partial slope collapse shown in Figures 4.11 and 4.13.

4.3 DATA REDUCTION

4.3.1 Film digitization

The 16 mm movie films taken at approximately 1600 frames per second during centrifuge slope failure tests 10 and 11 were magnified by screen projection

and inspected closely, both in forward and reverse motion, and frame by frame. Propagation of the failure surface through each slope specimen, however, occurred very rapidly — so rapidly in fact that the first of two consecutive frames of movie film at the time of failure *appeared* to show no evidence of a failure surface which was fully manifest in the second. Such direct film observation with the naked eye, therefore, failed to determine beyond doubt the sequence of events constituting the mechanism of slope failure and although the films *suggested* the mechanism of Figure 5.34 (determined predominantly from tests 15 and 17), the evidence was inconclusive. It was considered quite possible, however, that the failure surface was indeed propagating across successive frames of the movie film even though the naked eye could not apparently detect it before it was fully developed. A high resolution method of film analysis was thus needed — one that would be more consistent, systematic and reliable than the naked eye and would eliminate as much subjective judgment as possible. Digitization appeared to be able to meet these needs.

Film digitization, shown schematically in Figure 4.16, involves passing light through a suitably-sized aperture placed directly over the frame of film under consideration and measuring the intensity of light reaching a photovoltaic cell beneath the film. This cell produces a voltage proportional to the intensity of light striking it and the range of voltages emitted as the aperture is moved over the frame of film can be mapped onto a digital *gray scale* from 0 to 255 (the range

of 8-bit binary numbers). The aperture size determines the spatial resolution of the digitization and the frame of film is subdivided into x aperture lengths in the horizontal direction and y aperture lengths in the vertical direction. As the aperture is scanned across the film, the frame is *digitized* into a two-dimensional array of 8-bit binary numbers, with y rows and x columns. To produce the results presented below and in Section 5.2, the original gray scale of digitization (0 to 255) was further mapped onto a reduced gray scale from 0 to 7, with 0 indicating white and 7 representing black. Such a mapping generally reduces intensity resolution but this was not visually apparent in any of the images digitized from the centrifuge slope failure films.

The power of the digitization technique lies not in its ability to reproduce an analog frame of film in digital form, but in its capacity to allow subtraction of the arrays representing two different frames to produce a difference image. If the two frames are identical, their subtraction will yield zero or no difference. If, on the other hand, there *is* a difference between the two frames, such as the appearance of a displacement discontinuity across a propagating slope failure surface, the subtraction will be non-zero and might be detected at a lower displacement threshold than that required by the naked eye. It should be noted that the *difference* scale (-7 to 7) created by subtraction is also mapped onto the 0 to 7 gray scale for presentation of the results.

Difference images derived from the movie films of slope tests 11 and 12 were

the ultimate test of the digitization technique and these images are presented and discussed in Section 5.2. For illustrative purposes, however, the results of digitizing and subtracting Figures 4.10 and 4.11 are presented below. Figures 4.17 and 4.18 are the central areas of Figures 4.10 and 4.11 respectively, reproduced from the digitization of both 35 mm negatives. Figure 4.19 is the difference image formed by subtracting Figure 4.18 from 4.17. Since Figures 4.16 and 4.17 are pre-failure and post-failure images of slope test 12, the relative displacements of slope points between the two images are large and these are most clearly seen by the appearance of the orthogonal grid lines in the sliding region of Figure 4.19, in contrast to the absence of the clear grid in the bottom right-hand corner of Figure 4.19, where little or no movement of the soil occurred.

4.3.2 Pencil lead breakage

In parallel with film digitization, data from the pencil lead transducers were also expected to clarify the sequence of events constituting the mechanism of slope failure. After being readied for counting by the computer during a centrifuge slope failure test, the digital counters connected to each unbroken pencil lead were simultaneously triggered by the first subsequent pencil lead to break. Once this occurred, an assembly language routine first read the time, and then sampled and stored in computer memory the status of the leads 32000 times at approximately 14 μs intervals before reading the time again and stopping. Upon completion of the slope failure test, another assembly language routine scanned this region of

computer memory and retrieved the lead status and position within the 32000 samples of any change in lead status (indicating another broken lead). From these reduced data, the sequence of pencil lead breakage and elapsed time between breakages were computed. Higher resolution of the elapsed time between lead failures than 14 μs was obtained from the digital counters which counted in steps of 0.5 μs with a cycle time of 32 μs.

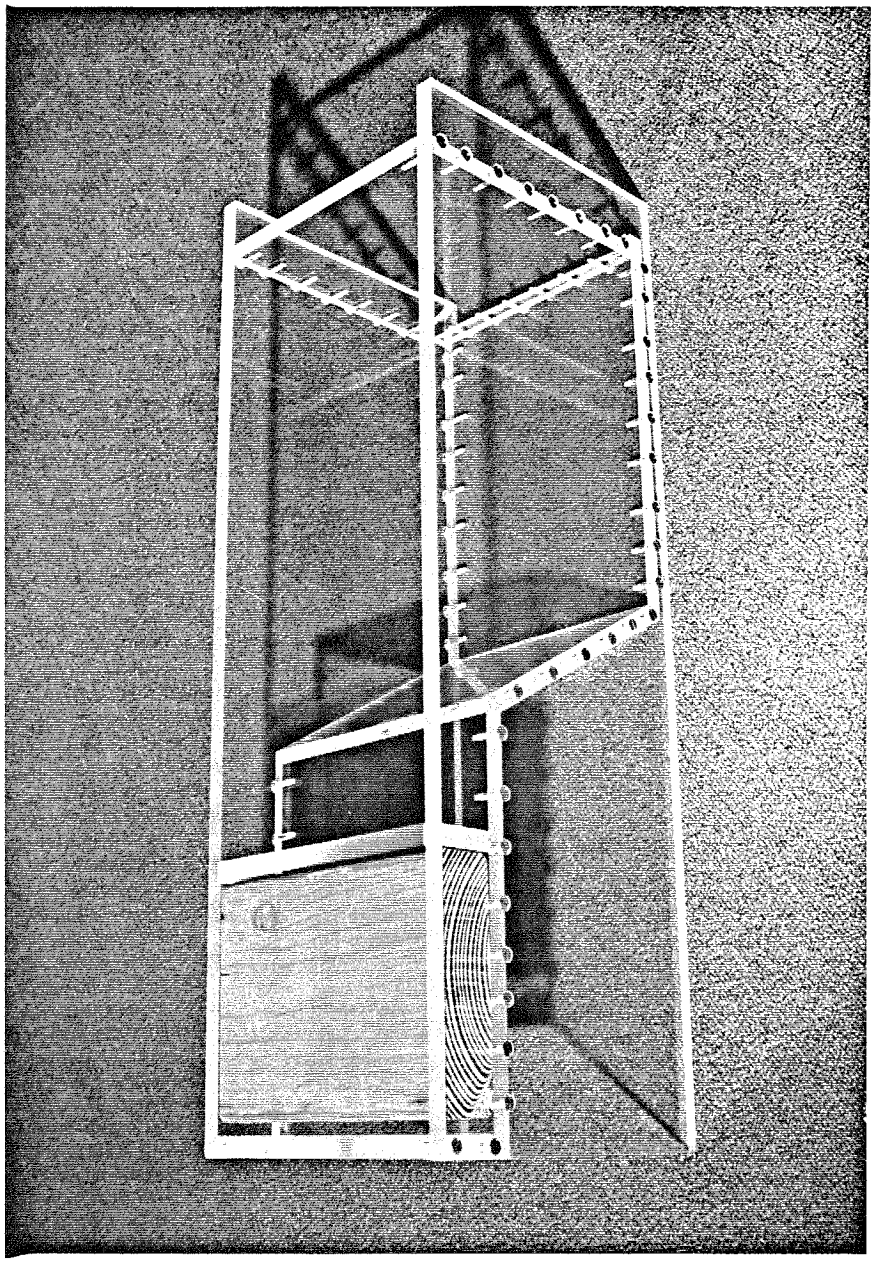

Figure 4.1 Lucite mold for slope test specimen, turned upside down for specimen compaction

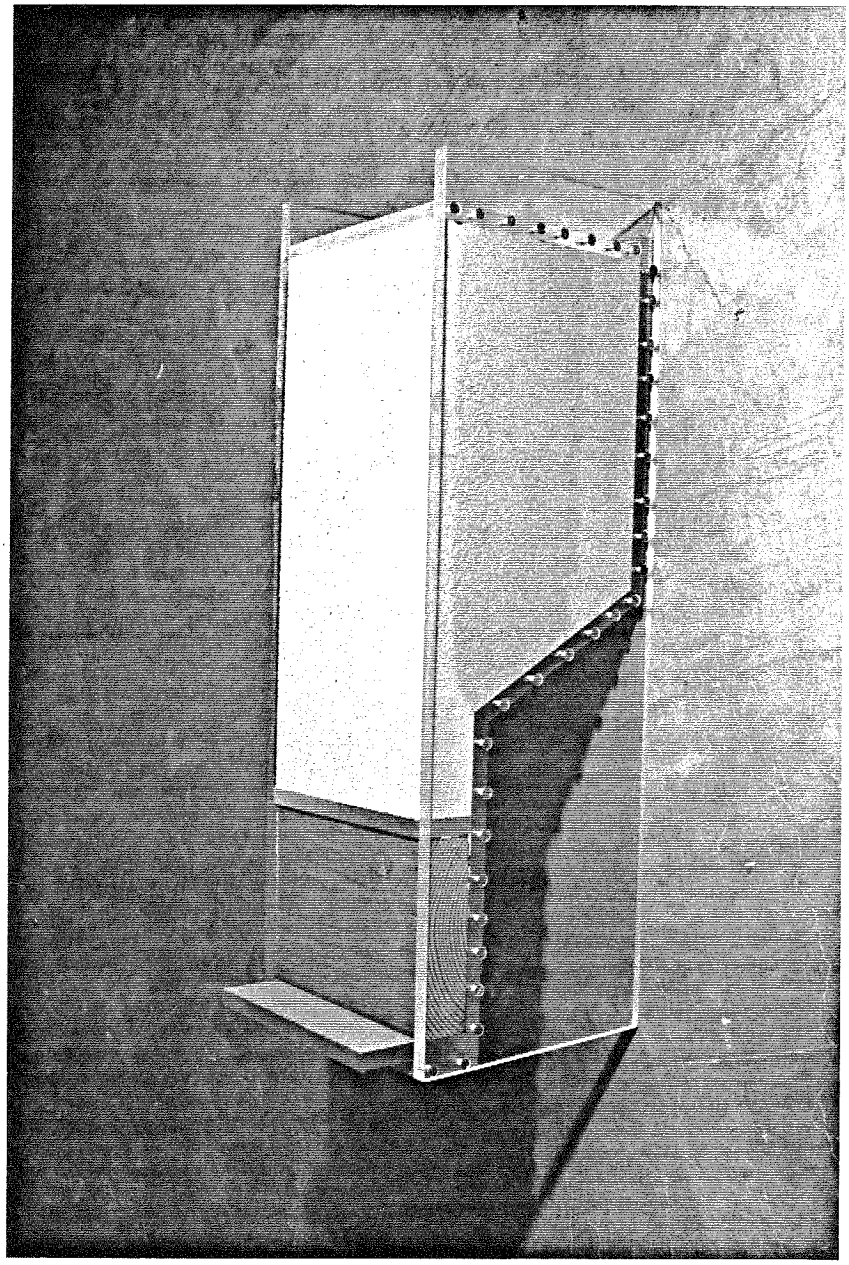

Figure 4.2 Compacted slope specimen in lucite mold, with wooden block as spacer at toe

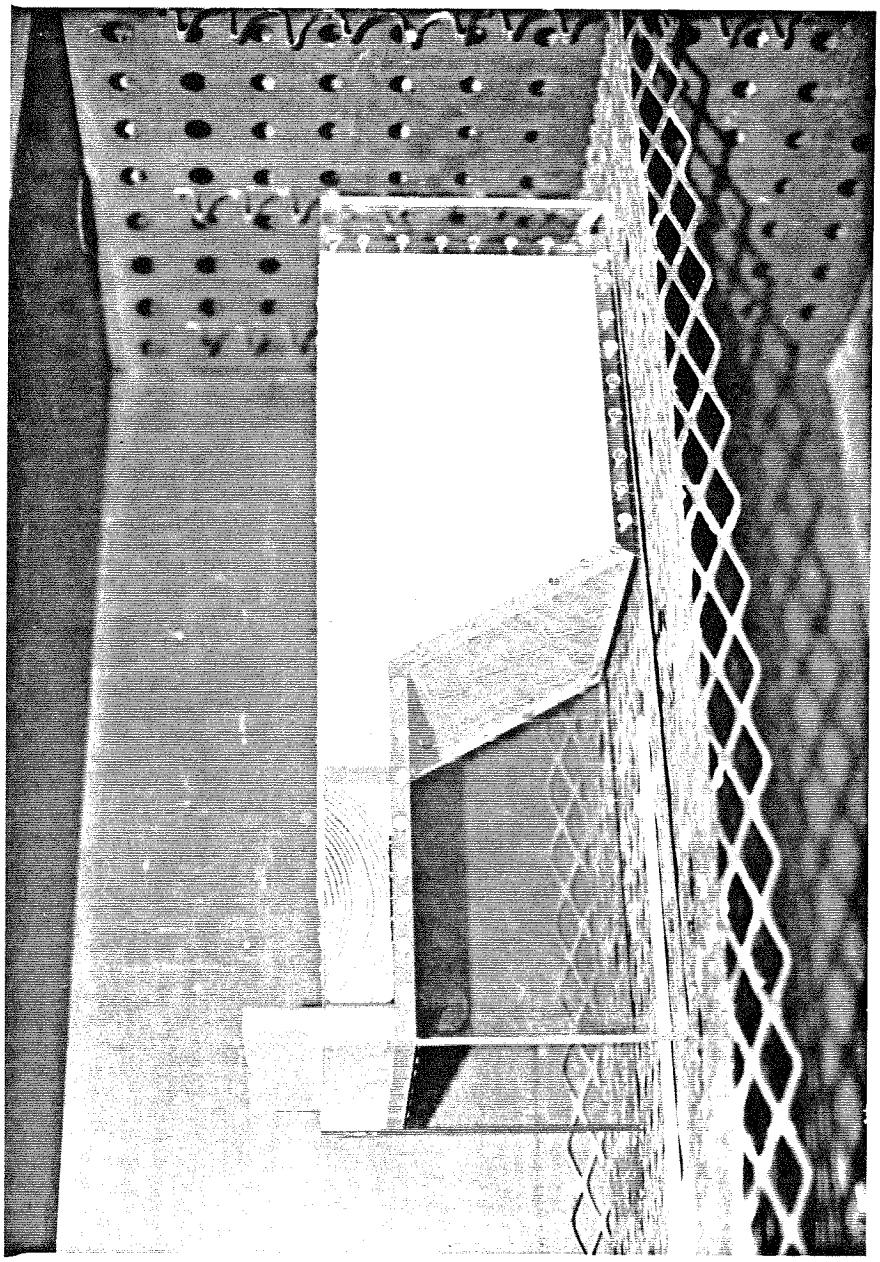

Figure 4.3 Lucite mold, complete with compacted slope specimen and inserted stainless steel rods, prior to removal from oven

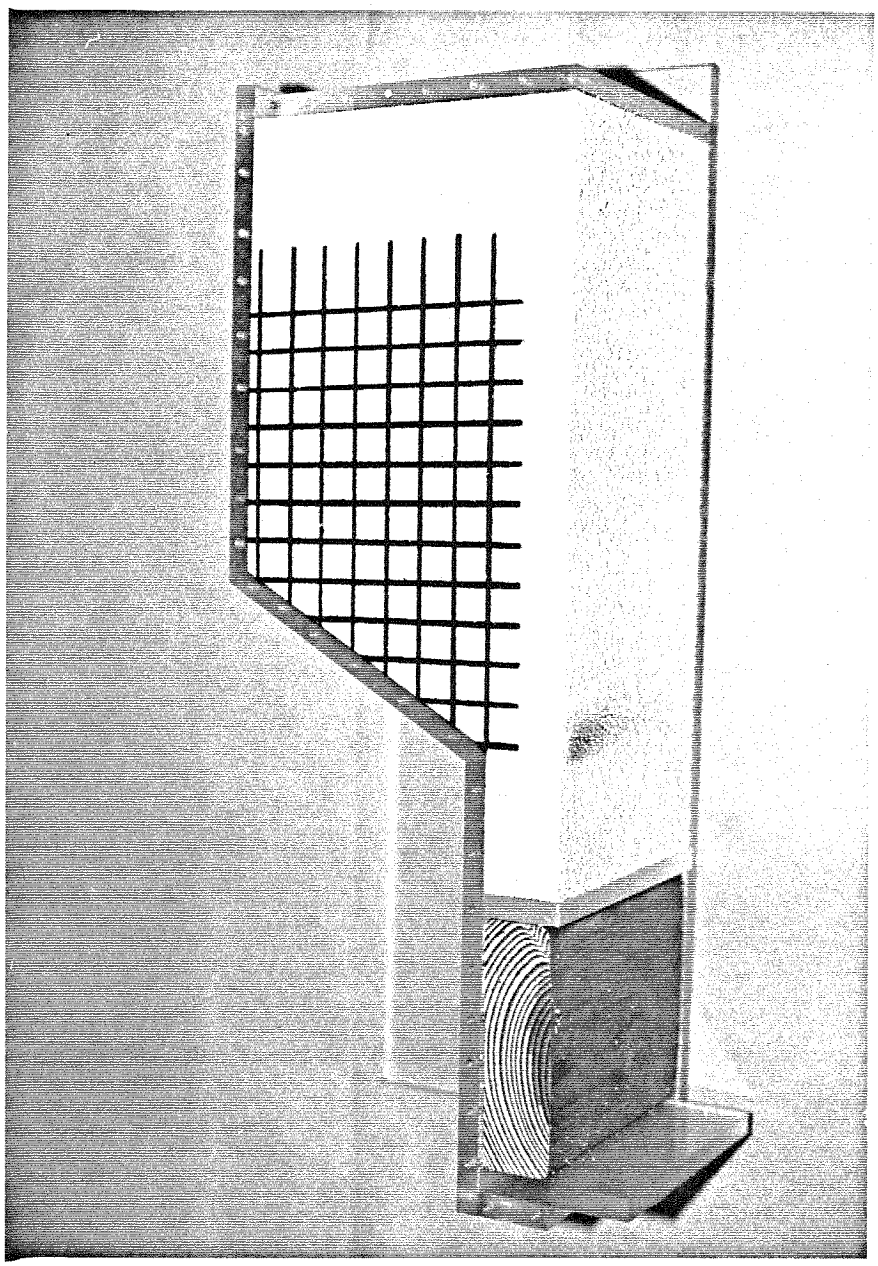

Figure 4.4 Grid of orthogonal black lines spray-painted onto exposed side of slope specimen

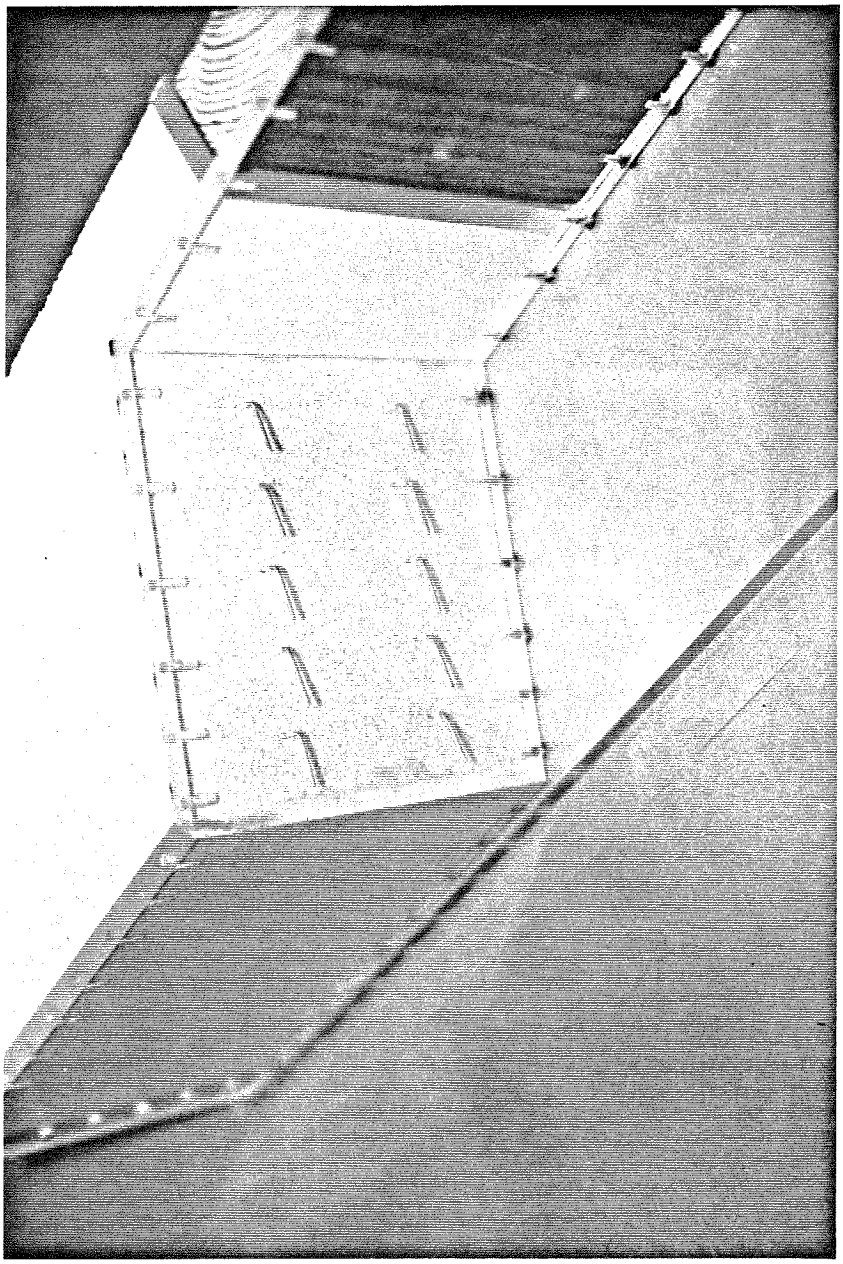

Figure 4.5 Stainless steel rods inserted through face of lucite mold and slope specimen

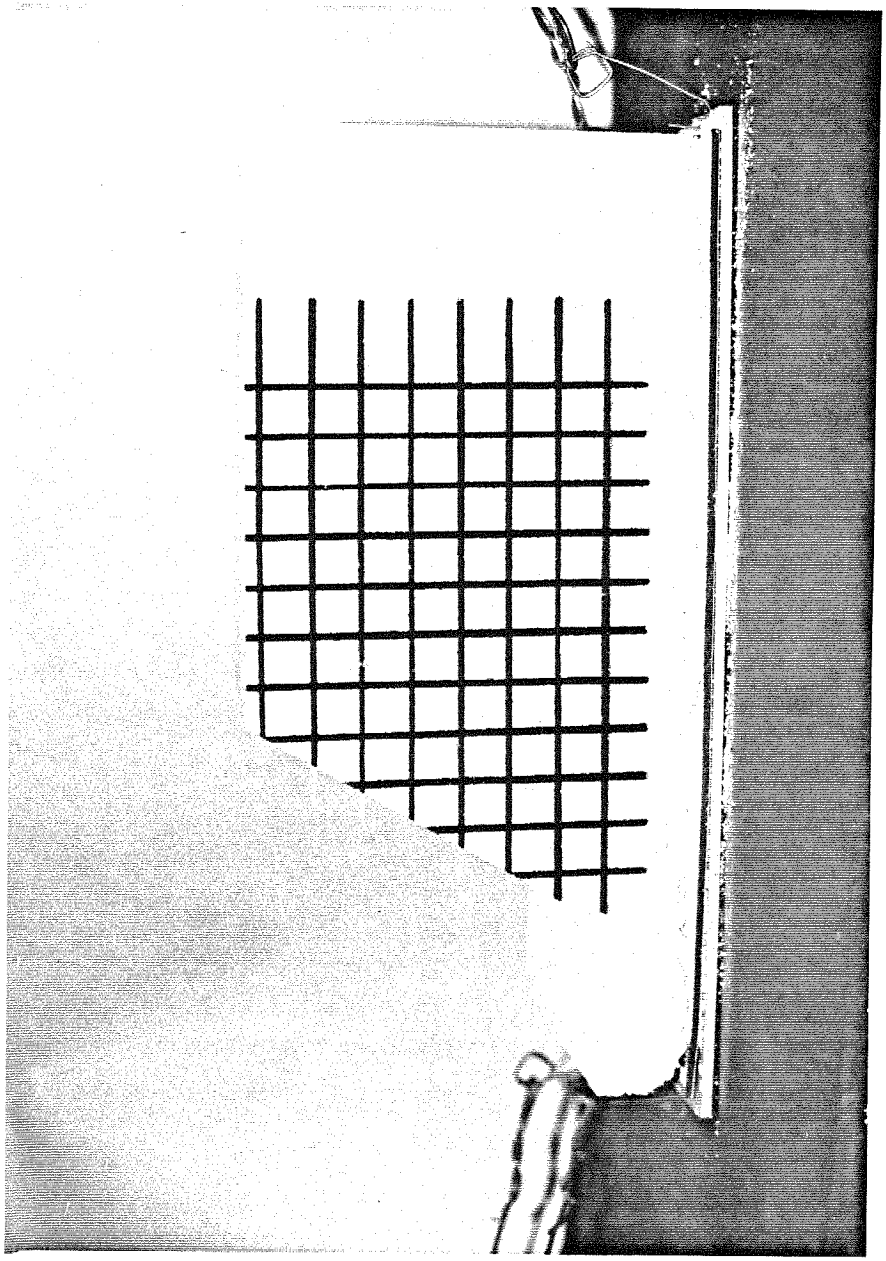

Figure 4.6 Free-standing slope specimen seated on rubber pad and aluminum baseplate, with wire hook lifting handles attached for transfer of specimen to centrifuge test container

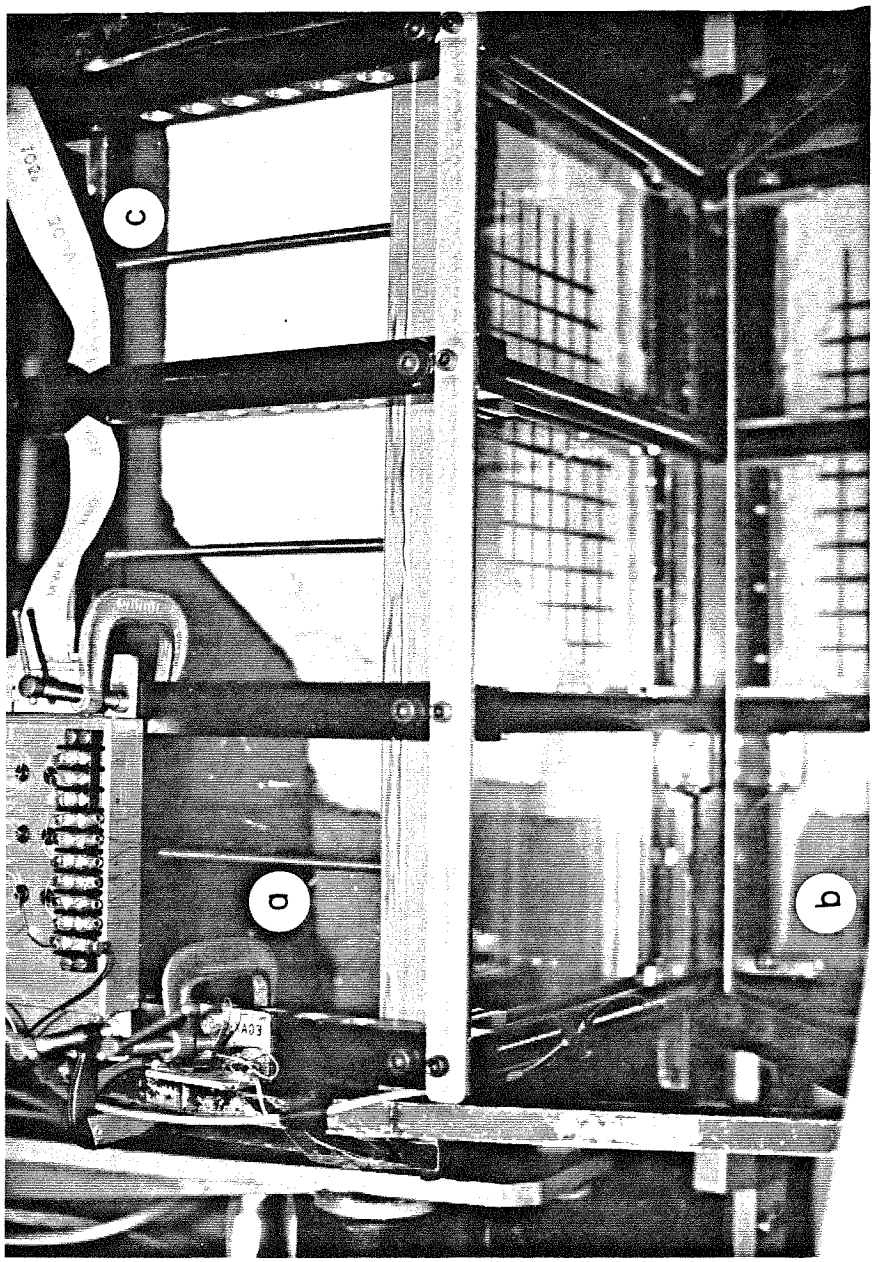

Figure 4.7 Slope specimen in centrifuge test container, showing wooden block wedged between toe of slope and end wall of container, 45° mirror, and plane strain tie rods
a = wooden block, **b** = mirror, **c** = tie rod

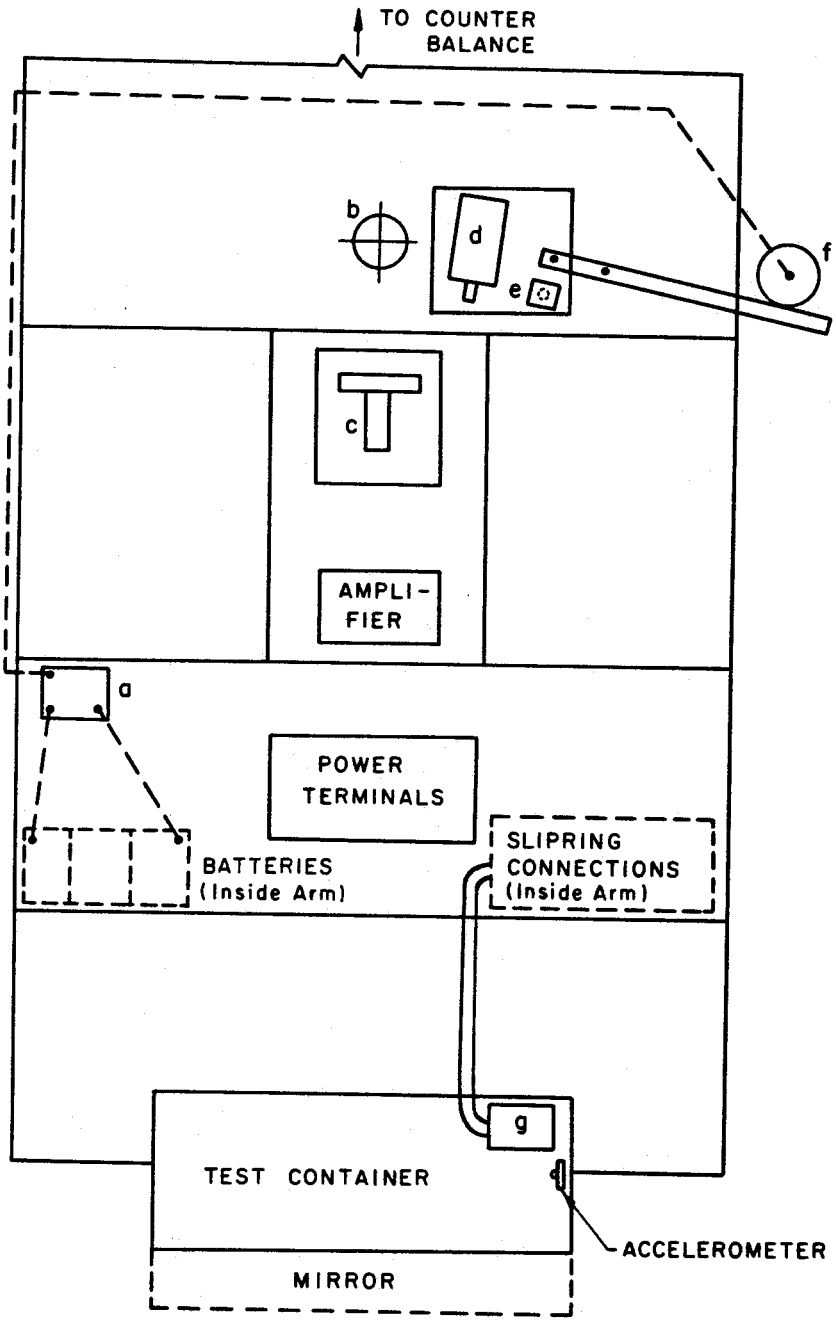

Figure 4.8 Configuration of centrifuge arm in plan for typical slope failure test (not to scale)
a = aircraft landing lamp relay
b = rotation axis and hydraulic union
c = 35 mm still camera, **d** = 16 mm movie camera
e = flash unit, **f** = aircraft landing lamp
g = bounce eliminator box
(Hydraulic hoses, accumulators and majority of wiring omitted)

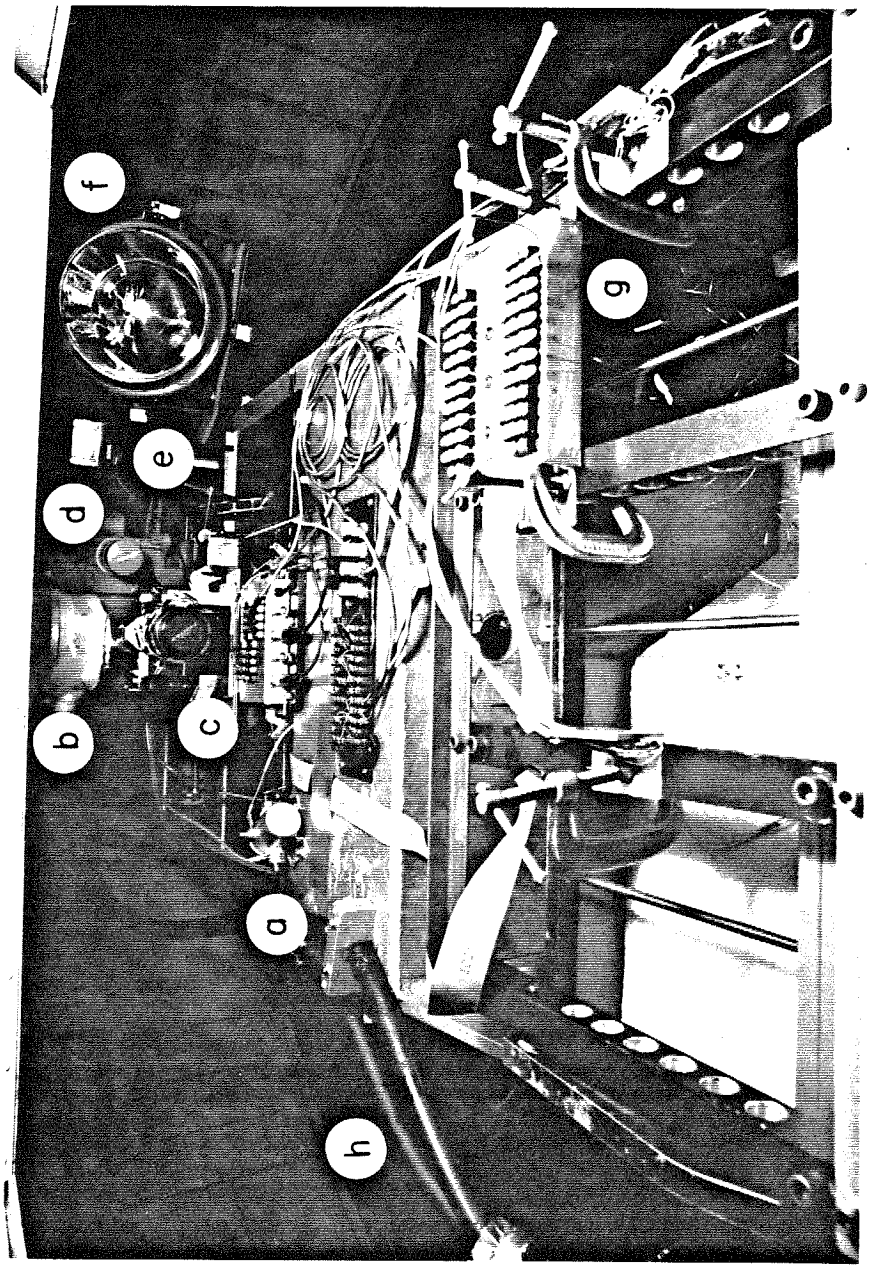

Figure 4.9 Centrifuge arm prior to typical slope failure test
a = aircraft landing lamp relay, **b** = rotation axis and hydraulic union
c = 35 mm still camera, **d** = 16 mm movie camera
e = flash unit, **f** = aircraft landing lamp
g = bounce eliminator box, **h** = hydraulic hoses

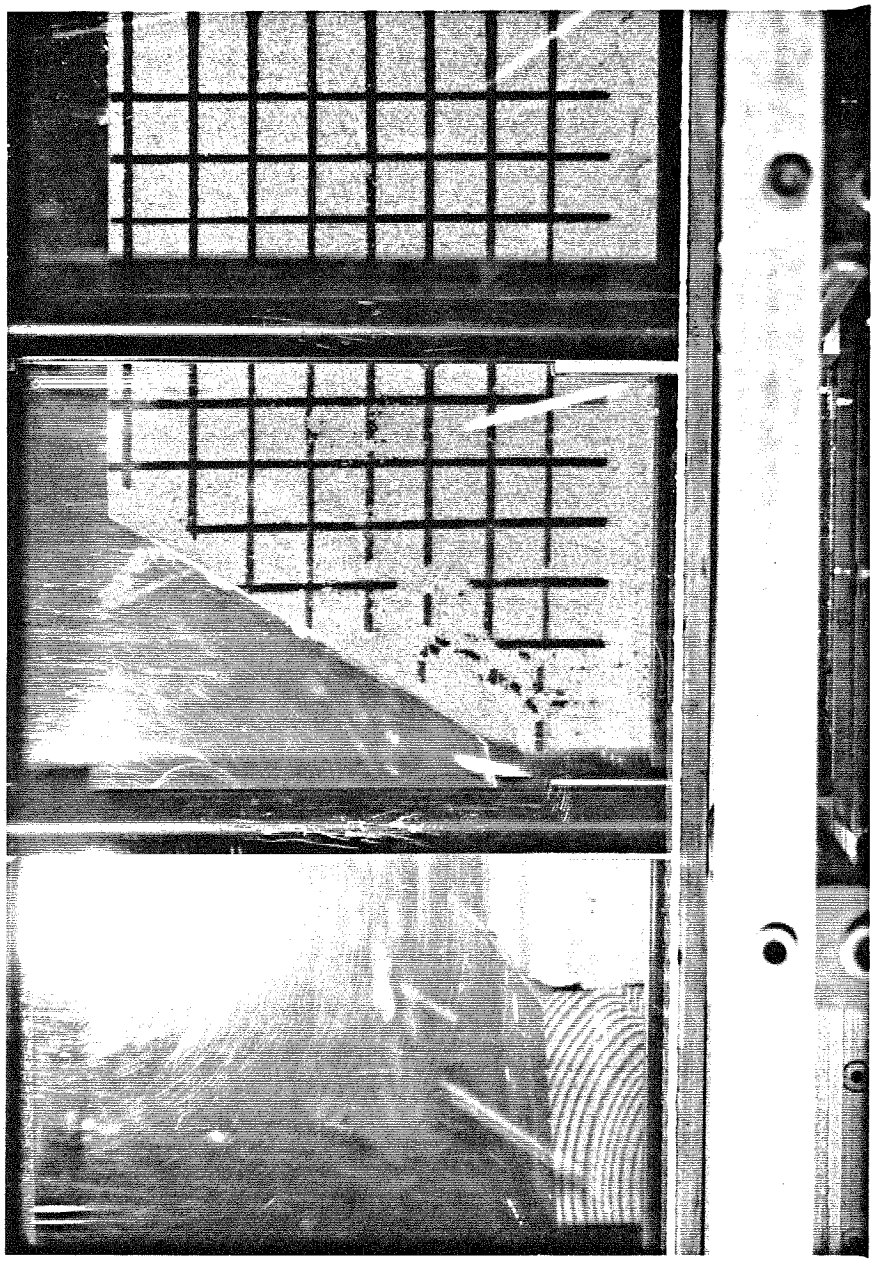

Figure 4.10 Pre-failure view of slope specimen 12 taken at 30*g*

Figure 4.11 Post-failure view of slope specimen 12 taken at $30g$

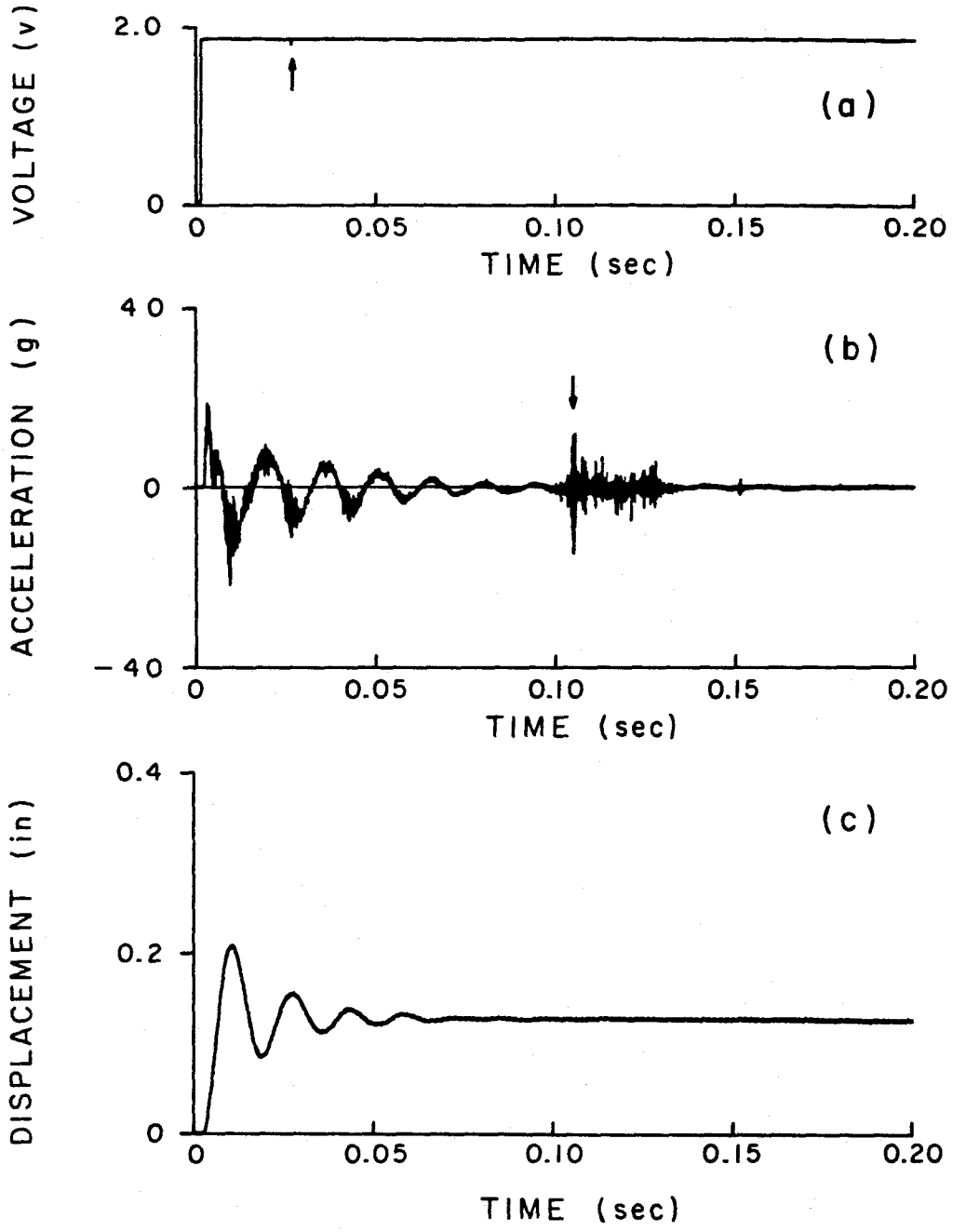

Figure 4.12 Slope test 12 results (centrifuge scale)
(a) Horizontal impulse given to servo-valve and actuating piston
(Arrow indicates loss of random bit of data by analog-to-digital converter)
(b) Measured horizontal acceleration of test container
(Arrow indicates debris from failing slope specimen striking accelerometer)
(c) Measured horizontal displacement of test container

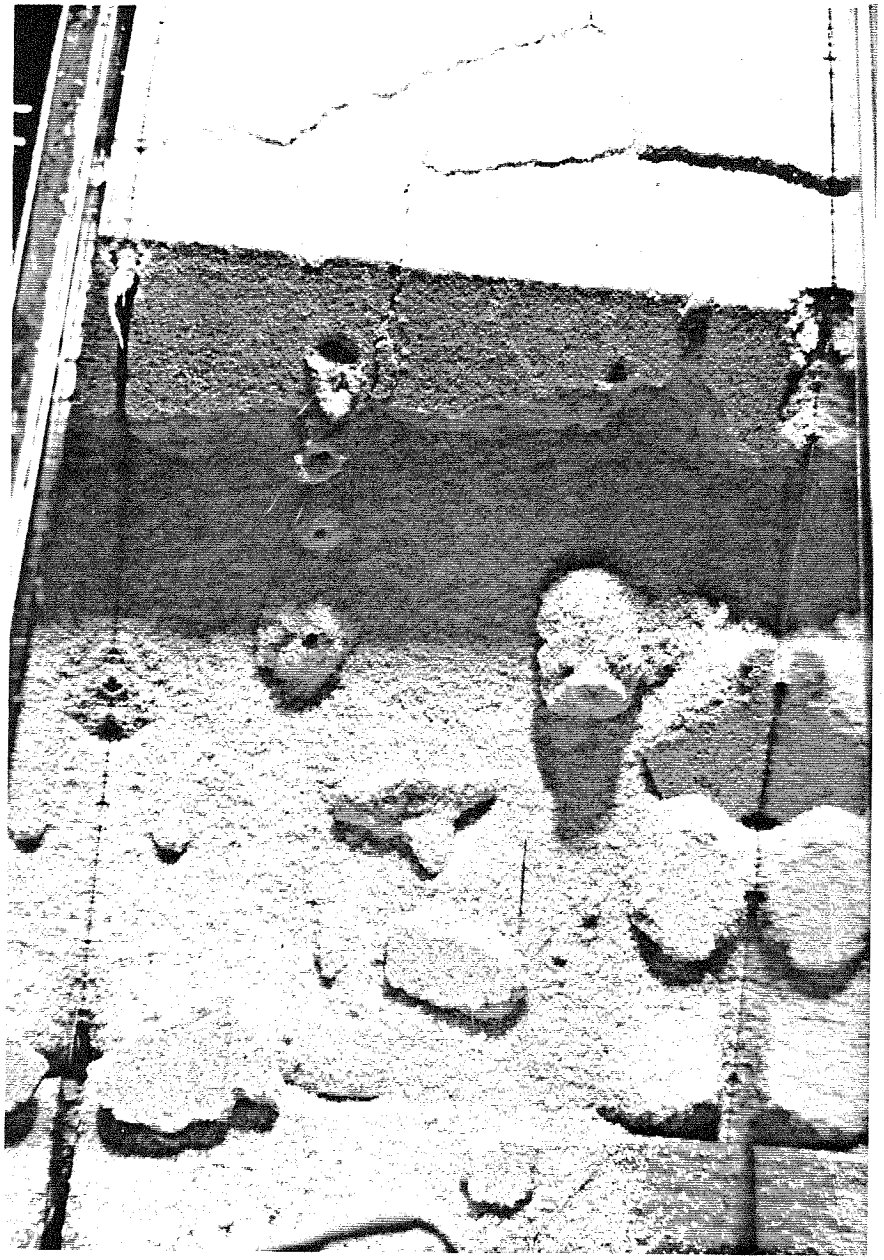

Figure 4.13 Post-failure debris of slope test 12

Figure 4.14 Plaster of Paris "columns" surrounding unbroken pencil lead transducers of slope test 12

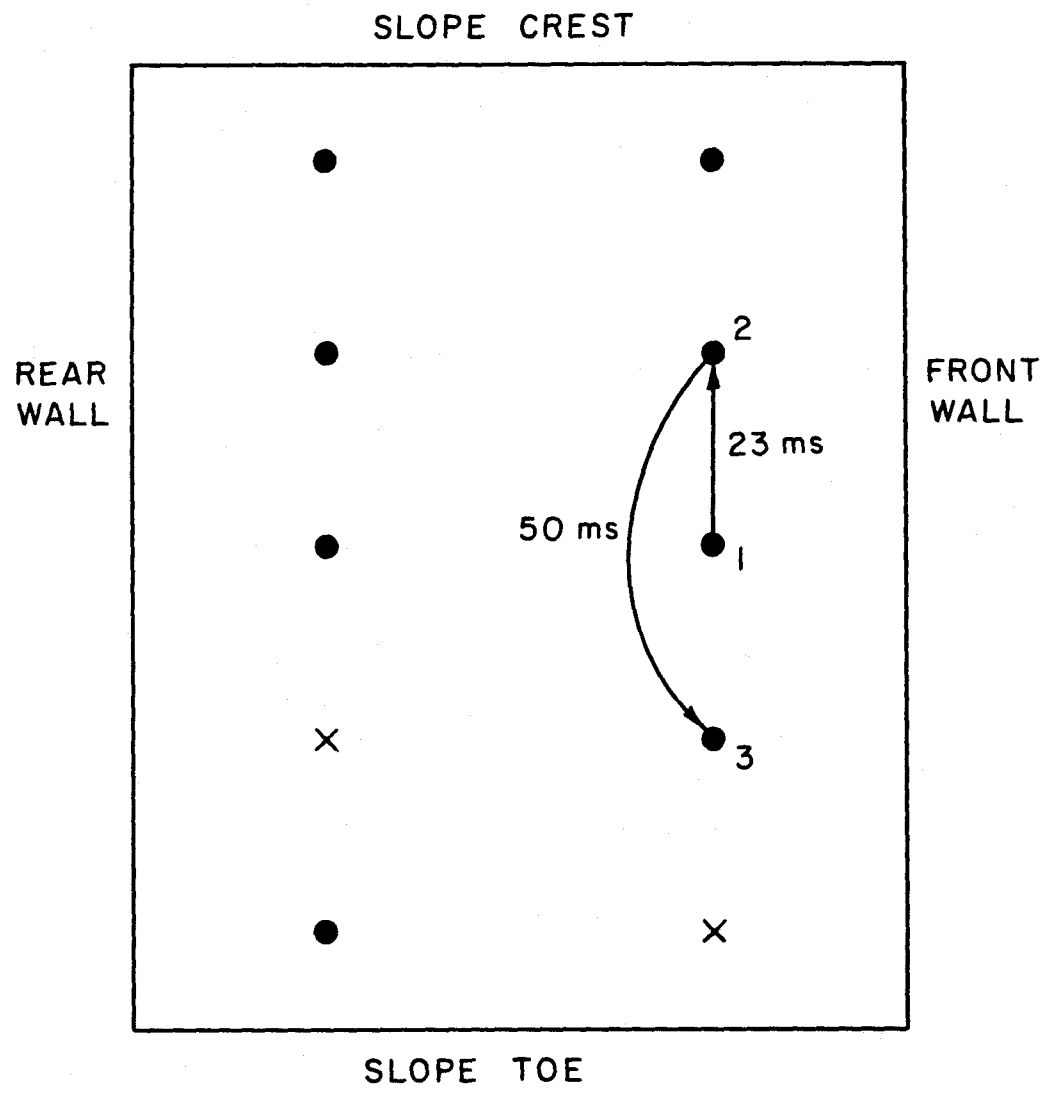

Figure 4.15 Failure sequence of pencil lead transducers during slope test 12. Leads are numbered in order of failure with arrows indicating time interval between breakage of successive leads. Unnumbered leads did not break, and crosses mark leads which broke during insertion (*i.e.* before test)

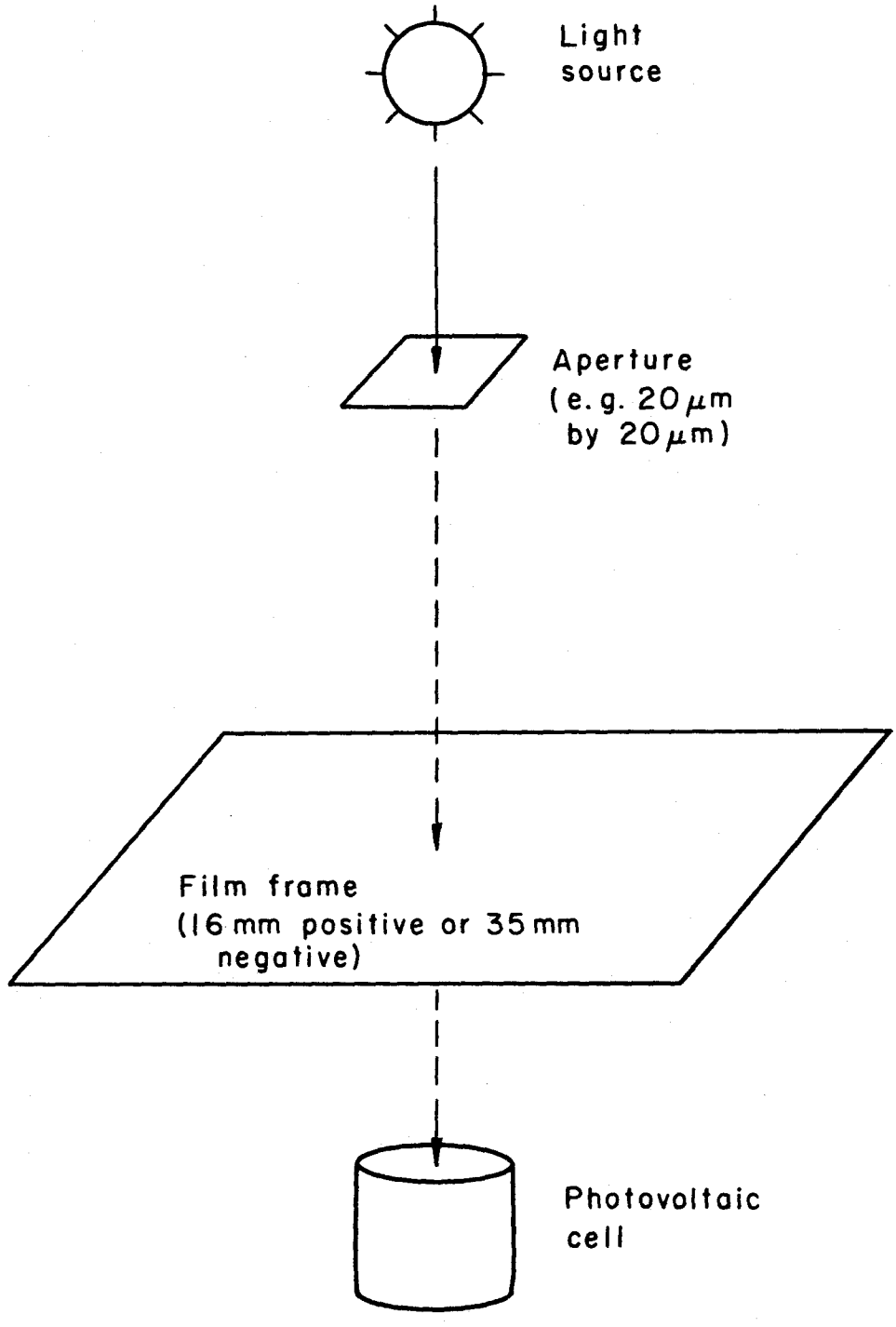

Figure 4.16 Film digitization

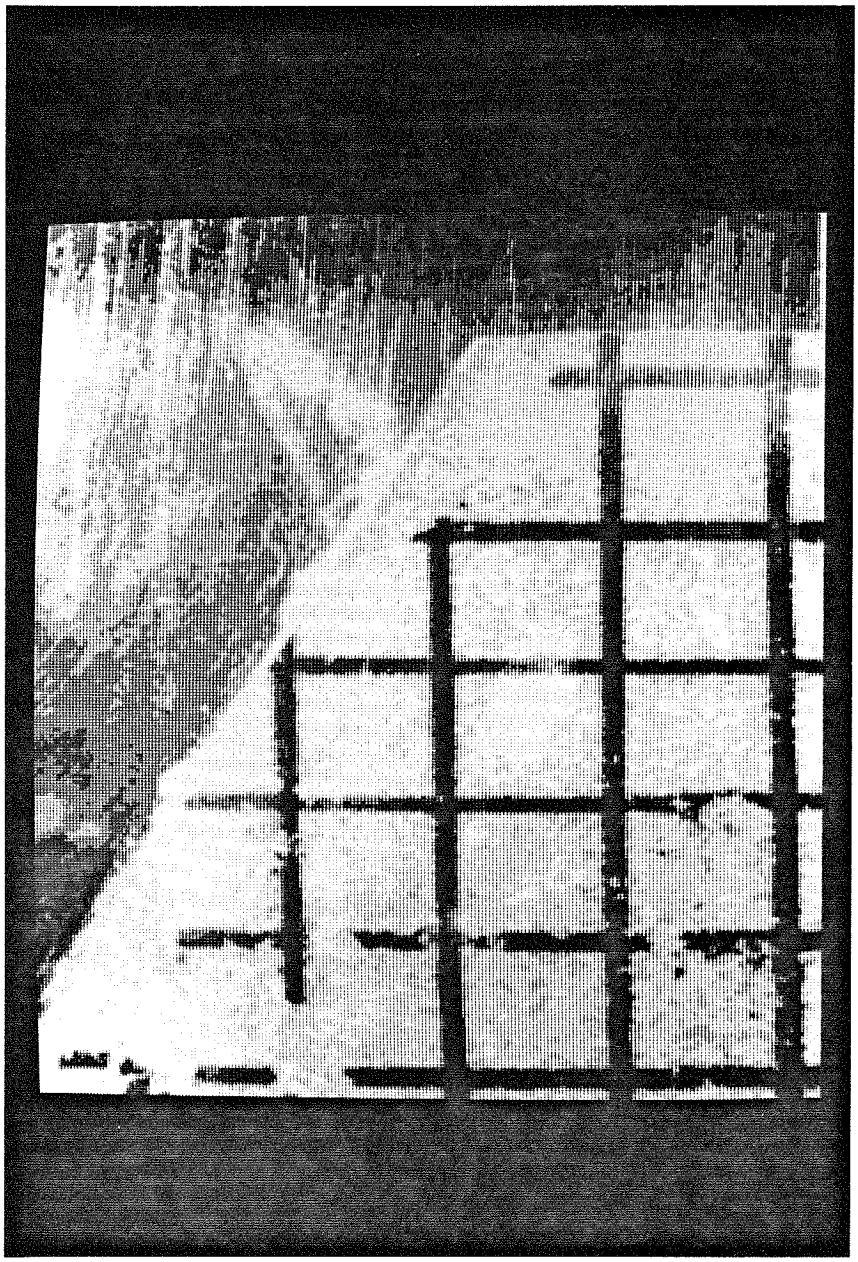

Figure 4.17 Reproduction of central region of Figure 4.10 from digitized data

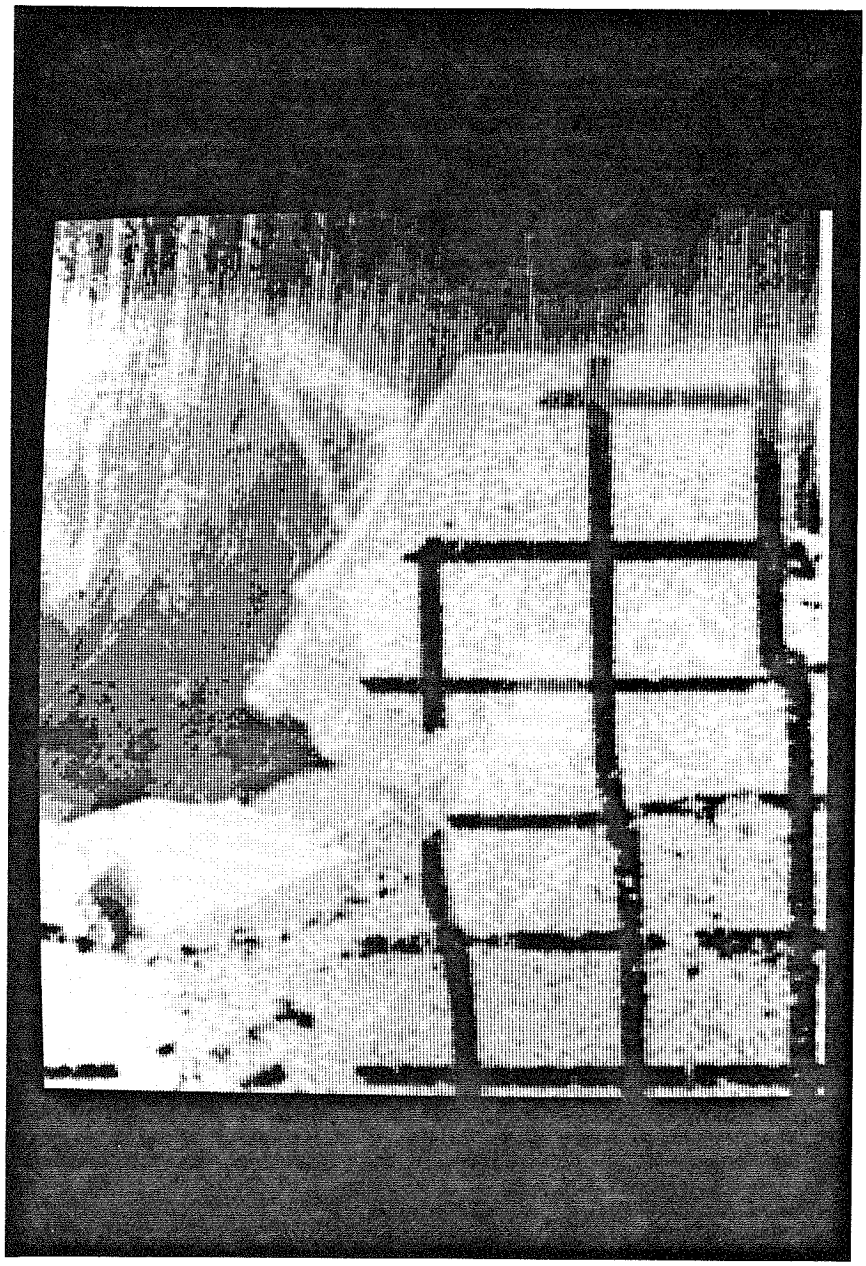

Figure 4.18 Reproduction of central region of Figure 4.11 from digitized data

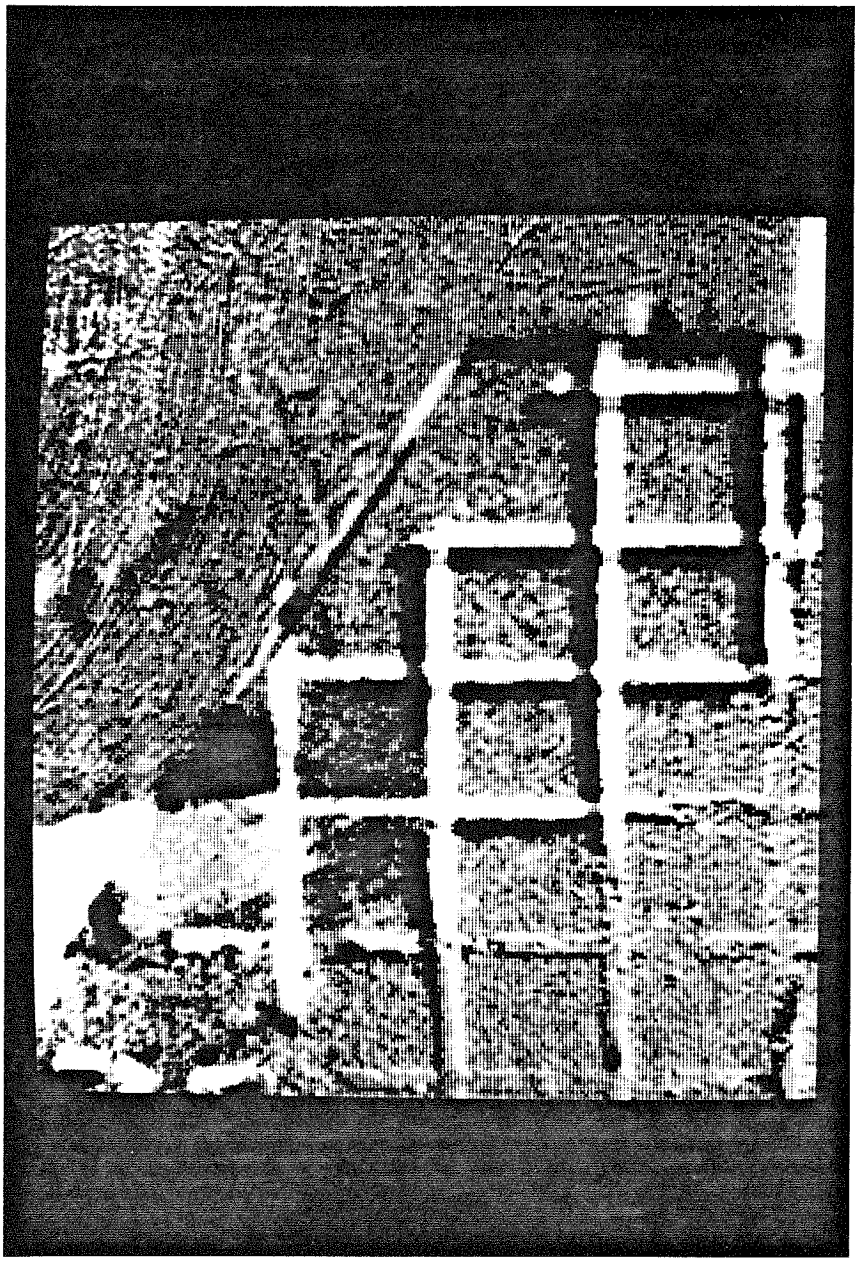

Figure 4.19 Difference image formed by subtraction of Figure 4.18 from Figure 4.17

Chapter 5

EXPERIMENTAL RESULTS

5.1 CENTRIFUGE SLOPE FAILURE TESTS

5.1.1 Introduction and overview

A total of 18 slope specimens was tested in the centrifuge to determine the mechanism of slope failure. The essential features of each test are summarized in Table 5.1 and those tests yielding results of sufficient importance are discussed in Sections 5.1.2 through 5.1.6. As with most experimental work, a number of trials was required before repeatable results could be obtained and tests 1 through 8 fell into this category. These tests will not be discussed here except to mention that they established by trial and error a gravitational acceleration of $42g$ as the approximate static failure level of the centrifuge specimens. At this gravity level, the slope test samples were found to be on the verge of collapse and hence in a suitable condition for the initiation of failure by impulsive or simulated earthquake loading. Subsequent slope tests 9, 10 and 11 were then the first to shed light on the dynamics of slope failure but produced sufficiently inconclusive results to require a second series of more complex experiments for clarification.

Slope tests 12 through 18 constituted the second series of centrifuge experiments and employed pencil lead transducers, 35 mm in-flight photographs and higher resolution movie filming in the attempt to clearly establish the slope failure mechanism. As the first of the new series, test 12 was discussed in Section 4.2.2 as an illustrative example of these improvements and the centrifuge test procedure. However, it was not until after trials 13 and 14, which are not discussed here but corrected the pencil lead problems of test 12, that slope test 15 established the initiation of shear failure at the slope toe, among other important observations discussed in Section 5.1.4. These conclusions were supported by test 17 of Section 5.1.5, which also made the presence of crest tension cracking apparent, after the failure of slope specimen 16 added no new information to the test 15 results. Slope test 18 was a static failure experiment for reasons given in Section 5.1.6 and was the final centrifuge test in this experimental study of slope failure.

5.1.2 Slope tests 9 and 10

Tests 9 and 10 both involved taking the slope specimen to $42g$, before inducing failure by a simulated earthquake instead of the single impulse described in Section 4.2.1 and shown in Figure 4.12(a). Since slope tests 9 and 10 yielded the same results, those of test 10 are representative and are presented below. Figure 5.1 shows the slope sample before flight and Figure 5.2 shows its post-failure state. The earthquake signal supplied to the servo-valve and actuating piston is shown in Figure 5.3(a), while the ensuing horizontal acceleration and displacement of the

test container and slope specimen appear in Figures 5.3(b) and (c) respectively. The vertical spikes appearing in these time histories and indicated by arrows are caused by the occasional loss of random bits of data by the analog-to-digital converter.

After inspection of Figure 5.2, it would probably be concluded that slope specimens 9 and 10 developed simple wedge failure mechanisms along the inclined plane separating the intact slope material below from the debris above. Such a conclusion is demonstrated to be incorrect, however, on the basis of the movie films taken of both slope failures. The movie films show earthquake failure to be a progressive phenomenon beginning with an initial, shallow, static slip-circle type of failure of the slope face, followed by propagation of the failure back into the slope mass as blocks of material close to the face and crest slide away in subsequent earthquake pulses and leave the remaining material unsupported and unstable. This "chain reaction" continues until a flatter slope is established — one that is stable even under continued earthquake motions. It is this finally created slope appearing in Figure 5.2 which leads the observer to the assumption of an incorrect failure mechanism in the absence of information on the dynamics of the failure.

5.1.3 Slope test 11

Slope specimen 11 was the first to be failed by the single horizontal impulse mentioned in Section 4.2.1. Figures 5.4 and 5.5 show the pre-failure and post-failure states of the slope sample respectively, and Figure 5.6 gives the horizontal

acceleration and displacement of the test container resulting from the impulsive input.

Figure 5.5 suggests a slip-circle type failure mechanism for slope test 11 and this was confirmed by the movie film taken of the failure. The more fundamental question to be addressed by the movie film, however, was where did the failure surface originate and how did it propagate through the specimen to give the final profile of Figure 5.5 ? To this end, the movie film of slope test 11 *suggested* the failure sequence of Figure 5.34 but could not confirm it due to inadequate resolution. This prompted digitization of the film (as described in Section 4.3.1) to give the results presented in Section 5.2.1, and further demanded a more complex series of subsequent experiments. Slope test 12 (see Section 4.2.2) was the first of the new series of higher resolution tests, using pencil lead transducers and a movie film taken at approximately 5000 frames per second.

5.1.4 Slope test 15

Test 15 developed from test 12, with higher resolution photography and continued use of the pencil lead transducers. Although the pencil lead problems of test 12 had been overcome, specimen 15 was similarly reluctant to fail and required three separate failure attempts. At the time, test 15 was considered just another unsuccessful test, but later proved to yield some of the most definitive observations of the initiation and propagation of slope failure.

Figures 5.7 and 5.8 show slope specimen 15 after the first impulsive failure attempt (slope test 15a) but before the second (test 15b). A casual glance at both photographs indicates little, if any, breakdown of the sample, and no slope collapse. Closer inspection, however, shows that although the slope has not collapsed, the failure surface has been initiated at the toe of the slope and has propagated almost halfway to the slope crest as indicated by discontinuities in the orthogonal grid of lines spray-painted onto the side of the specimen. Furthermore, no pencil leads were broken after this first failure attempt.

Figure 5.9 shows slope sample 15 after the second impulsive failure attempt (test 15b). Here the failure surface is seen to have propagated all the way to the face of the slope in an approximately circular arc, but still without collapse or breakage of any pencil leads. Neither of the movie films taken of tests 15a and 15b added any new information to the mechanism of slope failure determined from the still photographs of Figures 5.7, 5.8 and 5.9, and shown schematically in Figure 5.34.

Slope specimen 15 eventually collapsed as shown in Figure 5.10 after having an increased static gravity field of $46g$ applied in test 15c. No dynamic force was given to the sample to initiate this collapse.

5.1.5 Slope test 17

Test 17 was the final attempt made to simultaneously record a slope failure

with movie film and pencil lead transducers and hence the last test to induce failure by a single horizontal impulse to the test container. Figure 5.11 shows specimen 17 before commencement of the test and Figures 5.12 and 5.13 show the slope sample after failure.

Figure 5.12 shows the same type of slope collapse as Figure 5.10 for slope test 15c. The movie film of slope test 17 also confirmed the observations of tests 15a and 15b involving the development of an approximately circular failure surface between the toe and face of the slope followed by the rotational collapse of the enclosed mass of material to leave the crest block unsupported. The crest block of specimen 17 did not subsequently collapse, however, even though Figure 5.13 shows it to be laterally unrestrained, since the pencil lead transducer inside the block did not break and may have provided sufficient resistance to collapse. The failure sequence of the pencil leads driven into the face of slope sample 17 is presented in Section 5.3.

The movie film of slope test 17 also made the presence of crest tension cracking in the failure of the centrifuge specimens apparent since the tension crack near the crest in Figure 5.12 was seen to open with the failure impulse before collapse of the slope specimen began at the toe.

5.1.6 Slope test 18

Failure of slope specimen 18 was statically induced by steadily increasing

the gravity field until it collapsed under its own weight. The aim of this test was to determine where different regions of the slope finally came to rest after collapse, and whether the final slope profile and sequence of pencil lead failures was dependent on failure being statically or impulsively initiated. Figure 5.14 shows the three grids of orthogonal lines spray-painted in different colors on the side of the slope specimen for marking the toe, midheight and crest regions of the sample. Figure 5.15 shows specimen 18 prior to commencement of the test while Figure 5.16 shows the slope sample after failure. Figure 5.17 shows the pencil lead transducers inserted into the face of the slope specimen prior to testing and Figure 5.18 is a top view of the post-failure slope debris.

The final slope profile of Figure 5.16 is essentially the same as that of Figure 5.5 with the implication that static versus impulsive failure has little influence on the final post-failure state. Figure 5.16 also shows that slope collapse involves the black toe region sliding out from the slope first, followed by the green midheight region falling on top of the toe debris, with the blue and yellow crest region then coming to rest as the final, uppermost layer of the stratified debris. Plane strain conditions are seen to be well maintained for test 18, as verified in Figure 5.18 by the appearance of the crest of the slope specimen as a line of cracked blocks across the top of the debris, normal to the front and rear walls of the test container. The sequence of pencil lead failures for slope test 18 is presented, along with the breakage sequence of other tests, in Section 5.3.

5.2 FILM DIGITIZATION

5.2.1 Slope test 11

The 16 mm movie film taken as slope specimen 11 failed in the centrifuge was digitized as described in Section 4.3.1 in an attempt to clearly define the mechanism of slope failure. A total of 20 consecutive frames spanning the onset of failure was analysed by this technique. Using the first of the 20 frames as a reference in which slope failure had not yet been initiated, each of the 19 subsequent frames was subtracted from the first and the resulting difference images generated. The first indication of failure appeared after comparing difference images "1-6" and "1-7". Figures 5.19, 5.20 and 5.21 show frames 1, 6 and 7 respectively in their original analog form, while Figures 5.22, 5.23 and 5.24 show the central areas of the same respective frames reproduced from the digitized data. Figures 5.25 and 5.26 are respectively the difference images "1-6" and "1-7". In Figure 5.26, a vertical offset of the horizontal marking lines is apparent which is not present in Figure 5.25. This observation prompted the subtraction of frame 7 from frame 6 to produce the difference image "6-7" of Figure 5.27. Close inspection of Figure 5.27 *tends* to indicate that the horizontal marking lines closer to the toe of the slope (bottom left-hand corner) are vertically offset by a greater amount than the lines nearer the crest (top right-hand corner). If so, this would imply that the toe region has moved more than the rest of the slope mass and that slope collapse starts, or at least takes place more rapidly, at the toe. Inadequate clarity and

resolution of Figure 5.27 made these conclusions tentative, however, and higher quality images were required before the mechanism of slope failure could be accurately determined. Digitization of the films taken during slope test 12 was aimed at producing clearer images.

5.2.2. Slope test 12

Both the 16 mm movie and 35 mm still films taken during test 12 were digitized according to the procedure outlined in Section 4.3.1. Two 35 mm negative frames were analysed, one of them taken before slope failure, the other after. The digitization results of these two frames were presented in Section 4.3.1. A total of five 16 mm movie frames, not all of them consecutive, was digitized to determine whether difference images of adequate resolution could indeed be generated. It was not considered that the precise mechanism of slope failure could be established from the somewhat unsatisfactory partial collapse of specimen 12. Figures 5.28 and 5.29 show two consecutive frames respectively in their original analog form in which slope sample 12 has just begun to fail. Figures 5.30 and 5.31 show the same respective frames reproduced from the digitized data, and Figure 5.32 is the difference image generated by subtracting the latter of the two consecutive frames from the former.

Inspection of Figure 5.32, and comparison with Figure 5.27, does indicate improved clarity and resolution with the test 12 movie film compared to the test 11 digitized images. It was therefore hoped that digitization of the movie film

taken of the next complete centrifuge slope failure and collapse would establish the mechanism of failure beyond doubt. The next satisfactory film candidate, however, was not taken until slope test 17. By this time, test 15 had already adequately determined the sequence of events involved as the failure surface is initiated and propagated through a slope, and further film digitization was unnecessary.

5.3 PENCIL LEAD BREAKAGE

The pencil lead failure sequences of slope tests 17 and 18 are presented in Figure 5.33 as representative of the information provided by these transducers as a slope specimen is failed impulsively and statically respectively. The failure sequence of the pencil leads inserted into slope sample 12 was also presented as an illustrative example in Figure 4.15 of Section 4.2.2.

Figure 5.33 shows the configuration, order of failure, and time interval between breakage of the pencil lead transducers driven into slope specimens 17 and 18, and, within each vertical column of leads, several observations can be made. Firstly, lead failure takes place from toe to crest of the slope sample, leading to the conclusion that slope collapse also begins at the toe and propagates toward the crest. Secondly, the rate of collapse indicated by the time interval between breakage of vertically sequential leads is seen to start off relatively slowly near the toe, speed up dramatically on the way to midheight, then slow down slightly above midheight before falling off again on the way to the crest. The shortest

time interval (from Figure 5.33(b)) also indicates a maximum rupture velocity of approximately 60 m/s, equal to about half the shear wave velocity for the sand-plaster of Paris material of approximately 100 m/s. Comparison of the time intervals *between* the two tests additionally shows that the static collapse of slope 18 occurs more rapidly than the impulsively induced collapse of slope 17. This is to be expected, however, since the $70g$ gravity level of test 18 imparts a greater vertical acceleration on the slope's failure mass than the $46g$ of test 17 and it is this vertical component of motion to which the pencil lead configuration is sensitive (independent of any horizontal component from an impulse). Finally, and regardless of the differing collapse rates, both tests exhibit the same *order* of pencil lead failure within a vertical column of leads, and thus the order of slope collapse is concluded to be indifferent to an impulsive or static initiation force.

5.4 SUMMARY AND CONCLUSIONS

The centrifuge slope tests described in Section 5.1 were collectively successful in determining the sequence of events which take place when a slope fails and collapses. This sequence of events, which constitute the mechanism of slope failure, is shown schematically in Figure 5.34. Of critical importance to the establishment of the slope failure mechanism were the results of slope test 15, which primarily showed that the failure surface originates at the slope toe, where it is initiated by shear failure, before propagating toward the slope crest. However, propagation

of the failure surface in an approximately circular arc to the face of the slope *before* reaching the crest, as seen in tests 15 and 17 and suggested in other tests, is believed to be caused by an inhomogeneous centrifuge specimen, even though the same feature may be developed in full-scale failures in the field. This inhomogeneity is probably created during the compaction procedure of Section 4.1 where the slope specimen is constructed upside down in the lucite mold, giving the crest region greater strength from compaction against the rigid surfaces of the mold and from greater total compactive effort as construction of the rest of the slope specimen follows the crest region. Test 15 also pointed out that the displacement discontinuity across the failure surface is extremely small (of the order of several soil grain sizes) and insufficient to cause pencil lead breakage. This absence of pencil lead failure, however, is due in part to the small but unavoidable clearance between lead and slope material which must be closed before lead failure will occur.

As indicated above, slope test 17 confirmed many of the observations and conclusions of test 15, but more importantly, accentuated the significance of crest tension cracking in the development of slope failure. Crest tension cracks had not been observed in the centrifuge slope failures prior to test 17, even though Terzaghi's gelatine experiments [110] and a subsequent finite element analysis of a typical slope specimen under centrifuge test conditions (see Section 8.3) indicated their presence. The observations of slope test 17 alone, however, could not

establish the role of crest tension cracking in the evolution of slope failure, beyond indicating its presence prior to shear failure at the slope toe.

The observations of slope test 15 further showed that failure surface propagation takes place before and without slope collapse, suggesting that a distinction be made between the terms *failure* and *collapse* as they pertain to the slope stability problem. This would allow a slope to be described as having *failed* once the failure surface is established, and having *collapsed* once the blocks of material separated by the failure surface slide past each other and come to rest. The important point here is that a slope fails *before* it collapses, with failure hence being necessary for collapse. For the brittle centrifuge slope material, failure here implies breakdown of the plaster of Paris cementation while friction still holds, whereas both cohesion *and* friction would continue to hold at failure in an overconsolidated clay.

This distinction between the terms failure and collapse helps explain why the film digitization and pencil lead transducer results could not clearly define the mechanism of slope failure — the difference images and pencil leads were actually monitoring slope collapse, and not slope failure. With this hindsight, it seems clear that the failure surface had already propagated through the slope specimen before the difference images of test 11 (see Section 5.2.1) and pencil leads of tests 17 and 18 (see Section 5.3) responded to the collapsing sample.

The centrifuge experiments also lead to the important conclusion that slope failure in a brittle material is not a progressive phenomenon as assumed in Figure

1.3. Since the 35 mm in-flight photographs taken at $5g$ increments during the centrifuge tests gave no indication of progressive failure whatsoever, slope failure in a brittle material is concluded instead to occur at a well-defined loading threshold, below which signs of failure are completely absent. This conclusion is qualified, however, by the possibility that the displacement discontinuity across a growing failure surface may be too small to be detected by the particular photographic set-up used to record the slope failure tests. Furthermore, the progressive failure mechanism of Figure 1.3 may still be realistic for a plastic slope material such as overconsolidated clay.

Lastly, the results of the slope tests discussed in Section 5.1 collectively show that the final configuration or profile of a collapsed slope is a function of the duration of dynamic loading used to initiate failure, and that observation of the final profile (which is usually all that can be seen in the case of full-scale failures in the field), can lead to an erroneous understanding of the failure mechanism involved. These were the main conclusions of tests 9 and 10 in which the long duration earthquake motions produced much flatter final slopes extending further into the slope specimens than the shallow, slip-circle type profiles caused by impulsive failure in tests 11 and 17, and static failure in test 18. The close correspondence of the results of tests 11, 17 and 18 also establishes the equivalence of impulsive and static loading with respect to the final profile of the centrifuge slope collapses.

Slope Test No.	Test Date	Model Soil[a]	Unit Weight (pcf)	Approx. Water Content (%)	Slope Angle	Vertical Slope Height (mm)	Slope Width (mm)
1	13 Aug 84	Seal Beach silty sand	123	8.5	45°	150	175
2	15 Aug 84		112	11	60°	150	175
3	18 Aug 84		121	16	60°	150	175
4	21 Aug 84		118	14	60°	150	175
5	28 Aug 84	NH silt	Unknown	14	60°	102	175
6	16 Oct 84	SPP 50:1	~93	0	60°	150	174
7	18 Oct 84	SPP 60:1	~93	0	60°	150	174
8	20 Oct 84	SPP 60:1	~93	0	60°	150	174
9	21 Oct 84	SPP 60:1	~93	0	60°	150	174
10	24 Oct 84	SPP 60:1	~93	0	60°	150	174
11	29 Oct 84	SPP 60:1	~93	0	60°	150	174
12	11 Dec 85	SPP 60:1	~93	0	60°	150	170
13	2 Feb 86	SPP 60:1	~93	0	60°	150	170
14	18 Feb 86	SPP 60:1	~93	0	60°	150	170
15a	28 Feb 86	SPP 60:1	92	0	60°	150	170
15b	6 Mar 86						
15c	14 Mar 86						
16a	19 Mar 86	SPP 60:1	93.6	0	60°	150	170
16b	21 Mar 86						
17	23 Mar 86	SPP 60:1	93.5	0	60°	150	170
18	28 Mar 86	SPP 60:1	93.4	0	60°	150	170

a NH = New Hampshire
SPP= sand–plaster of Paris material (weight ratio of sand to plaster given)

Table 5.1

Summary of centrifuge slope failure experiments

(Page 1 of 3)

Fold out ⟶

Slope Test No.	Slope Markings[b]	Pencil Leads[c]	Gravity Level (g)	Force Applied to Slope[d]	Movie Film Taken?[e]	35 mm In-Flight Photos?[f]	Horiz. Accel. & Displ. Recorded?[h]
1	None	None	80	EQ	No	No	No
2	None	None	45–70	Static	No	No	No
3	None	None	90	EQ	No	No	No
4	None	None	< 85	Static	No	No	No
5	HFS	None	100	EQ	No	No	No
6	HBP	None	90	EQ	No	No	No
7	HBP	None	55	Static	No	No	No
8	HBP	None	43	Static	No	No	No
9	HBP	None	42	EQ	1600 fps, S	No	No
10	HBP	None	42	EQ	1600 fps, S	No	Yes
11	HBP	None	42	Impulse	1600 fps, T	No	Yes
12	HVBP	0.5, 40	30	Impulse	5000 fps, T	Yes	Yes
13	HVBP	0.7, 34	85	Impulse	No	No	No
14	HVBP	0.9, 34	42	Impulse	No	No	No
15a	HVBP	0.9, 34	42	Impulse	5000 fps, T	AB	Yes
15b	HVBP		46	Impulse	5000 fps, T	B42	Yes
15c	HVBP		46	Static	No	No	No
16a	HVBP	0.9, 34	46	Impulse	5000 fps, T	B42	Yes
16b	HVBP		82	Static	No	B42	No
17	HVBP	0.9, 34	46	Impulse	5000 fps, T	B42	Yes
18	DCO	0.9, 34	70	Static	No	B42	No

b HFS = horizontal lines of fine sand, HBP = horizontal lines of blue spray paint
HVBP = horizontal and vertical grid of black spray paint lines
DCO = different colored grids of orthogonal lines

c Lead diameter in mm, and AWG size of connection wire given (*e.g.*, 0.9 mm, 34 AWG)

d EQ = simulated earthquake, Static = gravitational acceleration only

e fps = frames per second, S = 25 mm standard lens, T = 50 mm telephoto lens

f AB = all blank, B42 = blank above 42g

h Indicates whether horizontal acceleration and displacement of test container and slope specimen recorded (in response to dynamic loading)

Slope Test No.	Slope Collapse?	Distinct Failure Surface?	Pencil Lead Breakage?[k]	Film Digitized and Analyzed?[m]	Results Presented and Discussed?[n]
1	No	No	N/A	N/A	No
2	Complete	Yes	N/A	N/A	No
3	Complete	Yes	N/A	N/A	No
4	Complete	Yes	N/A	N/A	No
5	Slumping	No	N/A	N/A	No
6	No	Yes	N/A	N/A	No
7	Complete	Yes	N/A	N/A	No
8	Complete	Yes	N/A	N/A	No
9	Complete	Yes	N/A	No	Yes: 5.1.2
10	Complete	Yes	N/A	No	Yes: 5.1.2
11	Complete	Yes	N/A	Yes: 5.2.1	Yes: 5.1.3
12	Partial	Yes	Partial	Yes: 4.3.1, 5.2.2	Yes: 4.2.2
13	No	No	No	N/A	No
14	Complete	Yes	Complete	N/A	No
15a	No	Yes	No	No	Yes: 5.1.4
15b	No	Yes	No	No	
15c	Partial	Yes	Partial	N/A	
16a	No	No	No	No	No
16b	Complete	Yes	Complete	N/A	Yes: 8.3
17	Partial	Yes	Complete	No	Yes: 5.1.5
18	Complete	Yes	Complete	N/A	Yes: 5.1.6

k N/A= not applicable

m Section numbers of film digitization and analysis given where applicable, N/A= not applicable

n Section numbers of presentation and discussion of results given

Table 5.1

Summary of centrifuge slope failure experiments

(Page 2 of 3)

Fold out $\longrightarrow$

Table 5.1

Summary of centrifuge slope failure experiments

(Page 3 of 3)

Fold out $\longrightarrow$

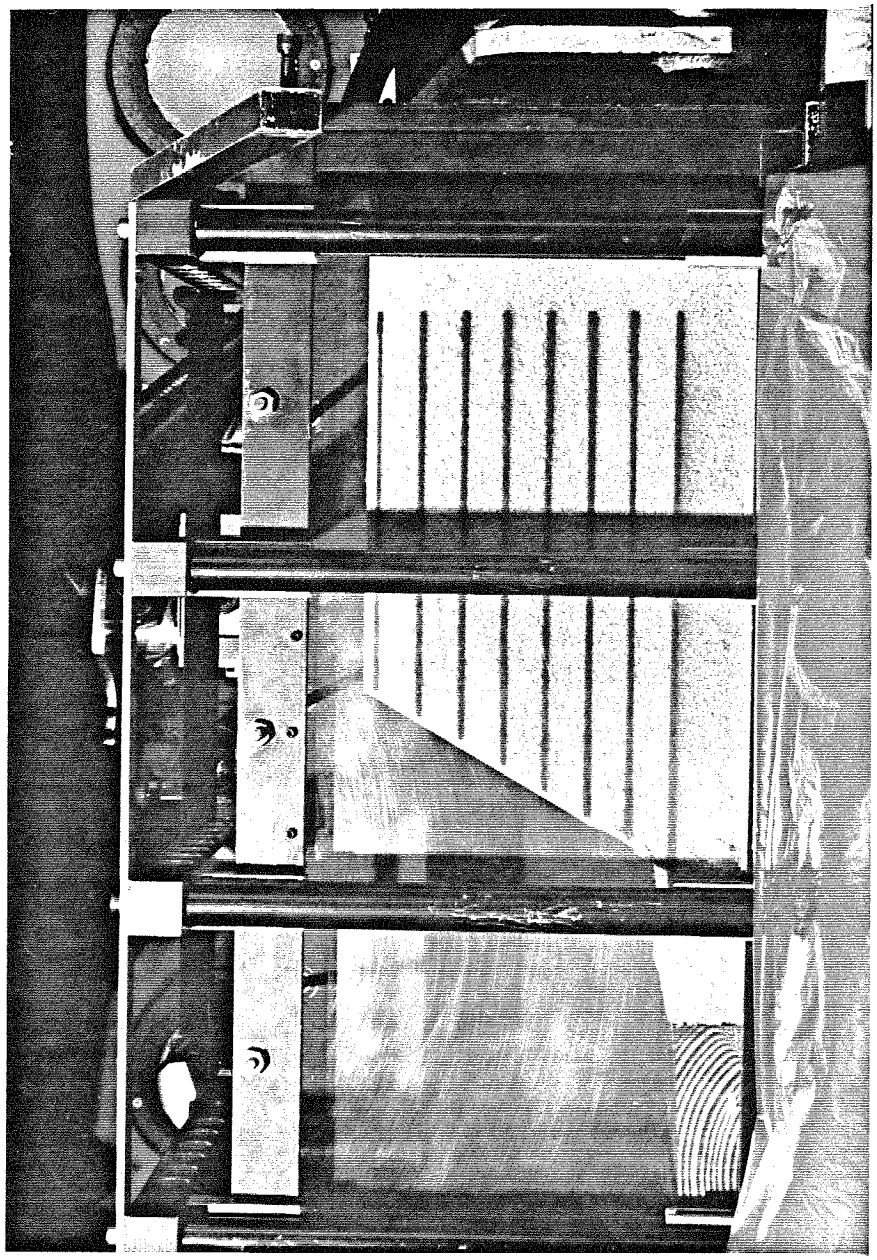

Figure 5.1 Pre-failure view of slope specimen 10

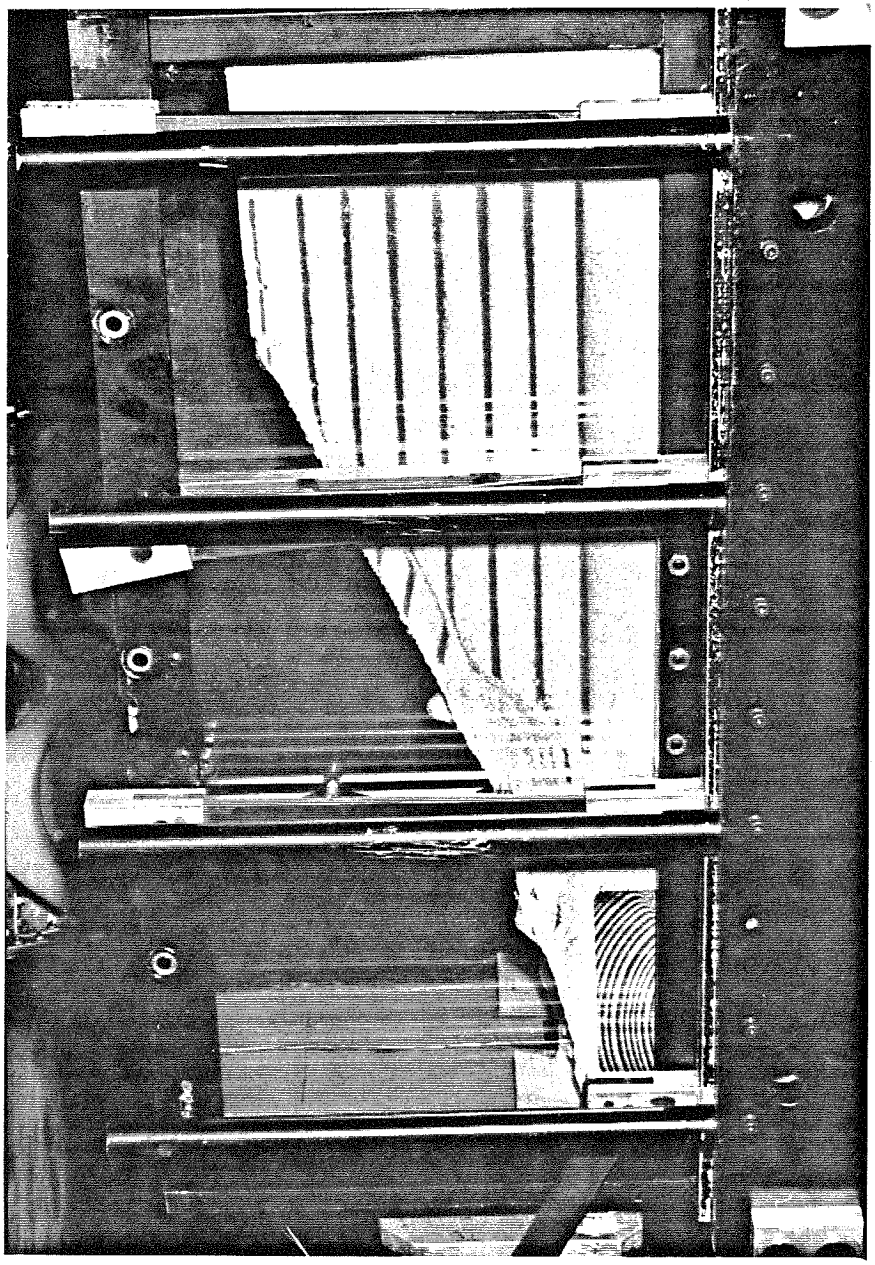

Figure 5.2 Post-failure view of slope specimen 10

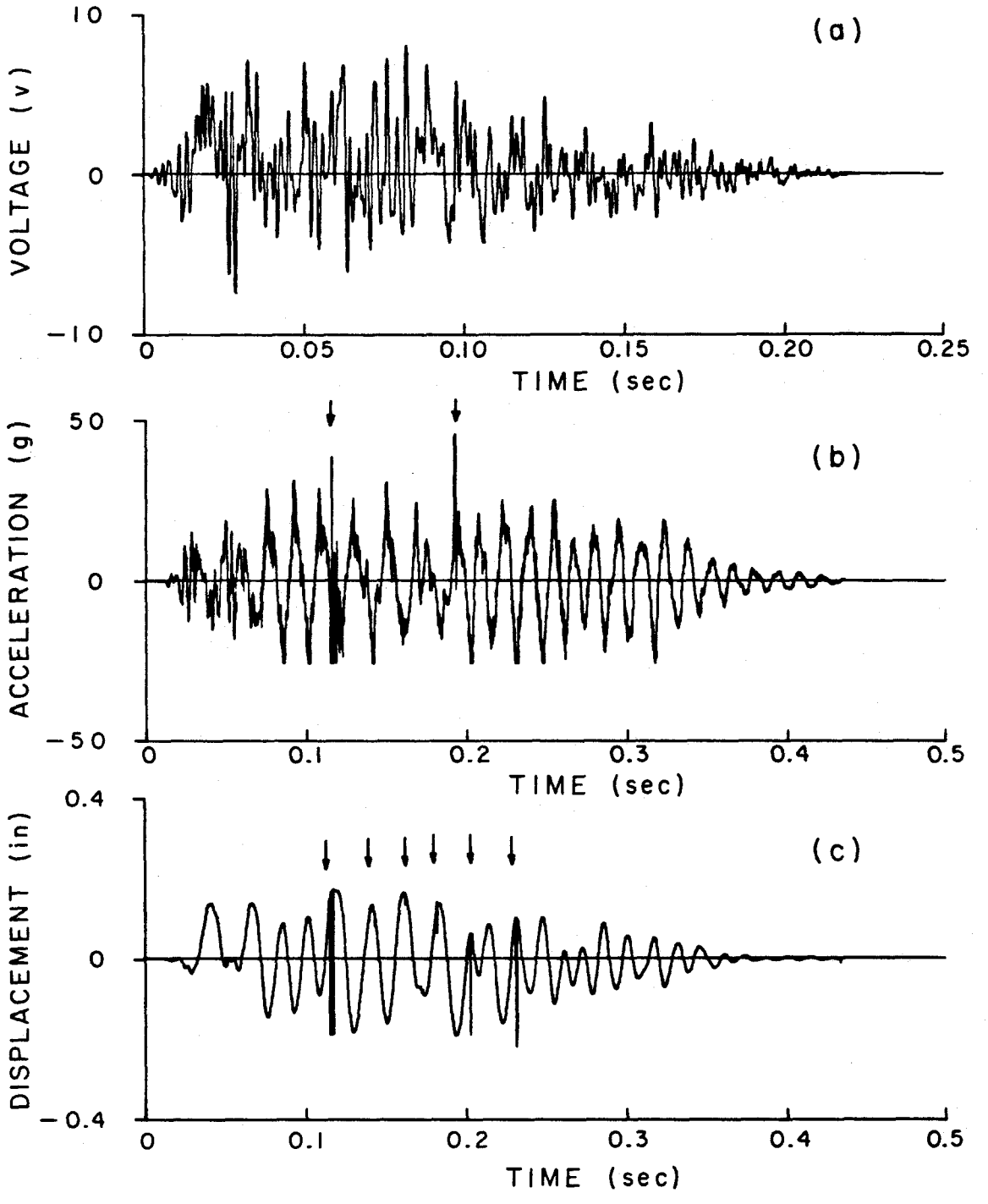

Figure 5.3 Slope test 10 results (centrifuge scale)
(a) Simulated earthquake signal given to servo-valve and actuating piston
(b) Measured horizontal acceleration of test container
(c) Measured horizontal displacement of test container
(Arrows indicate loss of random bits of data by analog-to-digital converter)

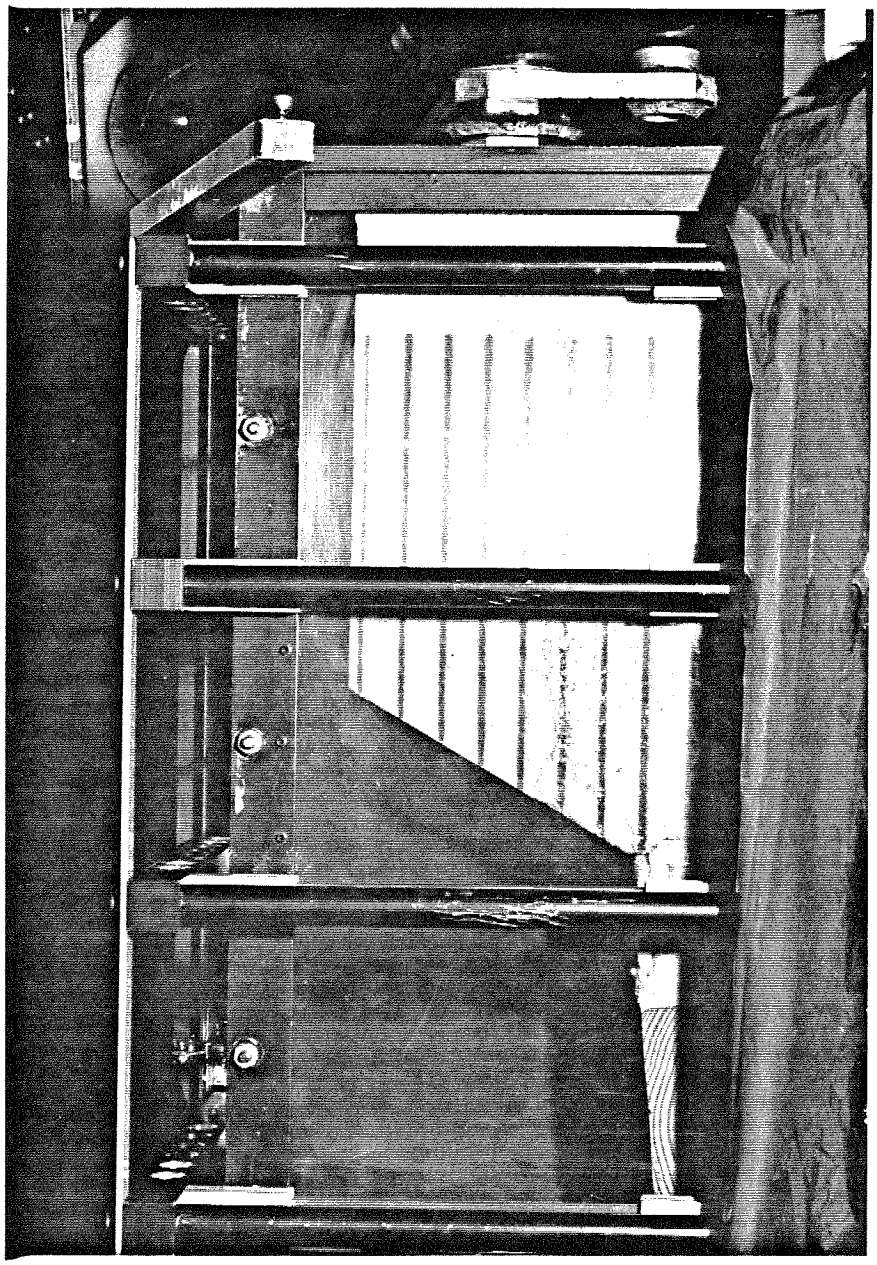

Figure 5.4 Pre-failure view of slope specimen 11

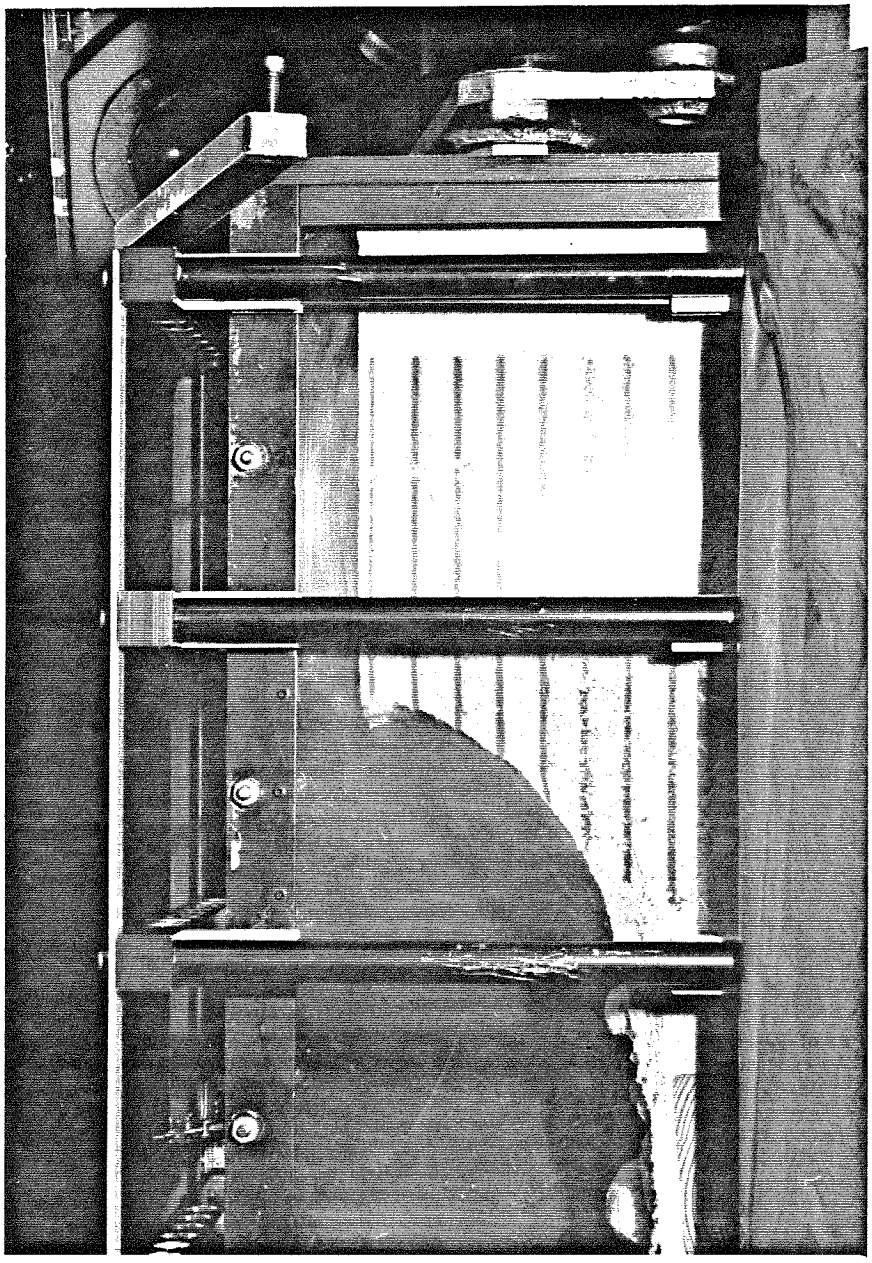

Figure 5.5 Post-failure view of slope specimen 11

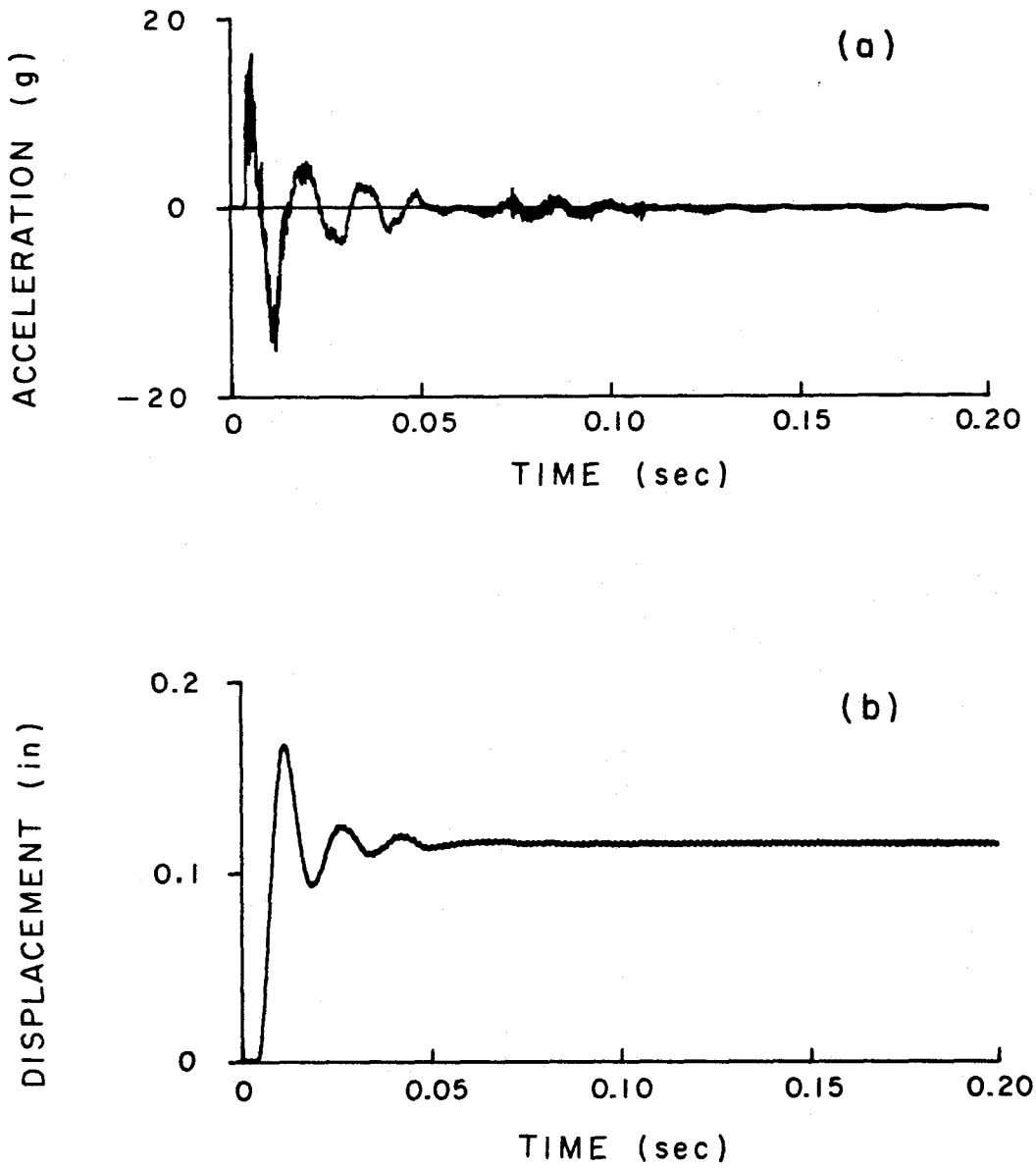

Figure 5.6 Slope test 11 results (centrifuge scale)
(a) Measured horizontal acceleration of test container for impulsive input
(b) Measured horizontal displacement of test container for impulsive input

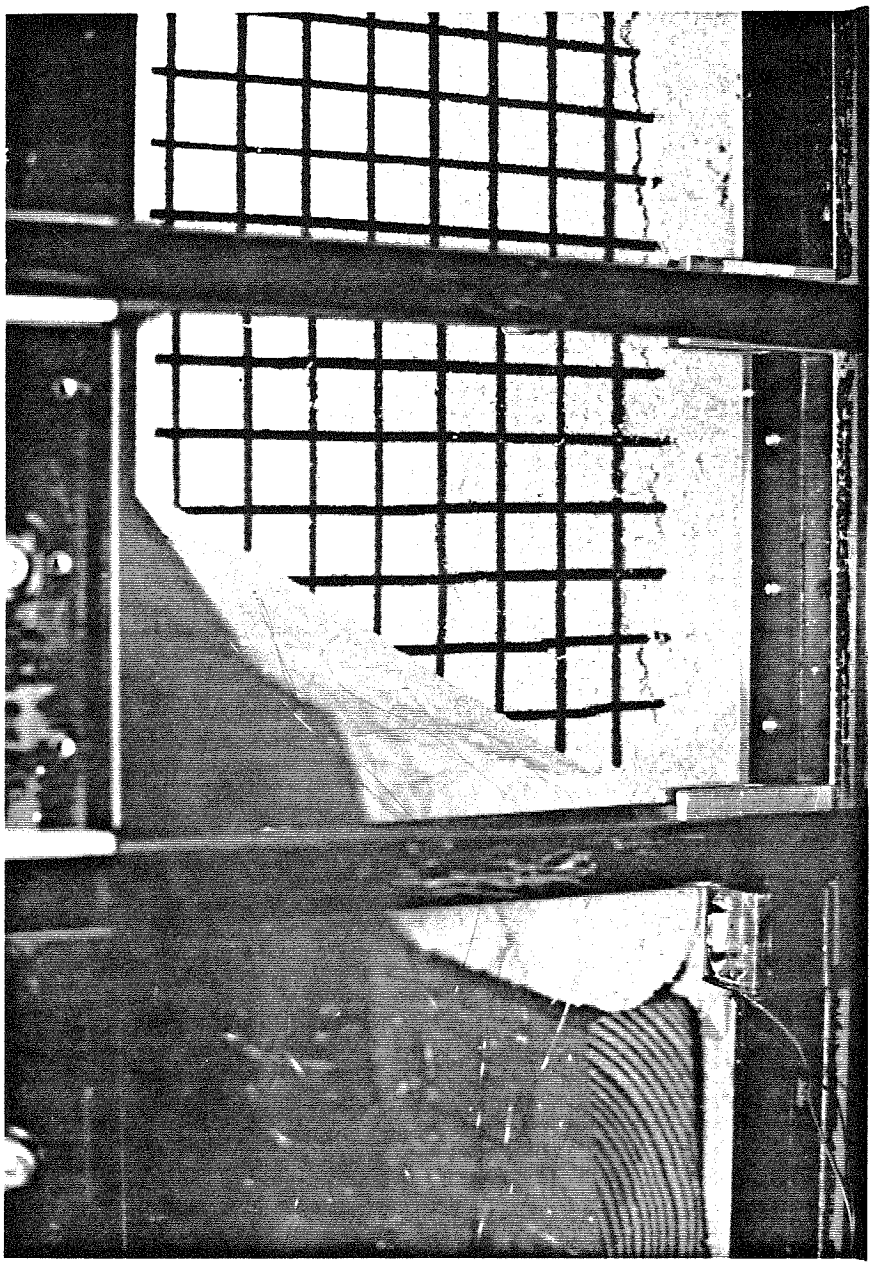

Figure 5.7 Slope specimen 15 after first impulsive failure attempt (centrifuge at rest)

Figure 5.8 Slope specimen 15 at $46g$ before second impulsive failure attempt

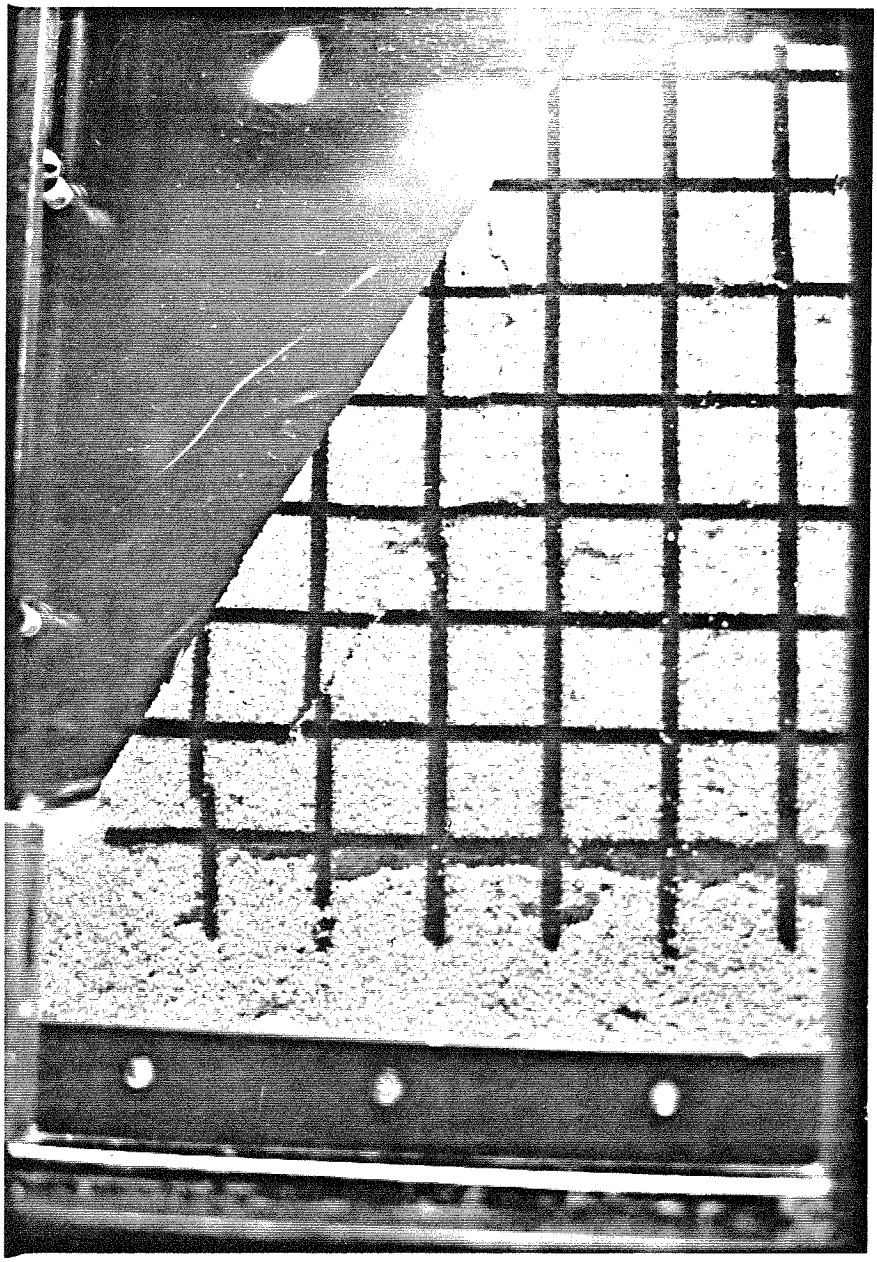

Figure 5.9 Slope specimen 15 after second impulsive failure attempt (centrifuge at rest)

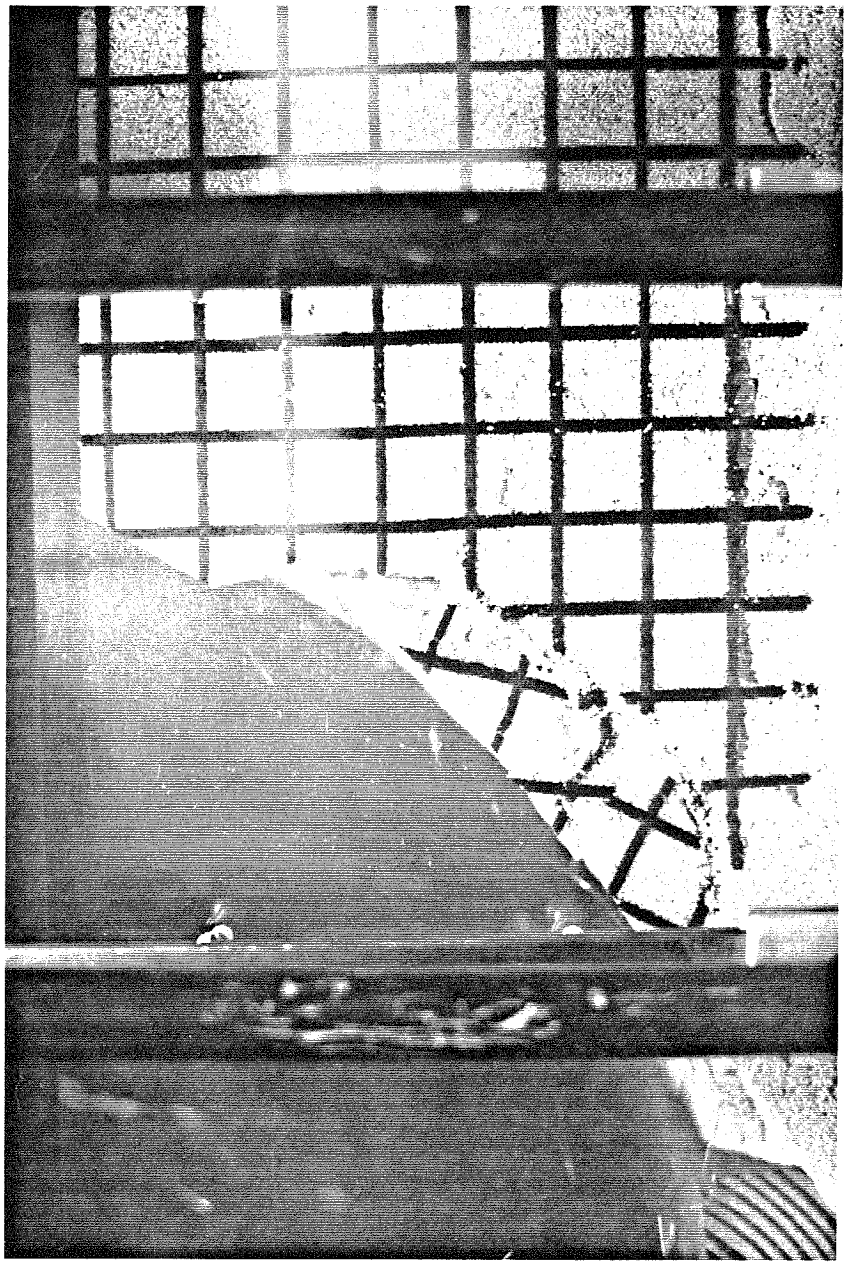

Figure 5.10 Post-failure view of slope specimen 15

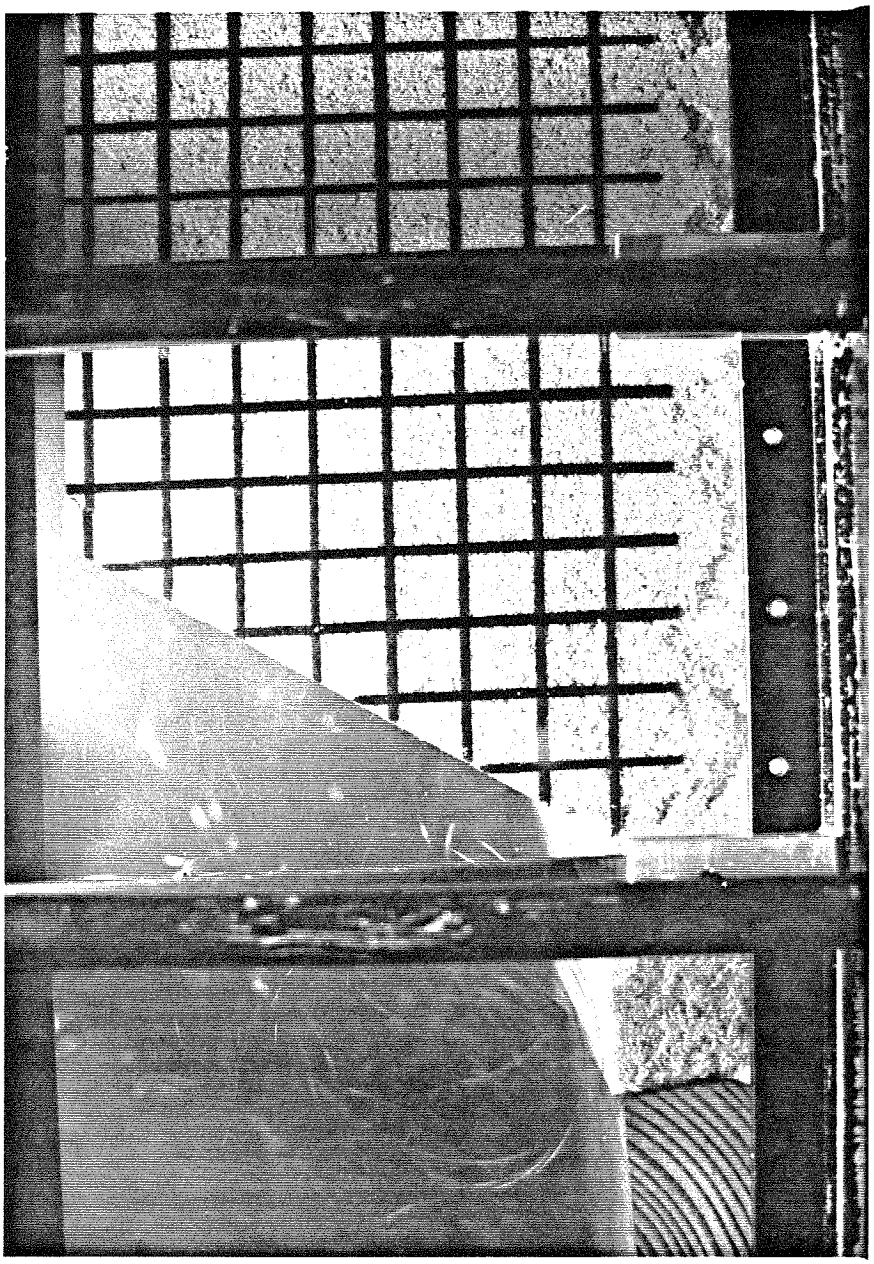

Figure 5.11 Pre-failure view of slope specimen 17

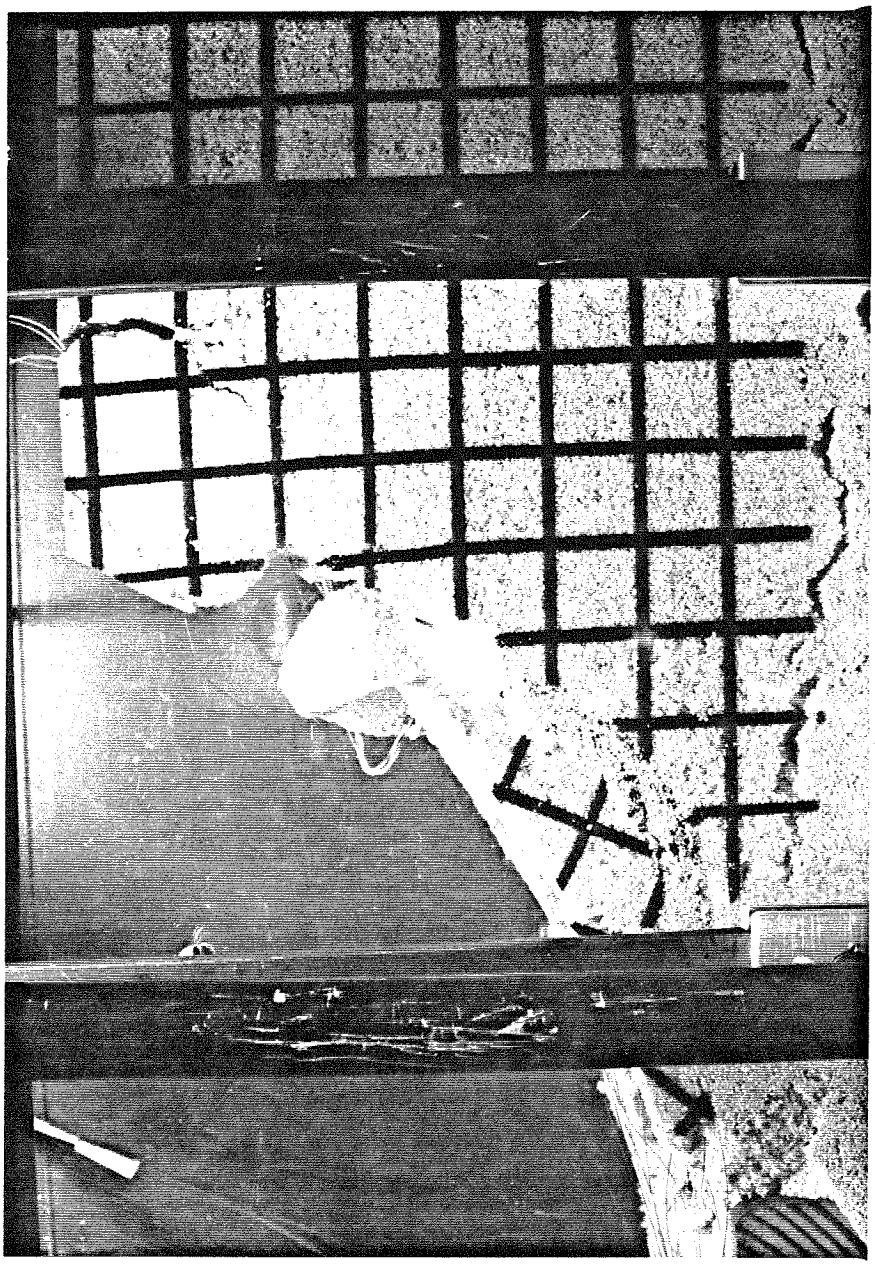

Figure 5.12 Post-failure view of slope specimen 17

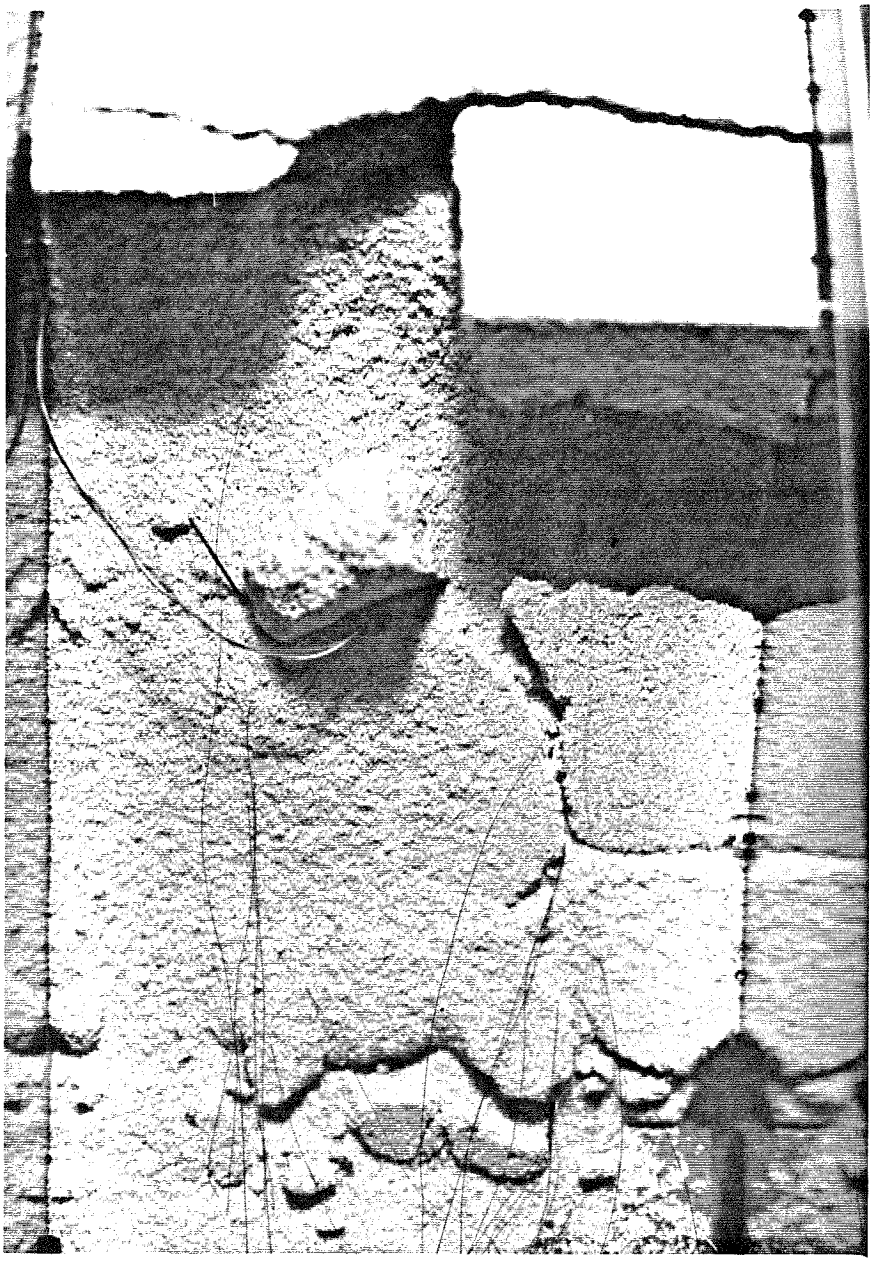

Figure 5.13 Post-failure debris of slope test 17 (top view)

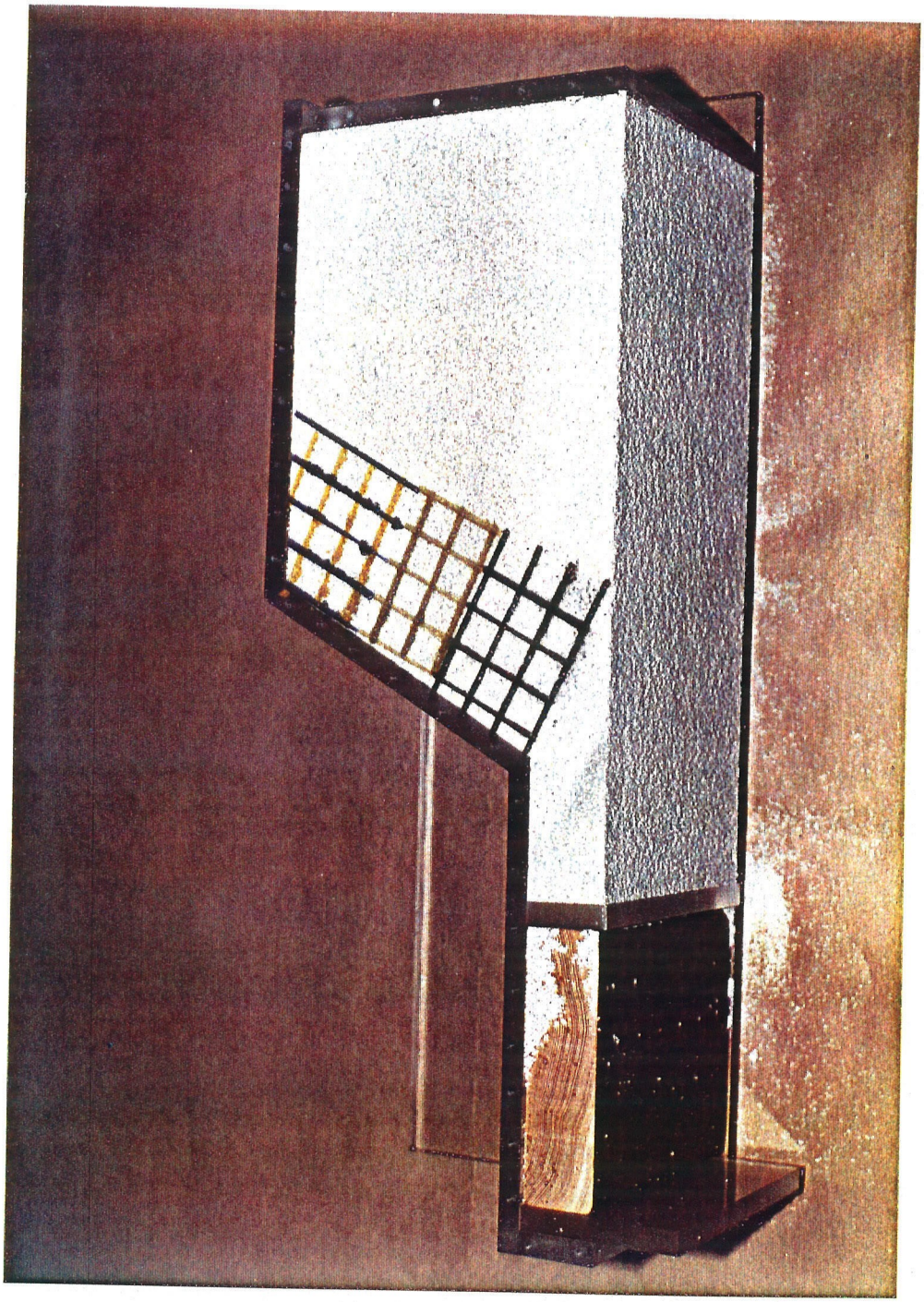

Figure 5.14 Colored grids of orthogonal lines for marking of slope specimen 18: black grid at toe, green grid at midheight, blue and yellow grid at crest

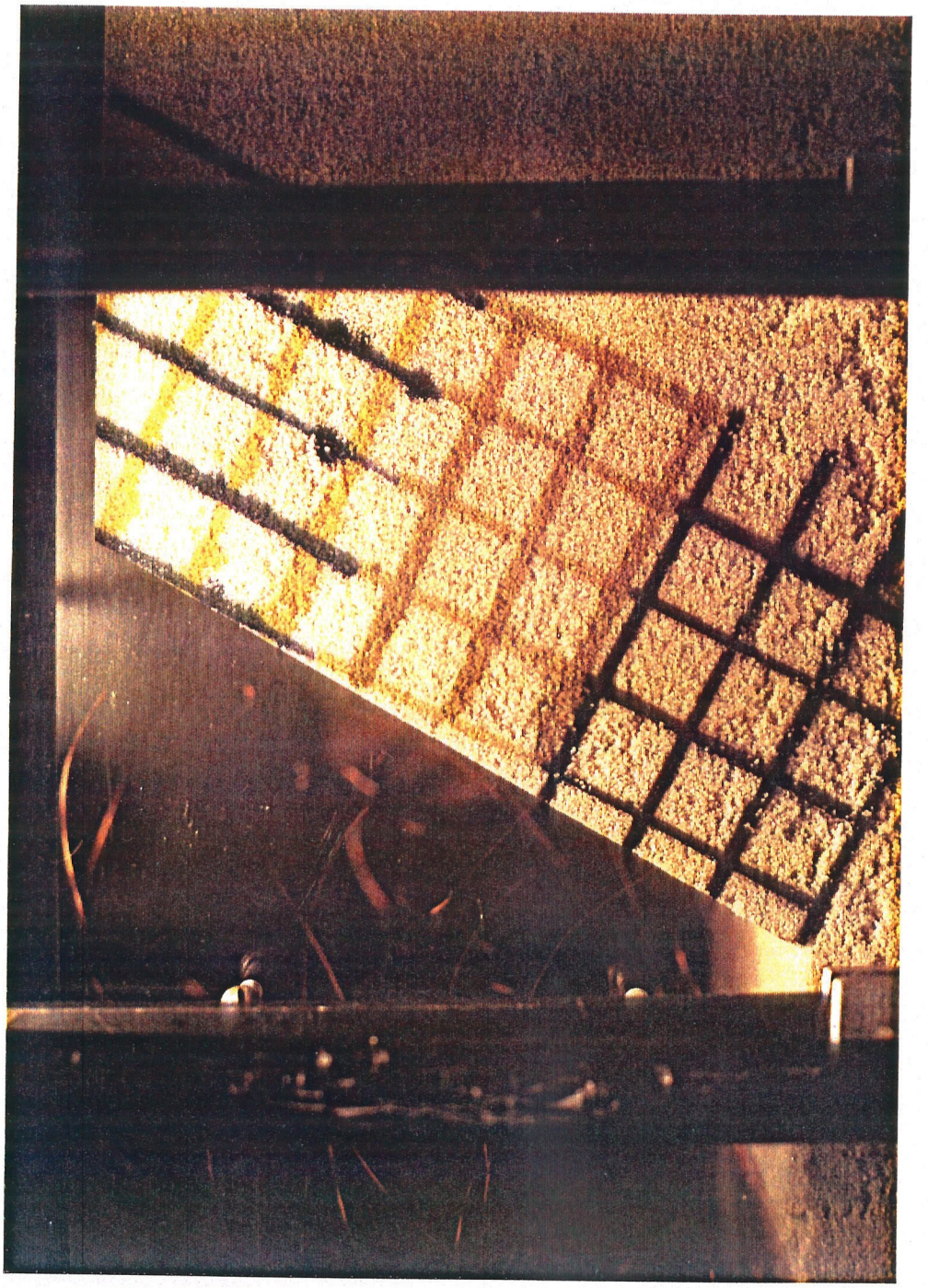

Figure 5.15 Pre-failure view of slope specimen 18

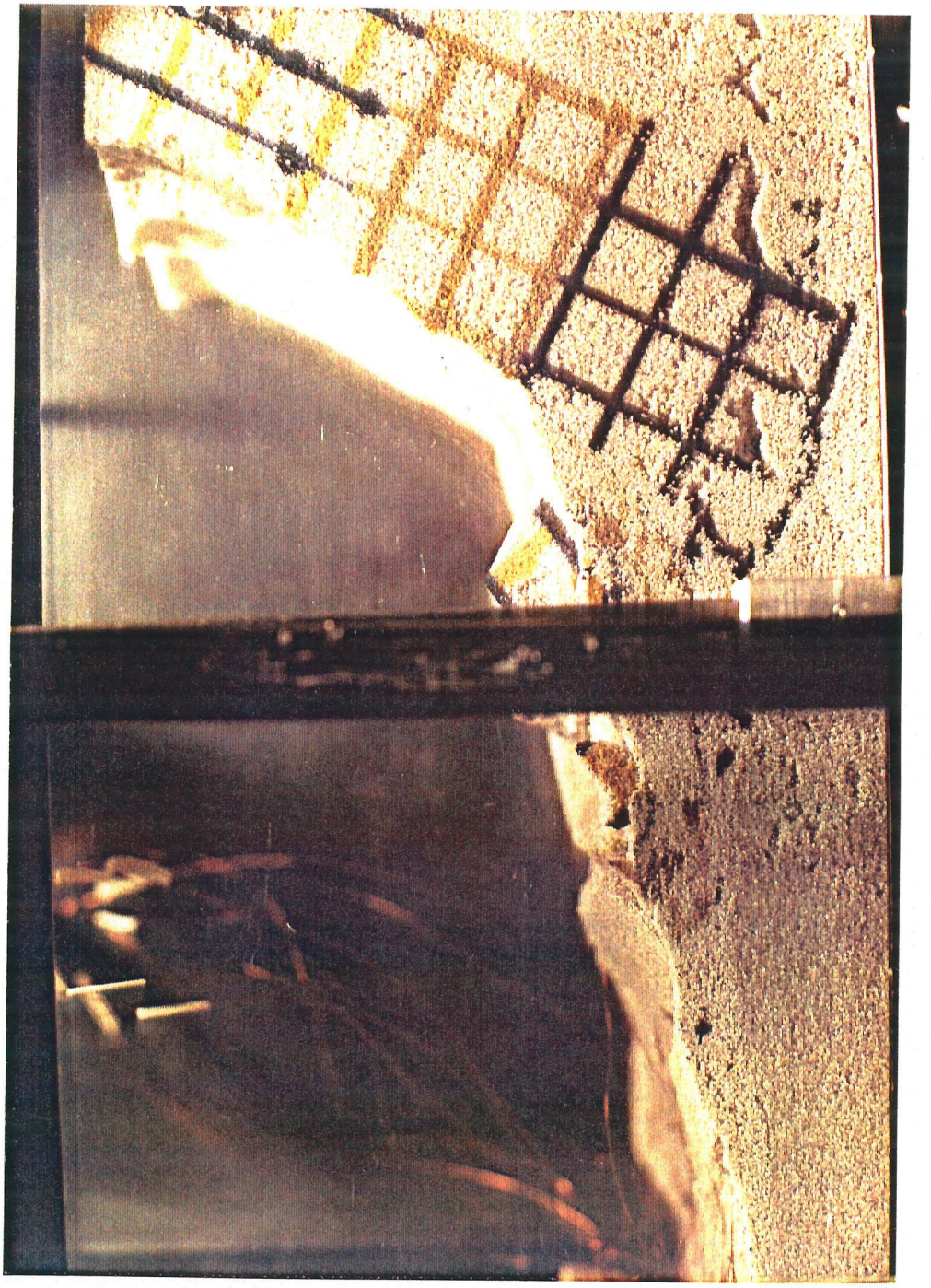

Figure 5.16 Post-failure view of slope specimen 18

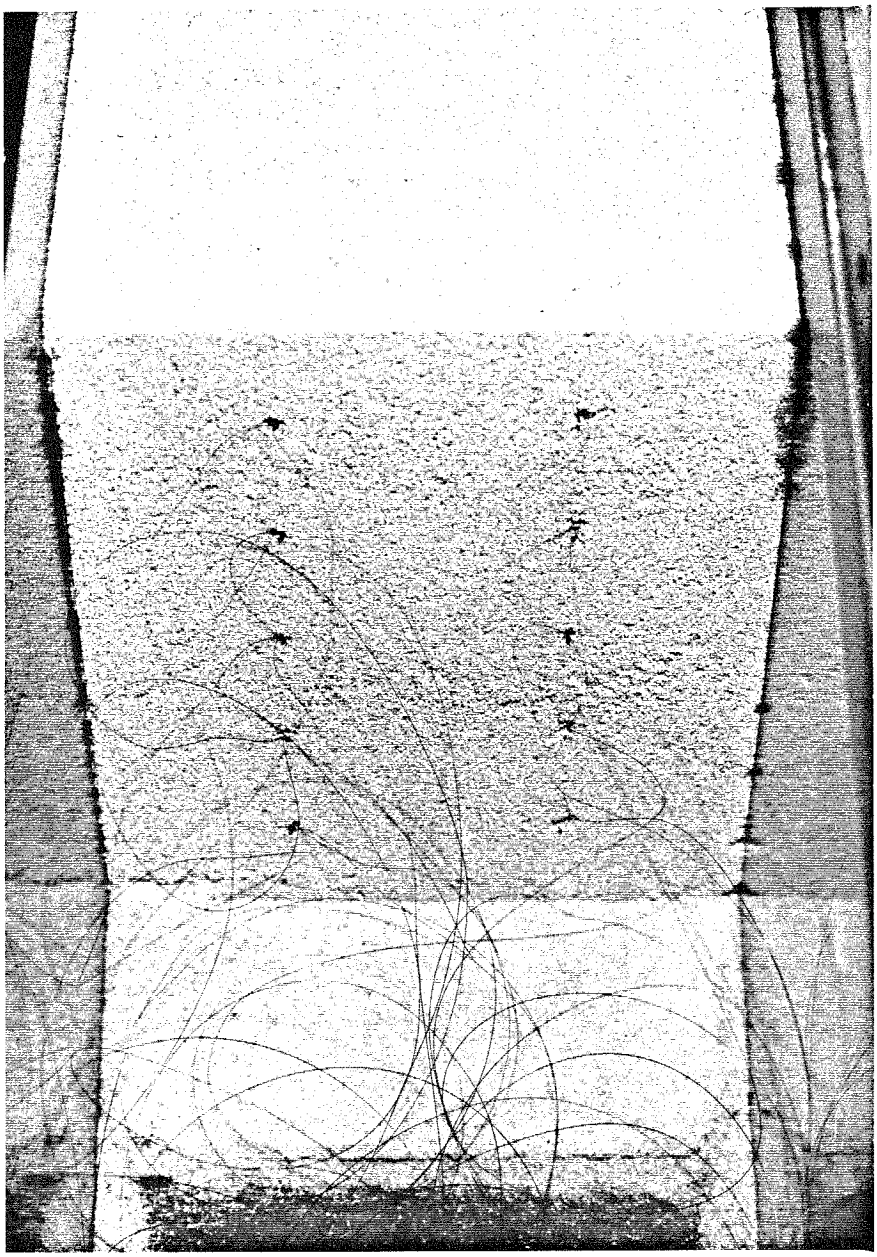

Figure 5.17 Pencil lead transducers inserted into face of slope specimen 18 prior to testing

Figure 5.18 Post-failure debris of slope test 18 (top view)

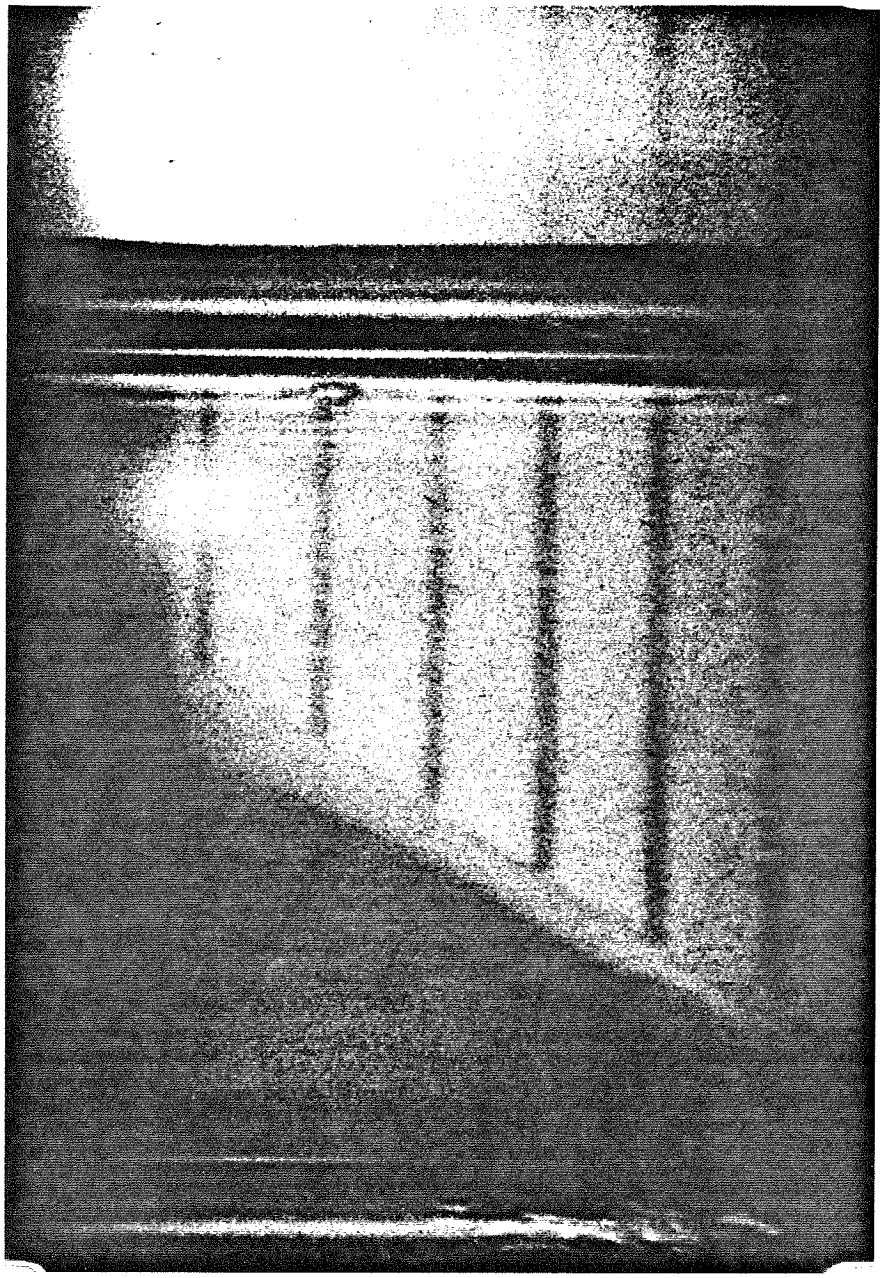

Figure 5.19 Reference frame (frame 1) of slope test 11 movie film

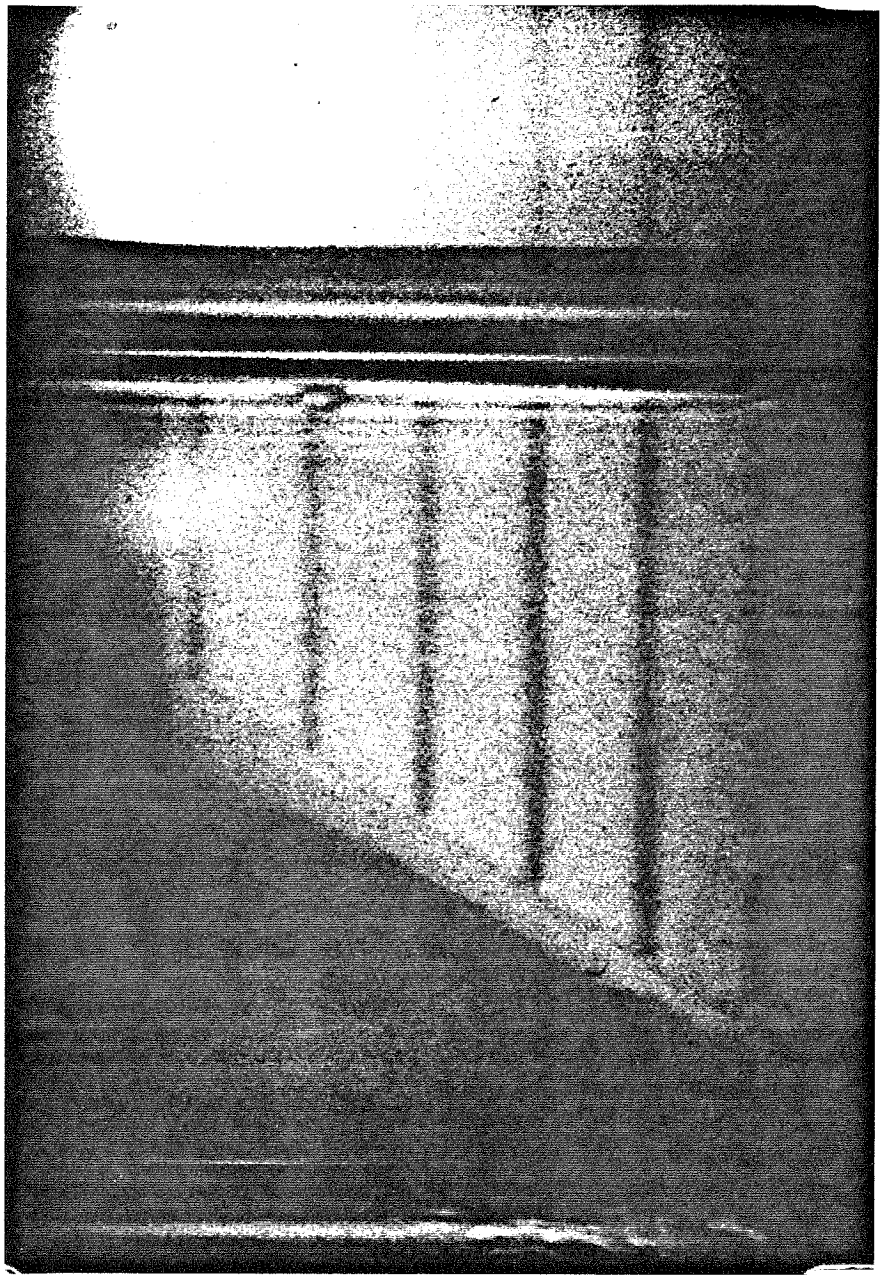

Figure 5.20 Frame 6 of slope test 11 movie film

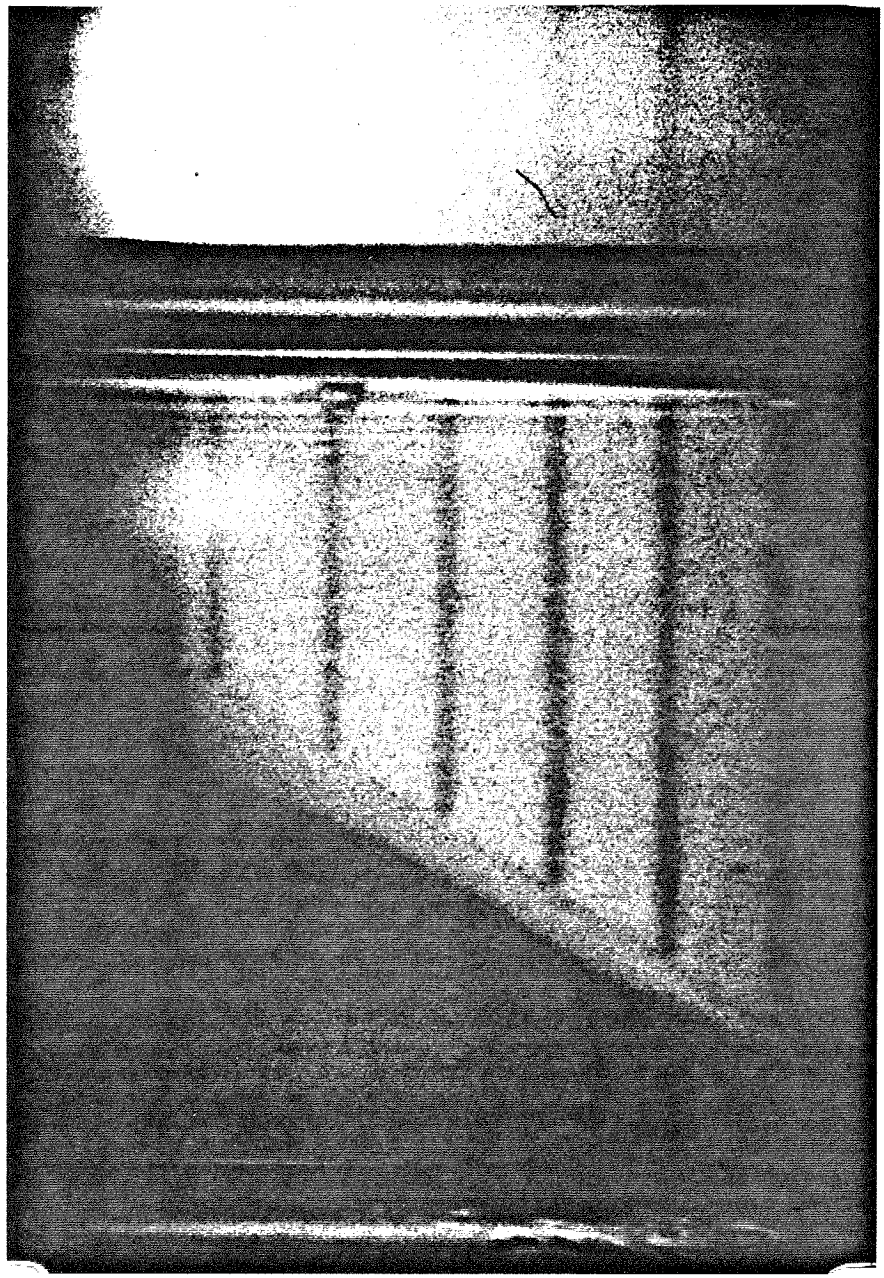

Figure 5.21 Frame 7 of slope test 11 movie film

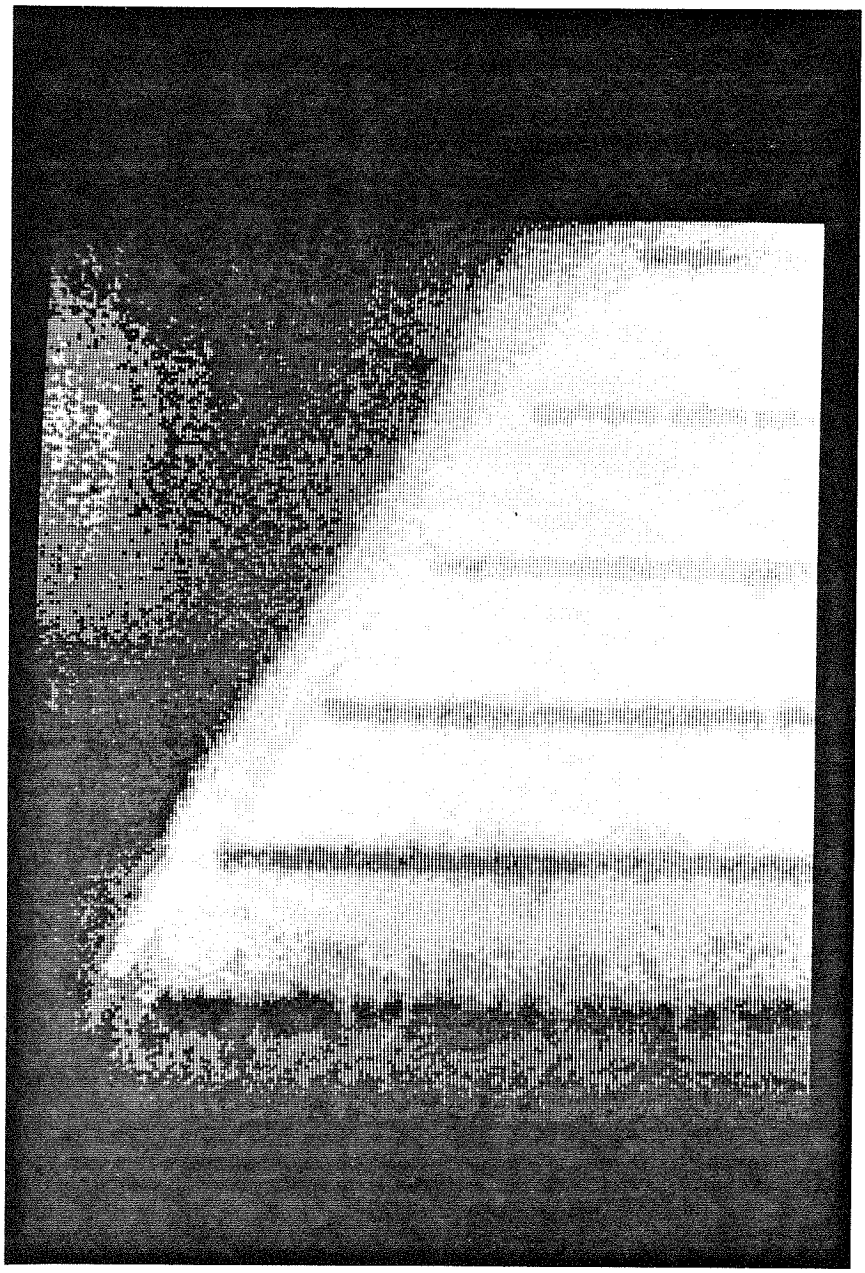

Figure 5.22 Reproduction of central region of Figure 5.19 from digitized data

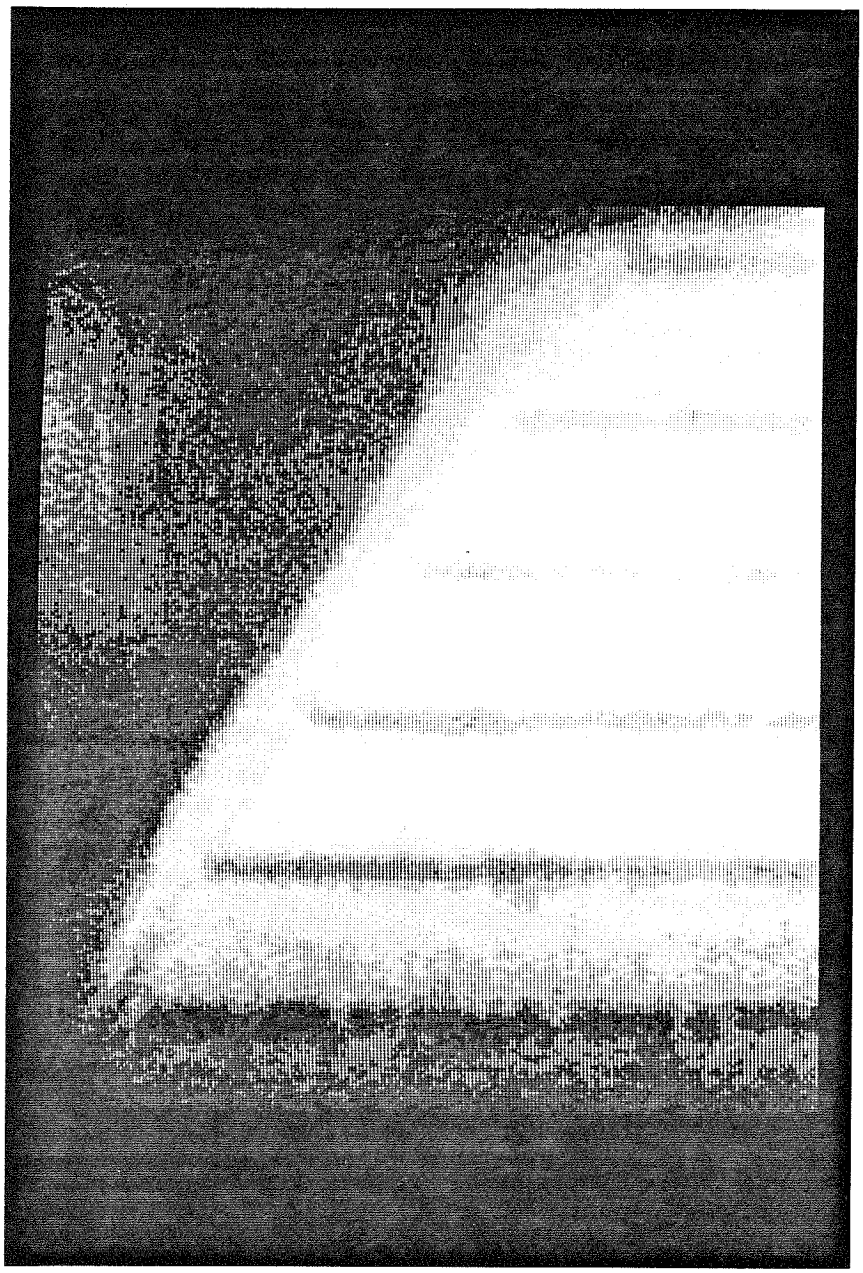

Figure 5.23 Reproduction of central region of Figure 5.20 from digitized data

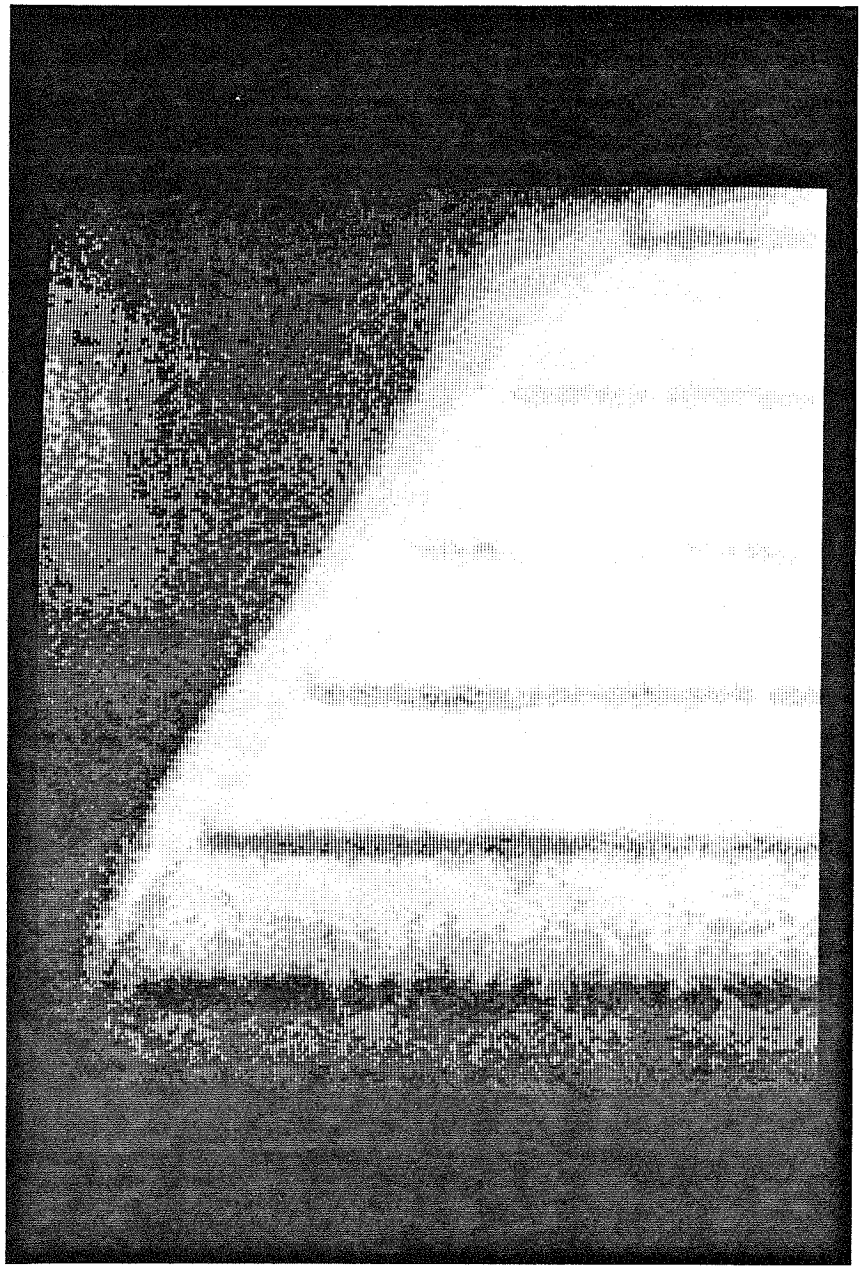

Figure 5.24 Reproduction of central region of Figure 5.21 from digitized data

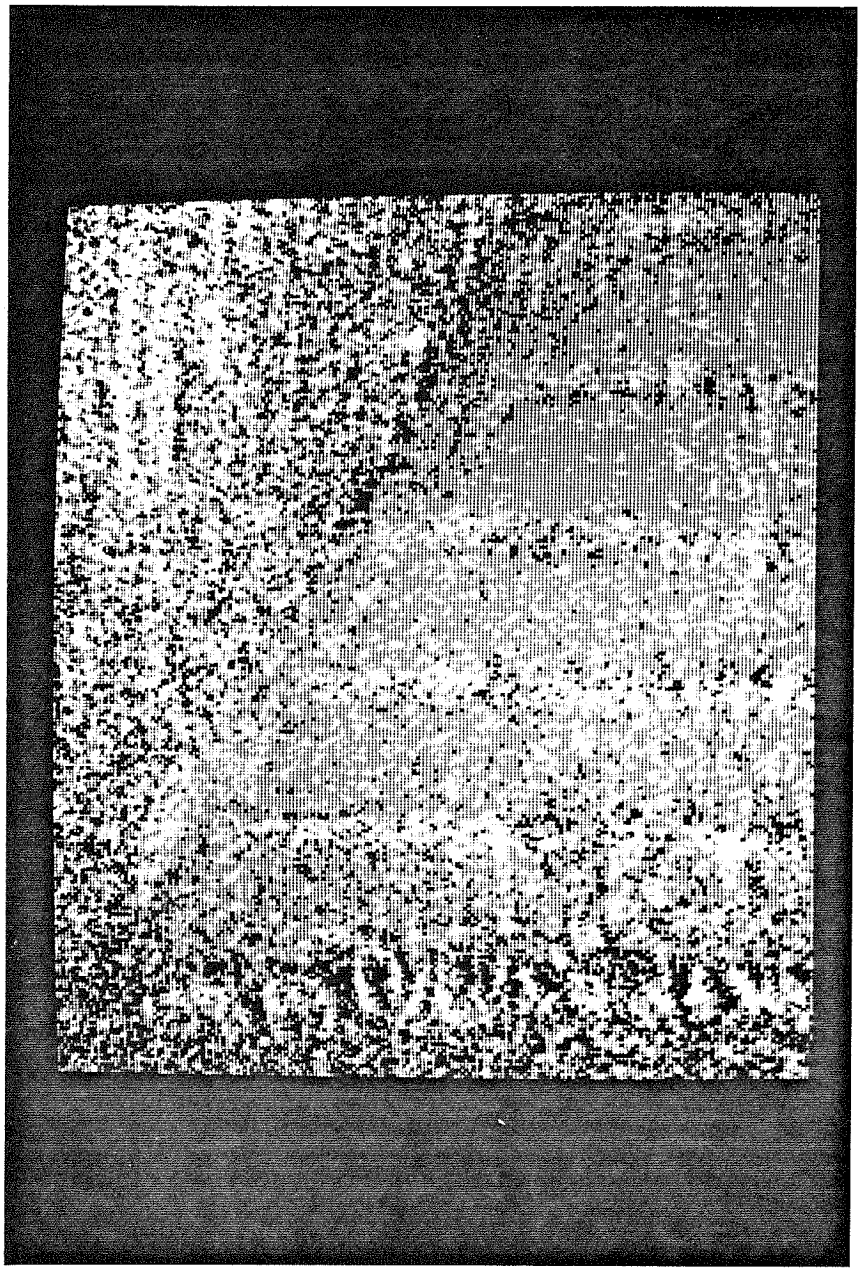

Figure 5.25 Difference image "1–6" of slope test 11

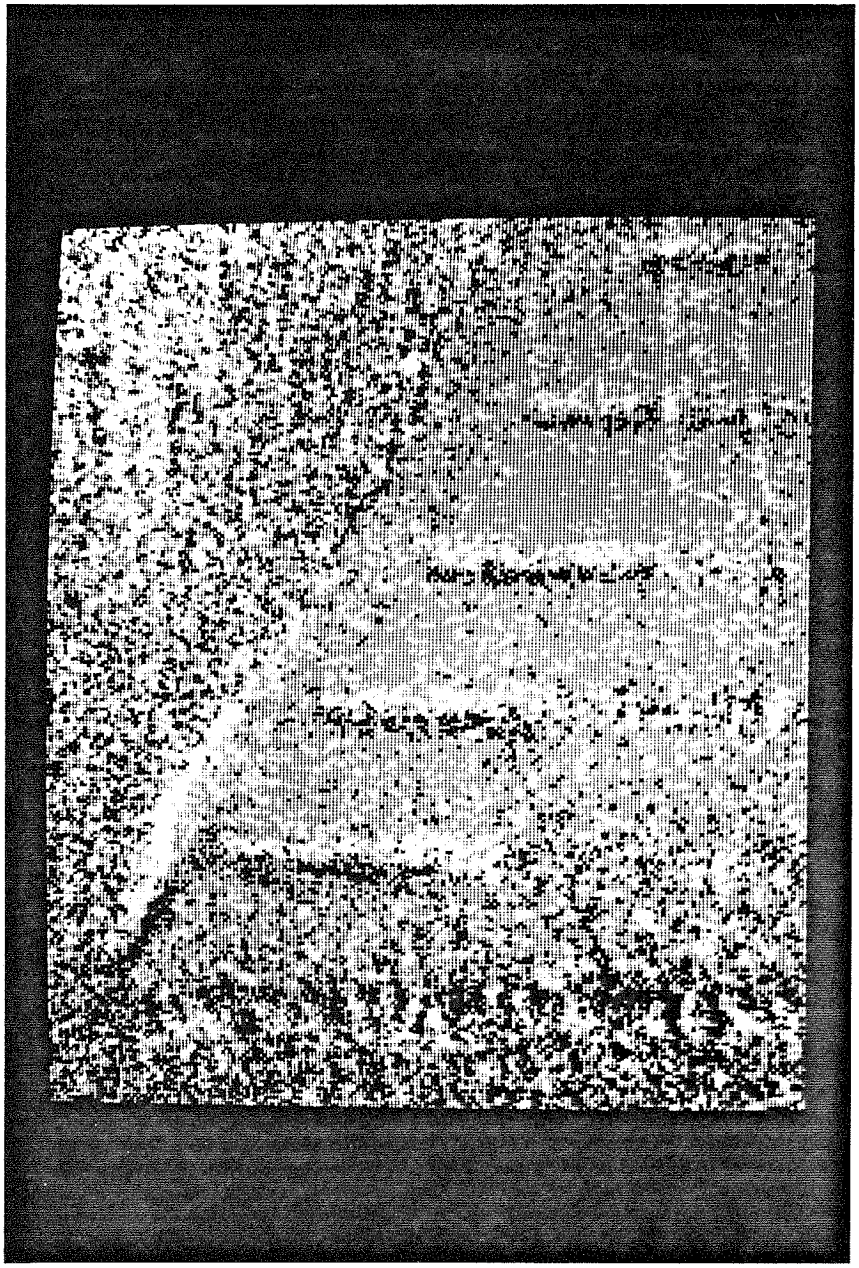

Figure 5.26 Difference image "1–7" of slope test 11

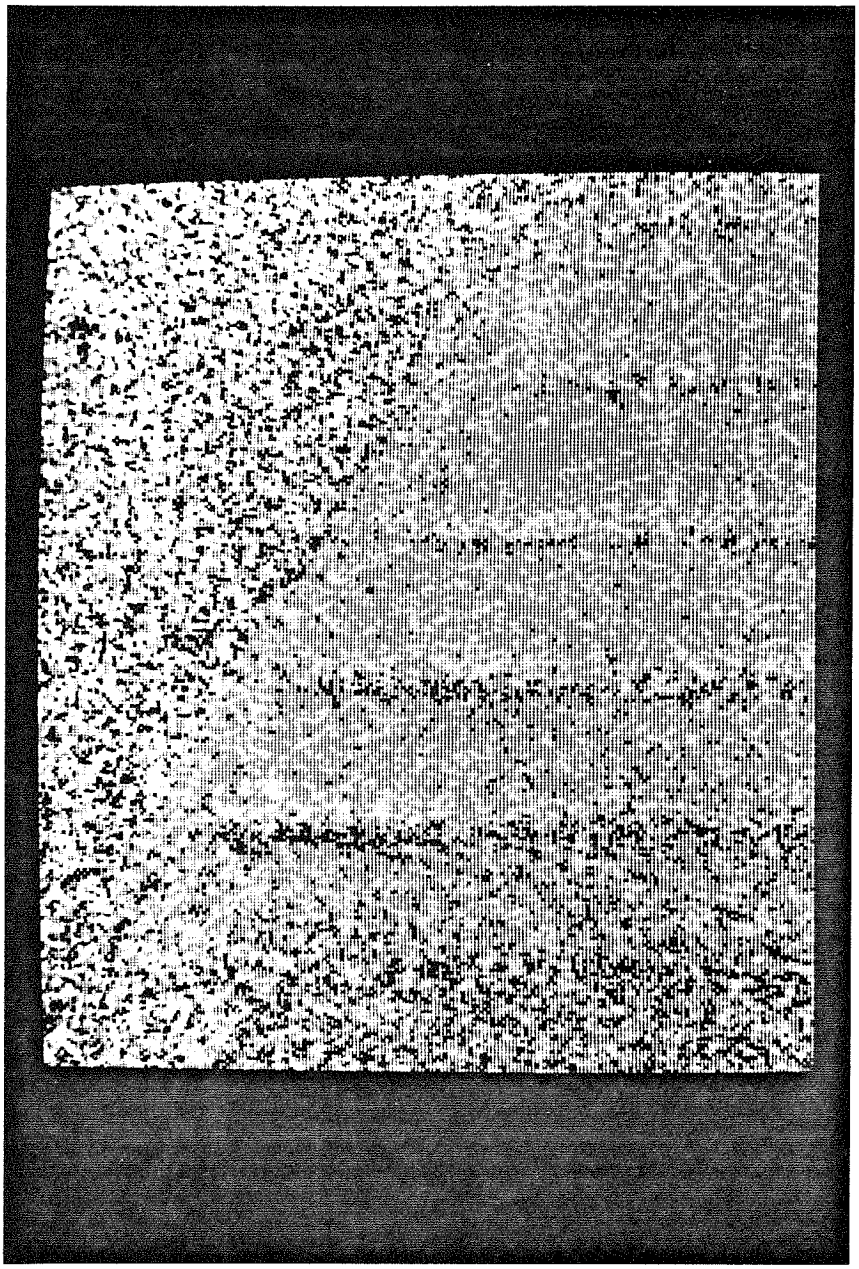

Figure 5.27 Difference image "6–7" of slope test 11

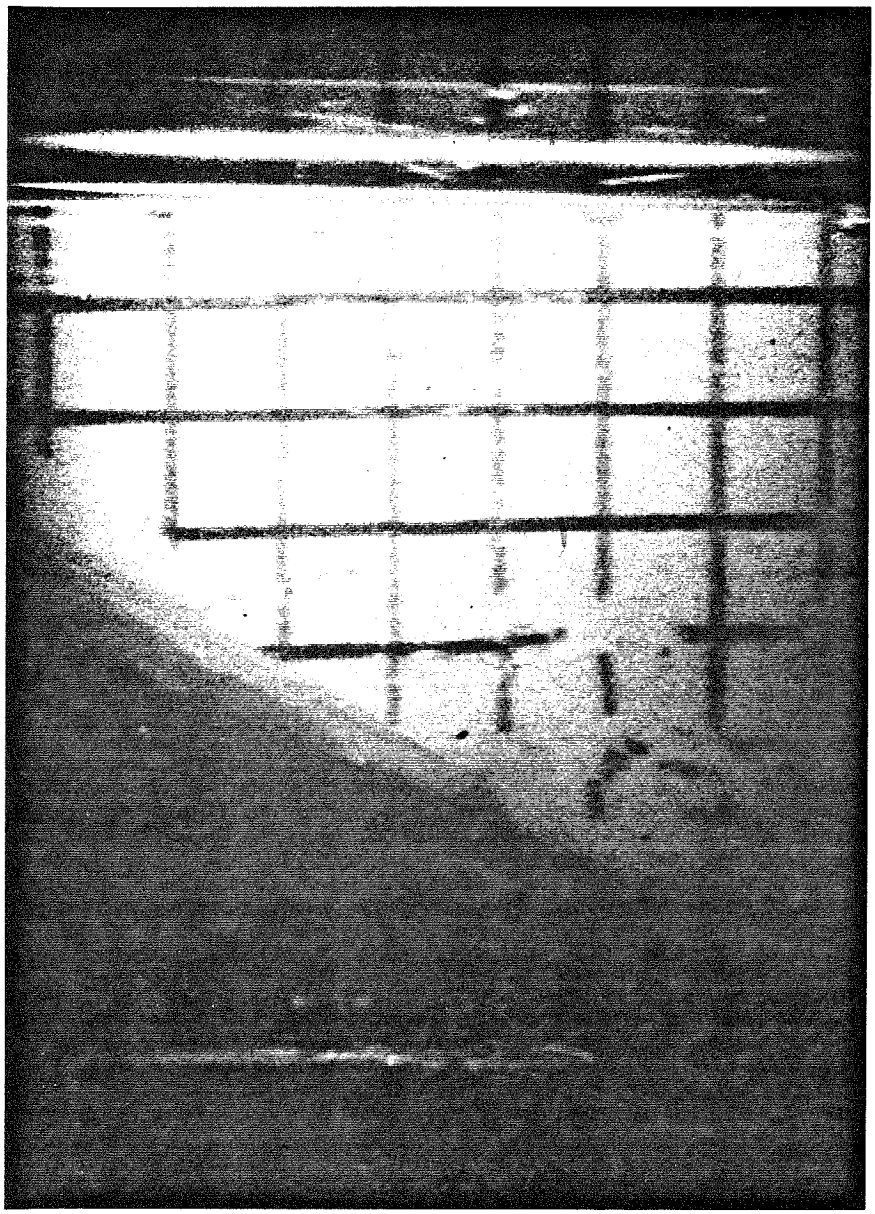

Figure 5.28 First of two consecutive frames of slope test 12 movie film

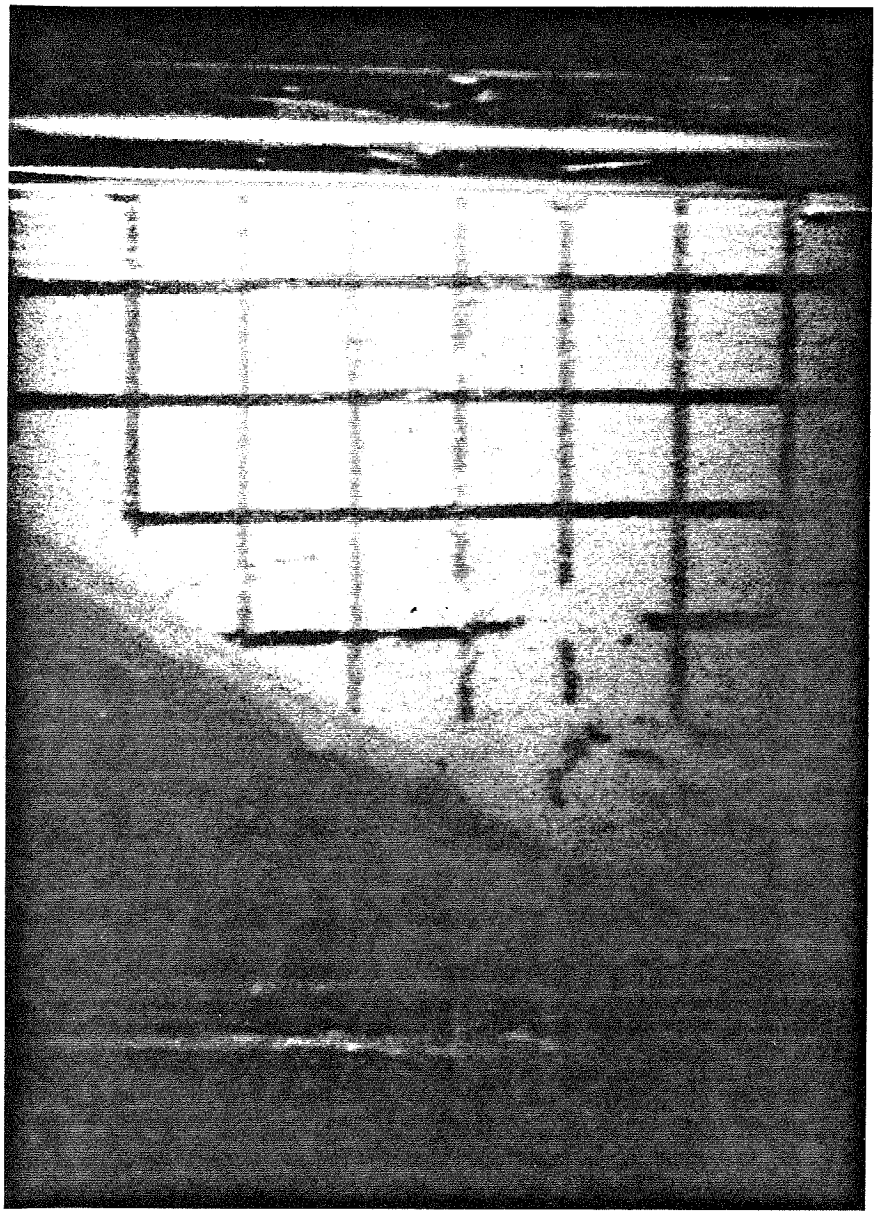

Figure 5.29 Second of two consecutive frames of slope test 12 movie film

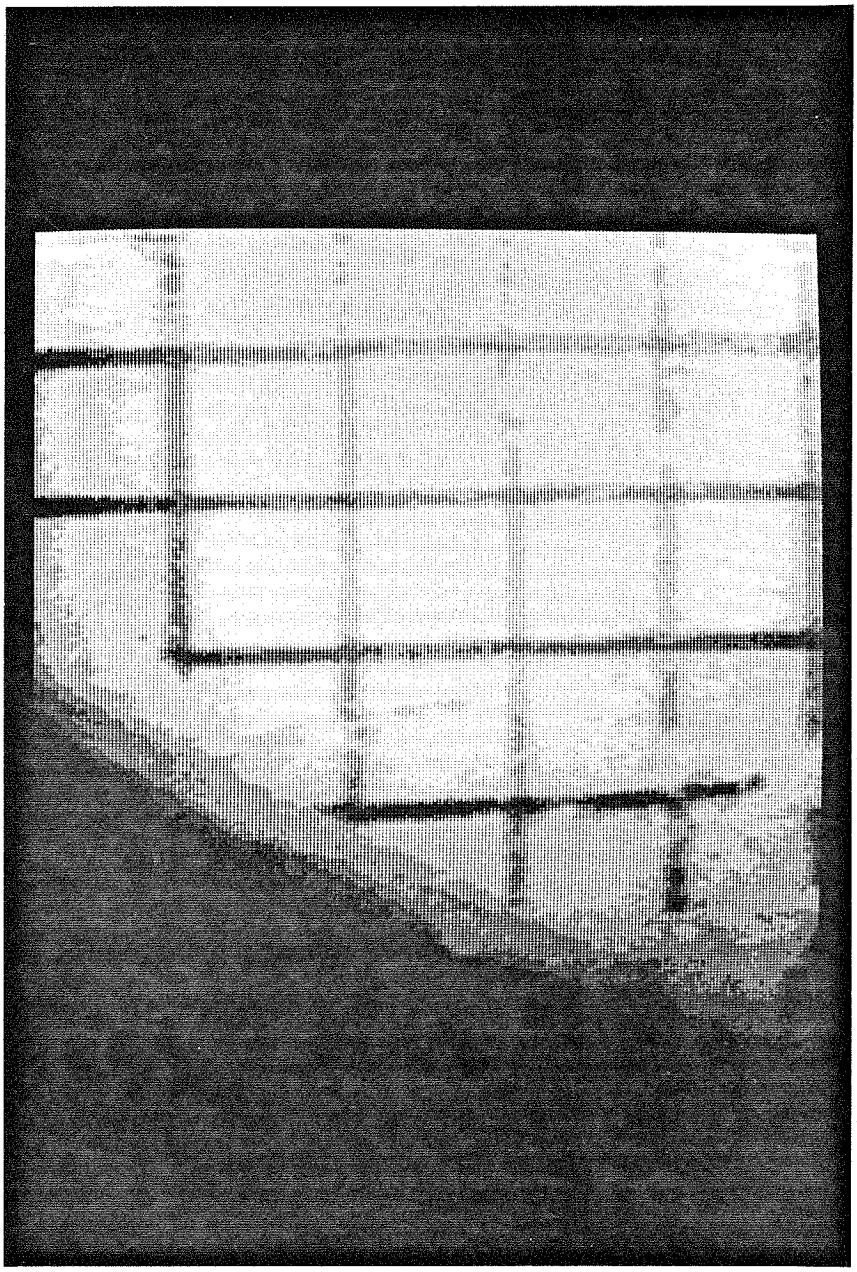

Figure 5.30 Reproduction of central region of Figure 5.28 from digitized data

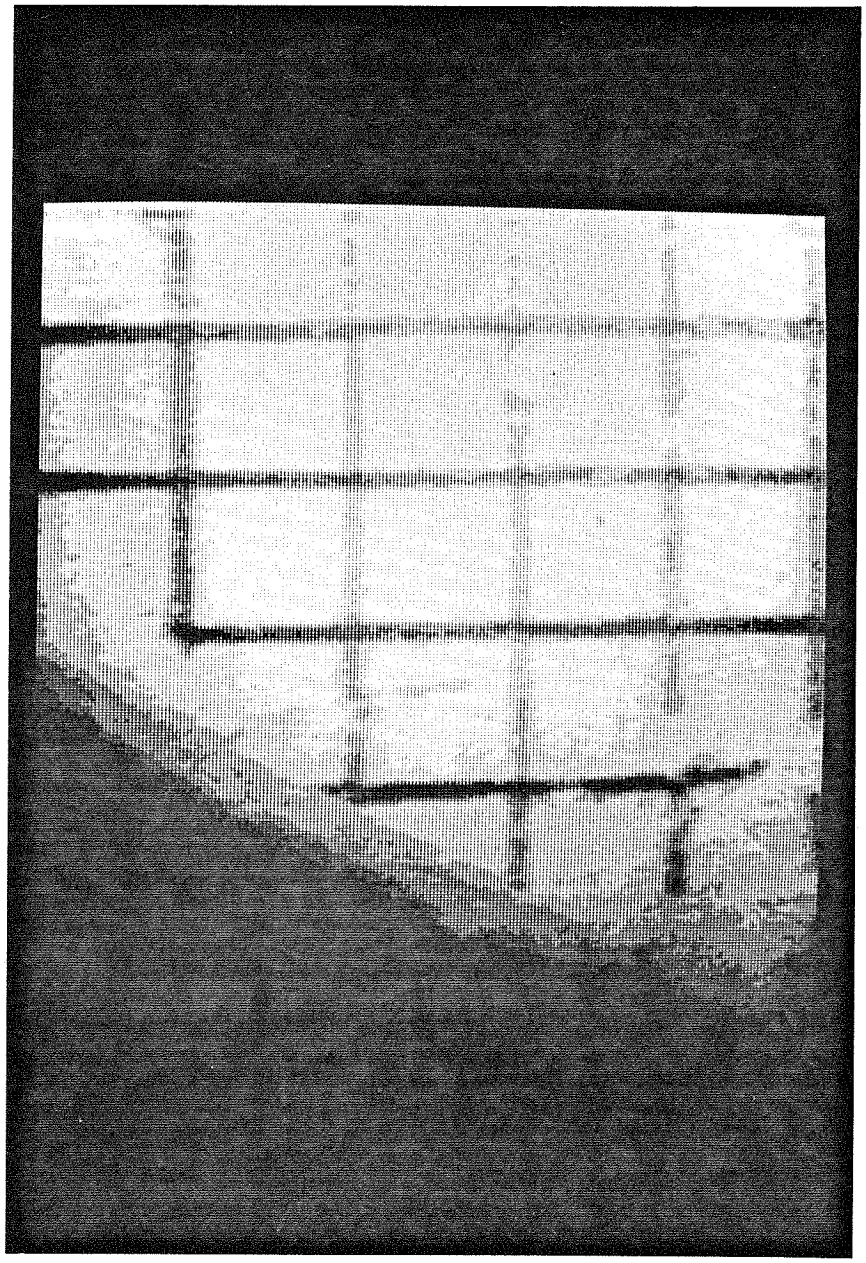

Figure 5.31 Reproduction of central region of Figure 5.29 from digitized data

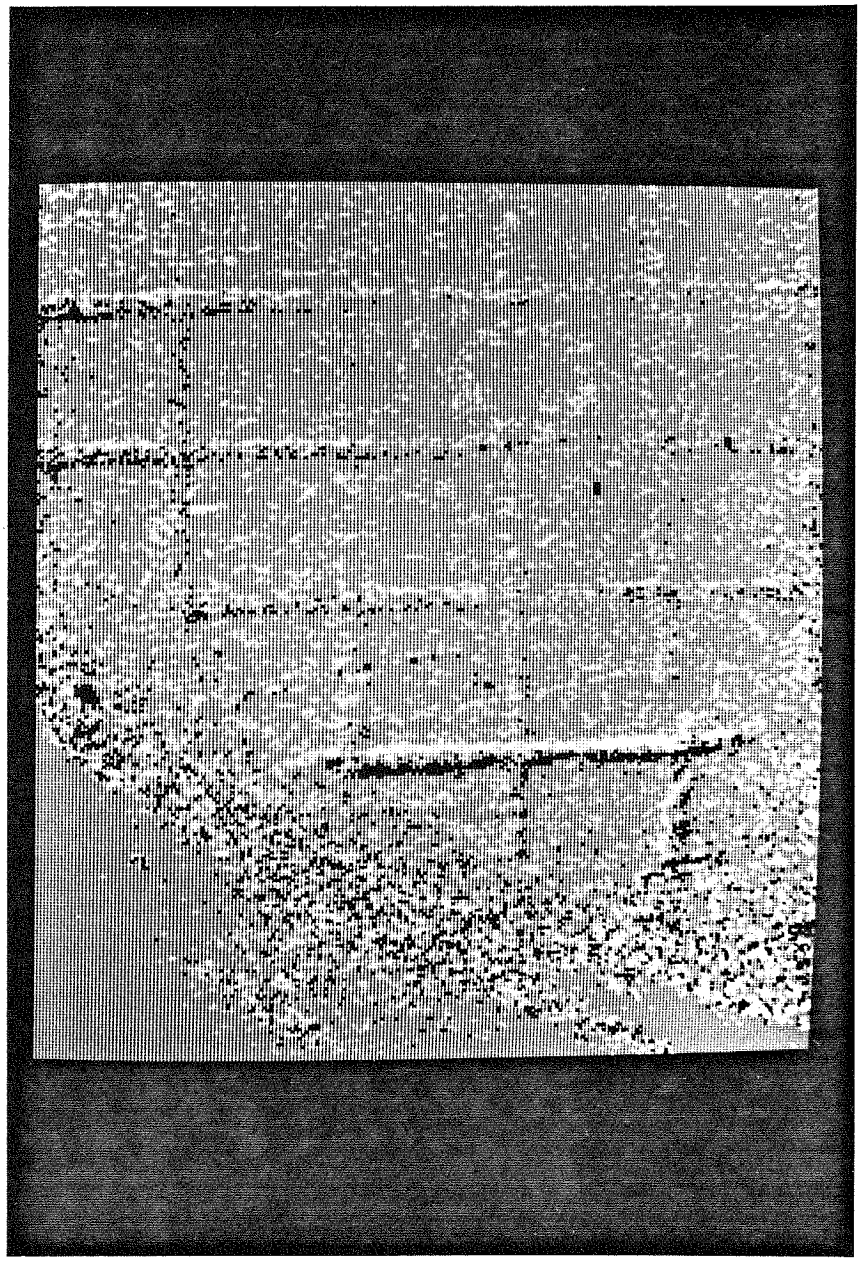

Figure 5.32 Difference image formed by subtraction of Figure 5.31 from Figure 5.30

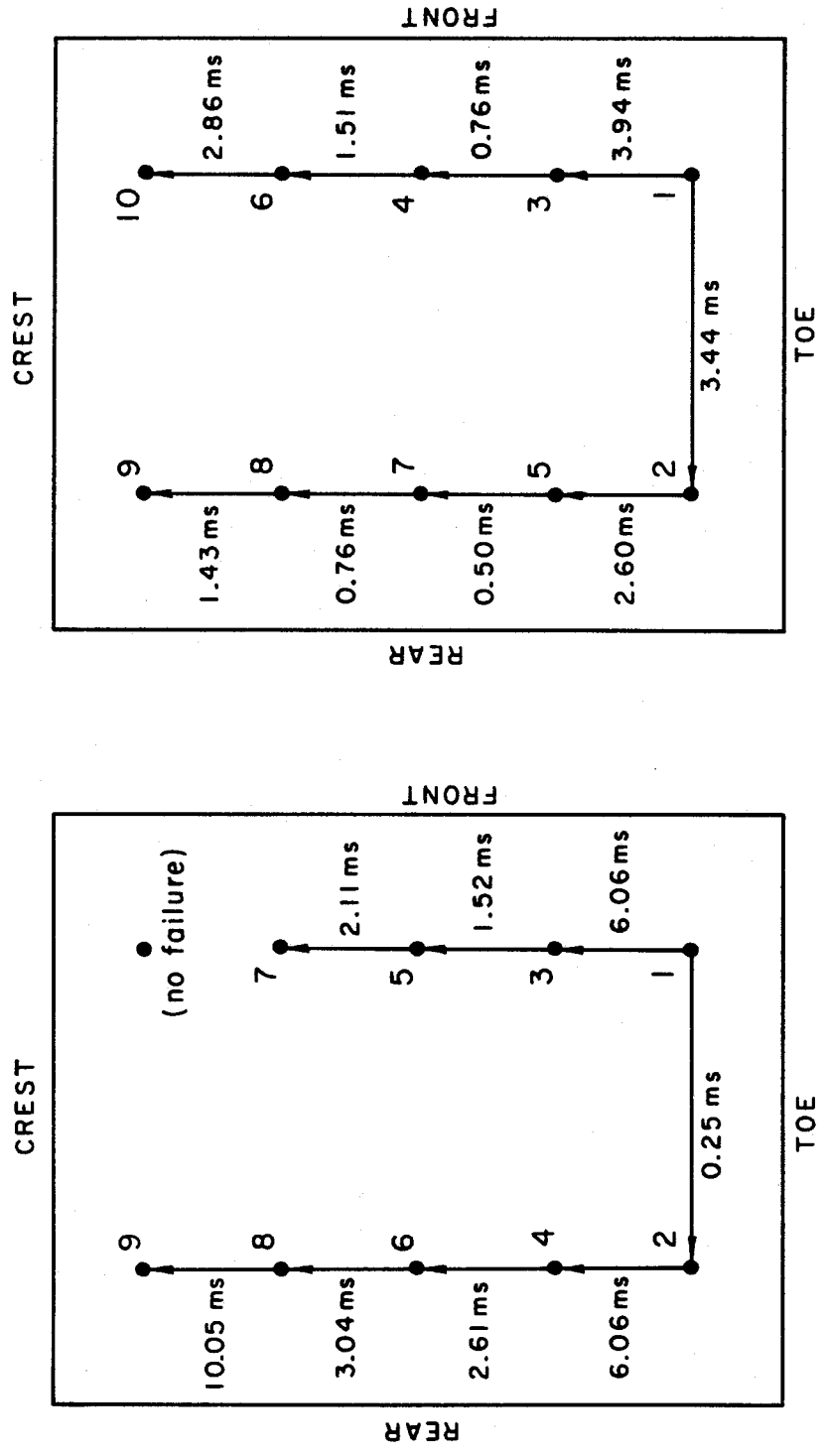

Figure 5.33 Failure sequence of pencil lead transducers during slope tests 17 and 18. Leads are numbered in order of failure with arrows indicating time interval between breakage
(a) Slope test 17
(b) Slope test 18

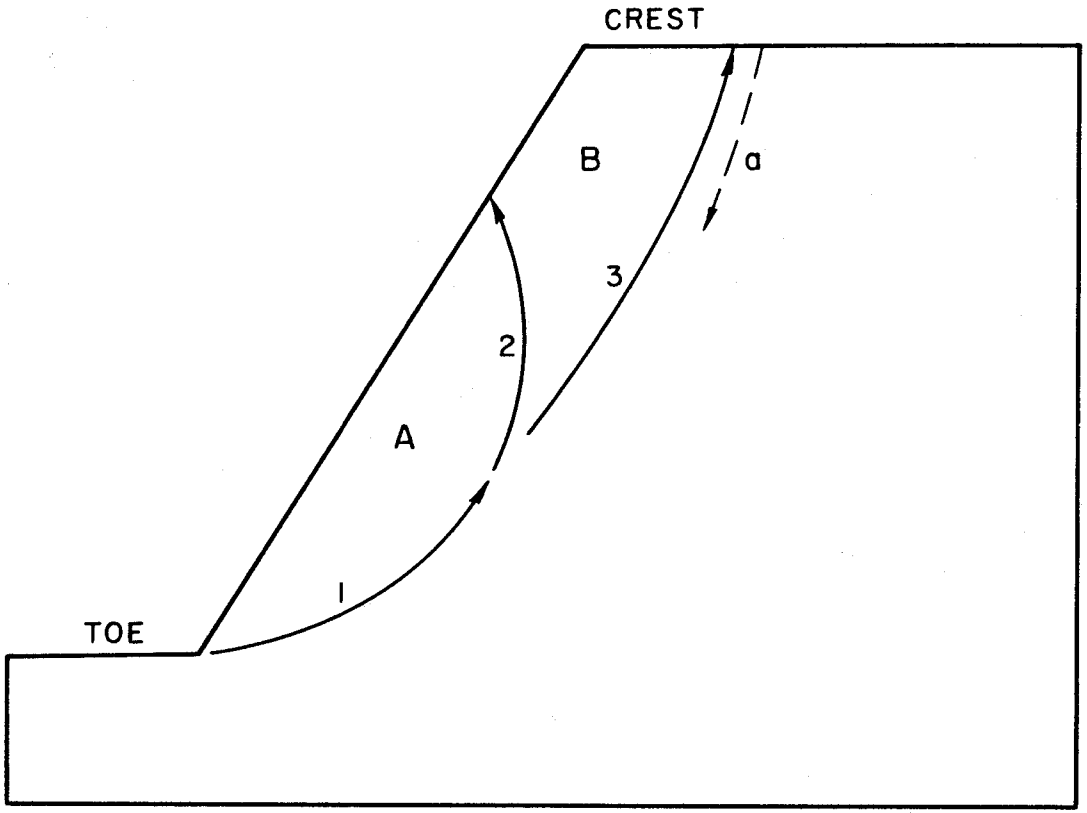

Figure 5.34 Observed mechanism of slope failure.
Shear failure initiates at toe and propagates in approximately circular arc to slope face (arrows 1 and 2) to allow block A to slide away and leave block B unsupported. Failure surface then propagates to crest (arrow 3) to allow block B to slide away and complete failure mechanism and slope collapse. Influence of crest tension crack (dashed arrow "a") on failure mechanism not determined from centrifuge experiments

Chapter 6

ATTEMPTS AT IMPROVED SLOPE STABILITY ANALYSIS

6.1 INTRODUCTION AND OVERVIEW

A number of different and varied approaches was taken to developing an improved method of plane strain slope stability analysis and they are briefly presented in chronological order below. Throughout these attempts, complex, material-specific constitutive models dependent on large deformation plasticity (*e.g.*, [7,53,72,112]) were excluded due to the similarity of failure modes (*e.g.*, shear band formation) in materials of quite different constitutive behavior (*e.g.*, soil and metal). This common feature of failure surface evolution in different materials was considered sufficient evidence to suggest that the specific constitutive behavior of a material is not the most important factor in the modeling of failure, and that a more simplistic approach to the problem might be taken with a different emphasis. In this light, the following attempts at improved slope stability analysis were essentially based on small deformation, linearly elastic material behavior (since the centrifuge slope failures involved negligible soil deformations right through to the completion of failure surface development) and modeled slope failure with a

greater emphasis on geometrical considerations.

The first attempt was an analytical solution based on linear fracture mechanics which quickly led to use of the numerical finite element method with an energy criterion for crack propagation, and a subsequent brief consideration of the boundary element method. Without success at modeling slope failure as a discontinuous phenomenon, the fracture mechanics approach was abandoned and a second attempt with the finite element method made, based on the weak element or smeared crack concept, also without satisfactory results. Finally, success was achieved in the form of a finite difference technique, using a Lagrangian differencing scheme in space and explicit integration in artificial time with dynamic relaxation. The major finite element results are presented in Section 6.2. Those derived from the energy-based crack propagation approach appear in Section 6.2.1, while those founded on the weak element concept appear in Section 6.2.2. The finite difference method is described in detail in Chapter 7.

The analytical solution was an attempt to treat slope failure as a discontinuous phenomenon, by modeling the development of the failure surface as a propagating crack within the framework of linearly elastic fracture mechanics. Here the aim was to solve for the stress field near the crack tip so as to propagate the crack according to the Mohr-Coulomb shear failure criterion of (3.12). In the fracture mechanics setting, this criterion finds the plane on which the maximum ratio of shear stress to normal stress acts (taking into account the cohesion of the material),

and advances the crack in that plane. However, a closed form analytical solution could not be found due to the complicated geometric boundary conditions of the slope, and numerical solution with finite elements was subsequently employed.

Linearly elastic finite element analysis was applied to the plane strain slope stability problem on the same fracture mechanics basis as the analytical effort. An accurate description of the infinite stresses at the crack tip, however, proportional to $1/\sqrt{r}$ for all conditions (where r is the radial distance from the crack tip), requires a very fine mesh or "singular" elements. It was considered desirable to avoid the necessity of either a fine mesh or singular elements, resulting in the stress-based Mohr-Coulomb criterion being discarded in favor of an energy criterion. The energy criterion required the crack to propagate in that direction which would minimize the potential energy of the whole mesh, not just near the crack tip. In other words, propagation would take place so as to maximize the total energy lost per unit length of advancing crack. The failure surface geometry was represented by internal element boundaries, with "double nodes" (*i.e.*, two nodes at each nodal location) along the selected boundaries. To prevent overlap of the mesh, stiff normal springs were placed between the double nodes, and tangential springs were introduced to simulate resistance to slip along the boundary. Propagation of the failure surface was then represented by successive release of the tangential springs. In practice, the direction of failure surface propagation was decided by moving the crack tip in an arc of constant radius about the last released double node, and

finding the direction which maximized the energy lost from the previous crack position where the last released double node was the crack tip. This technique was applied to a "Palmer and Rice" test problem [69], as well as to a finite element representation of the centrifuge slope specimen (see Section 6.2.1). For the "Palmer and Rice" geometry (see Figures 6.1 and 6.3), separate analyses were made with both quadrilateral and triangular elements with similarly unsatisfactory results — the change in potential energy of the entire mesh was very insensitive to even large changes in the direction of crack advance. For the slope mesh representing the centrifuge model (see Figure 6.2), where only linear quadrilateral elements were used, the preferred crack extension direction was horizontal rather than upward as required for a realistic representation of the observed slope failures. Although ultimately unsuccessful, the finite element results of both problems are presented in more detail in Section 6.2.1.

The possibility of using the same energy criterion in the close vicinity of the crack tip, rather than over the entire mesh (which tends to smear or average the energy changes near the crack tip over all elements) was then assessed. Considering only the near vicinity of the crack tip implies that the free surface boundaries of the slope (*i.e.*, the toe, face, and crest) are located an infinite distance from the crack tip where they can have little influence. However, these free surface boundaries are ultimately responsible for the propagation and geometry of a slope's failure surface and on these grounds alone the near-tip energy idea was discarded. Since

the energy concept did not prove successful, the Mohr-Coulomb failure criterion based on near-tip stresses was reconsidered. It was accepted that an accurate description of the crack tip stresses had to be obtained but the question arose: Could this be done without finite elements, which require a very fine mesh and yield mesh-dependent results ? A possible answer lay in the use of boundary elements (*e.g.*, [22]).

The boundary element method has several advantages, provided the field equations describing the domain of interest are linear — a condition which was satisfied by the present idealization of the plane strain slope stability problem. Firstly, boundary elements provide a better approximation to crack tip stresses since singular solutions are the very basis of the method. Secondly, the size of the problem can be reduced since only the boundary of the problem needs to be discretized, not the entire domain. Thirdly, the boundary element method is suited to infinite domains and no artificial lateral or bottom boundaries need be introduced, in contrast to the finite element method. However, the main disadvantage of the boundary element method is the difficulty of solving real, inhomogeneous (*e.g.*, layered) problems. In these situations, the boundaries between layers of homogeneous material need to be discretized and the solutions for each layer matched at the boundaries. An important objective of the slope stability analysis was to solve real practical problems and on this basis alone, no further investigation of the boundary element method was made. The finite element method was readopted

and the fine mesh requirement accepted as a necessary evil.

Since the initial finite element efforts with linear fracture mechanics were unsuccessful, a weak finite element or smeared crack approach similar to [73] was taken to the modeling of slope failure. This implies broadening of the failure surface representation to one element width compared to the initial discontinuous type description where the failure surface was represented by the boundary of zero thickness between elements. Such a representation of the failure surface would be adequate provided the finite element mesh was fine enough. The weak element approach was implemented by increasing the gravity loads on the centrifuge slope mesh until an element failed, at which time its modulus of elasticity E was reduced from its initial homogeneous value and the gravity loads subsequently increased until another element in the mesh failed. Here, failure was defined to occur when the principal shear stress reached a critical value, namely the cohesion of the material. In this way, it was hoped that the calculation would predict a sequence of element failures representing the failure surface geometry observed in the centrifuge slope failure experiments. This did not develop, however, since elements in the bottom right-hand corner and along the bottom boundary of the mesh (see Figure 6.5, for example) generally dominated the failure pattern, for both quadrilateral and triangular elements. Such yielding occurs for a material with uniform shear strength, because gravitational stresses increasing with depth eventually cause a principal stress difference exceeding twice the shear strength

through the effect of Poisson's ratio. The material will thus yield below some depth even under conditions of a flat surface and gravitational loading. In spite of the general similarity of the failure patterns, there were important differences between the two types of elements in terms of response and these are described in more detail in Section 6.2.2.

Since the soil in the failure zone of a slope is failing predominantly in shear, the reduction in E (and consequently shear modulus G) was not considered to be completely realistic since this also implied a reduction in the bulk modulus K for a constant Poisson's ratio ν. It was thought that a reduction in shear modulus alone, while maintaining a constant bulk modulus, would provide a better model of what was really happening to the soil in the failure zone. Such a representation implies an increasing Poisson's ratio. This modified version of the failure model was tested, with no improvement in the representation of slope failure, using a combination of quadrilateral and triangular finite elements in a pattern which was intended to assist in the development of an appropriate rupture zone without dictating the details of its propagation. The concept was therefore studied no further.

At this time, a special finite difference algorithm for solving boundary value problems in plane finite, linear and nonlinear elastostatics [100] became available. Originally applied to the numerical study of an anti-plane crack propagation problem, the algorithm was adapted to handle plane strain slope stability under gravity

loading and found to give very satisfactory results. The finite difference approach is described in Chapter 7 and the results generated by the method are presented in Chapter 8.

6.2 FINITE ELEMENT RESULTS

6.2.1 The energy-based crack propagation approach

As outlined in Section 6.1, finite element analysis of slope failure as a fracture mechanics problem was first applied to the "Palmer and Rice" geometry of Figure 6.1(a) with an energy-based criterion for crack propagation. However, while Palmer and Rice [69] originally used this geometry to determine the magnitude of applied loading required for further propagation of a pre-existing shear band of given length in a straight line, the purpose here was to look for any tendency of the growing shear band to develop a curved trajectory. In accordance with the regular rectangular mesh of Figure 6.1(b) then, the shear band or crack was initially advanced in three different directions: horizontally (node C to node P), vertically upward (node C to node R), and vertically downward (node C to node D). The potential energy of the whole mesh in each of these configurations was computed for body force loading applied at an inclination of 60° to the vertical, as shown in Figure 6.1(a), for which horizontal crack extension possessed the minimum energy, but only by a small margin over the vertically downward and vertically upward extensions. The inclined body force loading was intended to promote crack prop-

agation away from straight line continuation of the existing crack — a tendency that the advancing crack must exhibit if a curved failure surface is to be predicted for the slope stability problem.

Since the horizontal crack extension was only a slightly lower minimum than the other two cases, it appeared that such a tendency to develop a curved trajectory might become more apparent by investigating the extension of a crack through a mesh representing the slope tested in the centrifuge experiments (see Figure 6.2). The "Palmer and Rice" test problem was therefore temporarily set aside to examine the propagation of three different failure surfaces through the slope mesh of Figure 6.2(b). Each pre-assigned test failure surface was represented by a set of "double node" pairs connected by stiff normal and tangential springs, as for the initial test problem. Gravity loading was applied through a body force field directed vertically downward. Failure surface "3" lost more energy as it propagated through the mesh than did surfaces "1" and "2", suggesting that its geometry would be naturally favored over the other two. For each failure surface, however, the propagation was dominated by a preference for continued horizontal crack extension and a resistance to any upward turn toward the crest of the slope. Indeed, another failure surface with a longer horizontal section than surface "3" would be favored over all three of those actually considered. This outcome was clearly not a reasonable simulation of the observed centrifuge slope failures or full-scale slides, which indicated geometries closer to failure surfaces "1" or "2" of Figure 6.2(b),

and the linear quadrilateral elements used in the discretization thus demonstrated a preference for pure shear deformation. In retrospect, this preference is physically reasonable on the basis of energy considerations, which imply that elements subjected to deformations other than pure shear will require more energy to deform, making them stiffer and more resistant to such deformation. In order to model an arbitrary, curved shear failure surface passing through a regular mesh of elements, this situation cannot be avoided, for even if an element on the failure surface is subjected to pure shear, its neighbors will generally not be and it is the greater number of neighboring elements which will more dominantly influence the global energy requirements of deformation of the mesh.

Returning to the "Palmer and Rice" configuration of Figure 6.1(a), an attempt was made to clarify this apparent preference for horizontal extension of the failure surface through the finite element mesh. Referring to Figure 6.1(b), crack advance at various angles above the horizontal was investigated by moving the single crack tip node P to an appropriate position relative to the double node C on the crack surface immediately behind the tip. In particular, this was achieved by moving node P toward node Q, consequently distorting the quadrilateral elements connected to node P, and computing the total potential energy of the mesh for each configuration. The minimum energy occurred for the crack inclined at $45°$ to the horizontal, when node P was coincident with node Q. The same failure surface configuration was alternatively obtained by moving node R to be coincident

with node Q, and this too was the minimum energy state relative to intermediate positions of node R between its initial position and that of node Q. However, the energies of the system for the two alternative methods of generating the 45° crack extension did not match — a problem attributed to differences between the two configurations involving the distortion of different quadrilateral elements and the orientation of those elements to the applied body force loading. The fact that the energy minimum occurred for a crack angle of exactly 45° for the inclined body force loading was also alarming. This should have been expected in hindsight, however, since the vertical movement of node P toward node Q, and the horizontal movement of node R toward node Q, both increase the length of crack extension to a maximum at 45°, and a longer crack will release more energy than a shorter one.

Neither the energy mismatch for the 45° crack, nor the varying crack length, were acceptable results and an attempt was made to eliminate these problems by replacing the quadrilateral elements with triangular elements, and investigating the various angles of crack extension in a slightly different way. Specifically (see Figure 6.3), node S was moved in an arc of constant radius from its initial position of 45° relative to double node T, and the total mesh energy was computed for each corresponding angle of crack advance. Crack extension at 55° above horizontal was the energy minimum for body force loading inclined at 30° from the vertical, while extension at 60° above horizontal yielded the minimum energy for body

forces applied with a 60° inclination from the vertical. In both cases, however, the change in mesh energy for a 5° change in the angle of crack extension was of the order of 0.01 percent — too insensitive to be of practical use in the numerical prediction of slope failure.

6.2.2 The weak element approach

After the unsuccessful efforts of Section 6.2.1 to model slope failure as a discontinuous phenomenon, an attempt was made to model the process by successively softening appropriate elements within a finite element mesh representing the centrifuge slope specimens. The slope soil was modeled as a purely cohesive, elastic–perfectly plastic material (represented diagrammatically in Figure 6.4 where τ_S is the principal shear stress and γ_S is the principal engineering shear strain), and trials were made separately with quadrilateral and triangular elements, followed by a combination of the two arranged in a "flow net" pattern.

First using quadrilateral elements, the homogeneous finite element mesh, shown in Figure 6.5, was subjected to increasing gravity loads until an element yielded, as defined by the coincidence of its principal shear stress with the cohesion of the material. All elements initially had the same material properties, unlike the approach followed by Prévost and Hughes [73] who needed to artificially "seed" their nominally symmetric meshes with a weak element. The first element to fail was the element at the toe of the slope (see Figure 6.5(a)), which failed at $27g$ due to the natural stress concentration at the toe of the unsymmetric mesh. The

modulus of elasticity E of the "failed" toe element was reduced while increasing the gravity loading until another element in the mesh failed. The reduction in E was of such magnitude as to maintain the principal shear stress in the failed element constant at its yield level as strain increased, according to Figure 6.4. The next element to fail was immediately to the right of the toe element (see Figure 6.5(b)), failing at $34g$. E of both elements was then reduced while continuing to increase the gravity loads until $38g$ was reached, at which time the shaded elements of Figure 6.5(c) had all reached failure level. The process of E reduction and gravity load increase was repeated twice more to give the failure patterns of Figure 6.5(d) and (e) at $40g$ and $41g$ respectively. None of the large body of elements failing in the bottom right hand corner of the mesh had their moduli of elasticity reduced, however, since they were clearly not part of a propagating failure surface through the mesh.

These results suggested possible dependence of the failure pattern on the mesh configuration and element type. To help validate or refute this claim, a sensitivity analysis was conducted on the simplified problem of displacement-controlled plane strain compression (see Figure 6.6). A plane strain compression specimen of elastic–perfectly plastic material was discretized, and analysed, first with quadrilateral elements, then with triangular elements oriented in two different patterns. An intentional notch was made in one of the free surface boundaries of the mesh to "seed" the problem. The aim of the analysis was to see how the different element

types and orientations would affect the failure pattern, which, for a homogeneous material, should be a 45° shear band intersecting the free surface boundary at the notch. The results of the sensitivity analysis are presented in Figure 6.7 where the shear band failure pattern is seen to be highly dependent on element type and orientation. It is clear that different elements will produce different failure patterns depending on how easily an element can assume a particular deformation mode, given its orientation to the loading.

Regardless of the now-established dependence of failure pattern on element type and orientation, the slope failure problem was remeshed using triangular instead of quadrilateral elements, to see if a realistic failure pattern could still be generated, without erroneous yielding of the body of elements in the bottom right hand corner of the mesh. The results of this attempt are shown in Figure 6.8. Here the process of E reduction of failed elements was simplified so that once yielding occurred, E was immediately reduced by one-half for the element concerned and not altered thereafter. Figure 6.8 shows that no improvement in failure surface prediction was obtained with triangular over quadrilateral elements, and further shows the failure pattern to be dependent on the orientation of individual triangular elements with respect to the direction of gravity loading.

Another trial was made with a combination of quadrilateral and triangular elements arranged in a "flow net" pattern for the slope (see Figure 6.9). This mesh was designed so that a series of elements would approximately represent

a potential failure surface with a width of one element, and hence most readily allow successive element yielding in a realistic propagation sequence. The results for this mesh are shown in Figure 6.9 with no improvement apparent over the separate attempts with quadrilateral and triangular elements of Figures 6.5 and 6.8 respectively. As was done with the triangular element mesh, the modulus of elasticity of a "flow net" element was reduced to 50 percent of its original value upon failure and not modified subsequently.

Almost identical results were achieved with the "flow net" mesh, even when element failure was implemented in a slightly different manner. Instead of reducing E by one-half with ν constant, E and ν were adjusted so as to reduce G by 50 percent while keeping K constant. Since the soil in the failure zone is believed to lose much of its shear resistance but not its volumetric stiffness upon failure, this was thought to be a more realistic representation of the change in an element's properties at yield. The finite element results, however, neither validated nor refuted this hypothesis.

6.3 SUMMARY

The insensitivity of the discontinuous approach to slope failure prediction, as modeled by the energy-based criterion of crack propagation (see Section 6.2.1), and the mesh and element dependence of the weak finite element approach (see Section 6.2.2), were both unacceptable "diseases" of the attempts to develop an

improved method of slope stability analysis. Both approaches were consequently abandoned in favor of the finite difference technique of Chapter 7. The absence of these problems from the finite difference approach is evident from the results presented in Chapter 8.

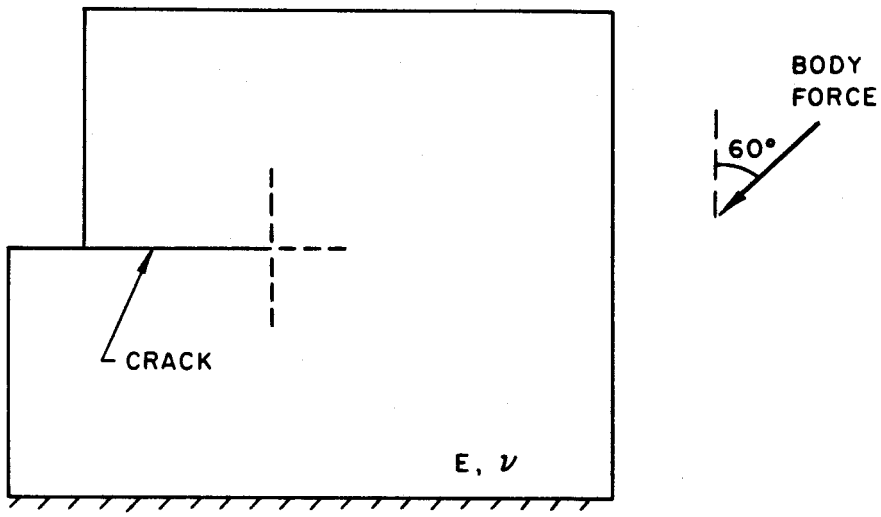

(a)

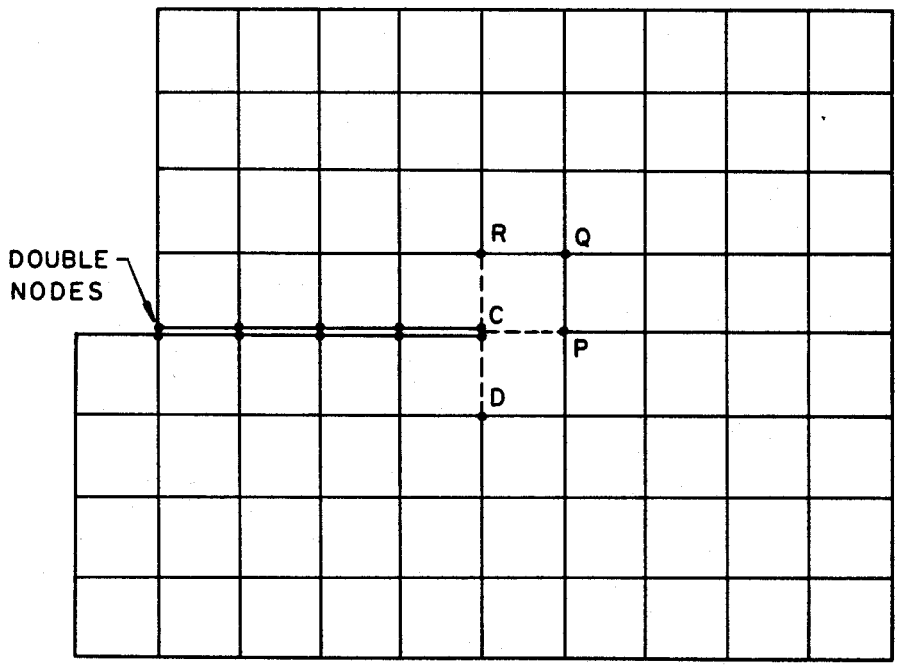

(b)

Figure 6.1 Test problem for energy-based crack propagation approach to slope failure
(a) Problem definition
(b) Quadrilateral finite element mesh

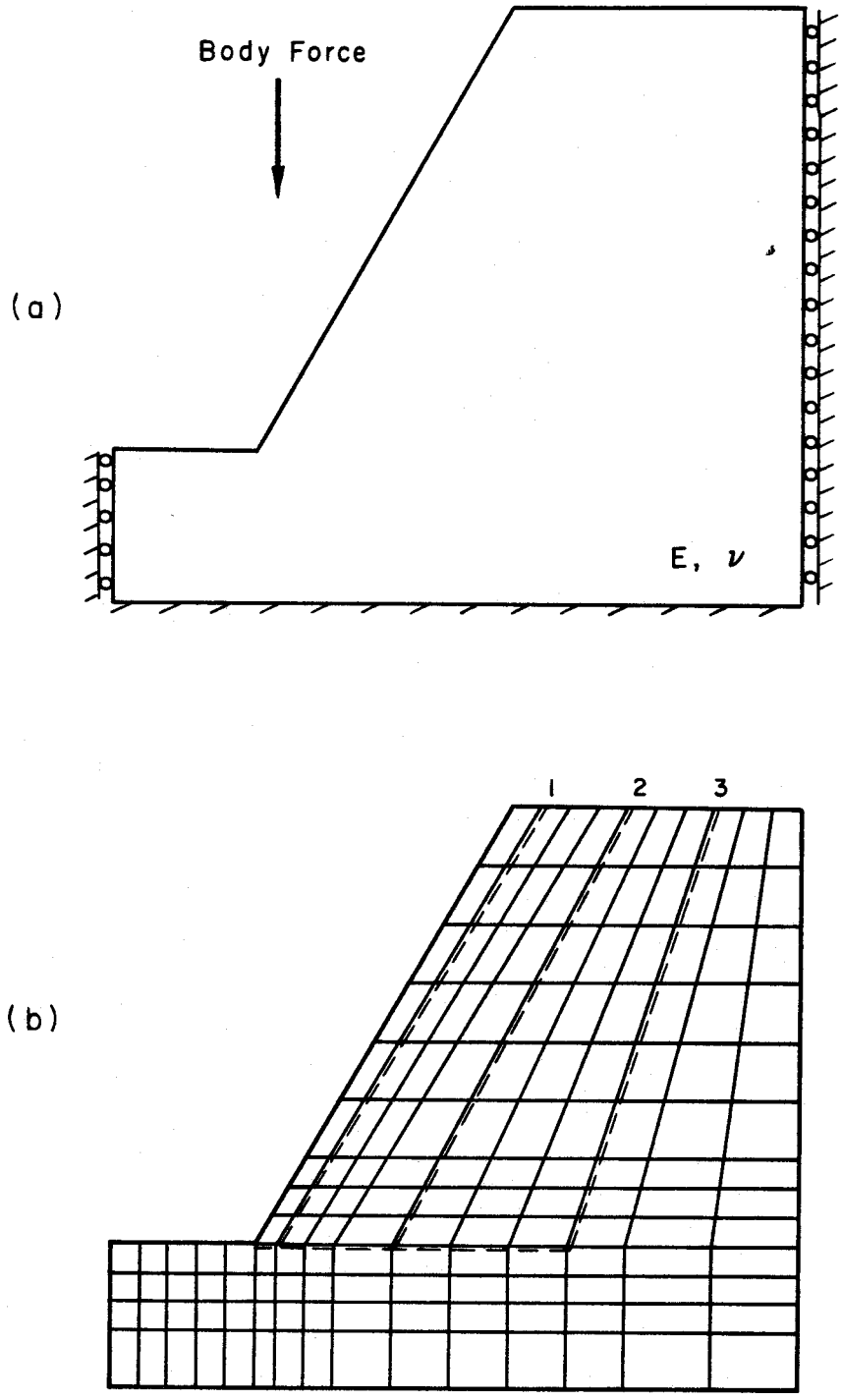

Figure 6.2 Centrifuge slope failure problem
(a) Problem definition
(b) Finite element mesh and trial failure surfaces

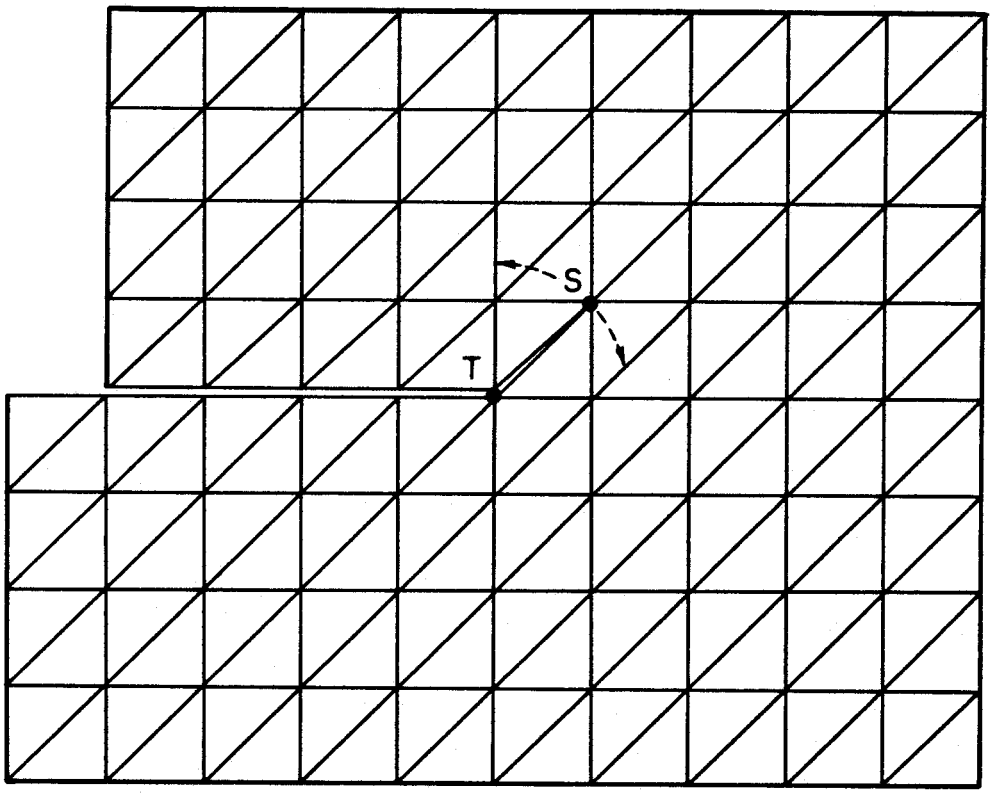

Figure 6.3 Triangular finite element mesh for test problem

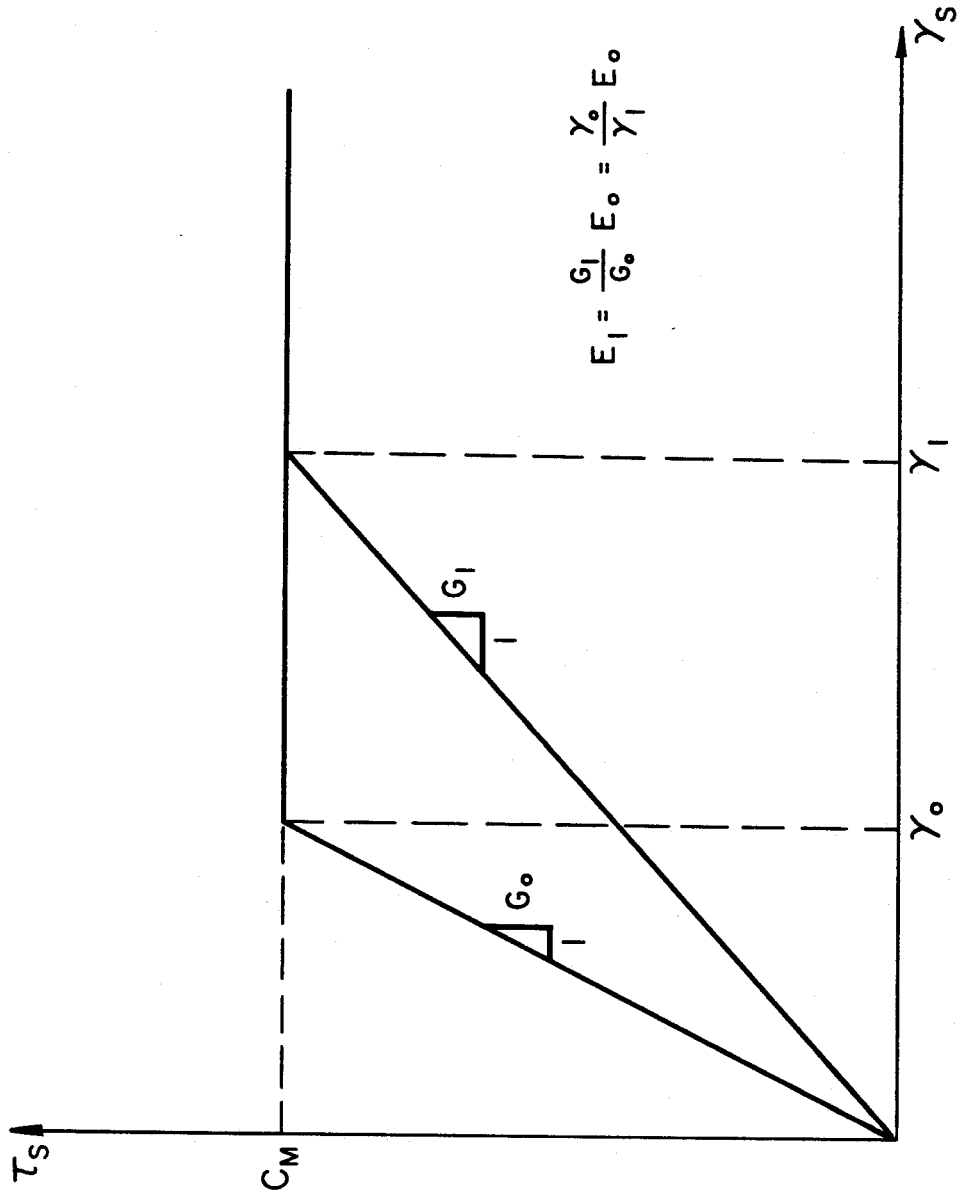

Figure 6.4 Elastic-perfectly plastic constitutive relation between principal shear stress τ_s and principal engineering shear strain γ_s

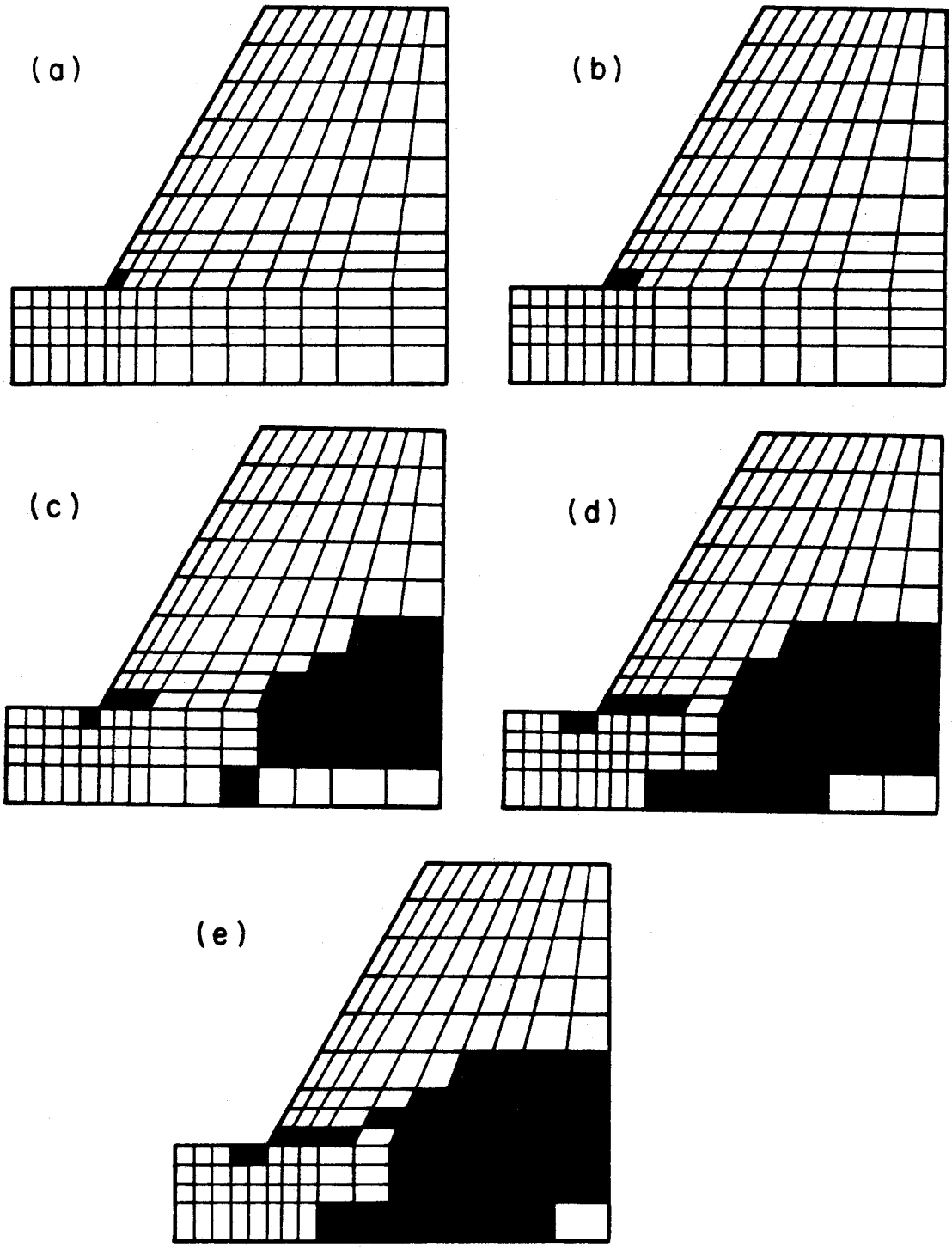

Figure 6.5 Development of "failure" with increasing gravity throughout quadrilateral mesh of centrifuge slope specimen (a) 27*g* (b) 34*g* (c) 38*g* (d) 40*g* (e) 41*g*

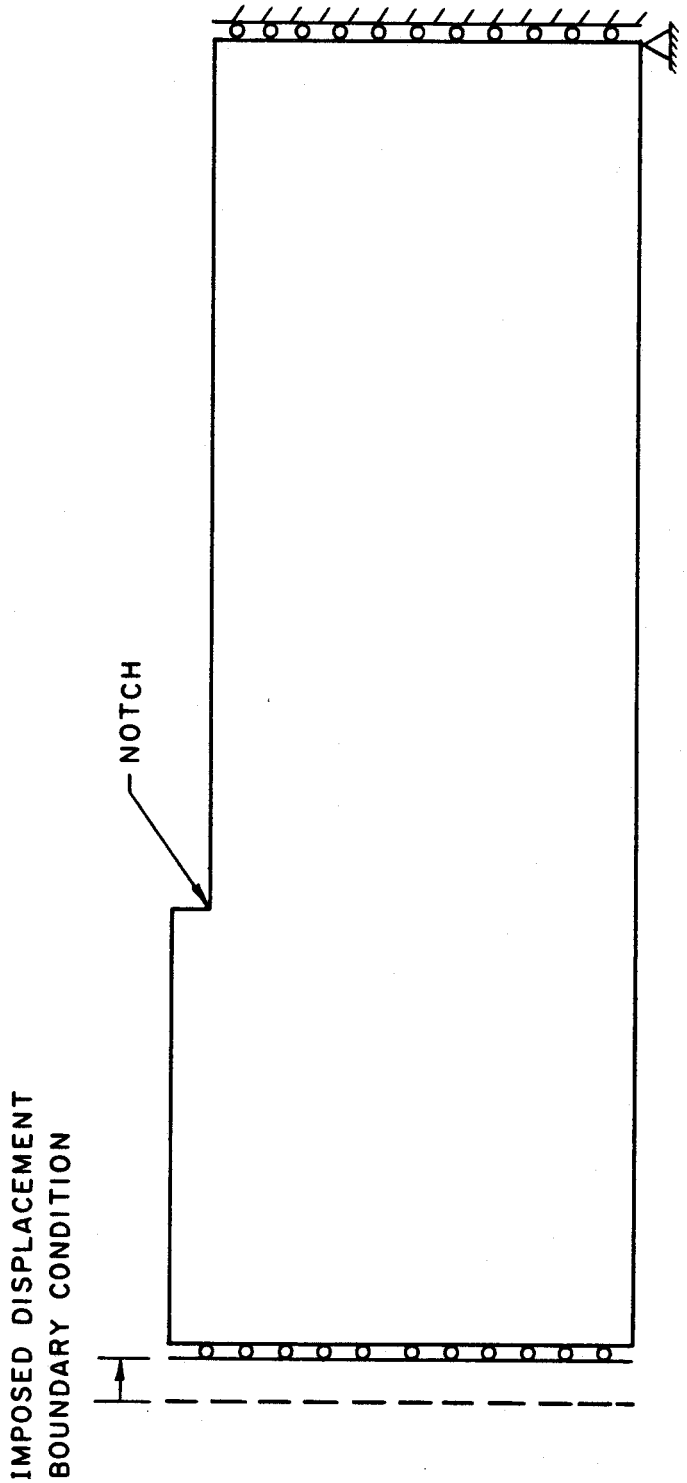

Figure 6.6 Displacement-controlled plane strain bar compression problem

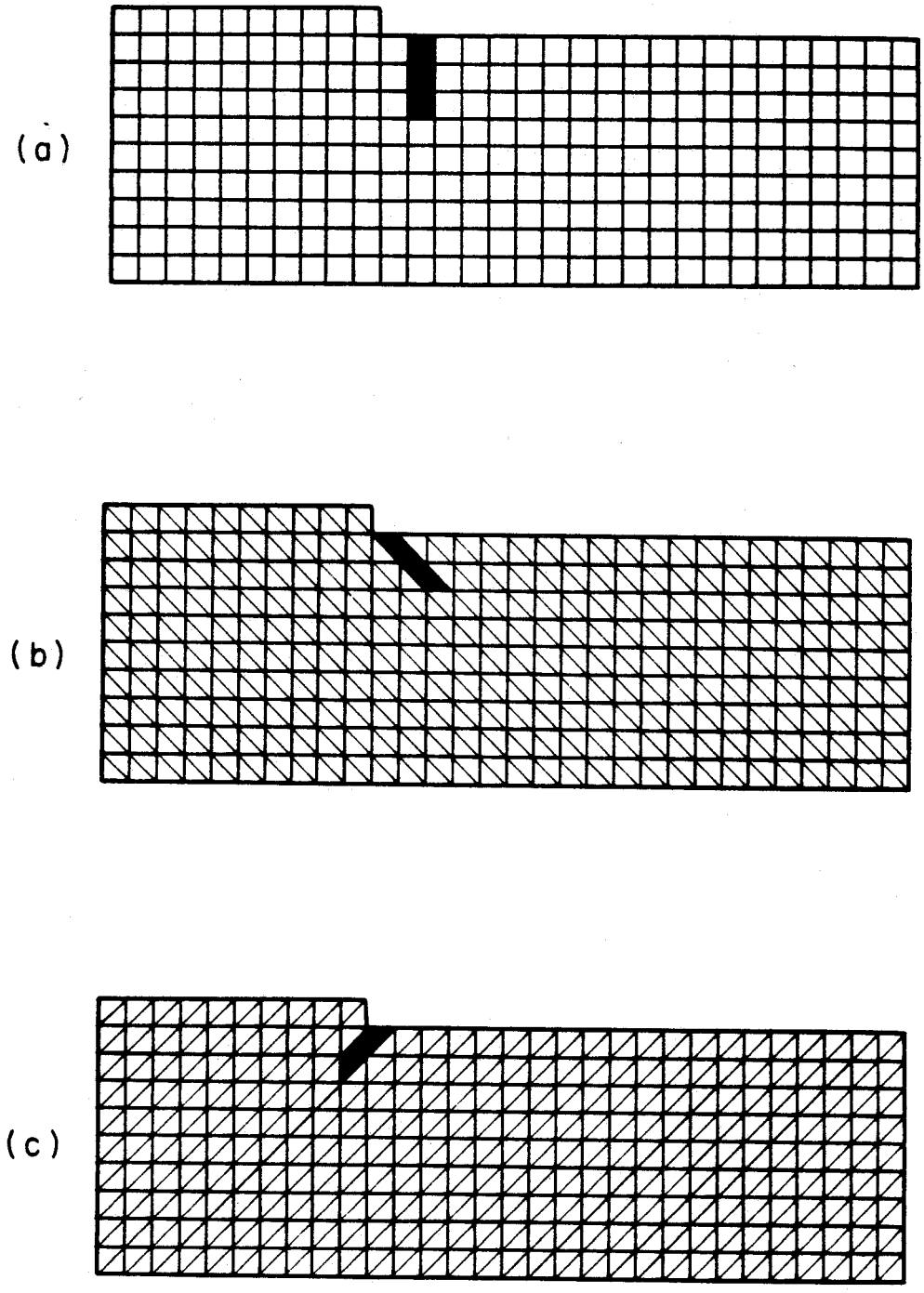

Figure 6.7 Mesh and element dependent "failure" in displacement-controlled bar compression specimen
(a) Square element mesh
(b) Triangular mesh with "right-hand" orientation
(c) Triangular mesh with "left-hand" orientation

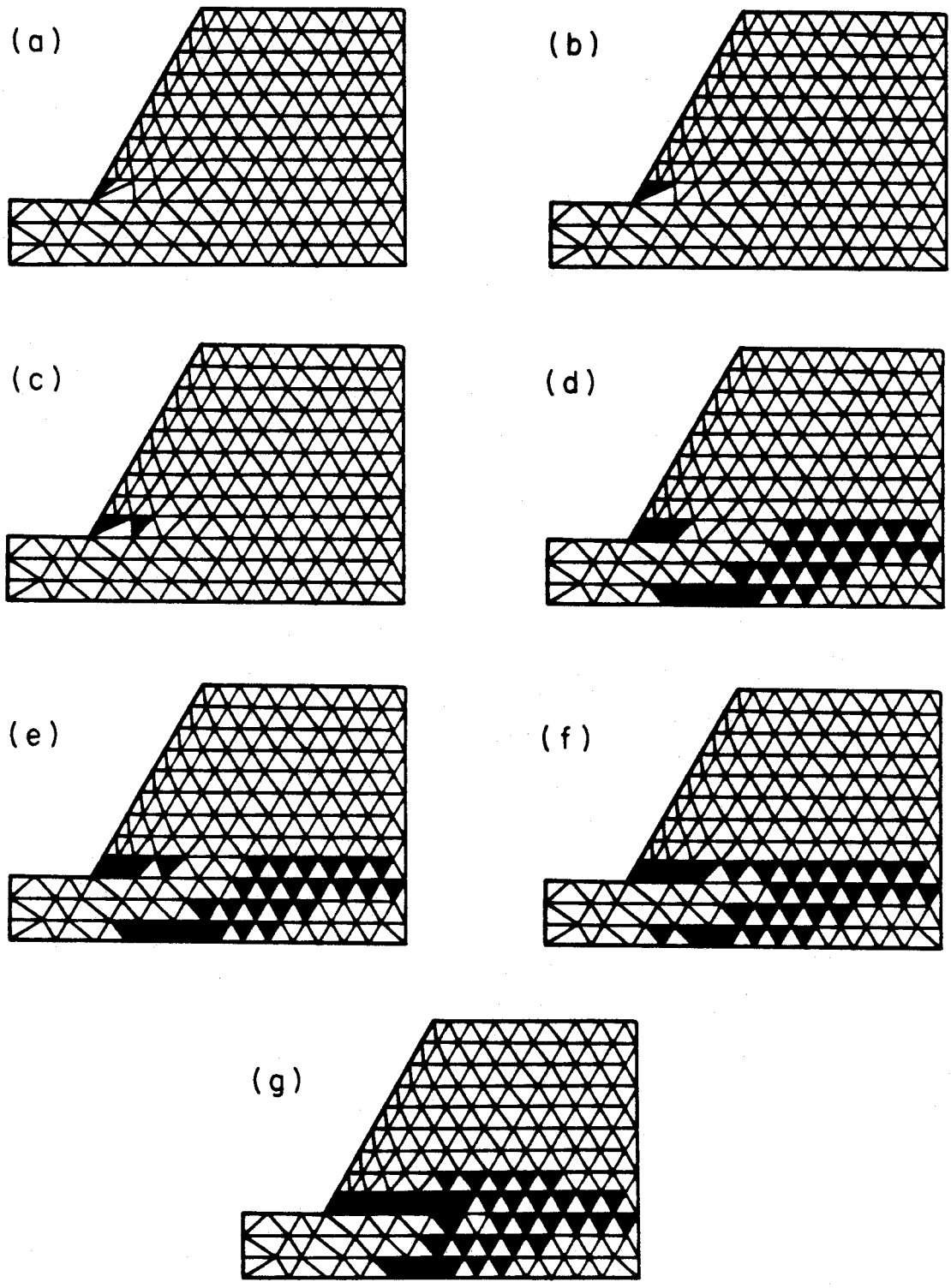

Figure 6.8 Development of "failure" with increasing gravity throughout triangular mesh of centrifuge slope specimen (a) 30*g* (b) 30*g* (c) 37*g* (d) 37*g* (e) 37*g* (f) 37*g* (g) 37*g*

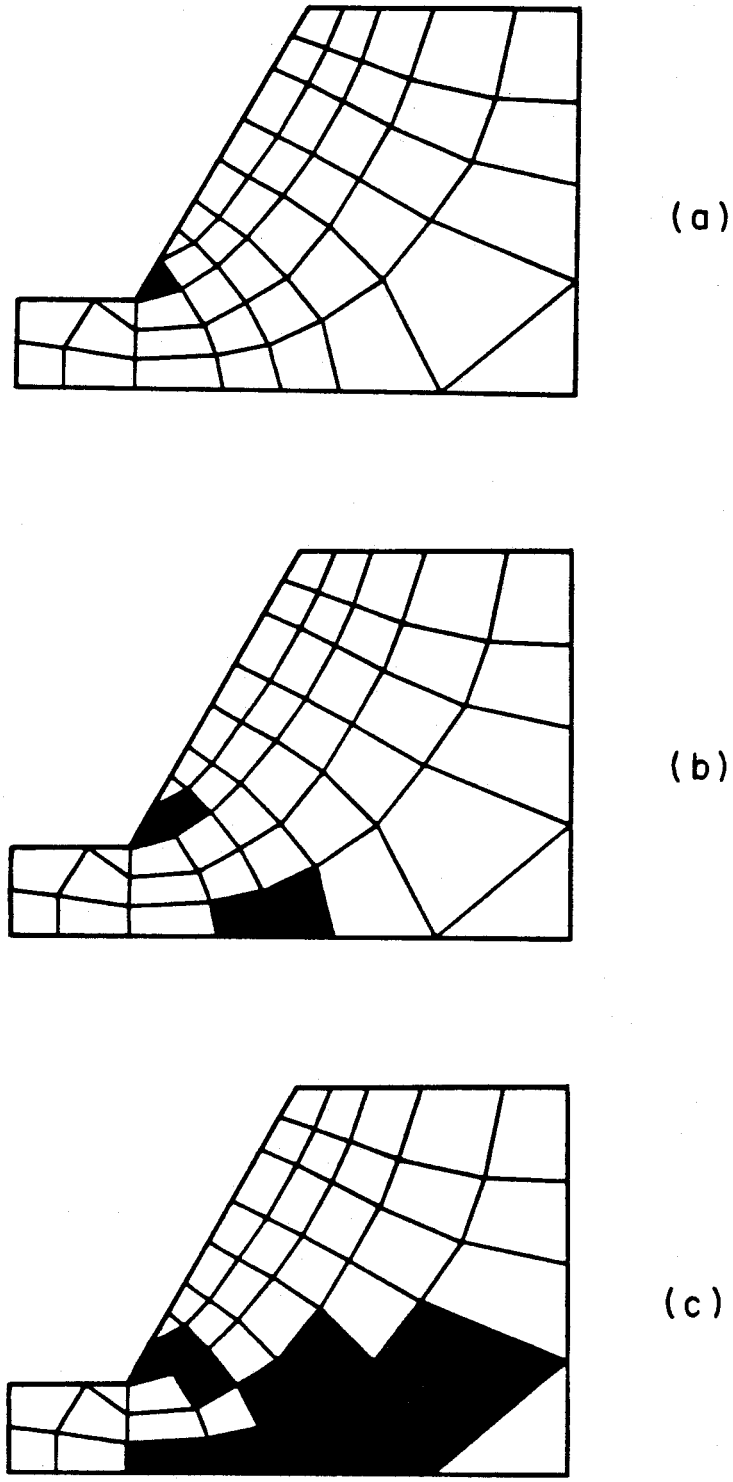

Figure 6.9 Development of "failure" with increasing gravity throughout "flow net" mesh of centrifuge slope specimen (a) 33*g* (b) 38*g* (c) 41*g*

Chapter 7

THE FINITE DIFFERENCE METHOD OF SLOPE STABILITY ANALYSIS

7.1 INTRODUCTION

After the unsuccessful attempts of Section 6.2 to force the finite element method to model slope failure (with or without fracture mechanics assistance), a finite difference program called CHIMP [100] was applied to the slope stability problem and found able to capture the mechanism of slope failure observed in the centrifuge experiments (see Section 8.3).

CHIMP (Caltech Homogeneous Isotropic Materials Program) was originally developed by Silling [101] as a tool for exploring large deformations of both compressible and incompressible elastic bodies, and employs an algorithm which corresponds closely to the general theory of finite elasticity (*e.g.*, [35,36]). The code was also designed to provide simultaneous local and global analysis of problems which may contain singularities, such as those arising in fracture mechanics. CHIMP's forte, however, is the study of boundary value problems involving loss of ellipticity, in which the underlying system of partial differential equations may change from elliptic to parabolic or hyperbolic within some local region of the problem

(*e.g.*, [50]). Such a change can occur, for example, during deformation of a certain type of material whose shear stress-shear strain curve has a downward-sloping limb (*e.g.*, [1]).

For any given boundary value problem, CHIMP introduces an artificial time variable into the field equations for the continuum and, for accuracy and efficiency of solution, uses a Lagrangian differencing scheme in space, and explicit integration in time with dynamic relaxation. All spatial derivatives are thus taken with respect to a fixed reference configuration which is typically unstressed and undeformed — an approach proven to be beneficial under conditions of large deformation. Dynamic relaxation (*e.g.*, [23,65,113]) is a technique which assumes an equilibrium solution can be found by an evolutionary path as the large-time limit of a damped dynamic problem. In addition to the time variable, this dynamic problem is artificial in the sense that fictitious masses are assigned to the finite difference zones and non-physical damping selected, purely on the basis of optimal stability and convergence of the numerical solution. In addition to the advantageous evolutionary nature of the final equilibrium solution, CHIMP's use of explicit time integration also eliminates the need for matrix operations of any kind.

CHIMP handles incompressible materials by an iterative pseudotemperature method which adjusts the hydrostatic pressure in each finite difference zone so that the net volume change tends to zero in the limit of large time. Since an incom-

pressibility constraint was not invoked in the analysis of slope stability presented here, a more detailed explanation of the pseudotemperature approach is given elsewhere by Silling [100]. Sections 7.2 and 7.3 below, which describe the main features of CHIMP, are also based on Silling's description of the finite difference algorithm [100].

7.2 FIELD EQUATIONS

As is usual in the mathematical formulation of boundary value problems (*e.g.*, [35,36,50]), consider some unstressed, undeformed reference configuration of the region of interest $\mathcal{R}$, and let $\mathbf{x}$ denote the location of any material particle in the reference configuration. Also consider a deformation $\hat{\mathbf{y}}$ that maps each point $\mathbf{x} \in \mathcal{R}$ to some point $\mathbf{y} \in \mathcal{R}^*$ where $\mathcal{R}^*$ denotes the deformed configuration or image of $\mathcal{R}$ under $\hat{\mathbf{y}}$. CHIMP's numerical method (see Section 7.3) is then based on following this deformation in time through the Lagrangian version of the dynamic local balance of linear momentum,

$$\nabla_{\mathbf{x}} \cdot \sigma(\mathbf{x}) + \mathbf{b}_0(\mathbf{x}) = \rho_0(\mathbf{x}) \frac{\partial^2 \hat{\mathbf{y}}(\mathbf{x})}{\partial t^2} \qquad \forall\, \mathbf{x} \in \mathcal{R} \;,\; t \in [t_1, t_2] \tag{7.1}$$

where σ is the *Piola stress tensor field*, $\mathbf{b}_0$ is the *Piola body force vector field* and ρ_0 is the *mass density field* (all in the reference configuration), and t is the *time* within some suitable interval $[t_1, t_2]$. Since time is introduced by CHIMP as an artificial variable, it is appropriate to emphasize that most other methods of analysis quite legitimately determine the equilibrium solution to the given boundary

value problem by solving the equation of *equilibrium*,

$$\nabla_{\mathbf{x}} \cdot \sigma(\mathbf{x}) + \mathbf{b}_0(\mathbf{x}) = \mathbf{0} \qquad \forall\, \mathbf{x} \in \mathcal{R} \quad , \tag{7.2}$$

which is the Lagrangian version and may be compared with the more common Eulerian version,

$$\nabla_{\mathbf{y}} \cdot \tau(\mathbf{y}) + \mathbf{b}(\mathbf{y}) = \mathbf{0} \qquad \forall\, \mathbf{y} \in \mathcal{R}^* \quad , \tag{7.3}$$

where τ is the familiar *Cauchy stress tensor field* and $\mathbf{b}$ is the *Cauchy body force vector field*. In the Lagrangian versions above, however, the divergence operator is taken with respect to the coordinates of the reference configuration, while the Eulerian version uses the coordinates of the deformed configuration.

It should also be noted at this point that while these equations are quite general, and appropriate for any three-dimensional boundary value problem, CHIMP specializes them by considering only two-dimensional plane strain deformations.

7.3 NUMERICAL METHOD

7.3.1 Spatial differencing

CHIMP uses the Green's theorem method (*e.g.*, [39]) for spatial differencing, performed with respect to the coordinates of the reference configuration $\mathcal{R}$, where the region of interest $\mathcal{R}$ is discretized into an $M \times N$ mesh of nodes, or grid points. Nodes are indexed by pairs of integers (i, j), $i = 1, 2, \ldots, M$; $j = 1, 2, \ldots, N$, and the quadrilateral region between each set of four adjacent nodes, called a *zone* (see

Figure 7.1), is labeled by half-integer indices $(i+\frac{1}{2}, j+\frac{1}{2})$. Each node (i,j) also has associated with it a fixed position vector $\mathbf{x}^{i,j}$ in the reference configuration.

Certain quantities called *node-centered* variables can then be identified with nodes, and others, called *zone-centered* variables, are identified with zones. Node-centered variables include position, velocity, acceleration, stress gradient, body force, and damping force, while zone-centered variables include stress tensor components, deformation gradient tensor components (and strain tensor components), and mass density. Both nodes and zones are also assigned an area, as described below.

If α denotes a component in the plane of consideration $(\alpha = 1,2)$, then the Green's theorem differencing method leads to the following approximations for the α component of $\nabla_{\mathbf{x}} \cdot \sigma$ at node (i,j) at time step n :

$$\frac{\partial \sigma_{\alpha 1}}{\partial x_1} + \frac{\partial \sigma_{\alpha 2}}{\partial x_2} \approx \left(\frac{\partial \sigma_{\alpha 1}}{\partial x_1}\right)^{i,j,n} + \left(\frac{\partial \sigma_{\alpha 2}}{\partial x_2}\right)^{i,j,n} \tag{7.4}$$

where

$$\begin{aligned}\left(\frac{\partial \sigma_{\alpha 1}}{\partial x_1}\right)^{i,j,n} = \frac{1}{2A^{i,j}} \Big\{ & \sigma_{\alpha 1}^{i+\frac{1}{2},j+\frac{1}{2},n} \left(x_2^{i,j+1} - x_2^{i+1,j}\right) + \\ & \sigma_{\alpha 1}^{i-\frac{1}{2},j+\frac{1}{2},n} \left(x_2^{i-1,j} - x_2^{i,j+1}\right) + \\ & \sigma_{\alpha 1}^{i-\frac{1}{2},j-\frac{1}{2},n} \left(x_2^{i,j-1} - x_2^{i-1,j}\right) + \\ & \sigma_{\alpha 1}^{i+\frac{1}{2},j-\frac{1}{2},n} \left(x_2^{i+1,j} - x_2^{i,j-1}\right) \Big\}\end{aligned} \tag{7.5a}$$

and

$$\left(\frac{\partial \sigma_{\alpha 2}}{\partial x_2}\right)^{i,j,n} = \frac{-1}{2A^{i,j}}\Big\{\sigma_{\alpha 2}^{i+\frac{1}{2},j+\frac{1}{2},n}(x_1^{i,j+1} - x_1^{i+1,j}) + \sigma_{\alpha 2}^{i-\frac{1}{2},j+\frac{1}{2},n}(x_1^{i-1,j} - x_1^{i,j+1}) + \sigma_{\alpha 2}^{i-\frac{1}{2},j-\frac{1}{2},n}(x_1^{i,j-1} - x_1^{i-1,j}) + \sigma_{\alpha 2}^{i+\frac{1}{2},j-\frac{1}{2},n}(x_1^{i+1,j} - x_1^{i,j-1})\Big\} \tag{7.5b}$$

and where $A^{i,j}$ is one-half the area of the shaded quadrilateral in Figure 7.2, given by

$$A^{i,j} = \frac{1}{4}\Big\{(x_2^{i-1,j} - x_2^{i+1,j})(x_1^{i,j+1} - x_1^{i,j-1}) - (x_1^{i-1,j} - x_1^{i+1,j})(x_2^{i,j+1} - x_2^{i,j-1})\Big\} \quad . \tag{7.6}$$

For a node lying on a boundary of the mesh, the areas and stress components of the missing zones (*i.e.*, outside the boundary) are set to zero in these difference formulas.

The difference formulas (7.5a) and (7.5b) are derived by applying Green's theorem to the quadrilateral region D enclosed by the curve C of Figure 7.2 such that

$$\int_D \frac{\partial \psi}{\partial x_1} = \oint_C \psi \, dx_2 \qquad \text{and} \qquad \int_D \frac{\partial \psi}{\partial x_2} = -\oint_C \psi \, dx_1 \tag{7.7}$$

where ψ is any sufficiently smooth field on D (in this case the components of stress σ).

The stress components $\sigma_{\alpha\beta}$ depend through the constitutive relation (see Section 7.4) on the deformation gradient tensor components $\partial y_\alpha / \partial x_\beta$ $(\beta = 1, 2)$,

whose components are evaluated by the following difference formulas:

$$\left(\frac{\partial y_\alpha}{\partial x_1}\right)^{i+\frac{1}{2},j+\frac{1}{2},n} = \frac{1}{2A^{i+\frac{1}{2},j+\frac{1}{2}}}\Big\{(x_2^{i,j+1} - x_2^{i+1,j})(y_\alpha^{i+1,j+1,n} - y_\alpha^{i,j,n}) - (x_2^{i+1,j+1} - x_2^{i,j})(y_\alpha^{i,j+1,n} - y_\alpha^{i+1,j,n})\Big\} \tag{7.8a}$$

$$\left(\frac{\partial y_\alpha}{\partial x_2}\right)^{i+\frac{1}{2},j+\frac{1}{2},n} = \frac{-1}{2A^{i+\frac{1}{2},j+\frac{1}{2}}}\Big\{(x_1^{i,j+1} - x_1^{i+1,j})(y_\alpha^{i+1,j+1,n} - y_\alpha^{i,j,n}) - (x_1^{i+1,j+1} - x_1^{i,j})(y_\alpha^{i,j+1,n} - y_\alpha^{i+1,j,n})\Big\}. \tag{7.8b}$$

The difference formulas (7.8a) and (7.8b) are derived by an analogy to Green's theorem similar to that used for the stress gradient formulas (7.5a) and (7.5b), in which the theorem is applied to a path around the edges of the zone (see Figure 7.1). The values of y_α on each edge are supplied by the average value along the edge, for example $(y_\alpha^{i,j} + y_\alpha^{i+1,j})/2$, and these average values have already been substituted to give (7.8a) and (7.8b) as shown.

7.3.2 Dynamic relaxation and differencing in time

As mentioned in Section 7.1, dynamic relaxation models the equilibrium solution to a static boundary value problem as the large-time limit of a damped dynamic problem, which CHIMP solves by introducing an artificial time variable. With time steps labeled by the index n (where $n = 0$ represents initial conditions), the discretized version of (7.1) for node (i,j) is multiplied through by $A^{i,j}$ and a mass-proportional viscous damping term introduced to give

$$\mathbf{f}_{\text{int}}^{i,j,n} + \mathbf{f}_{\text{body}}^{i,j,n} + \mathbf{f}_{\text{bdry}}^{i,j,n} = \mathbf{f}_{\text{tot}}^{i,j,n} = m_0^{i,j}\mathbf{a}^{i,j,n} + \xi m_0^{i,j}\mathbf{v}^{i,j,n} \quad . \tag{7.9}$$

Here the nodal force from internal stresses is given by

$$\mathbf{f}_{\text{int}}^{i,j,n} = A^{i,j} \left\{ \left(\frac{\partial \sigma_{\alpha 1}}{\partial x_1} \right)^{i,j,n} + \left(\frac{\partial \sigma_{\alpha 2}}{\partial x_2} \right)^{i,j,n} \right\} \quad , \tag{7.10}$$

evaluated using the difference formulas (7.5a) and (7.5b), while the nodal force from body forces is given by

$$\mathbf{f}_{\text{body}}^{i,j,n} = A^{i,j} \mathbf{b}_0^{i,j,n} \quad , \tag{7.11}$$

applied to the node as a ramp function in time as shown in Figure 7.3. The quantity $\mathbf{f}_{\text{bdry}}^{i,j,n}$ represents the nodal force from a possible traction field applied at the boundary and since a gravitationally loaded soil slope has no such traction field, this term is null and will not be considered further. The nodal mass $m_0^{i,j}$ is computed from the surrounding zone densities and areas by

$$m_0^{i,j} = \frac{1}{4} \left\{ (A\rho_0)^{i+\frac{1}{2},j+\frac{1}{2}} + (A\rho_0)^{i-\frac{1}{2},j+\frac{1}{2}} + (A\rho_0)^{i-\frac{1}{2},j-\frac{1}{2}} + (A\rho_0)^{i+\frac{1}{2},j-\frac{1}{2}} \right\} \tag{7.12}$$

and ξ is the damping coefficient for dynamic relaxation whose determination is discussed further below.

Dividing (7.9) through by $m_0^{i,j}$ and swapping sides gives

$$\mathbf{a}^{i,j,n} + \xi \mathbf{v}^{i,j,n} = \frac{\mathbf{f}_{\text{tot}}^{i,j,n}}{m_0^{i,j}} \quad , \tag{7.13}$$

into which the following central difference approximations for acceleration and velocity may be substituted:

$$\mathbf{a}^{i,j,n} = (\mathbf{v}^{i,j,n+\frac{1}{2}} - \mathbf{v}^{i,j,n-\frac{1}{2}})/h^n \tag{7.14}$$

and

$$\mathbf{v}^{i,j,n} = \frac{1}{2}(\mathbf{v}^{i,j,n+\frac{1}{2}} + \mathbf{v}^{i,j,n-\frac{1}{2}}) \quad , \tag{7.15}$$

where

$$\mathbf{v}^{i,j,n+\frac{1}{2}} = (\mathbf{y}^{i,j,n+1} - \mathbf{y}^{i,j,n})/h^{n+\frac{1}{2}} \tag{7.16a}$$

and

$$\mathbf{v}^{i,j,n-\frac{1}{2}} = (\mathbf{y}^{i,j,n} - \mathbf{y}^{i,j,n-1})/h^{n-\frac{1}{2}} \quad . \tag{7.16b}$$

In the above expressions, h^n and $h^{n+\frac{1}{2}}$ are the time steps, related by

$$h^n = \frac{1}{2}(h^{n-\frac{1}{2}} + h^{n+\frac{1}{2}}) \quad , \tag{7.17}$$

where $h^{n+\frac{1}{2}}$ is computed from (7.24) below, and $h^{n-\frac{1}{2}}$ represents $h^{n+\frac{1}{2}}$ from the previous time step. With these approximations, (7.13) becomes

$$\frac{\mathbf{v}^{i,j,n+\frac{1}{2}} - \mathbf{v}^{i,j,n-\frac{1}{2}}}{h^n} + \frac{\xi}{2}(\mathbf{v}^{i,j,n+\frac{1}{2}} + \mathbf{v}^{i,j,n-\frac{1}{2}}) = \frac{\mathbf{f}_{\rm tot}^{i,j,n}}{m_0^{i,j}} \quad . \tag{7.18}$$

Multiplying through by h^n and rearranging gives

$$\left(1 + \frac{\xi h^n}{2}\right)\mathbf{v}^{i,j,n+\frac{1}{2}} - \left(1 - \frac{\xi h^n}{2}\right)\mathbf{v}^{i,j,n-\frac{1}{2}} = \frac{\mathbf{f}_{\rm tot}^{i,j,n} h^n}{m_0^{i,j}} \quad , \tag{7.19}$$

and solving for $\mathbf{v}^{i,j,n+\frac{1}{2}}$ yields

$$\mathbf{v}^{i,j,n+\frac{1}{2}} = \frac{1}{1+\eta}\left\{(1-\eta)\mathbf{v}^{i,j,n-\frac{1}{2}} + \frac{\mathbf{f}_{\rm tot}^{i,j,n} h^n}{m_0^{i,j}}\right\} \tag{7.20}$$

where $\eta = \xi h^n/2$ and h^n is given by (7.17). In practice, CHIMP uses $h^{n+\frac{1}{2}}$ instead of h^n in the expression for η so that

$$\eta = \frac{\xi h^{n+\frac{1}{2}}}{2} \quad , \tag{7.21}$$

and the new position of node (i,j) is finally given by

$$\mathbf{y}^{i,j,n+1} = \mathbf{y}^{i,j,n} + \mathbf{v}^{i,j,n+\frac{1}{2}} h^{n+\frac{1}{2}} \tag{7.22}$$

from (7.16a). Note that the difference representation (7.9), and consequently (7.20) and (7.22), is an explicit differencing scheme, since $\mathbf{y}^{i,j,n+1}$ depends only on quantities which are known for the time step n.

The numerical stability condition for the time integration method (7.9) can be shown (*e.g.*, [113]) to be identical to that of the undamped explicit central differencing method:

$$h^{n+\frac{1}{2}} \leq 2/\omega_{\max} \tag{7.23}$$

where $\omega_{\max}$ is the highest natural angular frequency of the undamped mesh, and may be conservatively estimated using the local speed of infinitesimal waves, leading to

$$h^{n+\frac{1}{2}} \leq \min_{\mathcal{R}} \{\epsilon/c\}^{i+\frac{1}{2},j+\frac{1}{2},n} \quad . \tag{7.24}$$

Here ϵ is the zone width, equal to the minimum of the lengths of the zone edges and diagonals, and c is the local speed in the reference configuration of whatever type of infinitesimal wave moves fastest. Details of the calculation of c are presented in Appendix A.

For quickest approach to the equilibrium solution, the damping coefficient ξ is chosen to provide critical damping of the fundamental mode of the mesh, and although various methods have been proposed for estimating this value of ξ

(*e.g.*, [70]), CHIMP chooses it by crudely estimating the fundamental frequency of the grid from the approximate transit time for infinitesimal waves through the entire width of the mesh. This leads to the estimate

$$\xi \approx \frac{\pi \bar{c}}{2L} \tag{7.25}$$

where $\bar{c}$ is the area-average wave speed in the mesh and L is a characteristic length.

On the assumption of a uniform wave speed throughout the mesh, the stability condition (7.24) would determine the time step from the smallest zone size ϵ, and since ϵ may vary over orders of magnitude through the mesh, (7.24) would severely limit CHIMP's efficiency. It is possible, however, to manipulate the local wave speeds through the mass density ρ_0, since c is proportional to $1/\sqrt{\rho_0}$ for a given constitutive relation and may consequently be set to any desired value by adjusting the local density. CHIMP therefore finds a density distribution which makes the stable time steps for all zones equal and, if necessary, will change this distribution at intermediate stages of the solution to reflect sometimes large changes in local wave speeds. Since the *equilibrium* equations (7.2) or (7.3) do not contain a mass density term, these adjustments can be made arbitrarily, without affecting the asymptotic solution to the artificially dynamic equation (7.1) for local balance of linear momentum.

7.3.3 Boundary conditions

CHIMP imposes *position* boundary conditions, of the form

$$\hat{\mathbf{y}} = \mathbf{Y} \qquad \text{on } \partial\mathcal{R} \tag{7.26}$$

where $\mathbf{Y}$ is a given vector field and $\partial\mathcal{R}$ denotes the boundary of $\mathcal{R}$, by setting

$$\mathbf{y}^{i,j,n} = \mathbf{Y}(\mathbf{x}^{i,j}, t^n) \tag{7.27}$$

for any node (i,j) on the position boundary, where t^n is the time at time step n. In the case of a lubricated wall boundary, the motion of a node on the wall is computed at each time step as though the wall were a *free surface* or zero-traction boundary, with the displacement, velocity, and acceleration components normal to the wall immediately reset to zero.

The manner in which CHIMP imposes non-zero traction boundary conditions is discussed elsewhere [100] since the modeling of a gravitationally loaded soil slope requires no such condition.

7.4 SOIL MODEL

7.4.1 Introduction

The original CHIMP code was used to study large deformations of both compressible and incompressible materials and hence incorporated a constitutive relation which allowed for finite strains. For the present analysis of slope stability,

however, the constitutive model was limited to small strains of an inhomogeneous, isotropic soil on the basis of experimental observations made during the centrifuge slope failure tests. In particular, each centrifuge slope failure was characterized by the development of a very narrow shear zone or failure surface which separated the slope into two large blocks, with strains in the blocks being small and deformation being almost entirely limited to the narrow shear zone between them. Furthermore, when the failure surface had propagated fully through the slope and the two blocks were about to start sliding past each other, the strains even within the narrow shear zone were still small. Since it is only the development of the failure surface and its resulting geometry, and not the subsequent sliding of the separated blocks which the CHIMP calculation models, the small strain assumption for the slope soil is considered valid and realistic.

Inhomogeneity was introduced into the CHIMP soil model by specifying that the soil stiffness increase linearly with confining pressure and hence depth for a slope under gravitational loading. This degree of complexity (and reality) was added after homogeneous soil gave rise to yielding at the bottom right-hand corner of the slope mesh (similar to the finite element results of Figure 6.5) and prevented the analytical slope from developing a failure surface similar to those observed in the centrifuge tests. Yielding of this nature is to be expected in a material of uniform shear strength, for reasons already given in Section 6.1.

Inelastic strain unloading was also added to the CHIMP soil model to better

describe real soil behavior and is described in more detail below.

7.4.2 Constitutive relation

The constitutive relation used by CHIMP to represent the slope soil may be classified as a strain-space model, whereby the stresses are computed from the strains. This is in contrast to stress-space models which compute strains from stresses, and typically require an incremental approach to handle nonlinear stress-strain relations [61]. CHIMP requires no such incremental formulation, however, since the strain-space model uniquely defines the stress for any given strain, except for strain unloading which will be discussed later.

More specifically, CHIMP's constitutive law for the slope material is given in terms of a trilinear relationship between the radius of the Mohr's circle of stress τ_M and the radius of the Mohr's circle of strain ϵ_M as shown in Figure 7.4, where ϵ_{M1} , ϵ_{M2} and τ_R are specified soil constants. In order to be able to use this strain-space relation, CHIMP finds ϵ_M from the expression

$$\epsilon_M = \sqrt{e_{12}^2 + \left(e_{11} - \frac{\theta}{2}\right)^2} \tag{7.28}$$

where e_{11} and e_{12} are the plane strain components of the familiar linearized *Lagrangian strain tensor*, and θ is the *dilatation* or *volumetric strain*. To evaluate (7.28), however, the strain components $e_{\alpha\beta}$ must first be computed from the deformation gradients $y_{\alpha,\beta}$ of (7.8a) and (7.8b) according to the relation

$$e_{\alpha\beta} = \frac{1}{2}(y_{\alpha,\beta} + y_{\beta,\alpha}) - \delta_{\alpha\beta} \tag{7.29}$$

where $\delta_{\alpha\beta}$ is the Kronecker delta, and the dilatation θ can then be found from

$$\theta = e_{\gamma\gamma} \quad . \tag{7.30}$$

It may also be noted in passing that the CHIMP "shear strain" ϵ_M differs from the principal engineering shear strain γ_s of Figure 6.5 used for the earlier attempts at improved slope stability analysis.

The slope (*i.e.*, shear stiffness or shear modulus) of limb A of the τ_M versus ϵ_M curve of Figure 7.4 is defined by

$$S = S_1 + S_2 p \tag{7.31}$$

where p is the confining pressure, and S_1 and S_2 are specified soil constants. Since p is normally defined in terms of stresses as

$$p = \frac{1}{3}\sigma_{kk} \quad , \tag{7.32}$$

and the stresses are still unknown at this stage of the calculation, an expression for p must be found in terms of the already known strains.

To this end, the slope material is first assumed to be compressible with constant Poisson's ratio ν. Hence the bulk modulus or volumetric stiffness K of the soil is directly proportional to the shear modulus S such that

$$K = f_\nu S = f_\nu (S_1 + S_2 p) \quad , \tag{7.33}$$

where f_ν is a constant given by

$$f_\nu = \frac{2(1+\nu)}{3(1-2\nu)} \tag{7.34}$$

and (7.31) has been used in the substitution for S. The confining pressure p is also given by

$$p = -K\theta \tag{7.35}$$

where negative dilatation θ (*i.e.*, compression) induces positive confining pressure p. Combining (7.33) and (7.35), and solving for K gives

$$K = \frac{f_\nu S_1}{1 + f_\nu S_2 \theta} \tag{7.36}$$

which, when substituted into (7.35) yields

$$p = \frac{-f_\nu S_1 \theta}{1 + f_\nu S_2 \theta} \quad . \tag{7.37}$$

This is the required expression for the confining pressure p in terms of the known strains, to be used in (7.31) to completely define the stress-strain relation of Figure 7.4.

Given ϵ_M as computed in (7.28), CHIMP enters the stress-strain relation to find the corresponding τ_M (*e.g.*, point Q of Figure 7.4), and computes an effective shear modulus S_{eff} given by

$$S_{\text{eff}} = \frac{\tau_M}{\epsilon_M} = \mu^* \tag{7.38}$$

where μ^* is one of two modified Lamé constants. The other modified Lamé constant λ^* is given by

$$\lambda^* = K - \frac{2}{3}\mu^* \tag{7.39}$$

where K and μ^* come from (7.36) and (7.38) respectively. Given λ^* and μ^*, CHIMP then computes the components of the stress tensor from

$$\begin{aligned} \sigma_{\alpha\beta} &= \lambda^* \delta_{\alpha\beta} e_{\gamma\gamma} + 2\mu^* e_{\alpha\beta} \\ &= \lambda^* \delta_{\alpha\beta} \theta + 2\mu^* e_{\alpha\beta} \end{aligned} \tag{7.40}$$

where θ is given by (7.30) and the $e_{\alpha\beta}$ come from (7.29).

Inelastic strain unloading is handled by tracking the maximum ϵ_M reached in each zone. Should ϵ_M in a subsequent time step fall below this maximum, unloading of the zone takes place along limb B of Figure 7.4 with slope S given by (7.31). Reloading follows the same limb until the maximum ϵ_M (at which unloading took place) is reached, and further loading follows the original trilinear stress-strain curve.

7.5 SUMMARY OF SOLUTION CYCLE

For each time step, CHIMP steps through the finite-difference mesh finding the new position of each node in succession, given the internal stress state and applied loading.

Assume that CHIMP is computing the nodal positions for time step n and has got to node (i,j) of the mesh. CHIMP now wishes to solve (7.9) at node (i,j). It starts by computing the total force on the node given by the right-hand side of (7.9). The force from the internal stresses is given by (7.10) and evaluated using the difference formulas (7.5a) and (7.5b). The force from the body force

field is given by (7.11) and its magnitude is determined by the time at time step n through the ramp function of Figure 7.3. The force from the traction field is zero since there is no traction field for the slope stability problem considered here — all applied loading comes from body forces alone. With the total force on node (i,j) now computed, (7.9) is actually solved via (7.20). The nodal mass is given by (7.12), h^n comes from (7.17), and $\mathrm{v}^{n-\frac{1}{2}}$ is known from the previous time step. Note that $h^{n+\frac{1}{2}}$ is computed from (7.24), and $h^{n-\frac{1}{2}}$ is the previous time step's $h^{n+\frac{1}{2}}$. The new position of node (i,j) is then given by (7.22). CHIMP next finds the components of the deformation gradient tensor using (7.8a) and (7.8b), and immediately computes the components of the Lagrangian strain tensor from (7.29). The radius of the Mohr's circle of strain is determined from (7.28) and (7.30), which in turn gives the radius of the Mohr's circle of stress through the constitutive relation of Figure 7.4. Knowing the modified Lamé constants from (7.38), (7.39) and (7.36), the components of the stress tensor can be found from (7.40) and the cycle is complete.

CHIMP is then ready to move to the next node of the mesh and repeat the cycle. After computing the new position of each node of the mesh for time step n, CHIMP starts all over again and finds the new nodal positions for time step $n+1$.

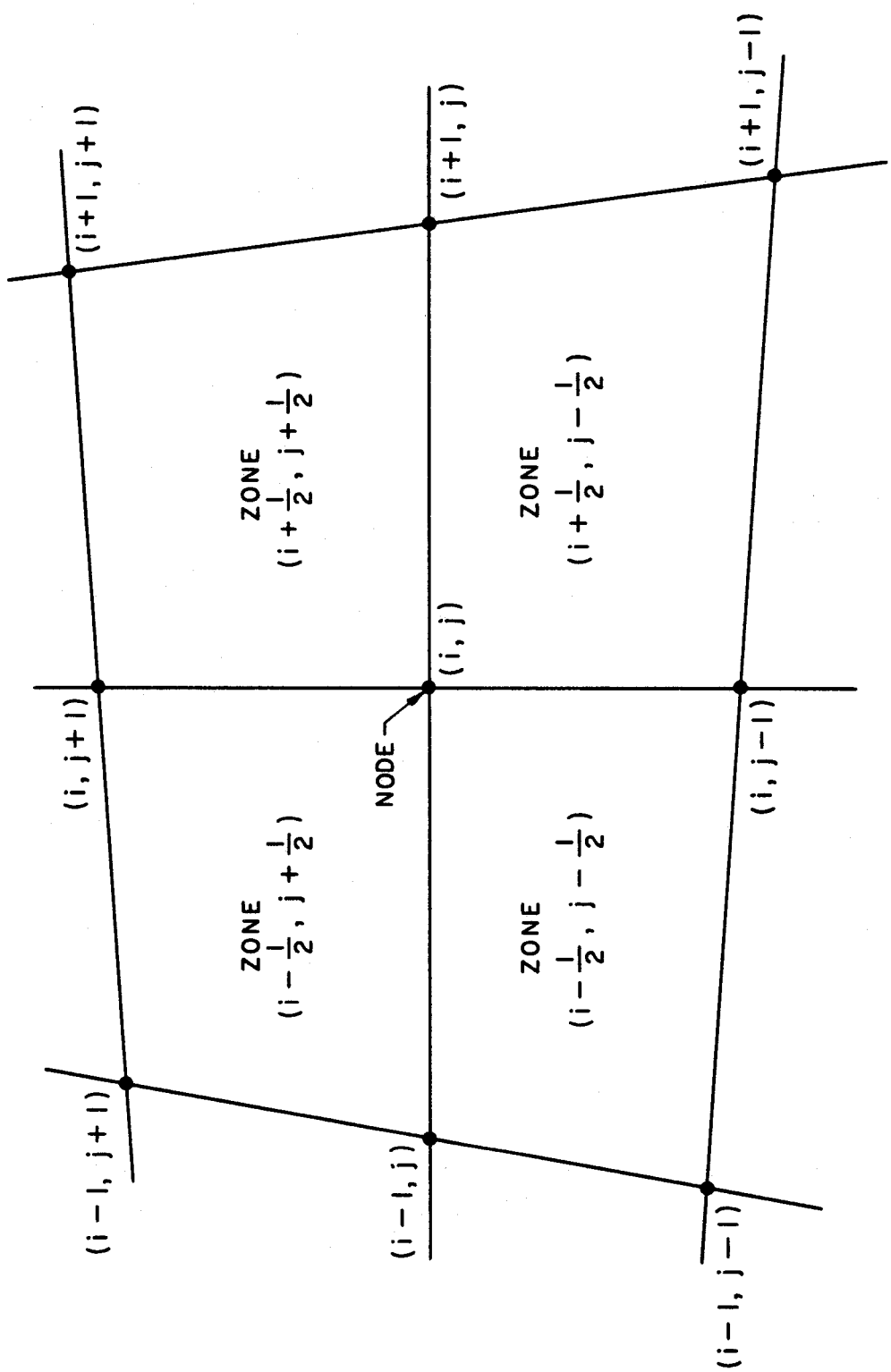

Figure 7.1 Labeling of nodes and zones

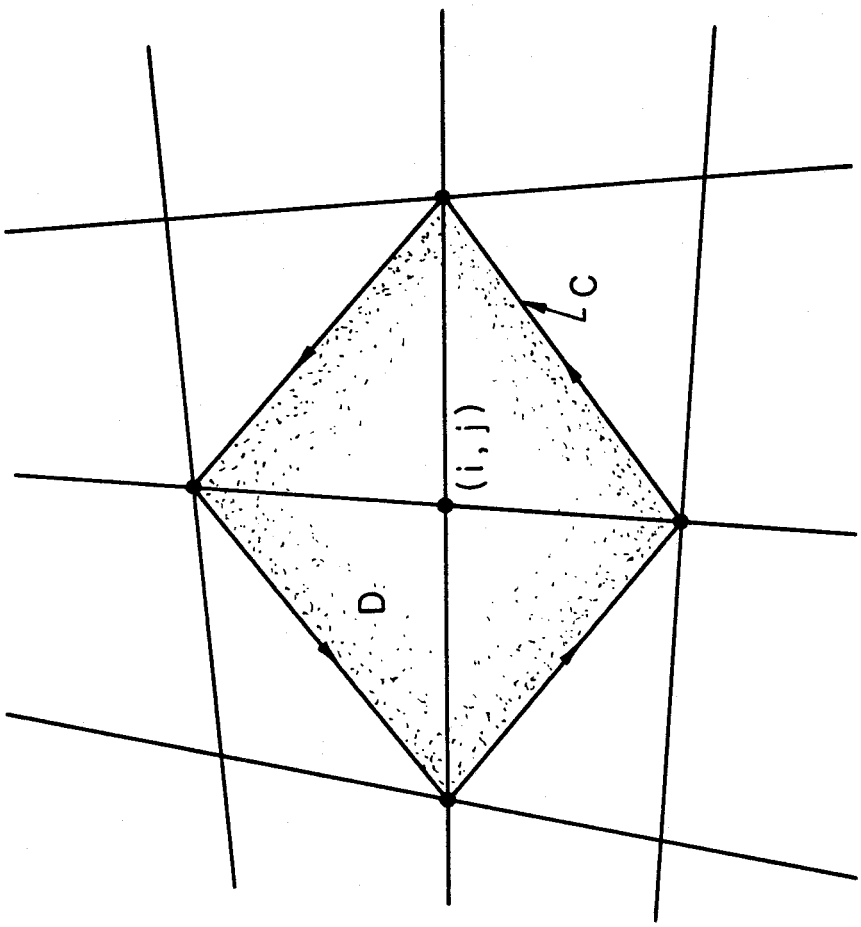

Figure 7.2 Integration path used in Green's theorem method for differencing stress gradient components

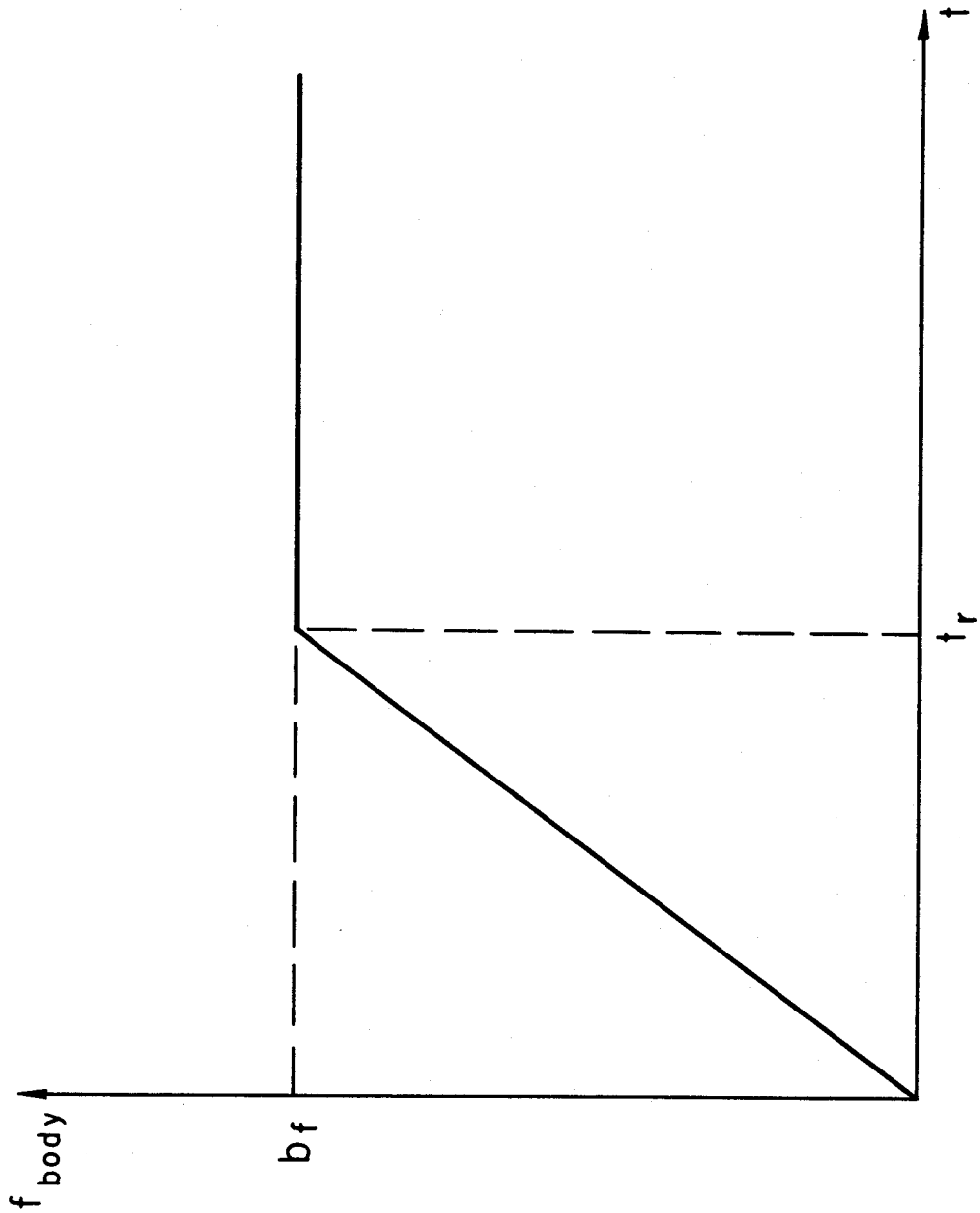

Figure 7.3 Relation between body force magnitude and time

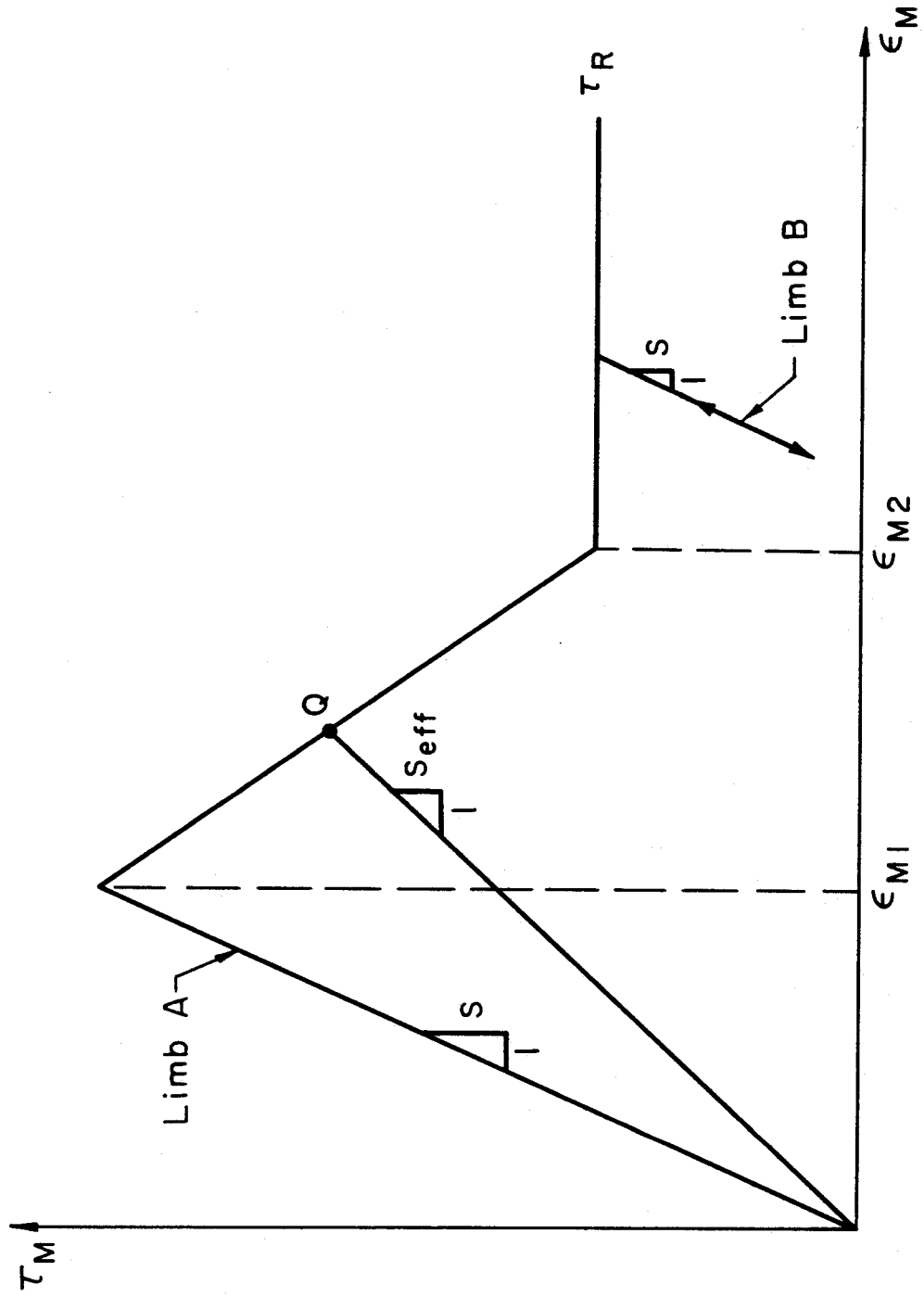

Figure 7.4 Constitutive relation between radius of Mohr's circle of stress τ_M and radius of Mohr's circle of strain ϵ_M

Chapter 8

FINITE DIFFERENCE RESULTS

8.1 INTRODUCTION

The finite difference method described in Chapter 7 was used to solve two independent plane strain boundary value problems. The first was a displacement-controlled bar compression test, and the second a centrifuge slope failure experiment. The bar compression results are presented in Section 8.2 while the centrifuge slope stability analysis appears in Section 8.3. The bar compression problem was simply a calibration test for the finite difference algorithm, to see if it could predict localization of deformation into shear bands without "seeding" by weak zones or boundary imperfections. The algorithm was then applied to the centrifuge slope stability problem. The solutions for both problems were based on the soil model represented in Figure 7.4, with *inelastic* strain unloading, although, in fact, these solutions were indistinguishable from those using reversible unloading.

8.2 BAR COMPRESSION

The displacement-controlled compression of a homogeneous, isotropic bar between two rigid parallel plates is represented in Figure 8.1(a) where one quarter of

the bar is modeled due to biaxial symmetry (see Figure 8.3). Figures 8.1(b) and (c) give the details of the bar's constitutive relation and displacement-controlled loading respectively. The finite difference results at successive stages of the solution are presented in Figure 8.2. The dot pattern of Figures 8.2(a) through (c) shows where the strain level has exceeded yield (1×10^{-4} in Figure 8.1(b)) and hence where shear failure is occurring. The density of dots is directly proportional to strain level so that the higher the strain, the greater the dot density. Figures 8.2(d) through (e) show the exaggerated deformed finite difference mesh corresponding to Figures 8.2(a) through (c) respectively.

Figure 8.2 shows how shear failure first occurs at the outside corner of the specimen, where the rigid end plate meets the free surface boundary. From there, failure propagates in a straight line across the specimen to the opposite free surface boundary, as shown in Figure 8.3 where the quarter specimen of Figure 8.2 has been used to infer the development of shear bands throughout the entire bar compression specimen. This same sequence and geometry of shear band development is observed in bar compression experiments on soils and metals. The finite difference algorithm thus demonstrates an ability to predict localization of shear deformation without "seeding" by artificial weak zones or boundary imperfections, and in a manner independent of the orientation of zones within the mesh. These conclusions are supported and reinforced by the centrifuge slope stability results of Section 8.3.

8.3 CENTRIFUGE SLOPE STABILITY

The centrifuge slope stability problem posed to the finite difference method is summarized in Figure 8.4, where the dimensions and geometry of the slope mesh of Figure 8.4(a) approximate those of the centrifuge slope specimens (see Figure 2.9), except for the omission of approximately 140 mm of material from the crest end of the real centrifuge specimen to reduce the size of the finite difference mesh. Figure 8.4(b) is the idealized, but experimentally based constitutive relation of Sections 3.3.3 and 7.4, representing the real centrifuge slope material. Figure 8.4(c) gives the details of the applied body force loading, where the ramp time and body force magnitude are chosen by a combination of judgment and trial and error to ensure computational stability and material failure in the numerical solution. The goal of the slope stability analysis was to examine the sequence and geometry of failure in the numerical solution to compare with that observed in the centrifuge slope tests, and, in the results which follow, it is to be noted that the elapsed time (in seconds) given for a particular stage of the numerical solution, is artificial and for comparison with the ramp time of body force loading only.

Figure 8.5 presents the sequence of finite difference results for the problem posed in Figure 8.4, where the solutions shown in Figures 8.5(a), (b) and (c) all occur at times greater than the ramp time of Figure 8.4(c). The sequence clearly shows how failure develops at the toe of the slope (Figure 8.5(a)) and propagates to the crest in a narrow shear zone (Figures 8.5(b) and (c)), as generally observed

in the centrifuge experiments. The failure sequence of Figure 8.5, however, is not identical to the experimentally observed sequence of Figure 5.34, even though the final geometry represented by the dot pattern of Figure 8.5(c) is a good fit to the post-failure profile of slope test 16b (reproduced in Figure 8.6(b)). In particular, the failure surface of Figure 8.5 shows no tendency to propagate toward the slope face before heading for the slope crest. As discussed in Section 5.4, the observed intersection of the failure surface with the slope face during the centrifuge tests may have been caused by an inhomogeneous slope specimen with high crest block strength, in which case the absence of slope face intersection by the failure surface of Figure 8.5 is appropriate. If, however, the slope failure mechanism of Figure 5.34 is correct in every detail, then the finite difference results have not recorded the true failure sequence, and cannot be expected to do so on the following grounds. As the propagating failure surface turns toward the slope face from the point where the two are parallel, the deformation at the leading edge of the failure surface changes from predominantly shear to one of predominantly tension as the now free toe region begins to pull away from the slope mass further up the face under gravity. Since the soil model of the finite difference method contains only a shear failure criterion and no provision for tensile failure, the numerical results will not be sensitive to this change in the nature of deformation as the failure surface propagates toward the slope face.

The $612g$ loading of Figure 8.4(c), which generated the results of Figure 8.5,

is also an order of magnitude greater than that required to fail any of the slope specimens tested in the centrifuge. As discussed later in this section, however, the numerical slope model shown in Figure 8.4(a) will still fail under a reduced gravity load of $320g$, and, with finer finite difference meshes, the failure load can be further reduced to a lower limit of between $100g$ and $150g$.

A more direct comparison of slope failure analysis and experiment is presented in Figure 8.6. Figure 8.6(a) is a reproduction of Figure 8.5(c) with the addition of the critical circular failure surfaces of a traditional Taylor analysis [107] for soil friction angles of $\phi = 16.7°$ and $\phi = 35°$ [92]. Figure 8.6(b) is the failure surface geometry observed after the slope collapse of centrifuge test 16b. Slope failure is estimated to occur at $57g$ for the $\phi = 16.7°$ Taylor circle and at $128g$ for the $\phi = 35°$ Taylor circle. Slope specimen 16 actually collapsed at $82g$ in centrifuge test 16b (see Table 5.1).

As previously discussed, the finite difference dot pattern of Figure 8.6(a) is a good fit to the final experimental profile of Figure 8.6(b) although the body force loading of the finite difference solution is an order of magnitude greater than that required for actual slope failure. The $\phi = 35°$ Taylor circle is similarly a reasonable approximation to the failure surface of Figure 8.6(b) but also overestimates the gravity load necessary for failure. Describing the centrifuge slope material as having a friction angle of $35°$, however, is considered inappropriate, as discussed in Section 3.4. The $\phi = 16.7°$ Taylor circle is based on a better soil description

and best predicts the failure gravity level, but its geometry is a poor approximation to the observed failure surface profile. In contrast to the finite difference results, and as discussed in Section 1.2.1, the Taylor limit equilibrium circles do not yield any information on the sequence of events constituting the mechanism of slope failure.

A number of slope stability analyses was made with the finite difference algorithm by varying the constitutive and loading parameters of the centrifuge slope model of Figure 8.4. The variation of shear modulus with confining pressure, however, given by $S = 20 + 300p$ MPa and representing a cohesive granular soil with a friction angle of $\phi = 16.7°$ as discussed in Section 3.3.3, remained unchanged. The sensitivity of the finite difference model to some of these stress-strain and body force variations can be seen in the results below.

To investigate the effect of increasing the rate of post-yield strain weakening on the predicted failure surface, ϵ_{M2} of Figure 8.4(b) was reduced to 2×10^{-3} from 4×10^{-3} to produce the results of Figure 8.7. The other numerical parameters given in Figure 8.4 were not altered. Comparison of Figure 8.7 with Figure 8.5 shows the two failure sequences to be almost identical although Figure 8.7 shows a slightly better defined failure surface after fewer computational time steps. The final geometry of Figure 8.7(c) is also more vertical near the slope crest than Figure 8.5(c) and hence an even better fit to the experimental post-failure profile of Figure 8.6(b).

The sensitivity of the finite difference model to the magnitude of body force loading was then determined by reducing the gravity level of Figure 8.4(c) from $612g$ to $340g$, $320g$ and $300g$, with only the $340g$ analysis being illustrated here. The $340g$ results for the constitutive relation of Figure 8.4(b) (with $\epsilon_{M2} = 2 \times 10^{-3}$) are presented in Figure 8.8, where significantly greater computational effort than that for the results of Figure 8.5 is required to capture the propagation of a shallower failure surface through the slope mesh. With further reduction to $320g$ (not illustrated), 4500 time steps (2529 seconds) were required to generate a dot pattern almost identical to Figure 8.8(c), and at $300g$, failure could not be propagated away from the toe of the slope, even after 3500 time steps (2041 seconds). Hence the gravity loading threshold for failure of the centrifuge slope model of Figure 8.4(a) by the finite difference method is a well-defined one at approximately $320g$, below which the failure surface will not propagate. Although a body force of $320g$ is still half an order of magnitude greater than that required for slope failure in any of the centrifuge experiments, it does provide analytical evidence to refute the gradually progressive nature of the slope failure mechanism postulated in Figure 1.3 and explain the absence of such progressive failure from the 35 mm in-flight photos taken at $5g$ increments during the centrifuge tests (see Section 5.4).

Finite difference meshes coarser *and* finer than Figure 8.4(a) were also studied briefly, and were found to strongly affect the gravity loading threshold for failure,

as summarized in Table 8.1. These results suggest a lower limit on the failure load of between $100g$ and $150g$ as the finite difference mesh is made extremely fine. This final discrepancy of approximately $50g$ between analysis and experiment is attributed to tension cracks in the centrifuge specimens, which extend from the horizontal surface behind the slope crest to deep within the slope mass, and allow centrifuge slope failure to take place at gravity loads well below those predicted by the finite difference method. These tension cracks are seen to be present in the impulsively failed slope specimens, where they may be accentuated by the dynamics of collapse (*e.g.*, slope test 17 of Section 5.1.5), but are also believed to be present in the slope specimens which collapse under static loading alone, even though they cannot be seen under these conditions. As the centrifuge spins up to the gravity level at which slope collapse occurs naturally or is impulsively induced, the tension cracks form within the specimen because a rigid vertical boundary condition is inadequately maintained behind the crest of the slope by the cohesionless sand compacted into the gap between the cemented slope specimen and the aluminum wall of the test container. This explanation is based on a two-dimensional, linearly elastic finite element analysis of the centrifuge slope specimen, with a free vertical boundary behind the slope crest, which indicates the occurrence of tension to a depth of approximately two-thirds of the slope height below the crest surface.

Since the triaxial test results of Section 3.3.2 on the centrifuge slope material

showed wide variation in Poisson's ratio, the effect of ν on the mechanism of slope failure was also investigated with the finite difference algorithm and illustrative results are presented in Figures 8.9 and 8.10. In contrast to Figures 8.5, 8.7 and 8.8, in which $\nu = 0.45$, Figures 8.9 and 8.10 were generated with $\nu = 0.3$, $\epsilon_{M2} = 2 \times 10^{-3}$ (Figure 8.4(b)), and a body force equivalent to $340g$. The sequence of Figure 8.9 shows a very different failure mechanism from that seen in the centrifuge experiments. Although the centrifuge slope failures seem best modeled with $\nu = 0.45$, the mechanism of Figure 8.9 may be realistic for a $\nu = 0.3$ material. Indeed, the exaggerated deformed finite difference mesh of Figure 8.10(b), which corresponds to the dot pattern of Figure 8.9(c), shows clear evidence of the toe bulging often observed in full-scale slope failures.

Although the advantage of the finite difference method, as described in Chapter 7, is its ability to handle the unstable material behavior of Figures 7.4 and 8.4(b) without numerical instability, it seemed appropriate to determine the effect of an elastic–perfectly plastic constitutive relation on the slope failure mechanism, using the same finite difference code, since soil is often represented by such a stress-strain law in mathematical models. With $\nu = 0.3$, body force loading of $340g$, and the soil model of Figure 8.11(a), the finite difference algorithm then gave rise to the shear distribution of Figure 8.11(b). The dot pattern of Figure 8.11(b) is very similar to the general spreading of failure in finite element solutions, described in Section 6.2.2 *and* exhibited by other finite element results (*e.g.*, [54,105]). Such

absence of localized deformation appears to be the direct consequence of a stable elastic–perfectly plastic constitutive relation since the unstable material behavior of Figure 8.4(b) leads to highly localized zones of shear failure.

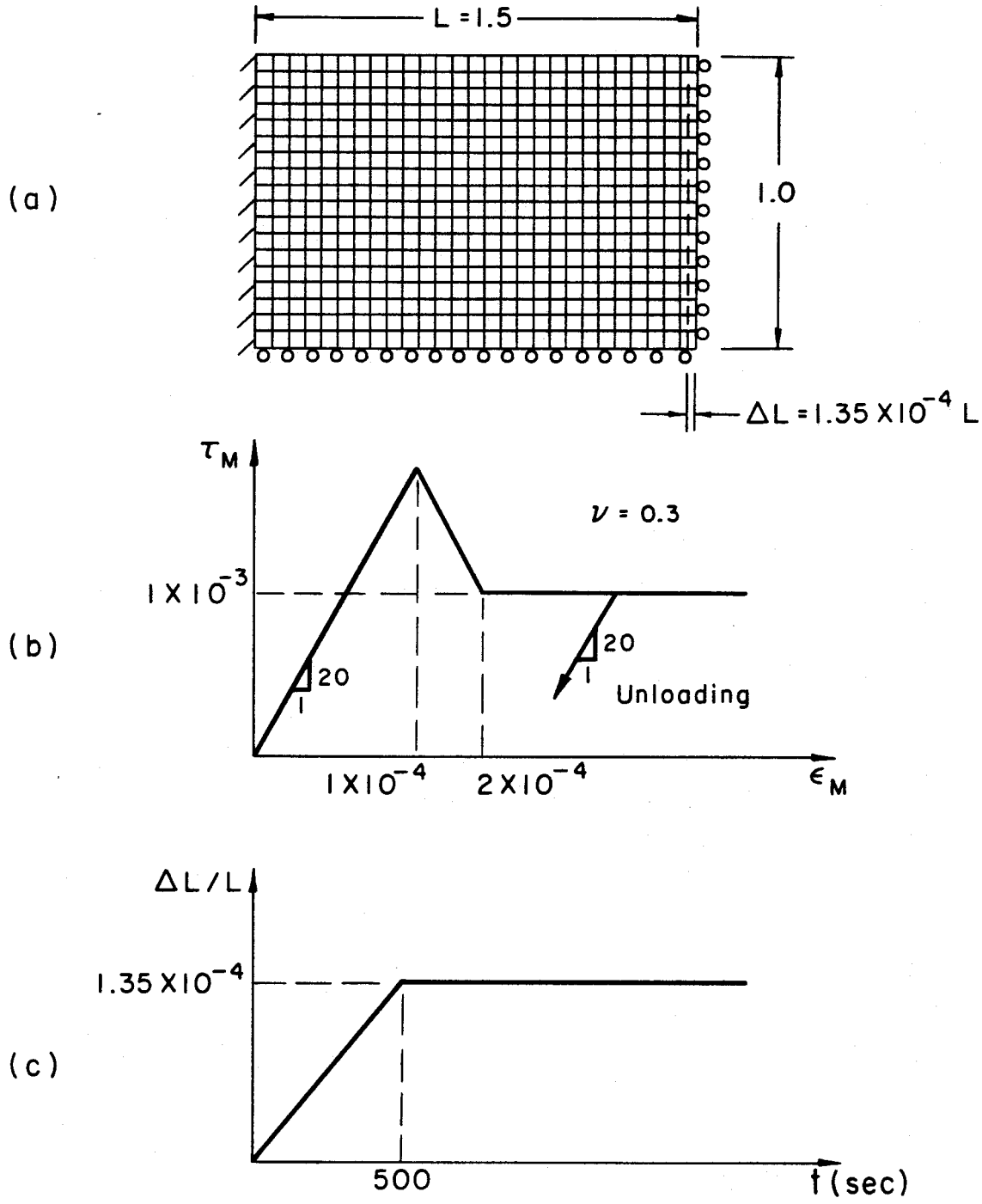

Figure 8.1 Bar compression problem
(a) Idealization and finite difference mesh
(b) Constitutive relation
(c) Displacement-controlled loading

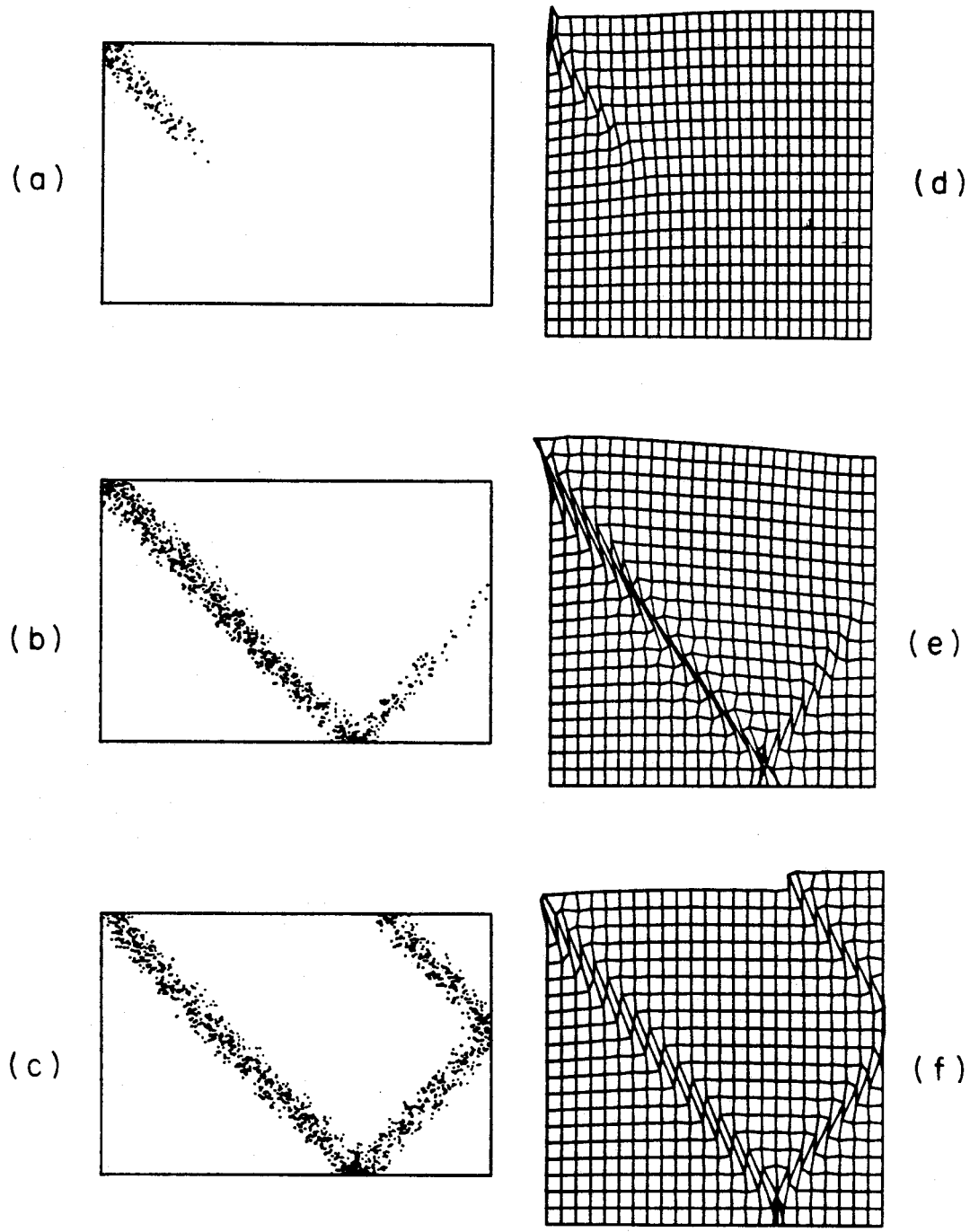

Figure 8.2 Bar compression results
(a) to (c) Shear strains exceeding yield level
(d) to (f) Exaggerated deformed mesh
(a),(c) 800 time steps (473 seconds)
(b),(e) 900 time steps (528 seconds)
(c),(f) 1100 time steps (639 seconds)

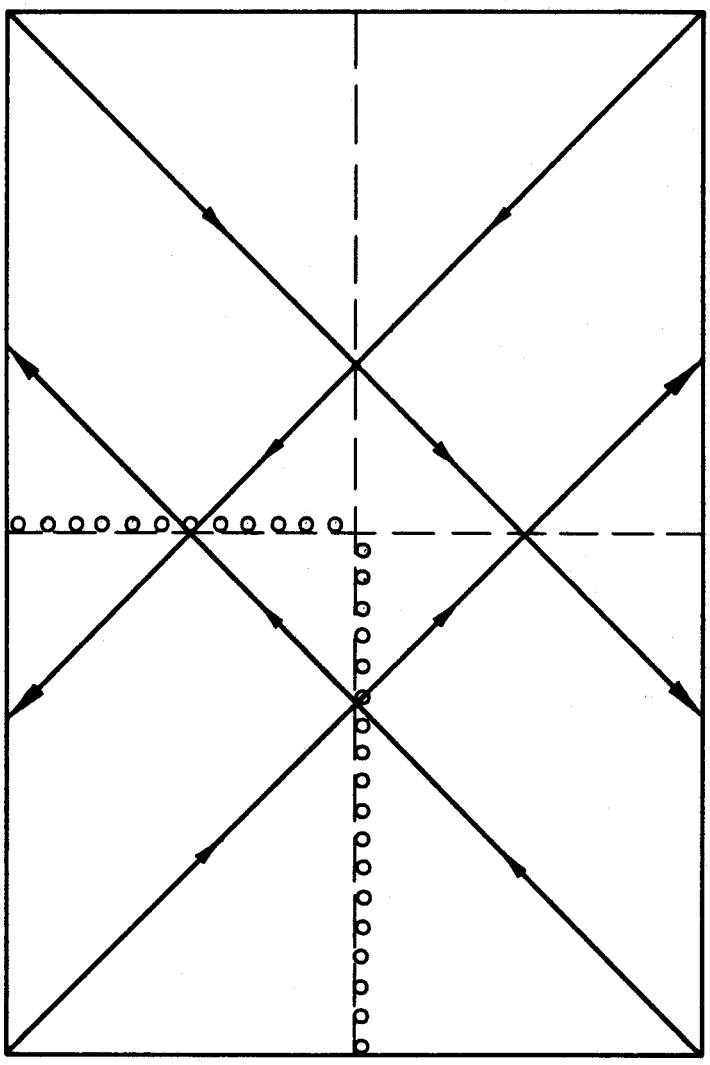

Figure 8.3 Development of shear bands throughout bar compression specimen

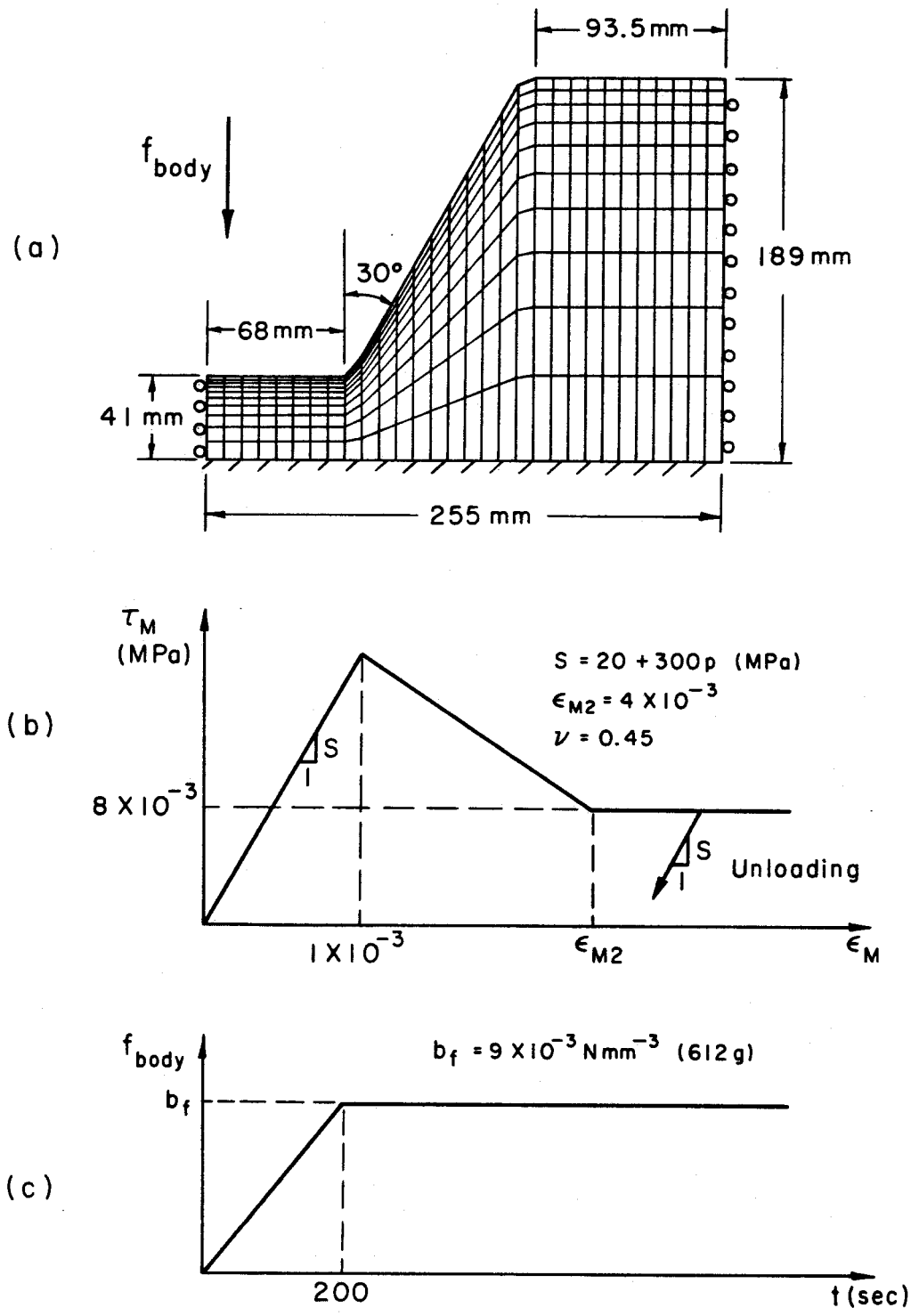

Figure 8.4 Centrifuge slope stability problem
(a) Idealization and finite difference mesh
(b) Constitutive relation
(c) Body force loading

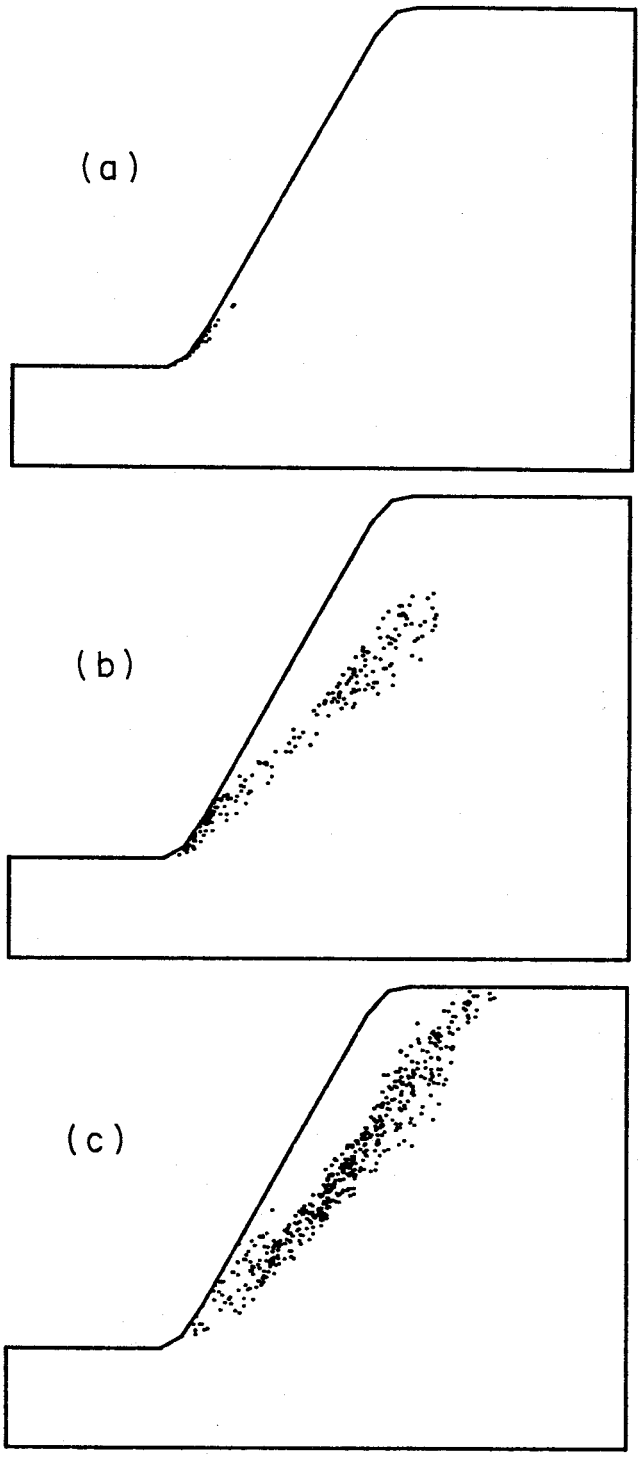

Figure 8.5 Centrifuge slope stability results for parameters of Figure 8.4
(a) 600 time steps (293 seconds)
(b) 900 time steps (470 seconds)
(c) 1200 time steps (639 seconds)

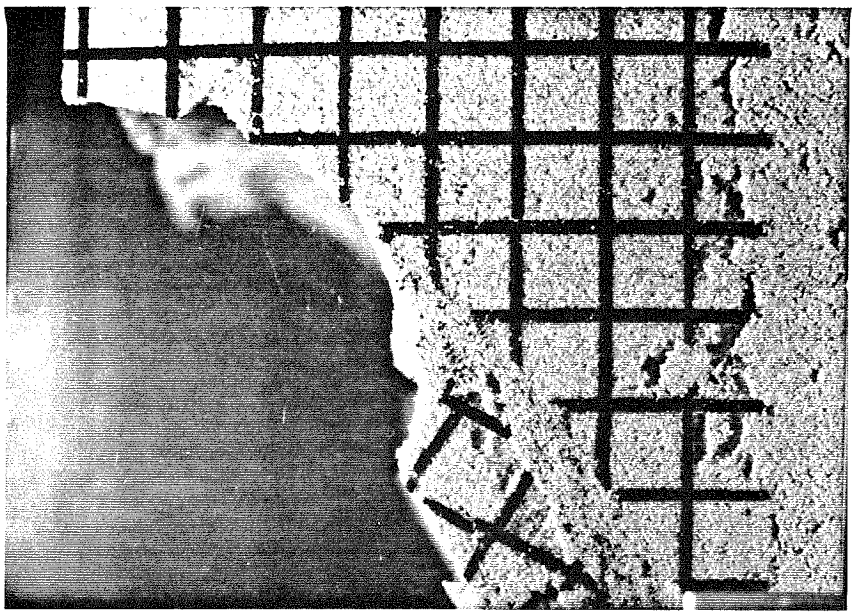

(b)

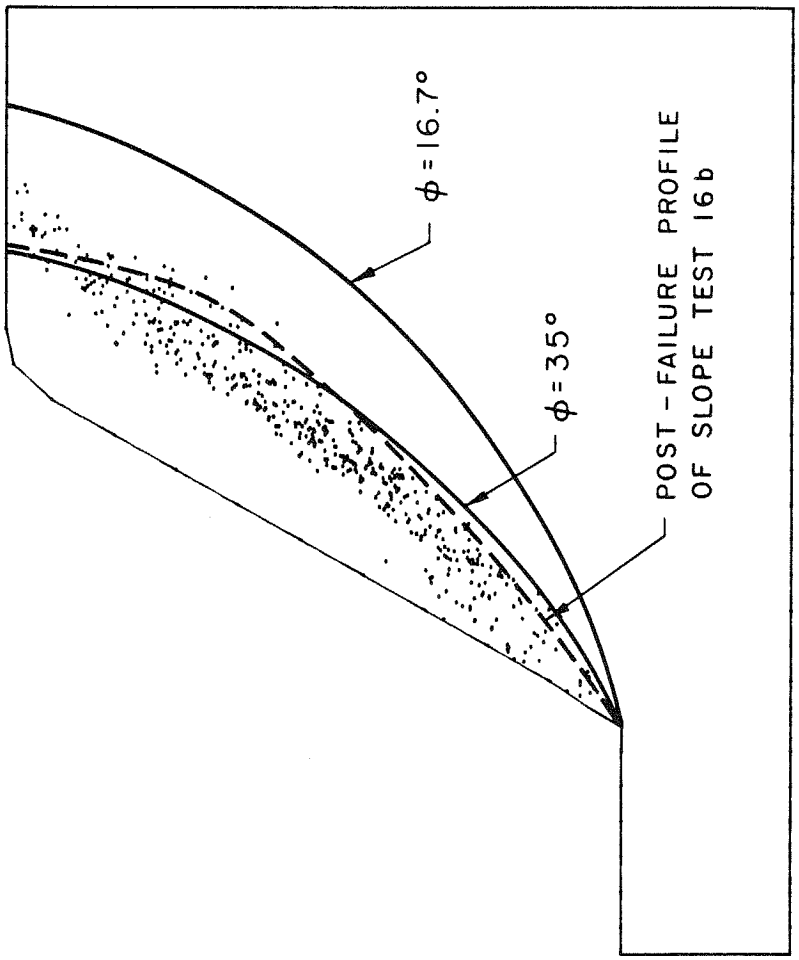

(a)

Figure 8.6 Comparison of analytical and experimental slope failure results
(a) Reproduction of Figure 8.5(c) superposed with critical Taylor slip circles for $\phi = 16.7°$ and $\phi = 35°$, and post-failure profile of slope test 16b
(b) Reproduction of post-failure profile of centrifuge slope test 16b

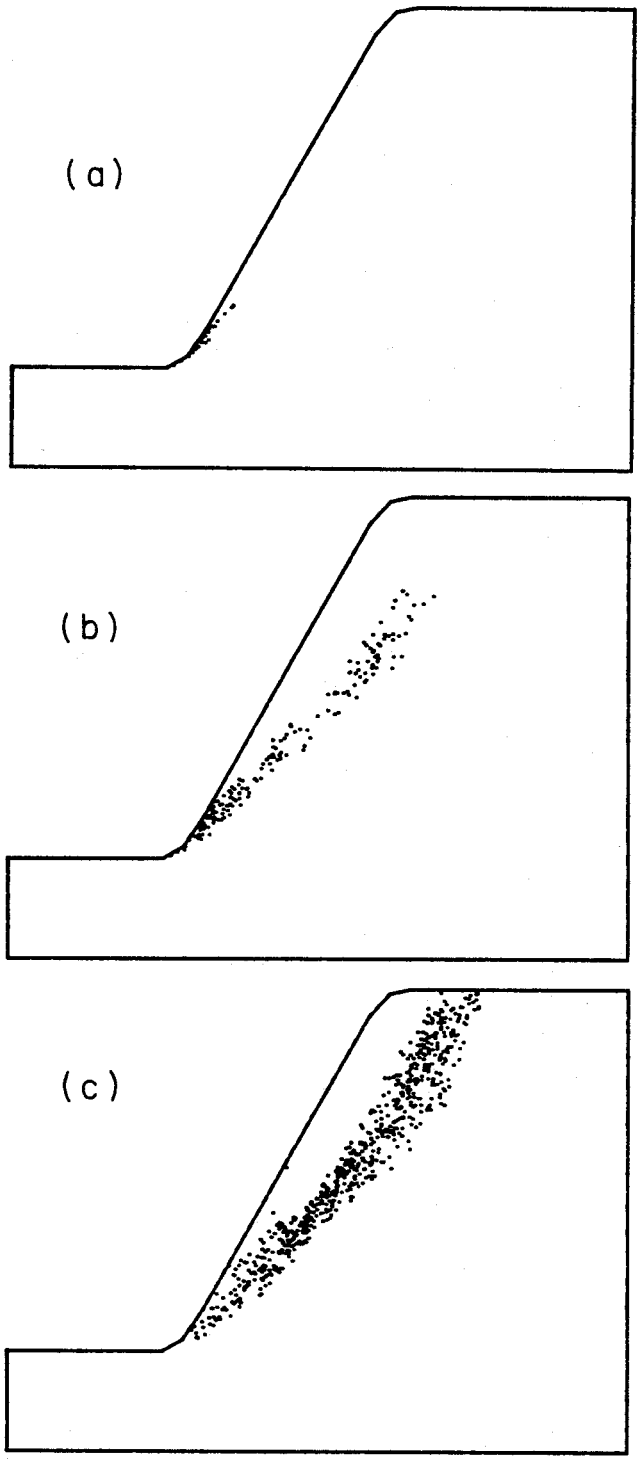

Figure 8.7 Centrifuge slope stability results for $\nu = 0.45$, $\epsilon_{M2} = 2 \times 10^{-3}$ and $612g$ body force
(a) 600 time steps (293 seconds)
(b) 800 time steps (410 seconds)
(c) 1000 time steps (510 seconds)

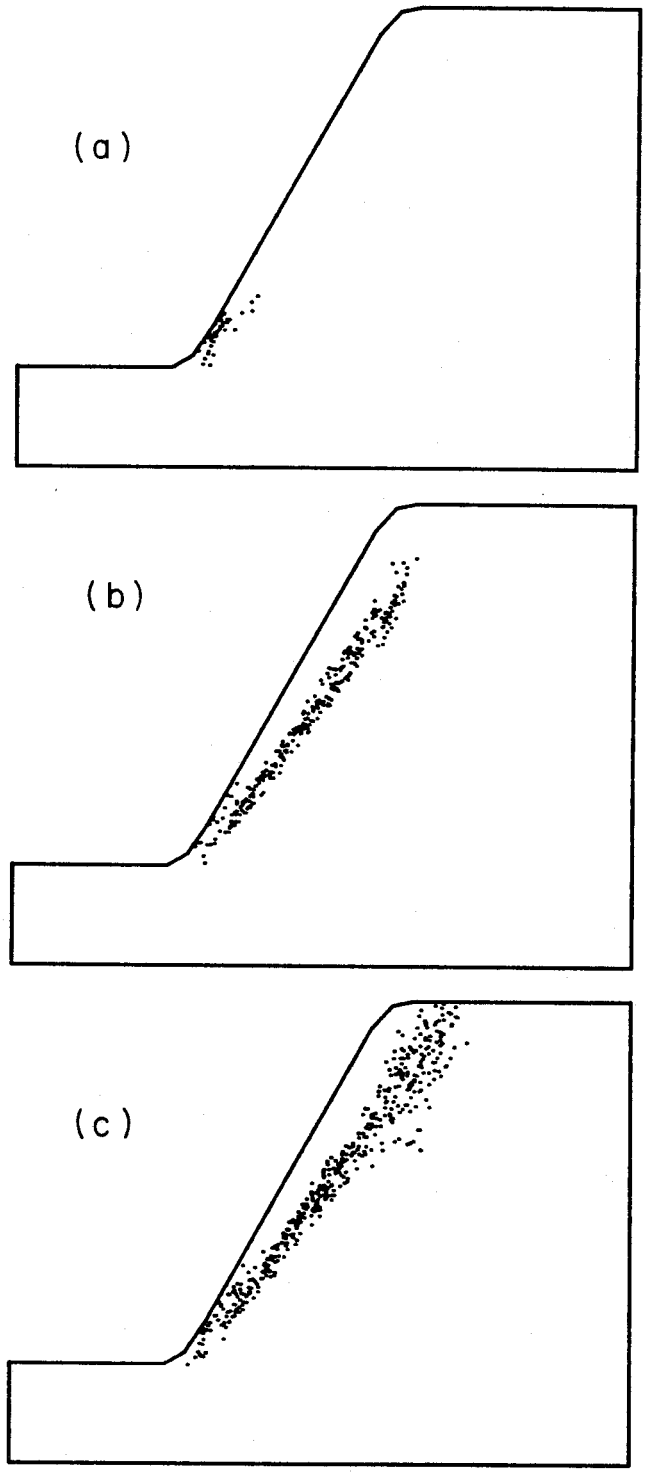

Figure 8.8 Centrifuge slope stability results for $\nu = 0.45$, $\epsilon_{M2} = 2 \times 10^{-3}$ and $340g$ body force
(a) 2000 time steps (1136 seconds)
(b) 2500 time steps (1409 seconds)
(c) 3000 time steps (1625 seconds)

Mesh size in nodes $i \times j$	**Mesh size in zones**	**Approximate minimum gravity load for failure**
16×6	15×5	$480g$
31×11	30×10	$320g$
61×21	60×20	$220g - 250g$
151×51	150×50	$150g - 200g$

Table 8.1 Reduction in slope failure load with increasing fineness of finite difference mesh

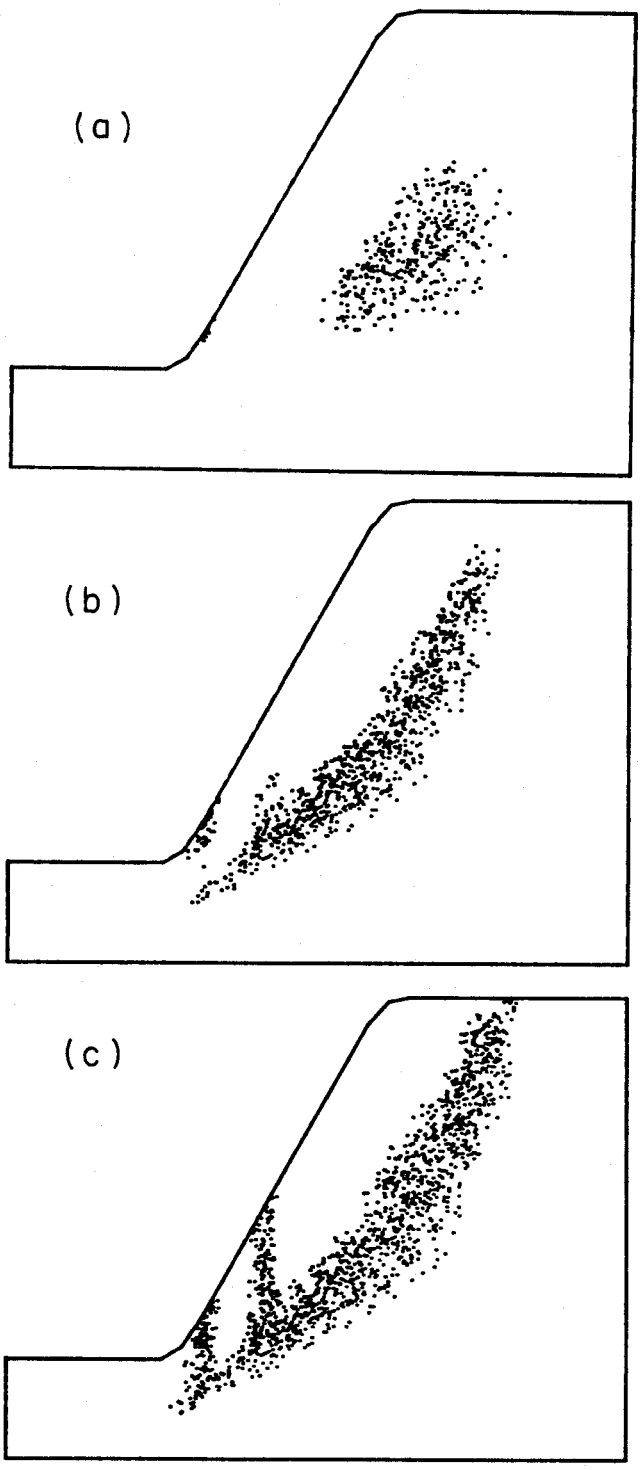

Figure 8.9 Centrifuge slope stability results for $\nu = 0.3$, $\epsilon_{M2} = 2 \times 10^{-3}$ and $340g$ body force
(a) 400 time steps (198 seconds)
(b) 500 time steps (245 seconds)
(c) 600 time steps (287 seconds)

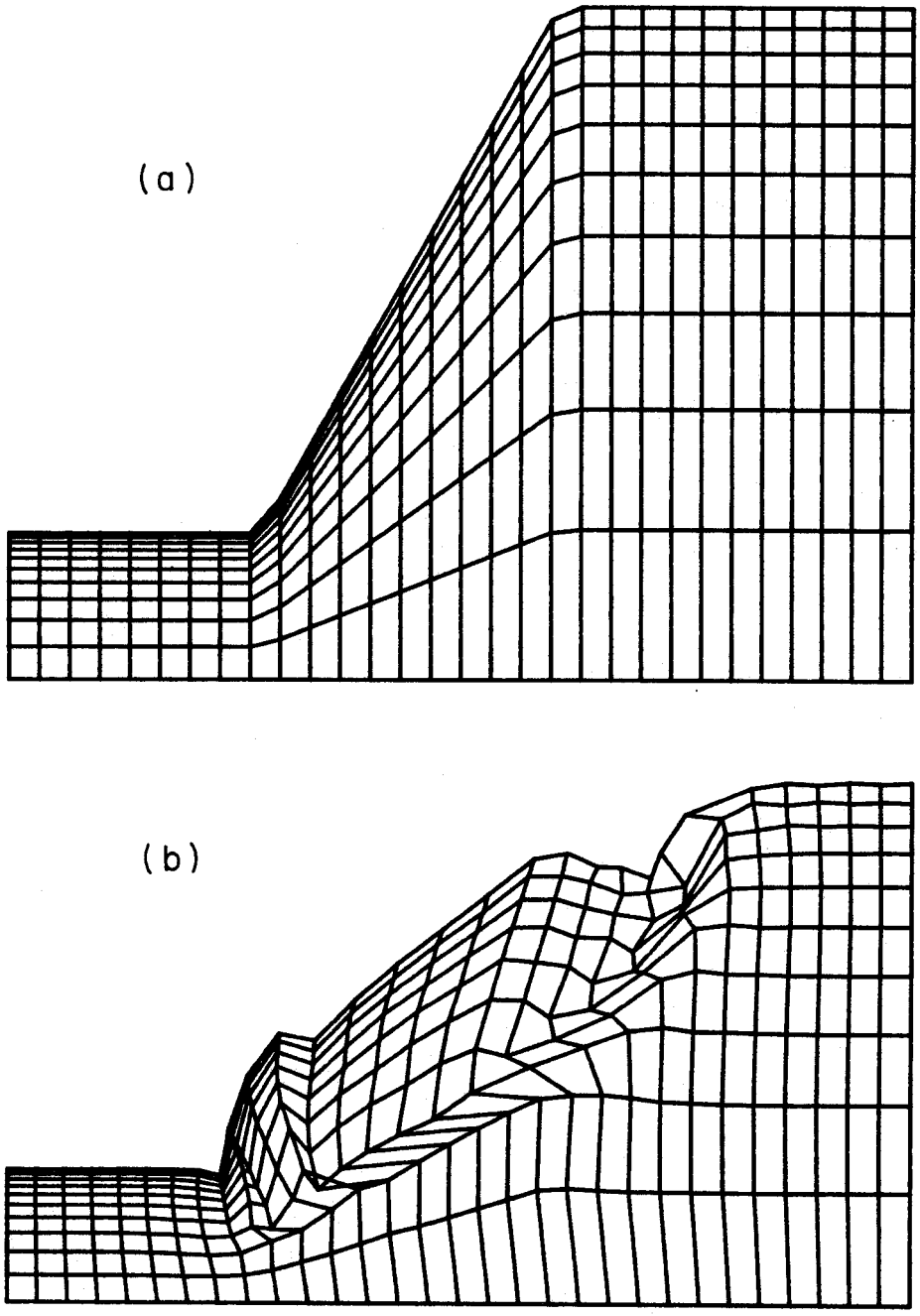

Figure 8.10 Centrifuge slope stability results for $\nu = 0.3$, $\epsilon_{M2} = 2 \times 10^{-3}$ and $340g$ body force
(a) Undeformed finite difference mesh (initial conditions)
(b) Exaggerated deformed finite difference mesh corresponding to Figure 8.9(c) (600 time steps, 287 seconds)

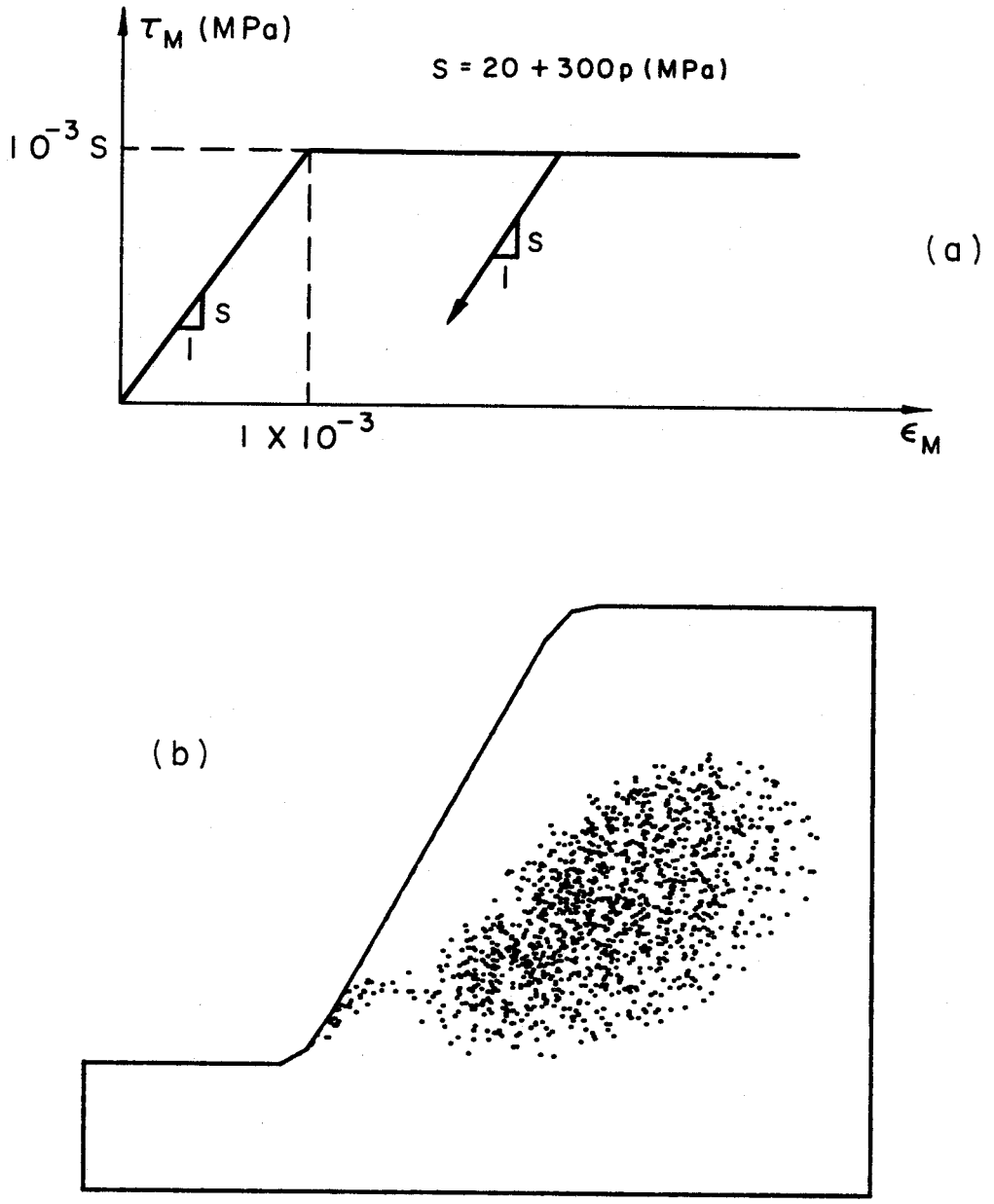

Figure 8.11 Centrifuge slope stability results for elastic-perfectly plastic constitutive relation ($\nu = 0.3$, $340g$ body force)
(a) Constitutive relation
(b) Distribution of shear strain exceeding yield (1×10^{-3}) after 600 time steps (315 seconds)

Chapter 9

CONCLUSIONS AND RECOMMENDATIONS

9.1 CONCLUSIONS

A series of two-dimensional model slope tests has been conducted in a geotechnical centrifuge to determine the mechanism of slope failure and subsequent slope collapse by direct observation. These experiments have shown that shear failure is initiated at the slope toe and propagated rapidly to the slope crest as a displacement discontinuity across a sharply defined, curved failure surface. Slope collapse may then occur by relative sliding between the two blocks of essentially undeformed material separated by the failure surface, with collapse being similarly observed to start at the toe and proceed as a "chain reaction" to the crest. It is also concluded that in spite of the very brittle nature of the model slope material, which made it rather dissimilar to real soil, the centrifuge slope failures exhibited the same distinct failure surface and final collapse profile as seen in full-scale failures in the field (*e.g.*, [98,104]), and thus the centrifuge tests were a valid means of studying the initiation and propagation of failure in prototype slopes.

In parallel with the centrifuge experiments, a finite difference method of anal-

ysis has been applied to the slope stability problem and found capable of representing the observed mechanism of failure by localization of shear deformation. Both the centrifuge model tests and finite difference results establish that slope failure in a brittle material occurs at a well-defined loading threshold, below which failure will not propagate. Progressive failure may still, however, be a valid description of the failure mechanism in a slope of plastic soil such as overconsolidated clay.

Of possibly greater importance, however, is the apparent capacity of this finite difference algorithm to predict shear failure mechanisms in the solid continua of many different fields of study (*e.g.*, foundation engineering, structural engineering, material science, seismology).

9.2 RECOMMENDATIONS

The experimental and analytical results of this research have contributed to a better understanding of slope failure but have also uncovered a need for further study. In particular, continuation of the centrifuge experiments is warranted, with different slope angles and materials (*e.g.*, overconsolidated clay), to determine the effect of these parameters on the mechanism of failure, and to resolve uncertainties in the nonuniformity of the slope specimen, brittle versus ductile soil behavior, and the role of crest tension cracking in the initiation and propagation of failure through the slope.

With regard to analytical estimation of slope failure, the finite difference algo-

rithm would benefit from inclusion of a tension failure criterion, improvements to the constitutive model to more closely represent real soil behavior, and modification of the dynamic relaxation procedure to permit real dynamic (*e.g.*, earthquake) analysis. A more detailed study of the effect of mesh fineness on failure load is also recommended.

Continuation of both the centrifuge experiments and finite difference analyses should also be used to further investigate the prototype performance of natural slopes, and man-made embankments, excavations and dams. The real effects of inhomogeneity, anisotropy, construction stress, pore water pressure and flow, and time (including aging and creep), are all likely to influence the mechanism, as well as the load and deformation conditions, under which failure and collapse of full-scale slopes will occur.

REFERENCES

[1] Abeyaratne, R.C., "Discontinuous Deformation Gradients Away from the Tip of a Crack in Anti-Plane Shear," *Journal of Elasticity*, **11** (1981) 373–393

[2] Abeyaratne, R. and N. Triantafyllidis, "The Emergence of Shear Bands in Plane Strain," *International Journal of Solids and Structures*, **17** (1981) 1113–1134

[3] Aboim, C., Scott, R.F., Lee, J.R., and Roth, W.H., "Centrifuge Earth Dam Studies: Earthquake Tests and Analyses," *Final Report to National Science Foundation* (1986) (Grant No. CEE–7926691)

[4] Al-Hussaini, M.M., D.J. Goodings, A.N. Schofield and F.C. Townsend, "Centrifugal Modelling of Coal Waste Embankments," *Journal of the Geotechnical Engineering Division, ASCE*, **107** (1981) 481–499

[5] Altiero, N.J. and G. Gioda, "An Integral Equation Approach to Fracture Propagation in Rocks," *Rivista Italiana di Geotecnica*, **16** (1982) 55–64

[6] Ambraseys, N.N. and S.K. Sarma, "The Response of Earth Dams to Strong Earthquakes," *Géotechnique*, **17** (1967) 181–213

[7] Asaro, R.J., "Material Modelling and Failure Modes in Metal Plasticity," *Mechanics of Materials*, **4** (1985) 343–373

[8] Avgherinos, P.J., "Centrifugal Testing of Models Made of Soil," *Ph.D. Thesis*, Cambridge University (1969)

[9] Baker, R. and M. Garber, "Theoretical Analysis of the Stability of Slopes," *Géotechnique*, **28** (1978) 395–411

[10] Bathe, K.-J., *Finite Element Procedures in Engineering Analysis*, Prentice-Hall, Englewood Cliffs (1982)

[11] Bishop, A.W., "The Use of the Slip Circle in the Stability Analysis of Slopes," *Géotechnique*, **5** (1955) 7–17

[12] Bishop, A.W., "Progressive Failure — With Special Reference to the Mechanism Causing It," *Proceedings of the Geotechnical Conference, Oslo*, **2** (1967) 142–154

[13] Bishop, A.W. and D.J. Henkel, *The Measurement of Soil Properties in the Triaxial Test*, Arnold, London (1957)

[14] Bishop, A.W. and N.R. Morgenstern, "Stability Coefficients for Earth Slopes," *Géotechnique*, **10** (1960) 129–150

[15] Bjerrum, L., "The Third Terzaghi Lecture: Progressive Failure in Slopes of Overconsolidated Plastic Clay and Clay Shales," *Journal of the Soil Mechanics and Foundations Division, ASCE*, **93** SM5 (1967) 3–49

[16] Bowles, J.E., *Engineering Properties of Soils and Their Measurement*, 2nd ed., McGraw-Hill, New York (1978)

[17] Chowdhury, R.N., *Slope Analysis*, Elsevier, Amsterdam (1978)

[18] Chugh, A.K., "Slope Stability Analysis for Earthquakes," *International Journal for Numerical and Analytical Methods in Geomechanics*, **6** (1982) 307–322

[19] Clough, R.W. and R.J. Woodward, "Analysis of Embankment Stresses and Deformations," *Journal of the Soil Mechanics and Foundations Division, ASCE*, **93** SM4 (1967) 529–549

[20] Collin, A. (1846), *Landslides in Clays*, W.R. Schriever translation, University of Toronto Press (1956)

[21] Craig, W.H., "Model Studies of the Stability of Clay Slopes," *Ph.D. Thesis*, University of Manchester (1974)

[22] Crouch, S.L. and A.M. Starfield, *Boundary Element Methods in Solid Mechanics*, George Allen and Unwin, London (1983)

[23] Day, A.S., "An Introduction to Dynamic Relaxation," *The Engineer (London)*, **219** (1965) 218–221

[24] de Josselin de Jong, G., "A Variational Fallacy," *Géotechnique*, **31** (1981) 289–290

[25] Dugdale, D.S., "Yielding of Steel Sheets Containing Slits," *Journal of the Mechanics and Physics of Solids*, **8** (1960) 100–104

[26] Endicott, L.J., "Centrifugal Testing of Soil Models," *Ph.D. Thesis*, Cambridge University (1970)

[27] Erdogan, F. and G.C. Sih, "On the Crack Extension in Plates Under Plane Loading and Transverse Shear," *Journal of Basic Engineering*, **85** (1963) 519–527

[28] Fellenius, W., "Calculation of Stability of Earth Dams," *Transactions of the Second Congress on Large Dams, Washington D.C.*, **4** (1936) 445–459

[29] Fragazy, R.J. and J.A. Cheney, "Drum Centrifuge Studies of Overconsolidated Slopes," *Journal of the Geotechnical Engineering Division, ASCE*, **107** (1981) 843–858

[30] Fuglsang, L.D., "Preliminary Centrifugal Studies of the Deformation and Failure of Uniform Earth Slopes," *M.Sc. Thesis*, University of Manchester (1971)

[31] Goodings, D.J., "Centrifugal Modelling of Slope Failures," *Ph.D. Thesis*, Cambridge University (1979)

[32] Goodings, D.J. and A.N. Schofield, "A Centrifuge Model Study of Slope Instability in Ottawa Area Champlain Sea Clay," *Canadian Geotechnical Journal*, **22** (1985) 102–109

[33] Griffith, A.A., "The Phenomena of Rupture and Flow in Solids," *Philosophical Transactions of the Royal Society of London*, **A221** (1921) 163–198

[34] Griffith, A.A., "The Theory of Rupture," *Proceedings of the First International Congress of Applied Mechanics, Delft*, (1924) 55–63

[35] Gurtin, M.E., *An Introduction to Continuum Mechanics*, Academic Press, New York (1981)

[36] Gurtin, M.E., "Topics in Finite Elasticity," *Society for Industrial and Applied Mathematics (SIAM)*, Publication 35 (1981)

[37] Hayashi, K. and S. Nemat-Nasser, "Energy-Release Rate and Crack Kinking Under Combined Loading," *Journal of Applied Mechanics*, **48** (1981) 520–524

[38] Hellan, K., *Introduction to Fracture Mechanics*, McGraw-Hill, New York (1984)

[39] Hermann, W. and L.D. Bertholf, "Explicit Lagrangian Finite-Difference Methods," *Computational Methods for Transient Analysis*, T. Belytschko and T.J.R. Hughes, eds., Elsevier, Amsterdam (1983) 361–416

[40] Hill, R. and J.W. Hutchinson, "Bifurcation Phenomena in the Plane Tensile Test," *Journal of the Mechanics and Physics of Solids*, **23** (1975) 239–264

[41] Hird, C.C., "Centrifugal Model Tests of Flood Embankments," *Ph.D. Thesis*, University of Manchester (1974)

[42] Iooss, G. and D.D. Joseph, *Elementary Stability and Bifurcation Theory*, Springer-Verlag, New York (1980)

[43] Irwin, G.R., "Analysis of Stresses and Strains Near the End of a Crack Traversing a Plate," *Journal of Applied Mechanics*, **24** (1957) 361–364

[44] Jackson, C.P. and K.H. Winters, "A Finite-Element Study of the Bénard Problem Using Parameter-Stepping and Bifurcation Search," *International Journal for Numerical Methods in Fluids*, **4** (1984) 127–145

[45] Janbu, N., "Application of Composite Slip Surfaces for Stability Analysis," *Proceedings of the European Conference on Stability of Earth Slopes, Stockholm*, **3** (1954) 43–50

[46] Janbu, N., "Earth Pressures and Bearing Capacity Calculations by Generalized Procedure of Slices," *Proceedings of the Fourth International Conference on Soil Mechanics and Foundation Engineering, London*, **2** (1957) 207–212

[47] Keller, J.B. and S. Antman, eds., *Bifurcation Theory and Nonlinear Eigenvalue Problems*, Benjamin, New York (1969)

[48] Kim, M.M., "Centrifugal Model Testing of Soil Slopes," *Ph.D. Thesis*, University of Colorado (1980)

[49] Kjellman, W., "Mechanics of Large Swedish Landslides," *Géotechnique*, **5** (1955) 74–78

[50] Knowles, J.K. and E. Sternberg, "On the Failure of Ellipticity and the Emergence of Discontinuous Deformation Gradients in Plane Finite Elastostatics," *Journal of Elasticity*, **8** (1978) 329–379

[51] Kubíček, M. and M. Marek, *Computational Methods in Bifurcation Theory and Dissipative Structures*, Springer-Verlag, New York (1983)

[52] Kutter, B.L., "Behaviour of Embankments Under Dynamic Loading," *M.Phil. Thesis*, Cambridge University (1979)

[53] LeMonds, J., R.J. Asaro and A. Needleman, "A Numerical Study of Localized Deformation in Bi-Crystals," *Mechanics of Materials*, **4** (1985) 417–435

[54] Lu, T.D. and R.F. Scott, "The Distribution of Stresses and Development of Failure at the Toe of a Slope and Around the Tip of a Crack," *Applications of the Finite Element Method in Geotechnical Engineering*, U.S. Army Engineer Waterways Experiment Station, Vicksburg (1972) 385–430

[55] Lyndon, A., "Centrifugal Model Test of a Natural Clay Slope Failure," *Ph.D. Thesis*, University of Manchester (1972)

[56] Lyndon, A. and A.N. Schofield, "Centrifugal Model Test of a Short-Term Failure in London Clay," *Géotechnique*, **20** (1970) 440–442

[57] Lyndon, A. and A.N. Schofield, "Centrifugal Model Tests of the Lodalen Landslide," *Canadian Geotechnical Journal*, **15** (1978) 1–13

[58] McMeeking, R.M. and J.R. Rice, "Finite-Element Formulations for Problems of Large Elastic-Plastic Deformation," *International Journal of Solids and Structures*, **11** (1975) 601–616

[59] Mikasa, M., N. Takada and K. Yamada, "Centrifugal Model Test of a Rockfill Dam," *Proceedings of the Seventh International Conference on Soil Mechanics and Foundation Engineering, Mexico*, **2** (1969) 325–333

[60] Morgenstern, N.R. and V.E. Price, "The Analysis of the Stability of General Slip Surfaces," *Géotechnique*, **15** (1965) 79–93

[61] Naylor, D.J., G.N. Pande, B. Simpson and R. Tabb, *Finite Elements in Geotechnical Engineering*, Pineridge Press, Swansea (1981)

[62] Needleman, A., "A Numerical Study of Necking in Circular Cylindrical Bars," *Journal of the Mechanics and Physics of Solids*, **20** (1972) 111–127

[63] Needleman, A., "Non-Normality and Bifurcation in Plane Strain Tension and Compression," *Journal of the Mechanics and Physics of Solids*, **27** (1979) 231–254

[64] Needleman, A. and V. Tvergaard, "Necking of Biaxially Stretched Elastic-Plastic Circular Plates," *Journal of the Mechanics and Physics of Solids*, **25** (1977) 159–183

[65] Newmark, N.M., "A Method of Computation for Structural Dynamics," *Journal of the Engineering Mechanics Division, ASCE*, **85** EM3 (1959) 67–94

[66] Newmark, N.M., "Effects of Earthquakes on Dams and Embankments," *Géotechnique*, **15** (1965) 139–159

[67] Ortiz, L.A., Scott, R.F., and Lee, J., "Dynamic Centrifuge Testing of a Cantilever Retaining Wall," *Earthquake Engineering and Structural Dynamics*, **11** (1983) 251–268

[68] Padfield, C.J., "The Stability of River Banks and Flood Embankments," *Ph.D. Thesis*, Cambridge University (1978)

[69] Palmer, A.C. and J.R. Rice, "The Growth of Slip Surfaces in the Progressive Failure of Over-Consolidated Clay," *Proceedings of the Royal Society of London*, **A332** (1973) 527–548

[70] Papadrakakis, M., "A Method for the Automated Evaluation of the Dynamic Relaxation Parameters," *Computational Methods in Applied Mechanics and Engineering*, **25** (1981) 35–48

[71] Peck, R.B., "Stability of Natural Slopes," *Journal of the Soil Mechanics and Foundations Division, ASCE*, **93** SM4 (1967) 403–417

[72] Peirce, D., R.J. Asaro and A. Needleman, "An Analysis of Nonuniform and Localized Deformation in Ductile Single Crystals," *Acta Metallurgica*, **30** (1982) 1087–1119

[73] Prévost, J.H. and T.J.R. Hughes, "Finite-Element Solution of Elastic-Plastic Boundary-Value Problems," *Journal of Applied Mechanics*, **48** (1981) 69–74

[74] Rabinowitz, P.H., ed., *Applications of Bifurcation Theory*, Academic Press, New York (1977)

[75] Revilla, J. and E. Castillo, "The Calculus of Variations Applied to Stability of Slopes," *Géotechnique*, **27** (1977) 1–11

[76] Rice, J.R., "A Path Independent Integral and the Approximate Analysis of Strain Concentration by Notches and Cracks," *Journal of Applied Mechanics*, **35** (1968) 379–386

[77] Rice, J.R., "The Localization of Plastic Deformation," *Theoretical and Applied Mechanics*, W.T. Koiter, ed., North-Holland, Amsterdam, *(Proceedings of the Fourteenth International Congress of Theoretical and Applied Mechanics, Delft)*, **1** (1976) 207–220

[78] Rice, J.R., R.M. McMeeking, D.M. Parks and E.P. Sorensen, "Recent Finite Element Studies in Plasticity and Fracture Mechanics," *Computer Methods in Applied Mechanics and Engineering*, **17/18** (1979) 411–442

[79] Rice, J.R. and J.W. Rudnicki, "A Note on Some Features of the Theory of Localization of Deformation," *International Journal of Solids and Structures*, **16** (1980) 597–605

[80] Rowe, P.W., "The Stress-Dilatancy Relation for Static Equilibrium of an Assembly of Particles in Contact," *Proceedings of the Royal Society of London*, **A269** (1962) 500–527

[81] Rudnicki, J.W. and J.R. Rice, "Conditions for the Localization of Deformation in Pressure-Sensitive Dilatant Materials," *Journal of the Mechanics and Physics of Solids*, **23** (1975) 371–394

[82] Sarma, S.K., "Stability Analysis of Embankments and Slopes," *Géotechnique*, **23** (1973) 423–433

[83] Sarma, S.K., "Seismic Stability of Earth Dams and Embankments," *Géotechnique*, **25** (1975) 743–761

[84] Sarma, S.K., "Stability Analysis of Embankments and Slopes," *Journal of the Geotechnical Engineering Division, ASCE*, **105** (1979) 1511–1524

[85] Sarma, S.K. and M.V. Bhave, "Critical Acceleration Versus Static Factor of Safety in Stability Analysis of Earth Dams and Embankments," *Géotechnique*, **24** (1974) 661–665

[86] Schofield, A.N., "Use of Centrifuge Model Testing to Assess Slope Stability," *Canadian Geotechnical Journal*, **15** (1978) 14–31

[87] Schofield, A.N., "Cambridge Geotechnical Centrifuge Operations," *Géotechnique*, **30** (1980) 227–267

[88] Scott, R.F., *Principles of Soil Mechanics*, Addison-Wesley, Reading (1963)

[89] Scott, R.F., "Centrifuge Studies of Cyclic Lateral Load-Displacement Behavior of Single Piles," *Soil Mechanics Laboratory*, Division of Engineering and Applied Science, California Institute of Technology (1977)

[90] Scott, R.F., "Slope Stability Studies in the Centrifuge," *International Symposium on Landslides, Roorkee*, **1** (1980)

[91] Scott, R.F., "Centrifuge Model Testing at Caltech," *Soil Dynamics and Earthquake Engineering*, **2** (1983) 188–198

[92] Scott, R.F., *Personal Communication*

[93] Seed, H.B., "A Method for Earthquake Resistant Designs of Earth Dams," *Journal of the Soil Mechanics and Foundations Division, ASCE*, **92** SM1 (1966) 13–41

[94] Seed, H.B. and R.E. Goodman, "Earthquake Stability of Slopes of Cohesionless Soils," *Journal of the Soil Mechanics and Foundations Division, ASCE*, **90** SM6 (1964) 43–73

[95] Seed, H.B. and H.A. Sultan, "Stability Analyses for a Sloping Core Embankment," *Journal of the Soil Mechanics and Foundations Division, ASCE*, **93** SM4 (1967) 69–83

[96] Seed, H.B. and I.M. Idriss, "Soil Moduli and Damping Factors for Dynamic Response Analyses," *Earthquake Engineering Research Center Report No. EERC 70–10*, University of California, Berkeley (1970)

[97] Seed, H.B., I.M. Idriss, K.L. Lee and F.I. Makdisi, "Dynamic Analysis of the Slide in the Lower San Fernando Dam During the Earthquake of February 9, 1971," *Journal of the Geotechnical Engineering Division, ASCE*, **101** (1975) 889–911

[98] Sevaldson, R.A., "The Slide in Lodalen, October 6th, 1954," *Géotechnique*, **6** (1956) 167–182

[99] Sih, G.C., "Introductory Chapter: A Special Theory of Crack Propagation," *Mechanics of Fracture* **1**, Noordhoff, Leyden (1972)

[100] Silling, S.A., "CHIMP–A Computer Program for Finite Elastostatics," *Applied Mechanics Technical Report No. 54*, Division of Engineering and Applied Science, California Institute of Technology (1985)

[101] Silling, S.A., "Singularities and Phase Transitions in Elastic Solids: Numerical Studies and Stability Analysis," *Ph.D. Thesis*, California Institute of Technology (1986)

[102] Skempton, A.W., "Long Term Stability of Clay Slopes," *Géotechnique*, **14** (1964) 77–101

[103] Skempton, A.W., "First-Time Slides in Overconsolidated Clays," *Géotechnique*, **20** (1970) 320–324

[104] Skempton, A.W. and J. Hutchinson, "Stability of Natural Slopes and Embankment Foundations," *Proceedings of the Seventh International Conference on Soil Mechanics and Foundation Engineering, Mexico*, State of the Art Volume (1969) 291–340

[105] Smith, I.M. and R. Hobbs, "Finite Element Analysis of Centrifuged and Built-Up Slopes," *Géotechnique*, **24** (1974) 531–559

[106] Spencer, E., "A Method of Analysis of the Stability of Embankments Assuming Parallel Inter-Slice Forces," *Géotechnique*, **17** (1967) 11–26

[107] Taylor, D.W., "Stability of Earth Slopes," *Journal of the Boston Society of Civil Engineers*, **24** (1937) 197–246

[108] Taylor, D.W., *Fundamentals of Soil Mechanics*, Wiley, New York, 1948

[109] Ter-Stepanian, G. and M.N. Goldstein, "Multi-Storied Landslides and Strength of Soft Clay," *Proceedings of the Seventh International Conference on Soil Mechanics and Foundation Engineering, Mexico*, **2** (1969) 693–700

[110] Terzaghi, K., *Theoretical Soil Mechanics*, Wiley, New York (1943) 146

[111] Toki, K., F. Miura and Y. Oguni, "Dynamic Slope Stability Analyses with a Non-Linear Finite Element Method," *Earthquake Engineering and Structural Dynamics*, **13** (1983) 151–171

[112] Tvergaard, V., A. Needleman and K.K. Lo, "Flow Localization in the Plane Strain Tensile Test," *Journal of the Mechanics and Physics of Solids*, **29** (1981) 115–142

[113] Underwood, P., "Dynamic Relaxation," *Computational Methods for Transient Analysis*, T. Belytschko and T.J.R. Hughes, eds., Elsevier, Amsterdam (1983) 245–265

[114] Vardoulakis, I., M. Goldscheider and G. Gudehus, "Formation of Shear Bands in Sand Bodies as a Bifurcation Problem," *International Journal for Numerical and Analytical Methods in Geomechanics*, **2** (1978) 99–128

[115] Wang, F.D., M.C. Sun and D.M. Ropchan, *Computer Program for Pit Slope Stability Analysis by the Finite Element Stress Analysis and Limiting Equilibrium Method*, RI 7685, Bureau of Mines (1972)

[116] Wu, C.-H., "Maximum-Energy-Release-Rate Criterion Applied to a Tension-Compression Specimen with Crack," *Journal of Elasticity*, **8** (1978) 235–257

[117] Wu, C.-H., "Fracture Under Combined Loads by Maximum-Energy-Release-Rate Criterion," *Journal of Applied Mechanics*, **45** (1978) 553–558

[118] Zienkiewicz, O.C., *The Finite Element Method*, 3rd ed., McGraw-Hill, London (1977)

Appendix A

COMPUTATION OF DILATATIONAL WAVE SPEED

The sound speed c_1 for dilatational waves in the x_1- direction is given by

$$c_1^2 = \frac{1}{\rho_0}\frac{\partial \sigma_{11}}{\partial e_{11}} \tag{A.1}$$

pectively, the plane strain components of the Piola

tensors, and ρ_0 is the mass density in the reference

(A.1), the constitutive relation (7.40) in the form

$$= -p(\theta)\delta_{\alpha\beta} + 2S(\theta)\left(e_{\alpha\beta} - \frac{\theta}{3}\delta_{\alpha\beta}\right) \tag{A.2}$$

$$r_{11} = -p(\theta) + 2S(\theta)\left(e_{11} - \frac{\theta}{3}\right) \quad . \tag{A.3}$$

Differentiating (A.3) with respect to e_{11} gives

$$\frac{\partial \sigma_{11}}{\partial e_{11}} = -\frac{dp}{d\theta}\frac{\partial \theta}{\partial e_{11}} + 2S(\theta)\left(1 - \frac{1}{3}\frac{\partial \theta}{\partial e_{11}}\right) + 2\frac{dS}{d\theta}\left(e_{11} - \frac{\theta}{3}\right) \quad . \tag{A.4}$$

But $\partial\theta/\partial e_{11} = 1$ from (7.30) so that differentiation of (7.37) with respect to θ gives

$$\begin{aligned}\frac{dp}{d\theta} &= \frac{-f_\nu S_1}{1 + f_\nu S_2 \theta} + \frac{f_\nu^2 S_1 S_2 \theta}{(1 + f_\nu S_2 \theta)^2} \\ &= K\left[-1 + \frac{f_\nu S_2 \theta}{1 + f_\nu S_2 \theta}\right] \quad ,\end{aligned} \tag{A.5}$$

using (7.36). Applying the chain rule to evaluate $dS/d\theta$ yields

$$\begin{aligned}\frac{dS}{d\theta} &= \frac{dS}{dp}\frac{dp}{d\theta} \\ &= S_2 K\left[-1+\frac{f_\nu S_2\theta}{1+f_\nu S_2\theta}\right]\end{aligned} \tag{A.6}$$

on the basis of (7.31) and (A.5). Combining (A.4), (A.5) and (A.6),

$$\begin{aligned}\frac{\partial\sigma_{11}}{\partial e_{11}} &= -K\left[-1+\frac{f_\nu S_2\theta}{1+f_\nu S_2\theta}\right]+\frac{4S(\theta)}{3}+2S_2K\left[-1+\frac{f_\nu S_2\theta}{1+f_\nu S_2\theta}\right]\left(e_{11}-\frac{\theta}{3}\right) \\ &= K\left[-1+2S_2\left(e_{11}-\frac{\theta}{3}\right)\right]\left[-1+\frac{f_\nu S_2\theta}{1+f_\nu S_2\theta}\right]+\frac{4S(\theta)}{3}\quad ,\end{aligned} \tag{A.7}$$

which holds for θ assumed to be non-positive (see (7.35)). Only the largest wave speed in any direction is of interest, and therefore, from the Mohr's circle of strain of Figure A.1, the most negative of the principal strains e_* is used for e_{11}, where

$$e_* = \frac{\theta}{2} - \epsilon_M \tag{A.8}$$

and ϵ_M is the radius of the Mohr's circle of strain given by (7.28). The strain term in parentheses in (A.7) then becomes

$$e_{11}-\frac{\theta}{3} = e_*-\frac{\theta}{3} = \frac{\theta}{6}-\epsilon_M \tag{A.9}$$

which, in conjunction with (A.1) and the remaining terms of (A.7), yields

$$c^2 = \frac{1}{\rho_0}\left\{K(\theta)\left[-1+2S_2\left(\frac{\theta}{6}-\epsilon_M\right)\right]\left[-1+\frac{f_\nu S_2\theta}{1+f_\nu S_2\theta}\right]+\frac{4S(\theta)}{3}\right\} \tag{A.10}$$

for the dilatational wave speed, where the subscript "1" on c_1 has simply been dropped.

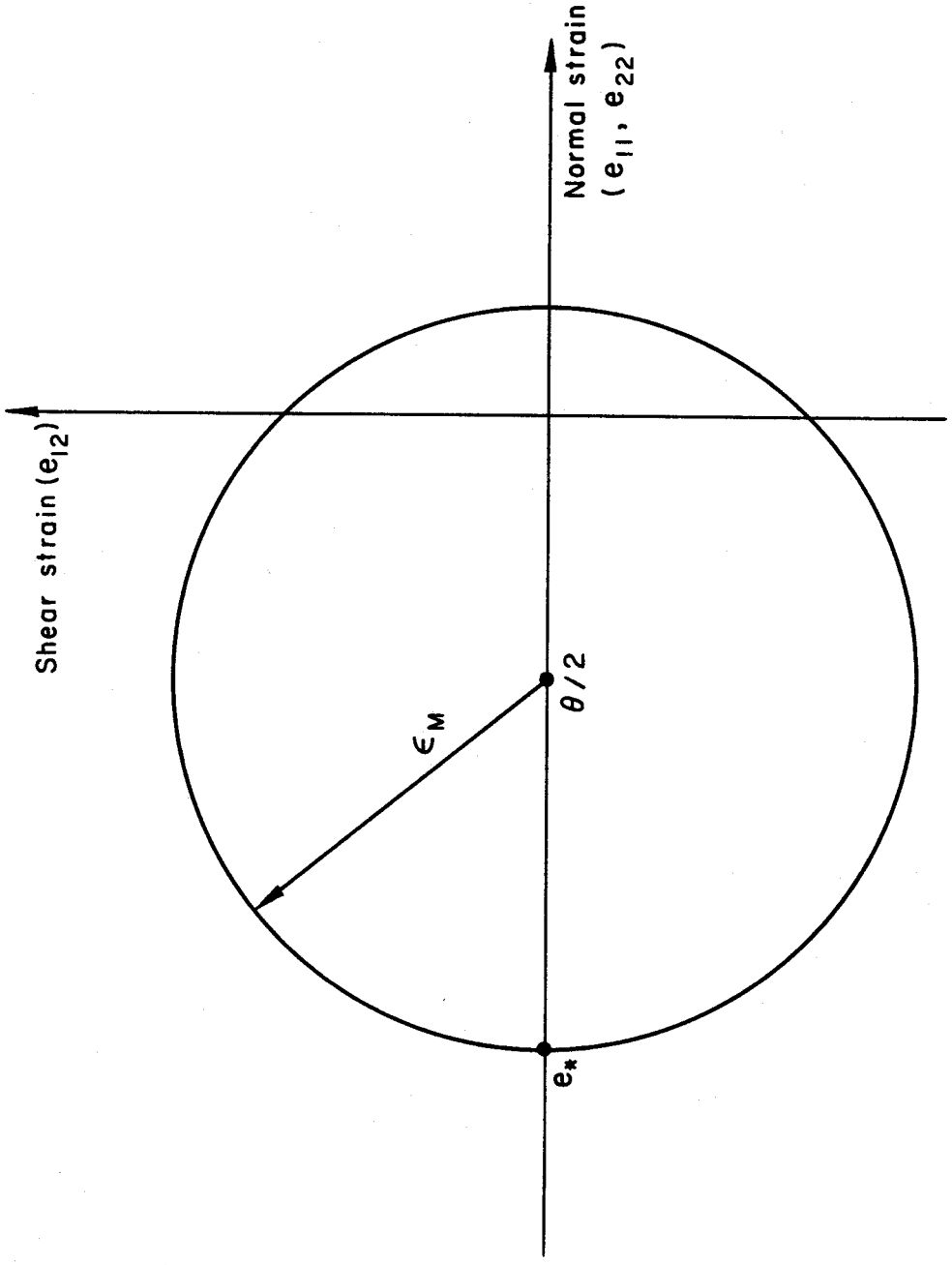

Figure A.1 Mohr's circle of strain